

KAUNAS UNIVERSITY OF TECHNOLOGY

ERNESTAS KASPARAVIČIUS

STABILITY OF ORGANIC HOLE  
TRANSPORTING MATERIALS AND WAYS TO  
ENHANCE IT USING CARBAZOLE AND  
DITHIENO[3,2-B:2',3'-D]-PYRROLE  
DERIVATIVES

Doctoral Dissertation  
Natural Sciences, Chemistry (N 003)

2021, Kaunas

This doctoral dissertation was prepared at Kaunas University of Technology, Faculty of Chemical Technology, Department of Organic Chemistry, during the period of 2016–2020. The studies were supported by the Research Council of Lithuania

**Scientific Supervisor:**

Assoc. Prof. Dr. Tadas MALINAUSKAS (Kaunas University of Technology, Natural Sciences, Chemistry, N 003).

Editor: Brigita Brasienė and Rozita Znamenskaitė (Publishing house “Technologija”).

KAUNO TECHNOLOGIJOS UNIVERSITETAS

ERNESTAS KASPARAVIČIUS

ORGANINIŲ SKYLES PERNEŠANČIŲ  
PUSLAIDININKIŲ STABILUMO IR BŪDŲ JAM  
GERINTI, NAUDOJANT KARBAZOLO IR  
DITIEN[3,2-B:2', 3'-D]PIROLO DARINIUS,  
TYRIMAS

Daktaro disertacija  
Gamtos mokslai, chemija (N 003)

2021, Kaunas

Disertacija rengta 2016-2020 metais Kauno technologijos universiteto Cheminės technologijos fakultete Organinės chemijos katedroje. Mokslinius tyrimus rėmė Lietuvos mokslo taryba;

**Mokslinis vadovas:**

Doc. dr. Tadas MALINAUSKAS (Kauno technologijos universitetas, gamtos mokslai, chemija, N003).

Redagavo:

Brigita Brasienė ir Rozita Znamenskaitė (leidykla „Technologija“).

## TABLE OF CONTENTS

1.	INTRODUCTION .....	10
2.	LITERATURE REVIEW .....	14
2.1.	Perovskite solar cells .....	14
2.1.1.	Perovskite solar cell architectures .....	15
2.1.2.	Main perovskite compositions used in PSC .....	16
2.1.3.	Most common perovskite problems .....	18
2.2.	HTMs for perovskite solar cells .....	19
2.2.1.	Small molecule organic hole transporting materials .....	19
2.2.2.	Organic dopant-free hole transporting materials .....	23
2.2.3.	Polymeric hole transporting materials .....	26
2.2.4.	Chapter summary .....	28
2.3.	Dithieno[3,2-b:2',3'-d]pyrrole derivatives .....	28
2.3.1.	Synthesis of dithieno[3,2-b:2',3'-d]pyrrole .....	29
2.3.2.	Synthesis of functionalized DTP small molecules .....	32
2.3.3.	Synthesis of functionalized DTP polymers .....	37
2.3.4.	Application of DTP in optoelectronic devices .....	40
2.3.5.	Application of DTP derivatives in PSC .....	42
2.3.6.	Chapter summary .....	44
3.	RESULTS AND DISCUSSION .....	45
3.1.	Dithieno[3,2-b:2',3'-d]pyrrole-based hole transporting materials .....	45
3.1.1.	Synthesis of dithieno[3,2-b:2',3'-d]pyrrole-based materials .....	45
3.1.2.	Thermal properties .....	49
3.1.3.	Optical, electrochemical and photoelectrical properties .....	51
3.1.4.	Chapter summary .....	56
3.2.	Long-term stability of the oxidized hole transporting materials used in perovskite solar cells .....	57
3.2.1.	Interaction with dopants used in perovskite solar cells .....	57
3.2.1.1.	Synthesis of the oxidized HTMs .....	58
3.2.1.2.	Thermal properties .....	59
3.2.1.3.	Long-term stability of the oxidized HTMs in the solution .....	61
3.2.1.4.	Long-term stability of the oxidized HTMs in the thin films .....	71
3.2.1.5.	Chapter summary .....	75
3.2.2.	Interaction with perovskite material .....	75
3.2.2.1.	Interaction of the oxidized HTM with perovskite forming components .....	76
3.2.2.2.	Interaction of the oxidized HTM with films of various perovskites .....	80
3.2.2.3.	Chapter summary .....	86
3.3.	Materials capable of forming self-assembled hole transporting monolayer .....	86
3.3.1.	Dimethoxydiphenylamine substituted carbazole and fluorene derivatives .....	87
3.3.1.1.	Synthesis of the compounds .....	88

3.3.1.2. Thermal and optical properties .....	89
3.3.1.3. Photoelectrical properties and photovoltaic performance in PSC ...	91
3.3.1.4. Chapter summary .....	94
3.3.2. Dithieno[3,2-b:2',3'-d]pyrrole based derivatives.....	94
3.3.2.1. Synthesis of dithieno[3,2-b:2',3'-d]pyrrole-based materials containing anchoring group.....	94
3.3.2.2. Optical, photoelectrical properties and photovoltaic performance in PSC .....	96
3.3.2.3. Chapter summary .....	98
3.3.3. Carbazole-based small molecule derivatives.....	98
3.3.3.1. Synthesis of carbazole derivatives .....	98
3.3.3.2. Thermal, optical and photoelectrical properties.....	100
3.3.3.3. Performance in perovskite single-junction solar cells.....	107
3.3.3.4. Versatility of SAM contact and tandem solar cell integration.....	110
3.3.3.5. Integration into monolithic perovskite/silicon tandem solar cells.	113
3.3.3.6. Stability assessment .....	116
3.3.3.7. Chapter summary .....	119
4. METHODS AND MATERIAL .....	120
4.1. General methods .....	120
4.2. Film preparation for the long-term stability testing of oxidized HTMs .....	125
4.3. Determination of iodine content in the mixtures of spiro[TFSI] <sub>2</sub> and FAI by iodometric titration .....	128
4.4. Determination of iodine content in the mixtures of spiro[TFSI] <sub>2</sub> and MAI by iodometric titration .....	129
4.5. Materials.....	130
5. CONCLUSIONS .....	163
6. REFERENCES .....	165
7. CURRICULUM VITAE.....	186
8. LIST OF PUBLICATIONS AND CONFERENC S .....	188
9. APPENDIX .....	190
10. ACKNOWLEDGEMENTS.....	227

## LIST OF ABBREVIATIONS AND PHYSICAL UNITS

$\Delta$	reflux temperature;
$\delta$	chemical shift parameter;
$^{13}\text{C}$ NMR	carbon ( $^{13}\text{C}$ ) nuclear magnetic resonance;
$^1\text{H}$ NMR	proton nuclear magnetic resonance;
Ac	acetic;
AgTFSI	silver bis(trifluoromethanesulfonyl)imide;
AIBN	2,2'-azobisisobutyronitrile;
ALD	atomic layer deposition;
Aliph	aliphatic;
Ar	aromatic;
BCP	bathocuproine;
BHJ-SC	bulk heterojunction solar cells;
BINAP	(R)-(+)-(1,1'-binaphthalene-2,2'-diyl)bis(diphenylphosphine);
$\text{C}_{60}$	buckminsterfullerene;
$\text{CDCl}_3$	deuterated chloroform;
CIGSe	copper indium gallium selenide solar cell;
CSA	camphorsulfonic acid;
CTL	charge transporting layer;
c-TiO <sub>2</sub>	compact layer of TiO <sub>2</sub> ;
CV	cyclic voltammetry;
<i>d</i> 8-THF	tetrahydrofuran- <i>d</i> 8;
DCM	dichloromethane;
DMF	<i>N,N</i> -dimethylformamide;
DMSO	dimethyl sulfoxide;
DMSO- <i>d</i> 6	dimethyl sulfoxide- <i>d</i> 6;
DSC	differential scanning calorimetry;
DTP	dithieno[3,2- <i>b</i> :2',3'- <i>d</i> ]pyrrole;
$E_g^{\text{op}}$	optical band gap;
$E_{\text{HOMO}}$	ionization energy;
$E_{\text{LUMO}}$	electron affinity;
EPIC	European Perovskite Initiative Consortium;
ETL	electron transporting layer;
ETM	electron transporting material;
EXO	exothermic;
eq	equivalent;
EQE	external quantum efficiency;
FA	formamidinium;
FAI	formamidinium iodide;
FF	fill factor;
FK209	tris(2-(1 <i>H</i> -pyrazol-1-yl)-4- <i>tert</i> -butylpyridine)cobalt(III) tri[bis(trifluoromethane)sulfonimide];

FTO	fluorine-doped tin oxide;
HOMO	highest occupied molecular orbital;
HPLC	high-performance liquid chromatography;
Ht	heterocyclic;
HTL	hole transporting layer;
HTM	hole transporting material;
$I_p$	ionization potential;
ITO	indium tin oxide;
IZO	indium zinc oxide;
$J_{sc}$	short-circuit current density;
LDA	lithium diisopropylamide;
J-V	current density–voltage characteristic;
Li-TFSI	bis(trifluoromethane) sulfonimide lithium salt;
LUMO	lowest unoccupied molecular orbital;
MA	methylammonium;
MABr	methylammonium bromide;
MAI	methylammonium iodide;
MAPI	$\text{CH}_3\text{NH}_3\text{PbI}_3$ ;
Me	methyl;
MeOD	methanol-d4;
MPP	maximum power point;
mp-TiO <sub>2</sub>	mesoscopic layer of TiO <sub>2</sub> ;
MS	mass spectrometry;
NaOtBu	sodium <i>tert</i> -butoxide;
NBS	<i>N</i> -bromosuccinimide;
NCS	<i>N</i> -chlorosuccinimide;
NMR	nuclear magnetic resonance;
NIS	<i>N</i> -iodosuccinimide;
OFET	organic field effect transistor;
OLED	organic light emitting diode;
OPV	organic photovoltaics;
P3HT	poly(3-hexylthiophene-2,5-diyl);
PC <sub>61</sub> BM	[6,6]-phenyl-C61-butyric acid methyl ester;
PCE	power conversion efficiency;
Pd <sub>2</sub> dba <sub>3</sub>	tris(dibenzylideneacetone)dipalladium(0);
Pd(OAc) <sub>2</sub>	palladium(II) acetate;
Pd(PPh <sub>3</sub> ) <sub>4</sub>	tetrakis(triphenylphosphine)palladium(0);
PEDOT:PSS	poly(3,4-ethylenedioxythiophene) polystyrene sulfonate;
PESA	photoelectron spectroscopy in air;
PL	photoluminescence;
poly-TPD	4-butyl- <i>N,N</i> -diphenylaniline homopolymer;
ppm	parts per million;
PTAA	poly[bis(4-phenyl)(2,4,6-trimethylphenyl)amine];
[ <i>P</i> ( <i>t</i> -Bu) <sub>3</sub> H]BF <sub>4</sub>	tri- <i>tert</i> -butylphosphonium tetrafluoroborate;



PSC	perovskite solar cell;
rpm	revolutions per minute;
RT	room temperature;
SAM	self-assembled monolayer;
SC	solar cell;
SEM	scanning electron microscopy;
spiro-MeOTAD	2,2',7,7'-tetrakis-( <i>N,N</i> -di- <i>p</i> -methoxyphenylamine)-9,9'-spirobifluorene;
SHJ	silicon hetero junction;
<i>T</i>	temperature;
TBAB	tetrabutylammonium bromide;
tBP	4- <i>tert</i> -butylpyridine;
t-Bu <sub>3</sub> P	tri- <i>tert</i> -butylphosphine;
<i>T<sub>cryst</sub></i>	crystallization temperature;
TCO	transparent conductive oxide;
<i>T<sub>dec</sub></i>	thermal decomposition temperature;
TFSI	bis(trifluoromethane)sulfonimide;
Thio	thiophene temperature;
<i>T<sub>g</sub></i>	glass transition temperature;
TGA	thermogravimetric analysis;
THF	tetrahydrofuran;
TLC	thin-layer chromatography;
<i>T<sub>m</sub></i>	melting temperature;
TosN <sub>3</sub>	<i>p</i> -toluenesulfonyl azide;
UPS	ultraviolet photoelectron spectroscopy;
UV	ultraviolet;
UV-vis	ultraviolet-visible light;
<i>V<sub>OC</sub></i>	open-circuit voltage;
V886	9,9'-[1,2-Phenylenebis(methylene)]bis[N <sub>3</sub> ,N <sub>3</sub> ,N <sub>6</sub> ,N <sub>6</sub> -tetrakis(4-methoxyphenyl)-9 <i>H</i> -carbazole-3,6-diamine];
V862	9,9'-(thiene-2,5-diyl)dimethylidene)bis[N,N,N',N'-tetrakis(4-methoxyphenyl)-9 <i>H</i> -fluorene-2,7-diamine];
XPhos Pd G2	chloro(2-dicyclohexylphosphino-2',4',6'-triisopropyl-1,1'-biphenyl)[2-(2'-amino-1,1'-biphenyl)]palladium(II).

## 1. INTRODUCTION

Due to the sharp increase in CO<sub>2</sub> concentration and resulting global warming, the EU has committed itself to achieve 25 % of electricity consumption from renewable sources by 2030. Solar energy is the most powerful source of renewable energy: the Earth's surface receives about 178 TWh of solar energy per hour, while the world's annual demand is only 1,400 TWh. Therefore, the energy needs of society can be fully met with the proper development of solar cell (SC) technology. In recent years, perovskite solar cells (PSC) have attracted a great deal of interest from scientists and industry working on the development of a new generation of photovoltaic devices, and their efficiency has already exceeded 25 %. Compared to the commercial silicon SC, the PSC are characterized by construction simplicity and relatively cheap raw materials. According to the Web of Science, more than 3000 articles have been published on the subject in recent year; a series of known semiconductors are being tested in PSC as well as new materials are being developed and patented, and the demand for the latter is growing rapidly every year. This growth is further guaranteed by the fact that these materials are attractive not only for PSC, but also for the development of other low-cost, high-performance optoelectronic devices, such as light-emitting diodes, phototransistors, photo-sensors etc. On the 6<sup>th</sup> of September in 2019, the European Perovskite Initiative Consortium (EPIC) in its White Paper announced the prospects for the PSC technology. It outlines the potential benefits of production and costs, the adaptation of different products and the overall plan of the European research community. EPIC forecasts the further development of PSC technology and the construction of devices demonstrating 30 % efficiency by 2028. Another very important aspect of this technology is its compatibility with current silicon SC available on the market. Combined, these technologies can form tandem SC with higher overall performance than the individual components. In this way, the existing industrial infrastructure (e.g., BodGroup, SoliTek, Precizika-MET SC, Saulės energija, etc. in Lithuania) can be effectively used to create a new generation of SC.

Although PSC efficiency has risen at a record pace over the last ten years (from 3.8 % to 25.2 %), there are still obstacles remaining to their commercialization. In particular, the problem of insufficient stability of PSC devices remains. Currently, PSCs are significantly lagging behind the commercial silicon solar cells in their longevity. To date, the processes leading to such an outcome have not been thoroughly investigated yet. If this problem is not solved, PSC technology will remain a "very interesting" but impractical idea.

Although perovskite light absorber demonstrates an efficient transport of both types of carriers, PSC devices without a layer of hole transporting material do not show an impressive efficiency; in fact, it is less than 14 %. Currently, the best performance in the PSC devices is achieved by using hole transporting organic semiconductors spiro-MeOTAD and PTAA. Unfortunately, due to their complex synthesis procedures, they are particularly expensive. Furthermore, spiro-MeOTAD, like many other organic semiconductors used in PSC, has low conductivity ( $10^{-5} \text{ S} \times \text{cm}^{-2}$ ). As a result, such semiconductors must be doped with various additives,

such as bis(trifluoromethane) sulfonimide lithium salt. During doping, the organic semiconductor is partially oxidized, thus increasing its conductivity; however, it is suspected that the aforementioned procedure can be one of the causes of PSC instability. Therefore, it is particularly important to investigate the stability of neutral and oxidized organic semiconductors in interaction with dopants and other PSC components.

Currently, the films of the most popular hole transporting materials used in PSC (e.g., PTAA, poly-TPD, PEDOT:PSS, spiro-MeOTAD) are formed by spin-coating. Unfortunately, this method of film formation is unsuitable for larger scale production due to high wastage, more than 90 % of the material land on the walls of the apparatus and not on the substrate. Alternatively, the vacuum deposition method can be used, although its application is only possible for small molecules. It is known that reducing the thickness of the hole transporting layer increases the SC fill factor, but as layer gets thinner, the open circuit voltage drops significantly, mostly due to incomplete surface coverage by the semiconductor layer. The above-mentioned film deposition problems can be circumvented by self-assembling monolayer (SAM) technology, it can provide high-quality coating of the required surface (including textured and rough surfaces), minimal layer thickness, minimal parasitic absorption, low material consumption, does not require the use of dopants and can be used for coating large surfaces. Therefore, it is important to synthesize and investigate compounds that can both form self-assembled monolayers and ensure efficient separation and transfer of positive charges.

**The aim of the work** is the identification of the degradation pathways in organic hole transporting materials used in perovskite solar cells and the development of simple and efficient hole-transporting materials to circumvent them.

**The objectives proposed to achieve the above-stated aim are as follows:**

1. To investigate the degradation process of oxidized hole-transporting materials induced by dopants at elevated temperature;
2. To investigate the degradation process of oxidized hole-transporting materials induced by ion migration from various perovskite absorbers at elevated temperature;
3. To investigate dithieno[3,2-b:2',3'-d]pyrrole-based derivatives as possible hole transporting materials for application in perovskite solar cells;
4. To develop new hole transporting materials capable of forming self-assembling monolayers for use as additive-free hole-selective layer in perovskite solar cells.

**Scientific novelty**

During the past ten years, significant progress has been made in terms of performance of perovskite solar cells, but much less attention has been paid to their long-term stability. Therefore, the next logical step is to address longevity of the devices. The stability of the perovskite solar cells depends on several potential

degradation factors. Some of them are obvious, for example, oxygen and moisture. Others, which are active as well under inert conditions and affect various materials, are harder to determine and eliminate due to the complex, multicomponent nature of the devices. Temperature induced degradation of perovskite solar cells is particularly interesting and an important topic, as device temperatures as high as 80–90 °C could be routinely encountered in the field. In this PhD thesis, the stability of the hole transporting materials at elevated temperatures in combination with various dopants used in the PSC as well as in contact with perovskite itself is studied. The major pathways responsible for the decline of the key characteristics have been identified and investigated.

Second part of the work has capitalized on the information gained in the first half. Hole transporting molecules, capable of forming self-assembling monolayers (SAM) on the surface of the transparent conductive oxides, have been synthesized and characterized. This approach allows for extremely thin films to be formed, thus ensuring good charge transport without the use of dopants or partially oxidized material, hence improving device stability, while maintaining excellent performance. Self-assembled monolayer approach as well simplifies perovskite solar cell construction procedure, as simpler and upscalable deposition methods (spraying, substrate dipping) could be used. Furthermore, due to the covalent linking to the substrate surface, these layers are relatively tolerant against perovskite processing and ensure full coverage of the textured surfaces. Thus, self-assembled hole-transporting monolayer was used for direct integration of perovskite solar cell on top of silicon or rough copper indium gallium selenide solar cells, thus simplifying tandem device construction.

These SAMs outperform the polymer PTAA, the material that enabled the highest performing p–i–n PSCs to date, in efficiency, stability and versatility. With a standard triple-cation absorber, a maximum power conversion efficiency of 20.9 % was demonstrated. Integrating a SAM contact into a monolithic CIGSe/perovskite tandem solar cell led to a stabilized, certified, record power conversion efficiency of 24.16 % on the active area of 1.03 cm<sup>2</sup>, surpassing the values achieved with a complex bilayer or mechanical polishing approaches. Monolithic perovskite/silicon tandem solar cells, constructed using SAM approach, demonstrated maximum certified power conversion efficiency of 29.15 %, which sets a new record for this type of solar cells. Most importantly, the herein demonstrated solar cells are fabricated without additional passivation layers, additives or dopants. Besides the increased power conversion efficiency (PCE), a non-encapsulated cell in ambient air exhibited excellent stability, retaining 95 % of its initial efficiency after 300 h of continuous maximum power point tracking. While devices with PTAA, degraded to 76 % of the initial efficiency after just 90 h.

### **The main statements presented for the defence:**

1. Under the influence of temperature and dopants, oxidized hole transporting materials in the film are reduced to neutral molecules, while in the presence of 4-*tert*-butylpyridine, pyridinated derivative is obtained as well.
2. Under the influence of temperature and iodide ions, migrating from the perovskite layer, the oxidized hole transporting material 2,2',7,7'-tetrakis[*N,N*-di(4-methoxyphenyl)amino]-9,9'-spirobifluorene. dibis(trifluoromethane)sulfonimide salt in the film is reduced to neutral spiro-MeOTAD.
3. Synthesized new hole transporting materials, containing dithieno[3,2-*b*:2',3'-*d*]pyrrole central moiety, are thermally stable, soluble in organic solvents and have suitable ionization potentials ( $I_p = 5.0\text{--}5.6\text{ eV}$ ), thus making them promising candidates for use in perovskite solar cells.
4. Synthesized compounds, containing carbazole central moiety and phosphonic acid anchoring group, form efficient hole selective contacts ensuring very good performance and stability of the perovskite solar cells.

## 2. LITERATURE REVIEW

### 2.1. Perovskite solar cells

During the past 50 years, world's energy consumption has been gradually increasing, while fossil fuels reserves are limited and finite; therefore, research on renewable energy is becoming indisputably relevant for the future energy security. Photovoltaic systems have the potential to play a significant part in electricity generation of the future, while simultaneously considerably reducing negative impact on the environment.

Metal-halide perovskites could play an important role in the next generation of solar cells, as perovskite solar cells have distinct advantages in both low fabrication cost and high efficiency. In a typical PSC device, the perovskite layer, functioning as a light absorber, is sandwiched between two charge-transporting layers and electrodes.

In 2009, T. Miyasaka et al. have published the first paper about the photovoltaic function of the organic-inorganic lead halide perovskites  $\text{CH}_3\text{NH}_3\text{PbBr}_3$  and  $\text{CH}_3\text{NH}_3\text{PbI}_3$  as visible-light sensitizers in liquid-state dye-sensitized solar cells [1]. After this publication, the study of hybrid perovskites and their use in solar cells began to expand very rapidly, and 25.5 % efficient perovskite solar cell has been reported recently [2].

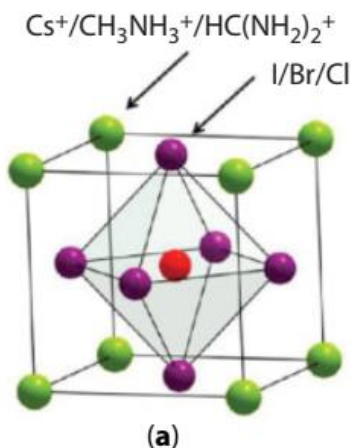


**Figure 2.1.** Crystal structure of  $\text{AMX}_3$  in a unit cell, composed of organic/inorganic cations ( $\text{Cs}^+$ ,  $\text{MA}^+$ ,  $\text{FA}^+$ ) in green, halides ( $\text{I}^-$ ,  $\text{Br}^-$ ,  $\text{Cl}^-$ ) in purple and lead as the metal in red [3]

The organic-inorganic hybrid perovskite, used in photovoltaic research, demonstrates  $\text{AMX}_3$  stoichiometry, where A stands for organic cation, M – metal and X – halide. The  $\text{AMX}_3$  perovskite crystal structure (Figure 2.1) is composed of the organic part ( $\text{MA}^+$ ,  $\text{FA}^+$ ) and the inorganic  $[\text{MX}_6]^{4-}$  octahedra, that share corner halide atoms in all three orthogonal directions, generating infinite three-dimensional  $[\text{MX}_3]^-$  frameworks [3].

### 2.1.1. Perovskite solar cell architectures

A PSC is composed of three main parts: electron transporting layer (ETL), perovskite light absorber and a hole transporting layer (HTL). According to the direction of flow of electrons and holes, PSC can be classified as regular (n-i-p) and inverted (p-i-n), while regular cells are often distributed into planar and mesoporous (Figure 2.2). Regular PSC are constructed by depositing electron transporting material (ETM), such as  $\text{TiO}_2$  or  $\text{SnO}_2$ , on the transparent conductive oxide (TCO), followed by the perovskite film, hole transporting material (HTM) and finally electrode (Au or Ag). In the inverted cell architecture, the order of ETM and HTM layers is inverted [4].

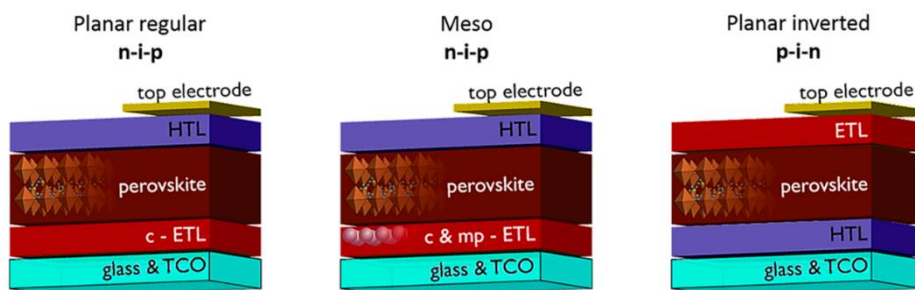


**Figure 2.2.** Schematics of the three PSC architectures: planar regular (n-i-p), mesoporous (n-i-p) and planar inverted (p-i-n) [4]

Mesoporous PSCs are among the first ones to be constructed and investigated, initially; Miyasaka and co-workers used perovskite material in dye-sensitized solar cell configuration together with the liquid electrolyte [1]. The idea was further developed, and recently, J. Seo and co-workers attained power conversion efficiency of 23.3 % for the best-performing mesoporous perovskite solar cell [5]. The device is composed of FTO/ETL ( $\text{c-TiO}_2/\text{mp-TiO}_2$ )/perovskite ( $\text{HTAB}_{0.3}(\text{FAPbI}_3)_{0.95}(\text{MAPbBr}_3)_{0.05}$ )/HTL (P3HT)/Au, and it is especially notable that a PCE 23.0 % is achieved with P3HT as an HTM without any dopants.

The efficiency record for planar n-i-p architecture PSC is reported to be 23.7 %, and it is confirmed for a small area ( $0.07 \text{ cm}^2$ ) cell, fabricated by the Institute for Semiconductors of the Chinese Academy of Sciences [6, 7]. The record was achieved with planar perovskite solar cell consisting of ITO/ETL( $\text{SnO}_2$ )/perovskite ( $\text{FA}_{0.92}\text{MA}_{0.08}\text{PbI}_3$ )/HTL(Spiro-MeOTAD)/Au. The best devices showed an open-circuit voltage ( $V_{\text{OC}}$ ) of 1.17 V, a short-circuit current ( $J_{\text{SC}}$ ) of  $25.40 \text{ mA} \times \text{cm}^{-2}$ , a fill factor (FF) of 79.8 % and a PCE of 23.7 % [6].

Inverted perovskite solar cells demonstrate lower efficiency than regular PSC; however, they have high potential for tandem solar cell construction. R. Zhu et al. achieved a high  $V_{\text{OC}}$  of 1.21 V without sacrificing photocurrent; this improvement allowed inverted planar PSCs to exceed 21 % PCE mark [8]. One of the best results for the inverted perovskite solar cells was realised using ITO/HTL(PTAA)/perovskite ( $(\text{FA}_{0.95}\text{PbI}_{2.95})_{0.85}(\text{MAPbBr}_3)_{0.15}$ )/ETM ([6,6]-phenyl-C<sub>61</sub>-butyric acid methyl ester (PC<sub>61</sub>BM)/buckminsterfullerene ( $\text{C}_{60}$ )/bathocuproine (BCP)/Cu device

stack, and champion device displayed a PCE of 21.51 % [8]. Additionally, excellent results have been shown by C. Wei et al., they demonstrated a NiO<sub>x</sub>-based inverted planar PSC comprised of ITO/HTL (NiO<sub>x</sub>)/perovskite ((Cs<sub>0.05</sub>FA<sub>0.54</sub>MA<sub>0.41</sub>)Pb(I<sub>0.98</sub>Br<sub>0.02</sub>)<sub>3</sub>)/QD/ETL (C60)/BCP/Ag achieving 1.162 V Voc, 22.88 mA×cm<sup>-2</sup> J<sub>SC</sub>, 81.4 % FF and PCE of 21.63 % [9].

### 2.1.2. Main perovskite compositions used in PSC

Perovskite compositions have a huge influence on the absorption spectra, PSC efficiency and stability. Earliest and one of the simplest is MAPbI<sub>3</sub>, first used by T. Miyasaka et al. in PSC achieving 3.8 % efficiency [1]. Methyl ammonium lead triiodide, CH<sub>3</sub>NH<sub>3</sub>PbI<sub>3</sub> (MAPI), demonstrated long carrier lifetimes and has exhibited electron-hole diffusion lengths in excess of 1 μm.

MAPbI<sub>3</sub> films are prepared by one or two-step solution processes: it crystallizes as a tetragonal perovskite at room temperature, whose octahedra are slightly distorted from the cubic structure (Figure 2.3a) [10]. The band gap of the single-crystal MAPbI<sub>3</sub> was measured to be 1.51 eV [11], and it displays strong absorption in the visible spectral region (Figure 2.3c). The photoluminescence (PL) properties of MAPbI<sub>3</sub> were measured at room temperature using a green light (532 nm) source; the material is emitting at about 760 nm (Figure 2.3d).

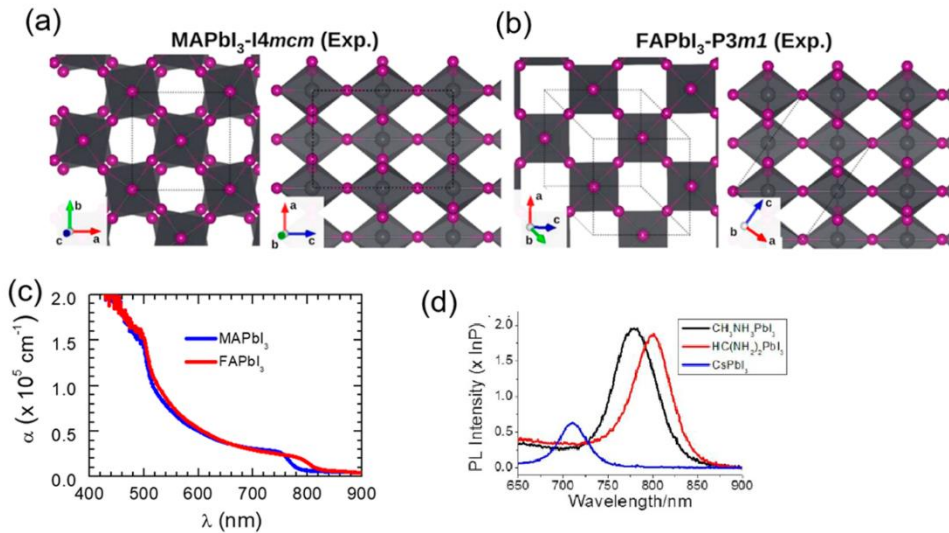


**Figure 2.3.** Crystal structure of (a) tetragonal MAPbI<sub>3</sub> and (b) cubic FAPbI<sub>3</sub> perovskites, (c) absorption coefficients of the MAPbI<sub>3</sub> and FAPbI<sub>3</sub> perovskites, (d) PL of the MAPbI<sub>3</sub>, FAPbI<sub>3</sub> and CsPbI<sub>3</sub> perovskites [12]

One of the best MAPbI<sub>3</sub> efficiency results was reported by Osman M. Bakr et al.; they fabricated single-crystal MAPbI<sub>3</sub> perovskite solar cell with the device stack ITO/PTAA/MAPbI<sub>3</sub> single crystal/C<sub>60</sub>/BCP/Cu. The constructed PSC displayed J<sub>SC</sub> of 23.46 mA×cm<sup>-2</sup>, V<sub>OC</sub> of 1.076 V, FF of 83.5 % and PCE reaching 21.09 % [13].



However, MAPbI<sub>3</sub> appears to undergo degradation under illumination or at elevated temperatures which is typically triggered by the volatilization of the MA cation [13].

T. M. Koh et al. have reported an alternative perovskite based on the formamidinium cation (HC(NH<sub>2</sub>)<sub>2</sub><sup>+</sup>) that showed a favourable band gap (1.47 eV) [14]. They investigated the formation of a black trigonal (*P3m1*) perovskite polymorph, the structure of which is shown in the Figure 2.3b. From the Figure 2.3c, it is evident that FAPbI<sub>3</sub> has a wider absorption spectrum than MAPbI<sub>3</sub> and fluoresces at about 800 nm. M. Grätzel et al. have demonstrated PSC configuration comprising of ITO/SnO<sub>2</sub>/FAPbI<sub>3</sub>/Spiro-MeOTAD/Au to achieve PCE of 23.1 %, *J*<sub>SC</sub> of 24.4 mA/cm<sup>2</sup>, *V*<sub>OC</sub> of 1.165 V and FF of 81.3 % [15].

Alternatively, methylammonium lead bromide MAPbBr<sub>3</sub> material has a wider band gap of 2.3 eV and high voltage output in PSC devices, making it a good candidate for tandem solar cell application [16]. MAPbBr<sub>3</sub> absorption spectra is narrower than MAPbI<sub>3</sub>, and photoluminescence peaks at 536 nm (Figure 2.4).

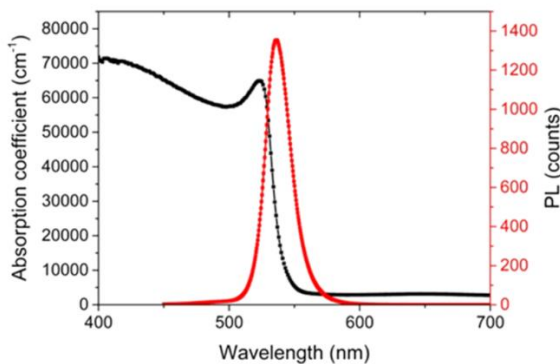


**Figure 2.4.** Absorption coefficient (black) and PL spectrum (red) of the CH<sub>3</sub>NH<sub>3</sub>PbBr<sub>3</sub> film [16]

One of the best results for MAPbBr<sub>3</sub> perovskite solar cell was achieved by J. Bisquert et al. with selective contacts treated with lithium-containing additives. PSC devices composed of FTO/c-TiO<sub>2</sub>/mp-TiO<sub>2</sub>/Li[TFSI]/MAPbBr<sub>3</sub>/HTL/Au showed PCE of 6.6 %, *J*<sub>SC</sub> of 5.5 mA×cm<sup>-2</sup>, *V*<sub>OC</sub> of 1.58 V and FF of 76 % [17].

Park et al. incorporated the Cs cation in FAPbI<sub>3</sub> composition to form an alternative light absorber to FAPbI<sub>3</sub> and MAPbI<sub>3</sub>. FA<sub>0.9</sub>Cs<sub>0.1</sub>PbI<sub>3</sub> perovskite forms a cubic phase at room temperature and demonstrates enhanced stability over the FAPbI<sub>3</sub> based devices under continuous illumination [18]. Fabricated PSC of FTO/c-TiO<sub>2</sub>/ FA<sub>0.9</sub>Cs<sub>0.1</sub>PbI<sub>3</sub>/ spiro-MeOTAD/Au showed PCE as high as 19.0 % [18].

H. J Snaith et al. have reported PSCs demonstrating high efficiency and stability; the MA cation was replaced with formamidinium and cesium. PSC devices composed of FTO/ZnO/FA<sub>0.83</sub>Cs<sub>0.17</sub>Pb(I<sub>0.83</sub>Br<sub>0.17</sub>)<sub>3</sub>/spiro-MeOTAD/Ag showed PCE of 21.1 %, *J*<sub>SC</sub> of 23.51 mA×cm<sup>-2</sup>, *V*<sub>OC</sub> of 1.20 V and FF of 78.5 % [19].

S. I. Seok's group in 2015 reported compositional engineering of (FAPbI<sub>3</sub>)<sub>1-x</sub>(MAPbBr<sub>3</sub>)<sub>x</sub> for efficient perovskite solar cells. This new improvement achieved good results at that time: *J*<sub>SC</sub>, *V*<sub>OC</sub> and FF values, averaged from the current voltage

(*J-V*) curves, were  $22.5 \text{ mA} \times \text{cm}^{-2}$ , 1.105 mV and 73.2 %, respectively, and PCE of 18.4 % was recorded [20]. Later on, J. You et al. have reported highly efficient and simple method for PSC performance enhancement, using phenethyl ammonium iodide (PEAI) for passivation of the perovskite surface. The constructed device ITO/SnO<sub>2</sub>/(FAPbI<sub>3</sub>)<sub>1-x</sub>(MAPbBr<sub>3</sub>)<sub>x</sub>/PEAI/spiro-MeOTAD/Au showed a record 23.32 % certified efficiency [21].

M. Saliba et al. used a mixture of triple Cs/MA/FA cations to achieve high efficiency perovskite solar cells with a stabilized PCE of 21.1 % [22]. The used solar cell architecture was FTO/c-TiO<sub>2</sub>/Li-doped mp-TiO<sub>2</sub>/Cs<sub>0.05</sub>(MA<sub>0.17</sub>FA<sub>0.83</sub>)<sub>0.95</sub>Pb(I<sub>0.83</sub>Br<sub>0.17</sub>)<sub>3</sub>/spiro-MeOTAD/Au. Using triple cation solution, the perovskite films were of better quality, and the material itself was more stable, enabling a breakthrough in device reproducibility.

### 2.1.3. Most common perovskite problems

PSC has received a lot of attention lately due to its high efficiency, cheap starting materials and simple production [23]. However, the stability of the devices is still a serious obstacle on the road to commercialization. The instability of device is most often caused by degradation of perovskite materials, especially under the influence of moisture and long-term thermal stress [24, 25]. Solving the problem of perovskite material instability is critical for long-term commercialisation prospects of the PSC technology.

Among the various factors, humidity is one of the biggest challenges. Due to the highly hydrophilic nature of perovskite, it can easily absorb water from the surrounding environment and cause the formation of hydrated products similar to (CH<sub>3</sub>NH<sub>3</sub>)<sub>4</sub>PbI<sub>6</sub> × 2H<sub>2</sub>O [26], which degrade further by losing methylamine group and forming yellow PbI<sub>2</sub> [27]. New methods are being investigated to improve the moisture resistance of the perovskite materials without compromising their optoelectronic properties. Among the most promising are various encapsulation methods or the addition of charge transporting layer designed to eliminate any contact between perovskite and humidity/water, thus stabilizing the material [24, 27].

In contrast to the problems associated with moisture, there is another important factor that affects the stability of perovskite solar cells, i.e., ultraviolet (UV) light exposure. For example, when MAPbI<sub>3</sub> film is exposed to UV light, it rapidly decomposes into methylamine, PbI<sub>2</sub> and I<sub>2</sub> [28]. There are various strategies to mitigate the degradation of the PSC devices caused by UV light exposure. One of them has been shown by M. Saliba et al., using compositional engineering, they have demonstrated MA-free perovskite solar cells with 1000 hours of lighting stability [29].

Another concern for scientists working with PSCs is thermal instability. Solar cells must be able to withstand higher temperature conditions, as the operating temperature of solar cells ranges from 40 °C up to 85 °C. Philippe et al. have studied the thermal stability of perovskite, performing measurements at room temperature, 100 °C and 200 °C for 20 min. They observed that MAPbI<sub>3</sub> began to decompose into PbI<sub>2</sub> as the temperature increased from room temperature to 100 °C and then to

200 °C [27]. One of the possible solutions is the replacement of MA organic cation with less volatile FA, which could potentially enhance thermal stability. And indeed, various researchers have confirmed that FAPbI<sub>3</sub> is more thermally stable [30, 31, 32].

Unlike the double cation perovskite system, which is sensitive to processing conditions due to its structural and thermal instability, the triple cation configuration yields very monolithic and pure perovskite grains. During the manufacturing process, the films are stronger and of better quality, which provides a breakthrough in reproducibility and the yield of cells with greater than 20 % efficiency [22, 33].

## 2.2. HTMs for perovskite solar cells

Hole transporting materials are an important active component in the PSC: they are used for efficient hole extraction from the perovskite and prevention of unwanted recombination processes by blocking electrons. One of the basic requirements for HTMs used in perovskite solar cells is energy level compatibility, as it allows to ensure smooth movement of carriers towards the electrode. Additionally, the ideal HTM should have high hole mobility and conductivity to reduce losses when transporting hole to the contact. Furthermore, good thermal, photochemical, oxygen and moisture stability are required. HTM must be well soluble in solvents that do not affect the quality of the perovskite layer, and finally, HTMs should be easy to synthesize with a minimal number of steps, simple to purify, non-toxic and economical.

To date, the greatest interest has been paid to doped, dopant-free and polymer hole transporting materials.

### 2.2.1. Small molecule organic hole transporting materials

One of the most widely studied and efficient HTMs used for PSCs is spiro-MeOTAD; the PCE of the devices using this material can exceed 23 % [21]. Spiro-MeOTAD has an ionization potential of around 5.1 eV, exhibits a hole mobility in the range of 10<sup>-5</sup> to 10<sup>-4</sup> cm<sup>2</sup>×V<sup>-1</sup>×s<sup>-1</sup> [34] and has high solubility in organic solvents. However, the performance of spiro-MeOTAD is dependent on the additives like bis(trifluoromethane)sulfonimide lithium salt (Li-TFSI), 4-*tert*-butyl pyridine (tBP) and tris(2-(1H-pyrazol-1-yl)-4-*tert*-butylpyridine)cobalt(III)tri[bis(trifluoromethane)sulfonimide] (FK209). Additionally, the multi-step synthesis process of spiro-MeOTAD is expensive and inefficient.

Carbazole derivatives are widely used as HTMs, as they demonstrate a number of interesting features such as low cost, good chemical and environmental stability, ease of incorporation of a wide variety of different functional groups, which allow for better solubility control and fine-tuning of the electronic and optical properties [35].

X. Wang et al. have published spirobisindane-based HTM (**1**), which forms amorphous films with high uniformity and morphological stability (Figure 2.5). Compound **1** exhibits an absorption band peaking at 307 nm with an optical band gap of 3.00 eV and HOMO energy level of -5.20 eV; the PSCs with a configuration

of FTO/TiO<sub>2</sub>/ Cs<sub>0.05</sub>(MA<sub>0.17</sub>FA<sub>0.83</sub>)<sub>0.95</sub>Pb(I<sub>0.83</sub>Br<sub>0.17</sub>)<sub>3</sub>/ **1**/Au were fabricated and demonstrated a good PCE of 18.57 % [36].

G.-Y. Lu et al. have reported carbazole-based starburst HTMs **2** and **3** obtained via tuning of the carbazole substitution position from 3,6- to 2,7-, respectively. In the PSC devices with the structure FTO/c-TiO<sub>2</sub>/mp-TiO<sub>2</sub>/CH<sub>3</sub>NH<sub>3</sub>PbI<sub>3-x</sub>Cl<sub>x</sub>/HTM/Au, 3,6-substituted **2** showed a slightly better device performance of 18.9 %, compared with that of 18 % in the case of 2,7-substituted HTM **3** [37].

**Table 2.1.** Optical and optoelectronic properties and PSC performance of doped HTMs

	$\lambda_{\max}$ [nm]	HOMO/LUMO [eV]	$V_{OC}$ [V]	$J_{SC}$ [mA cm <sup>-2</sup> ]	FF	PCE [%]	Ref.
<b>spiro-MeOTAD</b>	383	-5.0/-2.05	1.16	24.9	0.81	23.56	[21]
<b>1</b>	307	-5.20/-	1.06	24.67	0.71	18.57	[36]
<b>2</b>	306	-5.26/-2.43	1.05	22.93	0.79	18.87	[37]
<b>3</b>	270, 358, 390	-5.25/-2.22	1.06	22.32	0.76	18.00	[37]
<b>4</b>	304, 366	-4.93/-3.05	0.97	22.68	0.79	17.19	[38]
<b>5</b>	306, 346	-4.88/-2.62	1.04	23.24	0.76	18.23	[38]
<b>9</b>	303	-5.04/-	1.11	22.09	0.76	18.45	[39]
<b>10</b>	303	-5.06/-	1.10	22.43	0.76	18.92	[39]
<b>11</b>	303	-5.07	1.10	22.40	0.76	18.86	[39]
<b>12</b>	280, 326, 403	-5.01/-	1.07	22.5	0.74	17.8	[40]
<b>13</b>	301, 338	-5.11/-2.01	1.04	21.66	0.81	18.32	[41]
<b>14</b>	–	-4.85/-	1.09	21.71	0.78	18.8	[42]
<b>15</b>	337	-5.24/-1.93	1.1	21.61	0.76	18.04	[43]

D. Li et al. have reported two new HTMs based on carbazole and triphenylamine moieties denoted as **4** and **5**. The hole mobilities of doped **4** and **5** were estimated to be  $4.59 \times 10^{-4}$  and  $1.42 \times 10^{-3}$  cm<sup>2</sup> V<sup>-1</sup> s<sup>-1</sup>, respectively, although they are still lower than that of doped spiro-MeOTAD ( $\mu_h = 1.267 \times 10^{-2}$  cm<sup>2</sup> V<sup>-1</sup> s<sup>-1</sup>) [38]. In planar (FAPbI<sub>3</sub>)<sub>0.75</sub>(MAPbI<sub>3</sub>)<sub>0.17</sub>(MAPbBr<sub>3</sub>)<sub>0.08</sub>-based PSCs, they achieved 17.2 and 18.2 % PCE, respectively (Table 2.1).

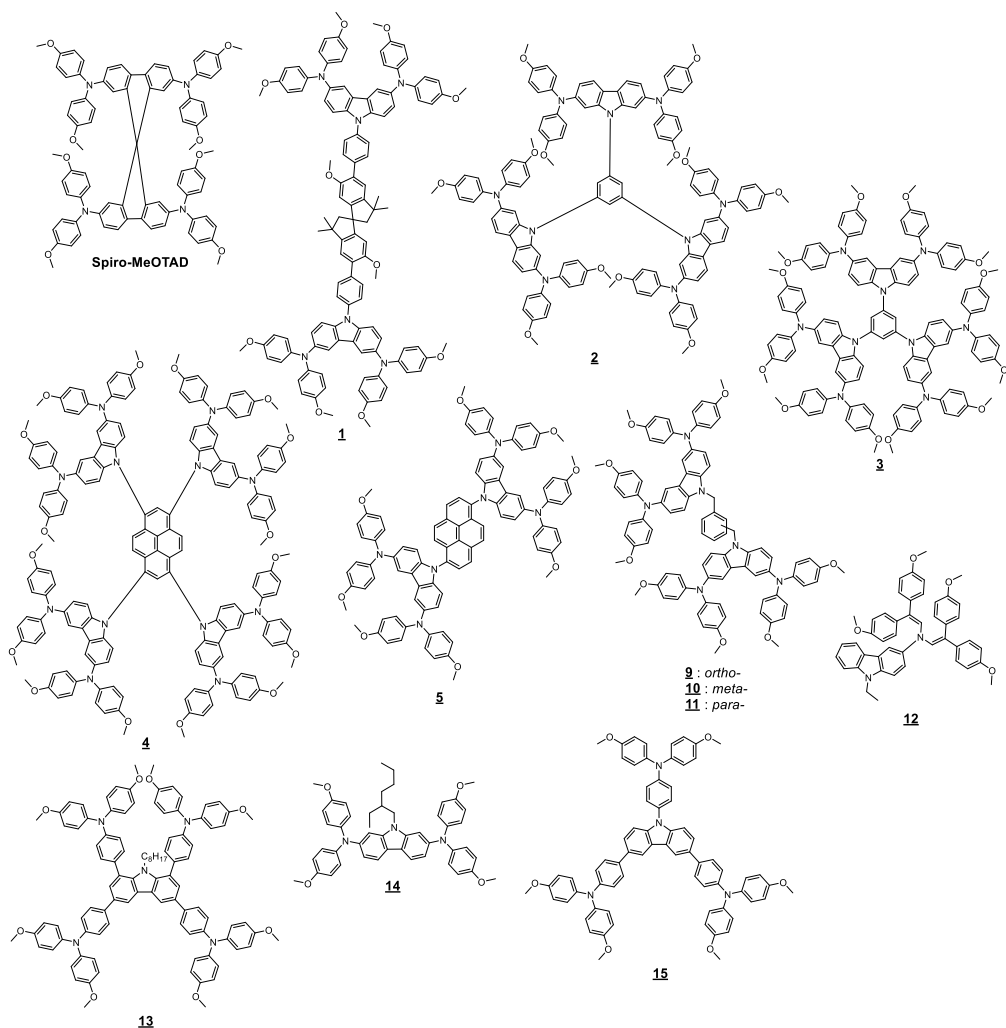
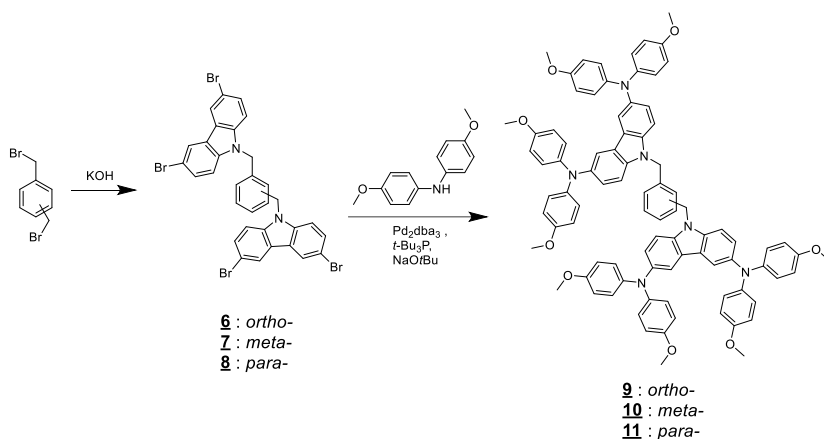


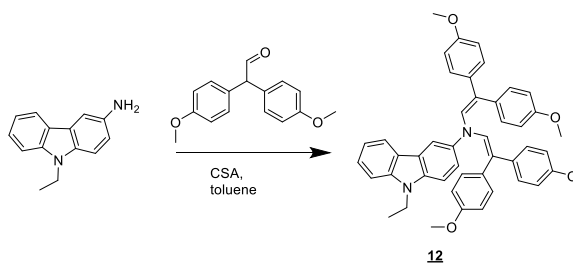
**Figure 2.5.** Molecular structures of doped HTMs

V. Getautis et al. have synthesized and extensively studied new HTMs containing two diphenylamine substituted carbazole fragments linked by a non-conjugated, variously substituted methylenebenzene unit [39] (Scheme 2.1). These materials are obtained via simple two-step process, by reaction of bromomethylbenzene derivatives with dibromocarbazole, utilising KOH [44], compounds **6–8** precipitate directly from the reaction mixture. In the second step, Buchwald–Hartwig amination reaction is performed utilising the palladium catalytic system to obtain new carbazole derivatives **9–11**.



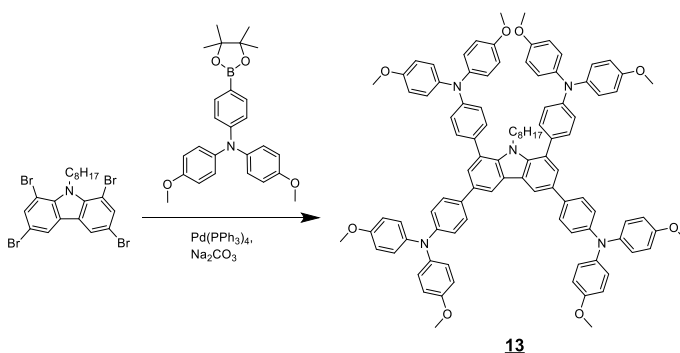
**Scheme 2.1.** General scheme for the synthesis of the twin carbazole-based HTMs **9–11**

New HTMs were tested in regular PSCs containing mixed cation and anion perovskite composition  $\text{Cs}_{0.1}(\text{MA}_{0.15}\text{FA}_{0.85})_{0.9}\text{Pb}(\text{I}_{0.85}\text{Br}_{0.15})$ . The performance of HTM **9**, **10** and **11** was very similar to that of spiro-MeOTAD, reaching PCE of 18.9 % (Table 2.1) [39]. The same group as well reported efficient carbazole-based HTM with enamine groups **12**, it was synthesized via an extremely simple route from commercially available and relatively inexpensive starting reagents (Scheme 2.2); **12** has been investigated in PSCs of different architectures, and the best results were demonstrated in FTO/c-TiO<sub>2</sub>/mp-TiO<sub>2</sub>/perovskite/**12**/Au device configuration reaching PCE of 17.8 % [40].



**Scheme 2.2.** Synthesis of the carbazole derivative **12**

Y. Yan et al. have reported new easily attainable carbazole-cored hole transporting material **13**. It is synthesized via one-step of the straightforward Suzuki coupling reaction between 1,3,6,8-tetrabromo-9-octylcarbazole and 4-methoxy-*N*-(4-methoxyphenyl)-*N*-(4-(4,4,5,5-tetramethyl-1,3,2-dioxaborolan-2-yl)phenyl)aniline (Scheme 2.3) [41].



**Scheme 2.3.** Synthesis of the carbazole derivative **13**

In the planar FTO/SnO<sub>2</sub>/C<sub>60</sub>-SAM/ MA<sub>0.7</sub>FA<sub>0.3</sub>PbI<sub>3</sub>/**13**/Au architecture, PSC exhibits very good performance, and the maximum PCE of 18.32 % is achieved (Table 2.1) [41].

Simple dimethoxydiphenylamine substituted *N*-ethylhexyl carbazole **14** was investigated by J. M. Luther et al. In PSC devices with architecture FTO/SnO<sub>2</sub>/FA<sub>0.76</sub>MA<sub>0.21</sub>CS<sub>0.03</sub>)<sub>0.67</sub>Pb(I<sub>0.89</sub>Br<sub>0.11</sub>)<sub>2.56</sub>/**14**/MoO<sub>x</sub>/Al, a PCE of 18.5 % with 1000-hour operational stability was recorded [42].

Finally, S. Dai et al. have reported star-shaped carbazole derivative **15**, which has excellent optoelectronic, electrochemical properties [43]. With mesoscopic perovskite solar cell architecture of FTO/c-TiO<sub>2</sub>/mp-TiO<sub>2</sub>/(FAPbI<sub>3</sub>)<sub>0.85</sub>(MAPbBr<sub>3</sub>)<sub>0.15</sub>/ HTM/Au, using **15** as HTM, PCE of over 18 % was measured.

### 2.2.2. Organic dopant-free hole transporting materials

The use of HTM with additives greatly increases the performance of the PSC, but the effectiveness of the treated HTMs decreases rapidly during the material degradation, which as well affects the PSC performance. One of the best solutions is HTMs demonstrating high efficiency without additional additives.

C. Huang et al. have reported new HTM with truxene-core **16**, which successfully demonstrates high-performance in PSCs (Table 2.2). Devices with p-i-n architecture and using compound **16** achieve respectable PCE of 18.6 % [45].

K. Rakstys et al. have reported new D-π-A architecture dopant-free HTM **17** with triazatruxene central core forming face-on columnar stacks, which is beneficial for charge transfer within n-i-p perovskite solar cell architecture. With this improvement, PSC achieve power conversion efficiency of over 19 % and demonstrate improved stability [46].

R. Azmi et al. have developed new high-performance dopant-free HTM **18** based on dibenzothienopyrrole and diphenylamine moieties (Table 2.2). ITO/ZnO/MAPbI<sub>3</sub>/**18**/Au architecture PSC, using dopant-free **18**, achieved PCE of 18.09 %, which was superior to that of doped spiro-MeOTAD (PCE = 17.82 %) with the same device architecture [47].

M. Chen et al. have published organic-inorganic integrated HTLs consisting of the solution-processable nickel phthalocyanine compound **19** and V<sub>2</sub>O<sub>5</sub>. After the

optimization, PSCs containing the combined HTL layer and device structure FTO/c-TiO<sub>2</sub>/mp-TiO<sub>2</sub>/(FAPbI<sub>3</sub>)<sub>0.85</sub>(MAPbBr<sub>3</sub>)<sub>0.15</sub>/**19**/V<sub>2</sub>O<sub>5</sub>/Au achieved good performance characteristics and PCE of 18.3 % (Table 2.2) [48].

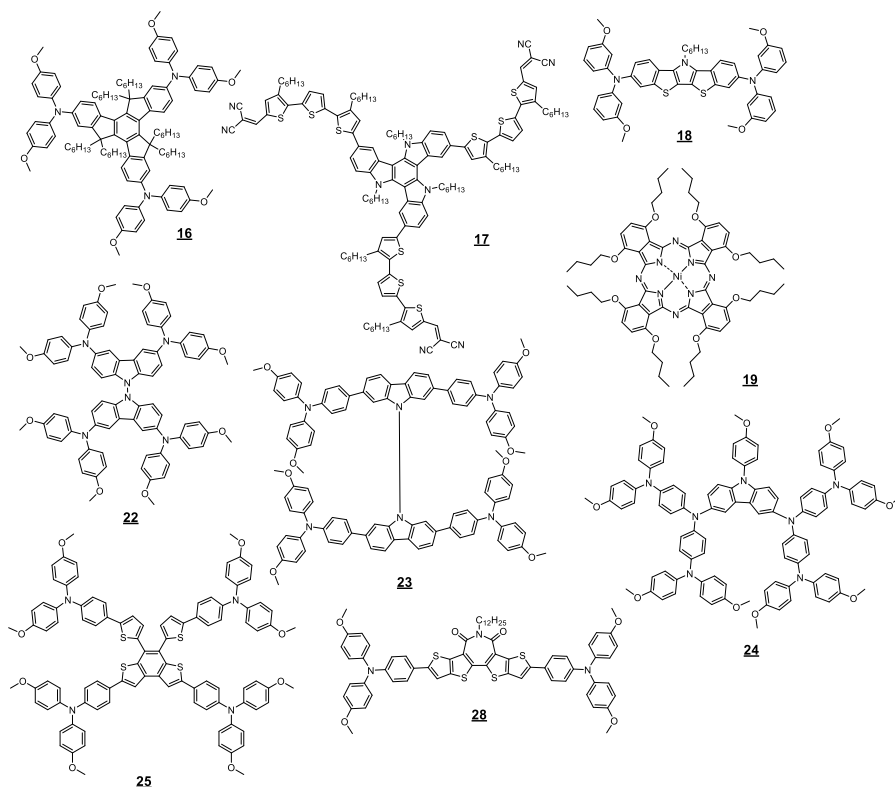
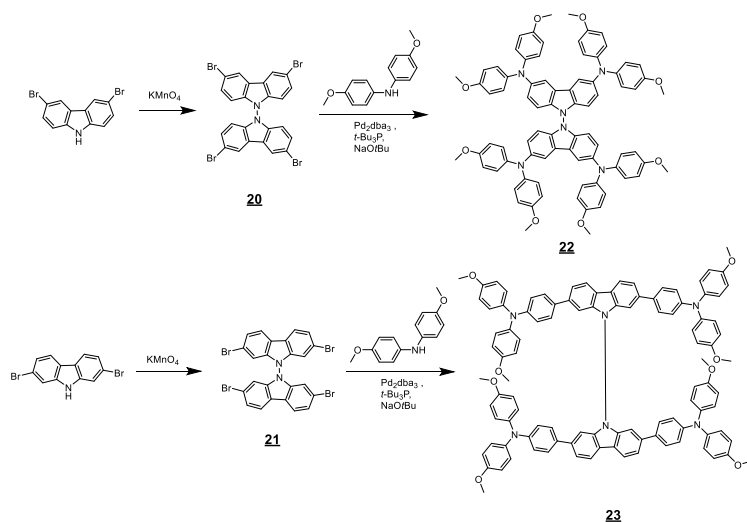


**Figure 2.6.** Molecular structure of dopant-free HTMs

W. Huang et al. have published new low-cost dopant-free HTMs **22** and **23**, which were prepared using a two-step synthesis procedure in high yields from very inexpensive bicarbazole derivatives [49]; **22** and **23** were obtained from the tetrabromo-*N,N'*-bicarbazoles (**20** and **21**), which were prepared from dibromocarbazoles through the oxidative coupling of the nitrogen atoms by KMnO<sub>4</sub>. Palladium-catalysed C–N cross-coupling reaction with 4,4'-dimethoxydiphenylamine was utilized to obtain two target compounds **22** and **23** (Scheme 2.4).





**Scheme 2.4.** Synthesis of bicarbazole derivatives **22** and **23**

Both **22** and **23** show promising results in larger-area PSCs, and the optimized 1 cm<sup>2</sup> devices achieved good PCEs of up to 17.0 % and 17.6 %, respectively [49].

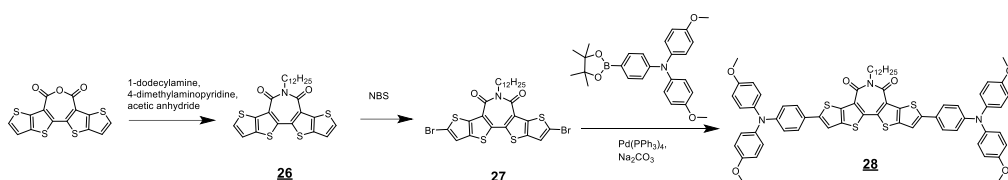
F. Zhang et al. reported new HTM **24** based on 9-(4-methoxyphenyl)carbazole core. The electron-rich carbazole and triphenylamine units combined into one molecule of **24** allowed for the construction of 16.04 % efficient PSCs based on triple-cation (CS<sub>0.05</sub>(MA<sub>0.17</sub>FA<sub>0.83</sub>)<sub>0.95</sub>Pb(I<sub>0.83</sub>Br<sub>0.17</sub>)<sub>3</sub>) perovskite [50].

**Table 2.2.** Optical and optoelectronic properties and PSC performance of dopant-free HTMs

	$\lambda_{\max}$ [nm]	HOMO/LUMO [eV]	$V_{oc}$ [V]	$J_{sc}$ [mA cm <sup>-2</sup> ]	FF	PCE [%]	Ref.
<b>Spiro-MeOTAD</b>	383	-5.0/-2.05	1.16	24.9	0.81	23.56	[21]
<b>16</b>	410	-5.28/-2.3	1.02	23.2	0.79	18.6	[45]
<b>17</b>	401, 515	-5.24/-3.19	1.13	21.7	0.78	19.03	[46]
<b>18</b>	405	-5.31/-2.44	1.12	21.13	0.76	18.09	[47]
<b>19</b>	742	-5.06/-3.61	1.08	23.1	0.73	18.3	[48]
<b>22</b>	301, 377	-5.11/-2.28	1.12	21.34	0.71	17.0	[49]
<b>23</b>	306, 386	-5.15/-2.25	1.09	22.38	0.73	11.6	[49]
<b>24</b>	316	-5.06/-1.94	1.14	21.52	0.69	16.04	[50]
<b>25</b>	409	-5.30/-2.68	1.11	23.26	0.78	20.04	[51]
<b>28</b>	343, 532	-5.24/-3.32	1.12	23.23	0.81	21.17	[52]

Promising HTM **25** with planar semi-locked tetrathienylethene core was reported by W.-H. Zhu et al. This HTM has deep lying HOMO level, excellent thin-film morphology, and the dopant-free **25**-based PSCs showed very promising photovoltaic performance (Table 2.2), PCE of over 20 % as well as excellent long-term environmental stability [51].

X. Guo et al. have designed new HTM with imide-functionalized thiophene acceptor as a core and triphenylamine side groups. HTM **28** was synthesized by imidization of thiophene-based anhydrides with 1-dodecylamine using 4-dimethylaminopyridine for ring-opening followed by acetic anhydride-assisted ring-closure reaction. The bromination of **26**, using brominating agent *N*-bromosuccinimide (NBS), resulted in dibromo derivative **27**. Finally, Suzuki coupling of **27** with corresponding boronic ester produced the target compound **28** (Scheme 2.5) [52].



**Scheme 2.5.** Detailed synthetic route to **28**

HTM **28** demonstrated excellent performance in inverted PSCs (Table 2.2). Due to good energy level alignment and appropriate hole-transporting ability, the **28**-based inverted PSC exhibits an excellent PCE of 21.17 % with  $V_{OC}$  of 1.12 V,  $J_{SC}$  of 23.23 mA $\times$ cm $^{-2}$  and an FF of  $\approx$ 81 %; additionally, the device shows good long-term stability and stability under illumination.

### 2.2.3. Polymeric hole transporting materials

Polymers are potentially attractive candidates for HTM in perovskite solar cells as they generally have good stability, processability, mechanical flexibility and film uniformity. Both high polymer density and hydrophobicity are as well very important in protecting the perovskite layer from moisture in the environment, thus potentially improving the stability of the PSC.

Poly[bis(4-phenyl)(2,4,6-trimethylphenyl)amine] (PTAA) is the most commonly used HTM for inverted planar PSCs. M. Stolterfoht et al. have published an article, in which they fabricated stable dopant-free PTAA perovskite devices with PCE of 20 %. After optimizing the electrode layout, a device PCE of 18.9 % in larger cells (with 1 cm $^2$  area) was achieved [53]. S. Il Seok et al. have reported regular n-i-p architecture PSC with multiple cations and mixed halide anions ((FAPbI $_3$ ) $_{0.95}$ (MAPbBr $_3$ ) $_{0.05}$ ) and PTAA polymer demonstrating at that time record power conversion efficiency of 22.1 % in small cells and 19.7 % in 1 cm $^2$  cells [54].

A new homopolymer-based HTM **29** was reported by J. Fang et al. When using this material in the inverted PSC configuration, very good performance results were realized (Table 2.3), and the efficiency of up to 19.6 % was achieved [55].

C. J. Brabec et al. have investigated a composition of tantalum-doped tungsten oxide ( $\text{Ta-WO}_x$ ) with polythiophene derivative **30**, demonstrating perovskite solar cells with maximum power efficiency of 21.2 %, the highest performance observed to date for PSCs with ionic dopant-free HTMs [56]. In addition, the same group investigated D-A type HTMs, such as **31** and **32**, PSC devices with architecture ITO/ $\text{C}_{60}$ -SAM/ $\text{SnO}_x$ / $\text{PC}_{60}\text{BM}$ / $\text{FA}_{0.83}\text{MA}_{0.17}\text{Pb}_{1.1}\text{Br}_{0.50}\text{I}_{2.80}$ /HTM/ $\text{Ta-WO}_x$ /Au demonstrated efficiencies of 18.9 % and 19.8 %, respectively [56].

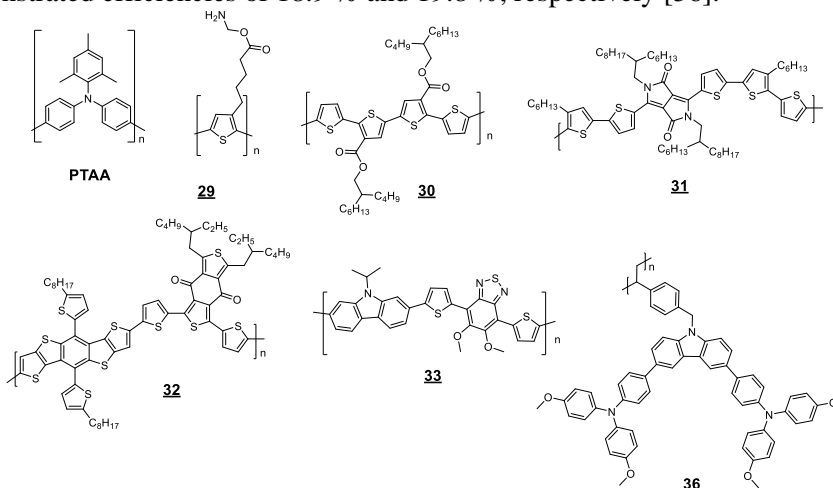


**Figure 2.5.** Molecular structure of polymeric HTMs

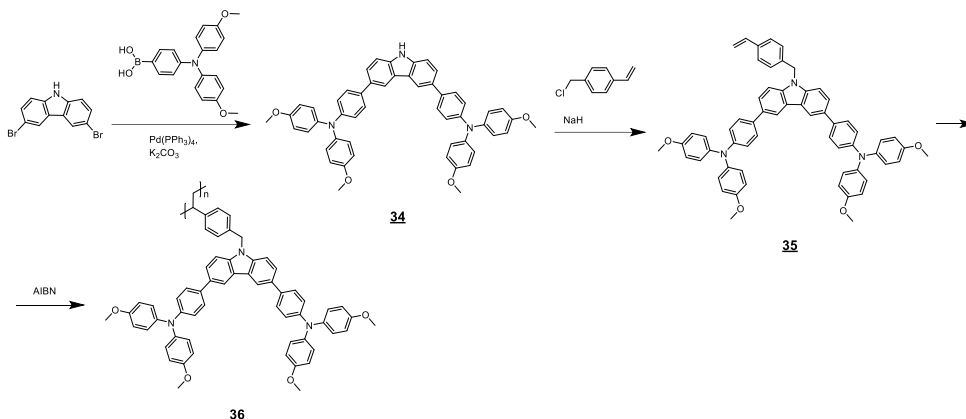
**Table 2.3.** Optical and optoelectronic properties and PSC performance of polymeric HTMs

	$\lambda_{\text{max}}$ [nm]	HOMO/LUMO [eV]	$V_{\text{oc}}$ [V]	$J_{\text{sc}}$ [mA $\text{cm}^{-2}$ ]	FF	PCE [%]	Ref.
<b>PTAA</b>	374	-5.14/-2.19	1.11	25.0	0.82	22.1	[54]
<b>29</b>	495	–	1.09	22.2	0.81	19.6	[55]
<b>30</b>	–	-5.3/-3.4	1.17	22.7	0.8	21.2	[56]
<b>31</b>	–	-5.3/-3.7	1.15	21.5	0.76	18.9	[56]
<b>32</b>	–	-5.3/-3.4	1.17	22.22	0.77	19.8	[56]
<b>33</b>	–	–	1.1	22.2	0.78	19.1	[57]
<b>36</b>	310, 333	-5.21/-2.02	1.13	22.34	0.73	18.45	[58]

Polymeric HTM **33** comprised of carbazole and thiophene donor moieties and functionalized electron accepting 2,1,3-benzothiadiazole unit with two methoxy substituents [57] was reported by F. Cai et al. Regular architecture PSC with device stack of ITO/ $\text{TiO}_2$ / $\text{PC}_{60}\text{BM}$ /MAPbI<sub>3</sub>/**33**/MoO<sub>3</sub>/Au showed promising performance and PCE of 19.1 % [57].

B. Xu and co-workers have presented a side-chain polymer, which was designed and synthesized by attaching carbazole-based hole-transporting units to a polystyrene chain [58]. Palladium-catalysed Suzuki cross-coupling reaction between

3,6-dibromocarbazole and 4-[di(p-methoxyphenyl)-amino]benzene-1-boronic acid resulted in intermediate compound **34**. During benzylation of the carbazole moiety **34** with 4-vinylbenzylchloride, the monomer **35** was obtained. The polymer **36** was then synthesized by the free-radical polymerization of monomer using 2,2'-azobisisobutyronitrile as the initiator (AIBN) (Scheme 2.6).



**Scheme 2.6.** Syntheses of the polymer **115**

Regular architecture n-i-p PSC devices having the structure ITO/SnO<sub>2</sub>/CS<sub>0.05</sub>FA<sub>0.81</sub>MA<sub>0.14</sub>PbI<sub>2.55</sub>Br<sub>0.45</sub>/**36**/Au reached a very respectable PCE of 18.45 % [58].

## 2.2.4. Chapter summary

From the information provided in this chapter, it is evident that large work has been done in the fields of perovskite and appropriate p-type organic semiconductor research. With new knowledge gained over the years, the perovskite structure got more nuanced and complex. The issues relate to material's stability are being addressed; more robust and reliable compositions are being developed. Similarly as with perovskite light absorber, various hole transporting materials are being developed each year. Obviously, it is not possible to review them all, and, in this overview, only a small portion of the HTM materials, demonstrating good efficiency or interesting structural ideas, were shown. It can be safely said that it is possible to obtain very good PSC performance with dopant-free hole transporting materials, although oftentimes, it requires relatively complex synthetic procedures. Ideally, one would wish for a HTM material that would function effectively in the PSC devices, could be deposited using easily upscalable methods, be simple and inexpensive to synthesize and demonstrate long-term stability under device operation conditions.

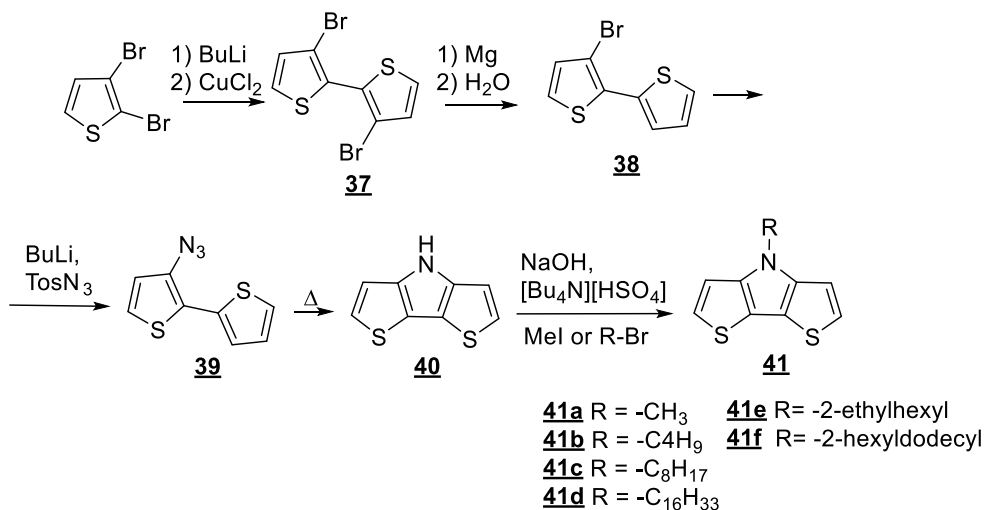
## 2.3. Dithieno[3,2-b:2',3'-d]pyrrole derivatives

Thiophene-fused molecules are a wide class of fascinating organic semiconductors with high charge transport properties; among them, dithieno[3,2-b:2',3'-d]pyrrole (DTP) is one of the universal electron donating blocks that contains heteroatoms of nitrogen and sulphur [59]. The occupied  $\pi$  orbitals of

heteroatoms are conjugated with  $\pi$  orbitals of aromatic units, thus improving p-type properties even further. While the presence of electron-rich nitrogen atom can increase the stability in the oxidized state and further decrease the band gap [59]. The nitrogen atom and thiophene unit can be chemically modified as well. As such, the electronic structure, crystallinity and thermal stability of DTP-based semiconductors can be readily tuned through molecular design. The pyrrole-containing DTP moiety is among the most widely used building blocks for the synthesis of p-type semiconductors used in the construction of efficient organic photovoltaics (OPV), organic field effect transistor (OFET) and organic light emitting diode (OLED) devices [59, 60, 61].

### 2.3.1. Synthesis of dithieno[3,2-b:2',3'-d]pyrrole

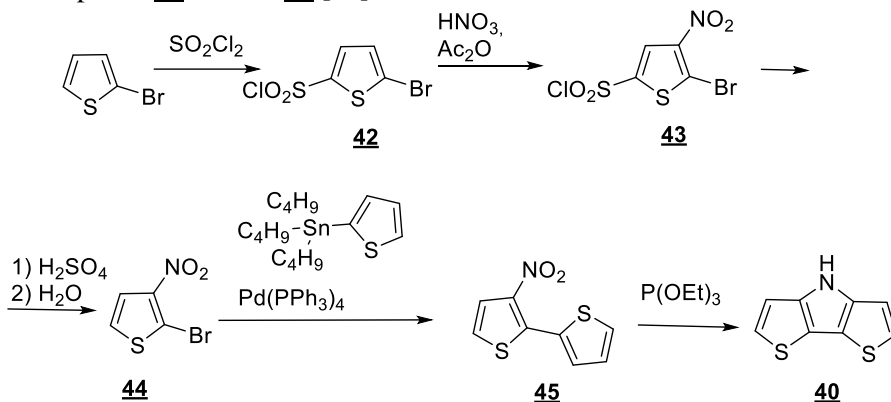
The synthesis of dithieno[3,2-b:2',3'-d]pyrrole (**41**) was reported for the first time by P. Zanirato and co-workers in 1983 [62]. The synthesis was conducted from 2,3-dibromothiophene starting material using S. Gronowitz method. The obtained 3,3-dibromo-2,2-bithiophene (**37**) [63] was partially debrominated to get compound **38**. In the next step, azidobithiophene was obtained by the reaction of corresponding thienyllithium derivative with p-toluenesulfonyl azide (TosN<sub>3</sub>) followed by the fragmentation of the resulting triazene salt **39** [64], resulting in the formation of dithieno[3,2-b:2',3'-d]pyrrole (**40**) (Scheme 2.7).



**Scheme 2.7.** Initial synthesis of DTP and its derivatives

A decade later, G. Zotti and co-workers have developed the alkylation procedure for the **40** to generate the *N*-functionalized DTPs **41a–d** with yields of ~70%. The primary motivation for the alkylation was an attempt to increase solubility and change the functionalization site with respect to the active  $\alpha$ -positions [65]. Later, J. Qin and co-workers have synthesized the DTPs containing branched side chains (**41e** and **41f**), applying the same procedure as G. Zotti [66].

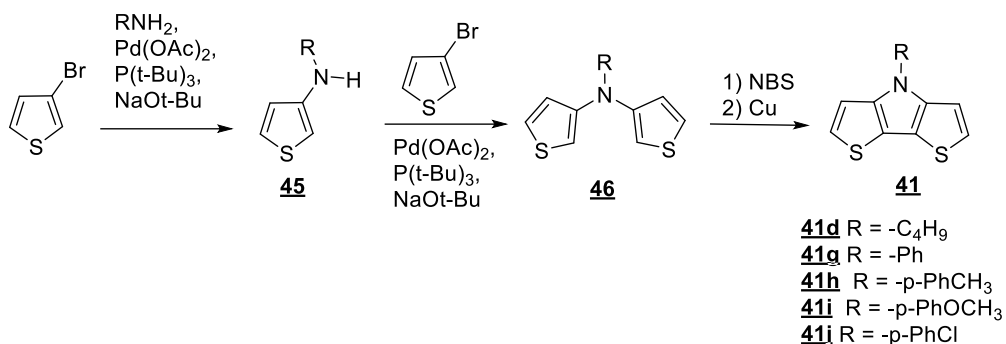
P. Bäuerle et al. has demonstrated new synthesis route to DTP by the means of a Cadogan ring closing reaction (Scheme 2.8) [67]. The synthesis was conducted from 2-bromothiophene; thionyl chloride was introduced in the unsubstituted  $\alpha$ -position to get 5-bromothiophene-2-sulfonyl chloride (**42**) [68]. According to C. Carpanelli, sulfonyl chloride group is required for the selective nitration to obtain 5-bromo-4-nitrothiophene-2-sulfonyl chloride (**43**) [69]. Sulphuric acid was used to eliminate the sulfonyl chloride group and obtain 2-bromo-3-nitrothiophene (**44**) [69]. Stille cross-coupling reaction of **44** and 2-(tributylstannyl)thiophene resulted in 3-nitro-2,2'-bithiophene (**45**), which was then used in Cadogan reaction to transform nitrobithiophene **45** to DTP **40** [67].



**Scheme 2.8.** Synthesis of DTP **4** via Cadogan reaction of nitrobithiophene **9**

Initially, this path seemed as a good attractive synthesis, as carbazole can be efficiently synthesized from 2-nitro-1,1'-biphenyl with triethylphosphite as a reducing agent; however, in this case, Cadogan reaction does not proceed as smoothly, and the overall yield of the product is low [67].

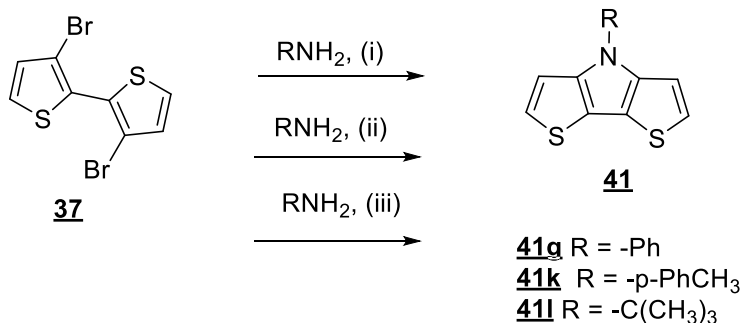
Multi-step synthesis of DTP moiety and the overall low yield significantly limited their application in conjugated p-type materials. Eventually, K. Ogawa and S. C. Rasmussen suggested a new synthesis route to DTP [70]. Buchwald–Hartwig amination of 3-bromothiophene resulted in a mixture of *N*-functionalized 3-aminothiophene (**45**) and *N*-functionalized *N*-(3-thienyl)-3-aminothiophene (**46**). After these two components had been separated, **45** was further coupled with 3-bromothiophene to convert it to **46** in high yield (Scheme 2.9) [71]. A one-pot bromination/cyclization of compound **46** via copper-mediated Ullman coupling resulted in the desired *N*-functionalized DTPs **41d**, **41g–41j** [70, 72].



**Scheme 2.9.** *N*-functionalized DTPs via Pd-catalysed amination

Compared to the previous route (Scheme 2.7), the shown method reduced the total number of steps and resulted in the increase of the overall yield. In addition, while the initial thiophenes of both routes are commercially available, the 2,3-dibromothiophene used in Scheme 2.7 is more expensive than the 3-bromothiophene used in Pd-catalysed amination [72].

Later, K. Nozaki and co-workers have developed a new strategy towards the synthesis of carbazole via double *N*-arylation reaction of primary amines and found that similar conditions could as well produce *N*-phenyl DTP (**41g**) from bithiophene **37** in moderate 35 % yield (Scheme 2.10) [73]. C. Samyn and co-workers have optimized the K. Nozaki method to prepare *N*-alkyl substituted DTPs and found that replacing P(tBu)<sub>3</sub> with 2,2-bis(diphenylphosphino)-1,1-binaphthyl (BINAP) and increasing the temperature could increase the yield to 80 % [74].

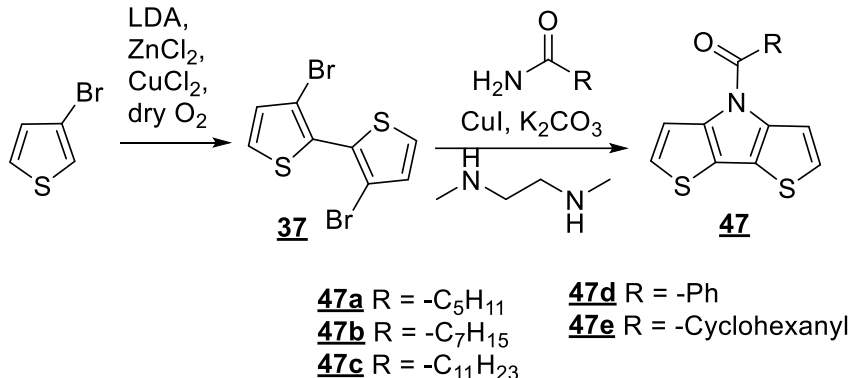


Reagents: (i) Pd<sub>2</sub>dba<sub>3</sub>, BINAP, NaOt-Bu; (ii) Pd<sub>2</sub>dba<sub>3</sub>, dppf NaOt-Bu;  
 (iii) Pd<sub>2</sub>dba<sub>3</sub>, P(*t*-Bu)<sub>3</sub>, NaOt-Bu

**Scheme 2.10.** Alternative synthetic routes to *N*-functionalized DTPs

Both methods utilizing Pd-catalysis (Scheme 2.9 and Scheme 2.10) have achieved similar overall yields of *N*-functionalized DTPs (40–45 %). However, the synthesis pathway shown in Scheme 2.10 has become the most favourable, as the intermediate **37** is more stable and simpler to use than the more reactive aminothiophenes **45** and **46**.

J. Evenson et al. have as well prepared *N*-acyl DTP compounds (**47a–e**) via copper-catalysed amidation of 3,3'-dibromo-2,2'-bithiophene **37** as shown in Scheme 2.11 [75].



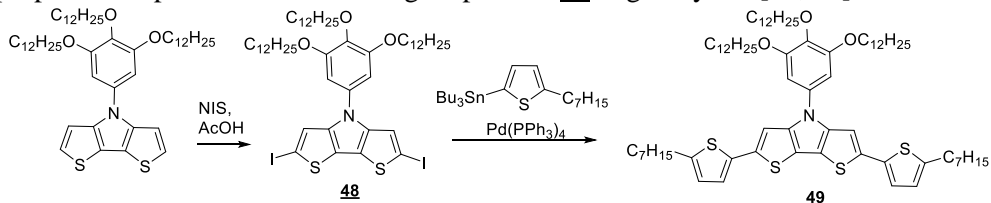
**Scheme 2.11.** Synthesis of *N*-acyl DTP derivatives

Bithiophene **37** is commonly produced via lithiation and oxidative Cu-coupling of 2,3-dibromothiophene [76]. To improve the utility of **37**, one-pot method was developed by utilizing lithium diisopropylamide (LDA) rather than BuLi; thus, selective deprotonation of the 3-bromothiophene can be employed to generate the lithiated intermediate. The transmetalation to the copper species by first reacting Li with ZnCl<sub>2</sub>, followed by CuCl<sub>2</sub> [77], and oxidative coupling of the copper intermediate by the addition of dry oxygen produces 3,3'-dibromo-2,2'-bithiophene in high yield (85–90 %). Finally, the synthesis of *N*-acyl DTPs (**47a–47e**) was conducted utilizing Cu-catalysed C-N bond formation via Buchwald method [78] with moderate yield (20–40 %).

### 2.3.2. Synthesis of functionalized DTP small molecules

Dithieno[3,2-b:2',3'-d]pyrrole is a universal electron donating heterocycle moiety and is widely used to obtain new, efficient, small molecule p-type semiconductors for OPV and OFET devices. Due to its symmetry, DTP core has regioregular structure, and minimal torsional effects have been observed, since solubilizing groups are placed in the middle ring.

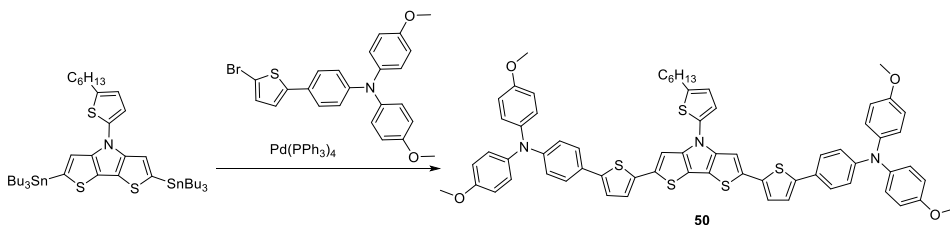
S. Barlow and co-workers have reported new DTP-based quaterthiophene **49** obtained via the 2,6-diiodo intermediate **48** (Scheme 2.12) [79]. Stille coupling with appropriate thiophene resulted in the goal product **49** in good yield [79, 80].



**Scheme 2.12.** Synthesis of quaterthiophene **49**

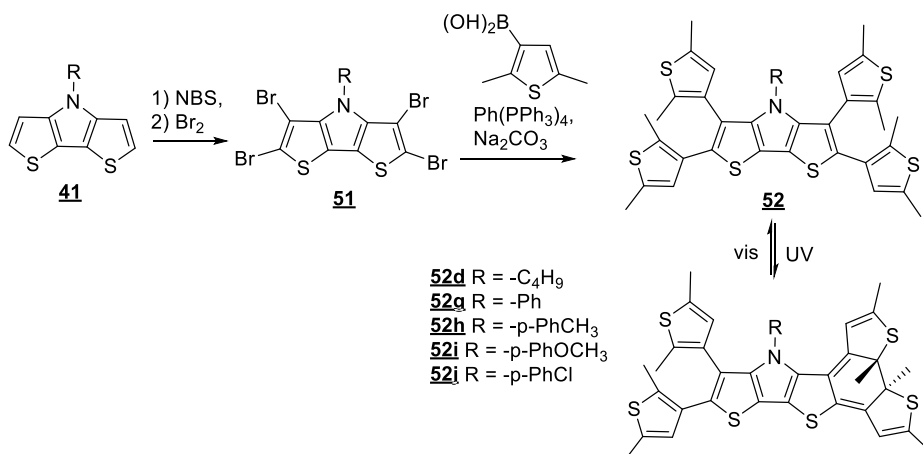


S. Yang and co-workers have reported new DTP triphenylamine based HTM **50**, the synthesis of which is outlined in Scheme 2.13. DTP-tin central moiety was prepared via a three-step procedure, i.e., cyclization, Buchwald–Hartwig cross-coupling and preparation of tin reagent [81]. The target compound **50** was then synthesized by a Pd-catalysed Stille coupling reaction. The HTM **50** showed good hole mobility of  $4.18 \times 10^{-4} \text{ cm}^2 \text{ V}^{-1} \times \text{s}^{-1}$ , which is one order of magnitude higher than spiro-MeOTAD ( $3.43 \times 10^{-5} \text{ cm}^2 \text{ V}^{-1} \times \text{s}^{-1}$ ) [82].



**Scheme 2.13.** Synthetic route for DTP triphenylamine derivative **50**

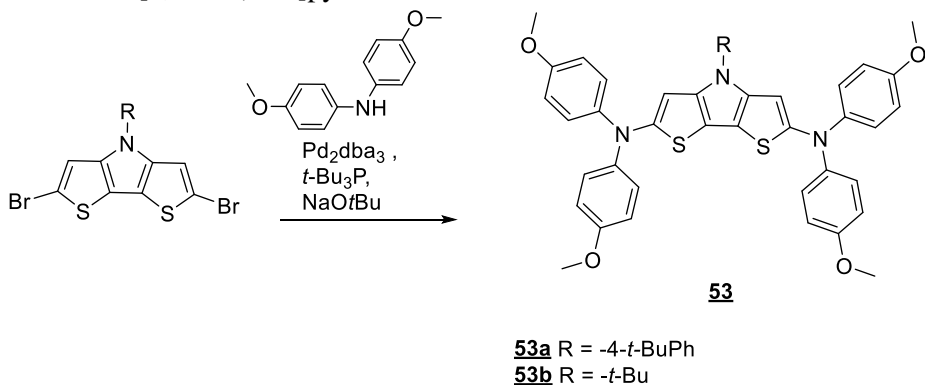
V. W. Yam and co-workers have reported new tetrasubstituted DTPs **52d**, **52g–52j** as potential photochromic materials [83]. The synthesis (Scheme 2.14) utilized the tetrabromo-DTP intermediates **41d**, **41g–41j**, produced by sequential bromination with NBS, followed by  $\text{Br}_2$  with a yield of 40–69 % [83]. In the next step, tetrabrominated dithieno[3,2-b:2',3'-d]pyrroles (**51d**, **51g–51j**) were utilized in Suzuki cross-coupling reaction with 2,5-dimethylthien-3-yl boronic acid to produce **52d**, **52g–52j** [84]. The compounds **52d**, **52g–52j** have been shown to successfully undergo the first photocyclization step; however, the fully closed form could not be obtained [83].



**Scheme 2.14.** Synthesis of DTP **52d**, **52g–52j** via tetrabrominated DTP **51**

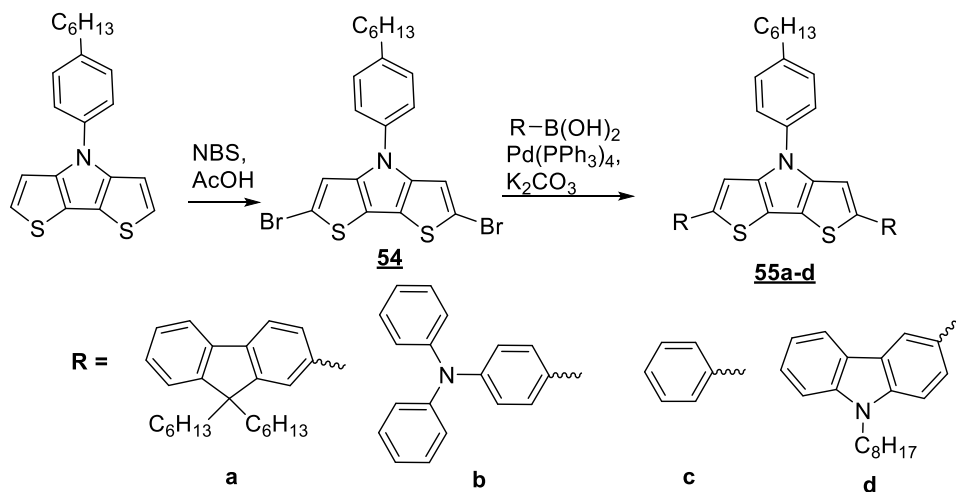
The diarylamino-functionalized DTPs **53a**, **53b** have been reported by S. Barlow and co-workers [85]. These HTMs were obtained in good yield (67 % and

72 %) via palladium-catalysed coupling of bis(4-methoxyphenyl)amine with 2,6-dibromo dithieno[3,2-b:2',3'-d]pyrrole.



**Scheme 2.15.** Synthesis of diarylamino-capped DTPs **53a**, **53b**

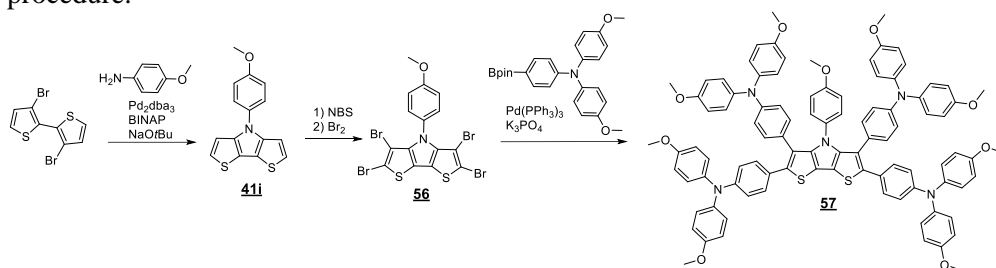
G. Balaji and co-workers have reported DTP series with phenyl, fluorene, triphenylamine and carbazole moieties at 2,6-positions of DTP core [86]. The synthesis was conducted by first brominating DTP with NBS in acetic acid-chloroform mixture. Then, the intermediate **54** was used in Suzuki coupling reaction with corresponding boronic acids to obtain derivatives **55a-d** in good yields (60–75 %) (Scheme 2.16) [86].



**Scheme 2.16.** Synthesis of diarylamino-capped DTPs **55a–55d**

The phenyl-containing compound **55c** with the weaker donating system showed a blue emission with a quantum yield of 57 % in the solution. Other oligomers with stronger electron donating systems showed green emission with quantum yields of 52–75 %. The strong fluorescence of **55a** and **55b** show promise for the application of these compounds in light emitting applications [86].

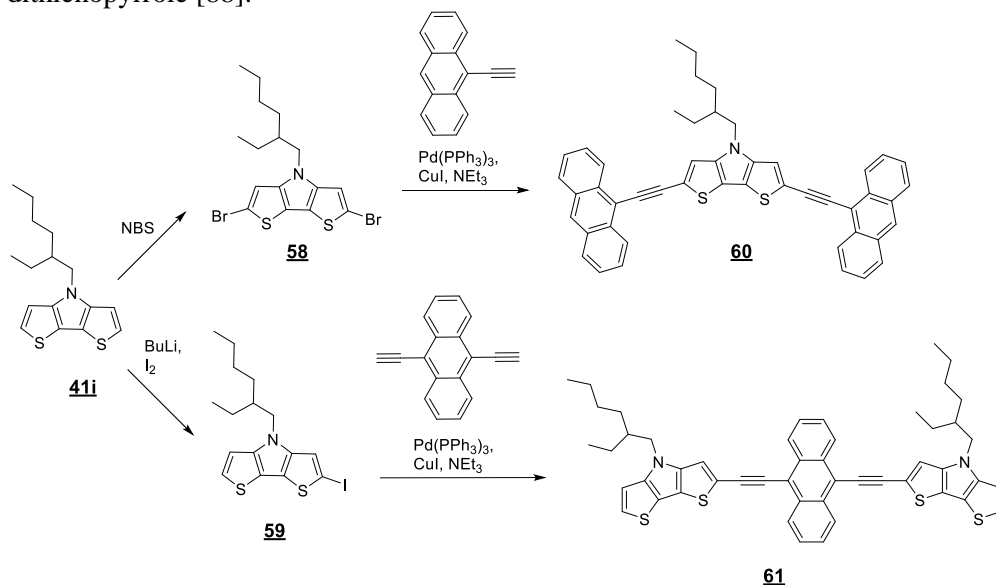
The synthesis of new DTP derivative with four triphenylamine moieties has been reported by M.K. Nazeeruddin and co-workers (Scheme 2.17) [87]. Compound **51** was synthesized in a straightforward manner using three-step synthetic procedure.



**Scheme 2.17.** Synthetic route for the preparation of the heterocyclic HTM **57**

The synthesis was conducted from 3,3'-dibromo-2,2'-bithiophene, utilising Buchwald–Hartwig cross-coupling reaction with *p*-anisidine; DTP core **41i** was obtained. The bromination of the DTP core was achieved by one-pot method via sequential treatment with NBS at room temperature, followed by the addition of bromine at reflux. The final product **57** is obtained by a Suzuki–Miyaura reaction with *p*-methoxy triphenylamine pinacol boronate. This electron-rich small molecule has successfully demonstrated functionality as efficient HTM in perovskite-based photovoltaic devices [87].

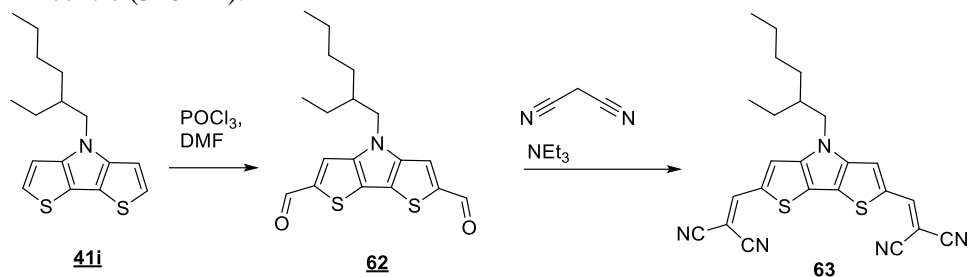
G. Gigli and co-workers have reported on the properties of a new class of arylene–ethynylene semiconductors incorporating electron-rich anthracene and dithienopyrrole [88].



**Scheme 2.18.** Synthetic sequence for the ethynylantracene-DTP derivatives **60** and **61**

The synthesis is conducted in two steps: first, the halogenation of **41i** was performed, and then, it was followed by the Pd/Cu-catalysed Sonogashira coupling reaction between 9,10-diethynylantracene and monohalogenated DTP **59** (58 % yield) or 9-ethynylantracene and dihalogenated DTP **58** (87 % yield) (Scheme 2.18) [88].

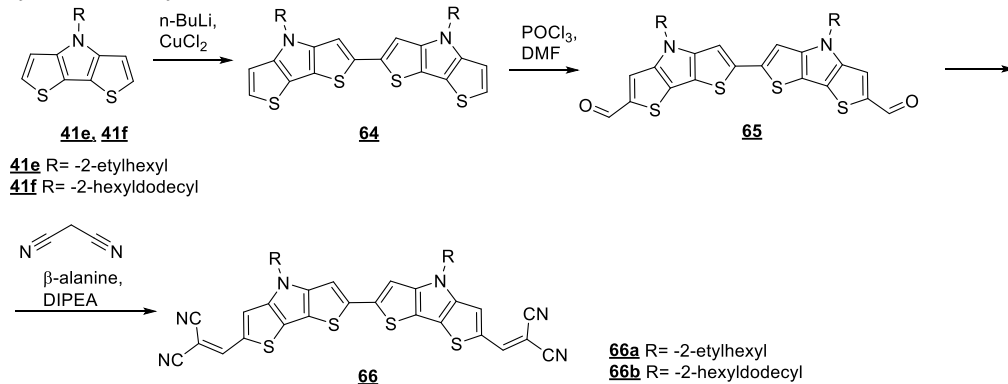
J. Roncali and co-workers have evaluated small-molecule DTP derivative with two dicyanovinyl substituents **63** as a possible light absorber [89] (Scheme 2.19) The ultraviolet–visible (UV-vis) spectra of the solution of **63** demonstrated absorbance at 520 nm, and a large bathochromic shift was registered, compared with DTP centre (310 nm).



**Scheme 2.19.** Synthesis of the DTP light absorber **63**

The synthesis of compound **63** is shown in Scheme 2.19 and is conducted from the DTP donor molecule, which was formylated by the Vilsmeier Hack reaction, obtaining intermediate **62** in 84 % yield. Knoevenagel condensation of dialdehyde **62** with malonodinitrile gave the target compound **63** in 55 % yield.

Similar DTP dimer terminated with dicyanovinylene acceptor groups was synthesized by D. Zhu and co-workers [90].



**Scheme 2.20.** Synthetic sequence for **66a** and **66b**

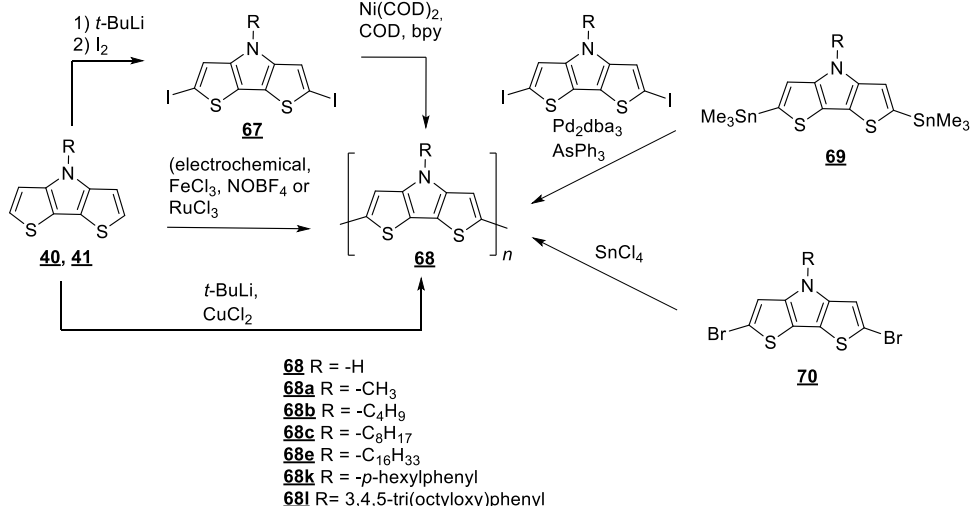
The dimers **66a** and **66b** were obtained from DTP in multi-step reaction procedure (Scheme 2.20). Carbon-carbon coupling of the DTP followed by formylation using Vilsmeier–Haack reaction resulted in dialdehyde **65**. Knoevenagel condensation of DTP dimer, using malononitrile, resulted in dicyano-vinyl-DTP

compounds **66a**, **66b** with reasonable yields [90, 91]. These two compounds exhibited very similar absorption maxima at around 597 nm in solution, and the presence of the additional DTP unit resulted in a bathochromic shift of the absorption maxima compared with **63**.

### 2.3.3. Synthesis of functionalized DTP polymers

Dithieno[3,2-b:2',3'-d]pyrrole is often used as a building block to produce polymeric p-type semiconductors for optoelectronic devices. Compared to other pyrrole-containing monomers, DTP has lower HOMO, and *N*-alkyl group in DTP moiety can be used to increase the solubility of the final polymer.

Zotti and co-workers first published DTP-based homopolymeric materials in which the electropolymerization of the appropriate monomers **40**, **41a–41e** was used (Scheme 2.21). These polymers (**68**, **68a–68c**, **68e**) demonstrated band gaps of  $\sim 1.7$  eV and remarkably high conductivity values as high as  $40 \text{ S}\cdot\text{cm}^{-1}$  [65].



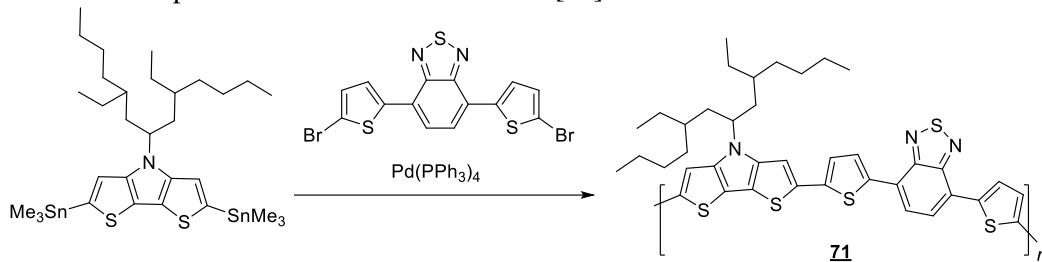
**Scheme 2.21.** Synthesis of DTP homopolymers **68**, **68a–68e**, **68k**, **68l**

C. S. Rasmussen and co-workers have demonstrated new *N*-functionalized DTP homopolymers (**68c**, **68k**), which were synthesized using FeCl<sub>3</sub> and electrochemical methods (Scheme 2.21) [72]. New DTP homopolymers had band gaps ranging from 1.6 to 1.8 eV, which were similar to those previously reported by G. Zotti and co-workers. Moreover, these polymers exhibited good fluorescence in solution with a quantum yield of 34 % (**68k**) [72].

G. Koeckelberghs and co-workers have reported the synthesis of poly(dithieno[3,2-b:2',3'-d]pyrrole)s (**68c**, **68e**) obtained in three different ways, i.e., the oxidative polymerization using RuCl<sub>3</sub>, Stille coupling and Yamamoto type polymerization (Scheme 2.21) [92]. According to the authors, Stille coupling appeared to be the best method of polymerization, and it demonstrated that soluble poly-DTPs with large molecular weights can be prepared in high yields [92]. Later, the same authors reported a new method of DTP polymerization utilizing dibromo-DTP and Lewis acids. According to the article, using SnCl<sub>4</sub> provided the best

polymerization results, and the obtained products showed similar optical properties as polymer (**68**) prepared via classical step growth approach [80].

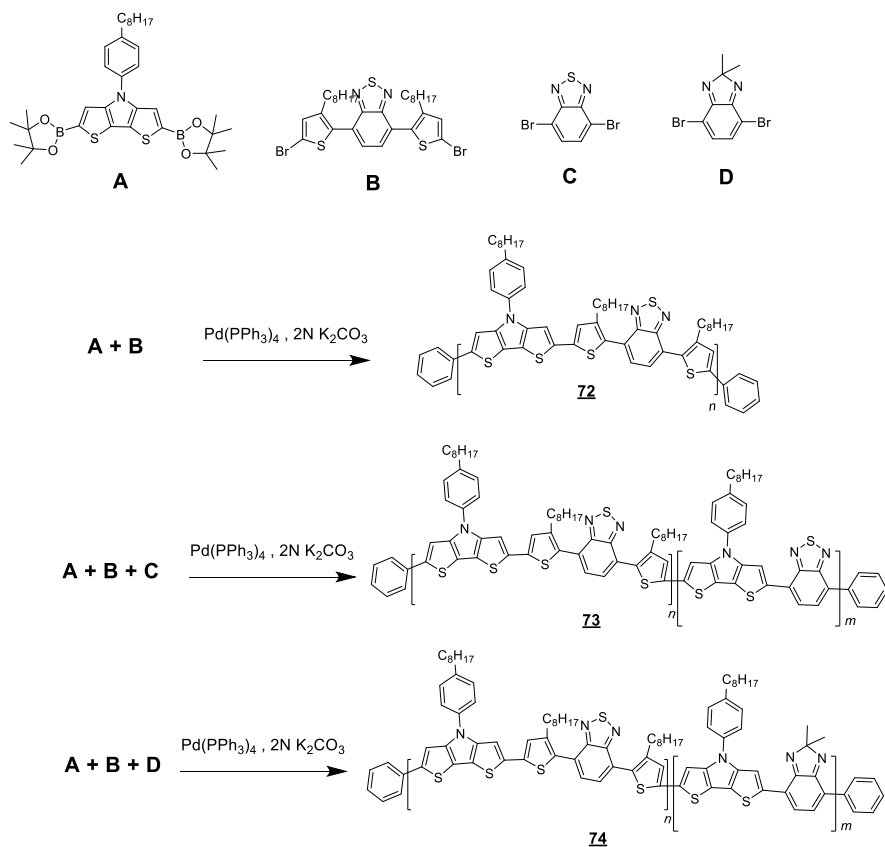
K. Hashimoto and co-workers have reported first DTP-based polymer (**71**) for the OPV application; they have demonstrated the copolymerization of *N*-substituted DTP with thiophene-flanked benzothiadiazole [93].



**Scheme 2.22.** Synthesis of DTP polymer **71**

The polymer was synthesized utilising Stille coupling reaction between 2,6-di(trimethyltin)dithieno[3,2-b:2',3'-d]pyrrole and 4,7-di(2-bromothiophen-5-yl)-2,1,3-benzothiadiazole in the presence of a palladium catalyst; the target polymer was obtained as a dark-green powder and could be easily dissolved in common organic solvents.

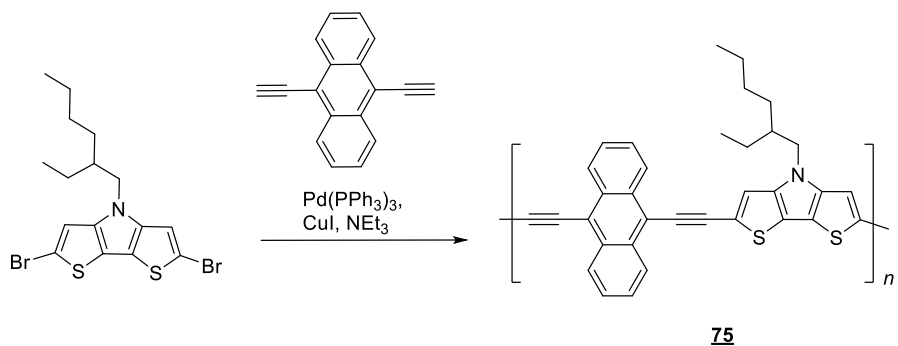
V. Tamilavan et al. have synthesized three new polymers **72**, **73** and **74** and applied them to the fabrication of bulk heterojunction solar cells [94].



**Scheme 2.23.** Synthesis of DTP polymers **72–74** via Suzuki coupling reaction

New polymer **72** was obtained by employing Suzuki coupling of the *N*-aryl DTP (**A**) and TBT (**B**) monomers. Suzuki random copolymerization was conducted by mixing the monomers **A**, **B** and **C** or **D** at 2:1:1 ratio to yield appropriate polymers **73** and **74**, respectively. Polymer **72** was synthesized in a similar manner from monomers **A** and **B**. The solubility of **72** was found to be excellent in all common organic solvents, whereas compounds **73** and **74** showed good solubility in chlorobenzene and dichlorobenzene but dissolved relatively poorly in chloroform and tetrahydrofuran at room temperature [94].

G. Gigli and co-workers have reported an interesting new alternating polymeric DTP derivative **75** using Sonogashira cross-coupling to obtain arylene-ethynylene semiconductors incorporating electron-rich anthracene and DTP units [88].



**Scheme 2.24.** Synthesis of DTP polymer **75** via Sonogashira coupling

Unfortunately, the polymer had low solubility, which led to the precipitation of the material during the polymerization.

### 2.3.4. Application of DTP in optoelectronic devices

The pyrrole fragment is widely used in the optoelectronics as a building block for small molecules and polymers; dithieno[3,2-b:2',3'-d]pyrrole is a promising and widely used moiety to produce efficient OPV, OFET and OLED devices. The report on conductivity and redox potential measurements of poly-(dithieno[3,2-b:2',3'-d]pyrrole) by A. Berlin et al. has had a huge influence on the development of new DTP-containing derivatives. As a result, there has been a gradual increase in interest in the use of DTP as a monomer [65]. Large series of polymers based on DTP and bithiophene have been synthesized, and the best among them is **76** (Figure 2.6). The blend of **76:PC71BM** as active film showed a PCE of 3.12 % in bulk heterojunction organic photovoltaic device (Table 2.4); however, the performance was not sufficient, and there was a need for further adjustment of the energy level to improve the device parameters and optimize the morphology of the active layer blend [95].

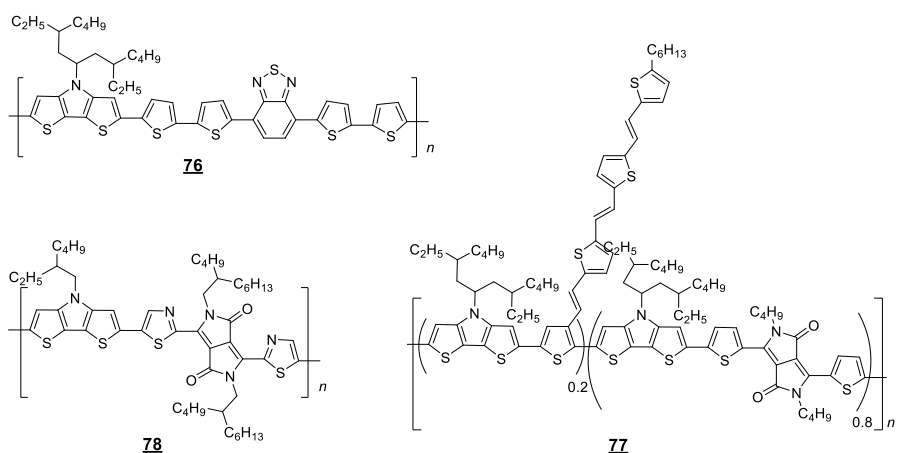


**Figure 2.6.** DTP-based polymers tested in OPV



**Table 2.4.** Optical and optoelectronic properties and OPV performance of polymers based on DTP moiety

	$\lambda_{\text{max}}$ [nm]	HOMO/LUMO [eV]	$V_{\text{oc}}$ [V]	$J_{\text{sc}}$ [mA $\text{cm}^{-2}$ ]	FF	PCE [%]	Ref.
<b>76</b>	464, 611	-4.99/-3.40	0.48	11.43	0.57	3.12	[95]
<b>77</b>	800	-4.86/-3.56	0.42	22.65	0.52	4.99	[96]
<b>78</b>	860	-5.61/3.94	0.69	14.9	0.54	5.6	[97]

Tajima and co-workers have reported a tris(thienylenevinylene) containing conjugated copolymer **77** (Figure 2.6). BHJ devices constructed utilizing **77** demonstrated  $J_{\text{sc}}$  of  $22.6 \text{ mA} \times \text{cm}^{-2}$ ; it is the first OPV device with a  $J_{\text{sc}}$  over  $20 \text{ mA} \times \text{cm}^{-2}$  (Table 2.4), and it still is one of the highest results for OPVs [96]. R. A. Janssen and co-workers have designed and synthesized DTP polymer bridged with thiazole moieties; the BHJ photovoltaic devices based on polymer **78** demonstrated relatively high external quantum efficiency (EQE) (up to 52 %) and PCE up to 5.6 %. This result indicated a possibility to enhance the efficiency further by reducing the energy loss of polymeric BHJ solar cells [97].

Although, a significant progress has been made in the development of DTP-containing polymers for light capture and charge transport in the BHJ solar cells. However, the result obtained with BHJ devices, combining fullerene derivatives and DTP-based conjugated polymers (PCE of 5.6 %), is still too low for practical application of such BHJ solar cells [97].

Another area of OPVs, which saw the use of DTP derivatives, was small donor-acceptor molecules. The devices utilizing these molecules realized better PCE, compared with the polymeric analogues, and those small molecule donor/acceptor systems opened a new era in the design of novel small molecules containing DTP fragment.

P. Bäuerle et al. have synthesized a series of A-D-A type compounds comprising of dithieno[3,2-b:2',3'-d]pyrrole as central donor and dicyanovinyl moieties as terminal acceptor fragments (**79- 82**); additionally, amphiphilic triethylene glycol side chain was utilized at the central DTP-nitrogen instead of the branched hydrocarbon (Figure 2.7). The solar cells constructed with these compounds have achieved power conversion efficiencies between 6.5 % and 7.6 % (Table 2.5) [98].

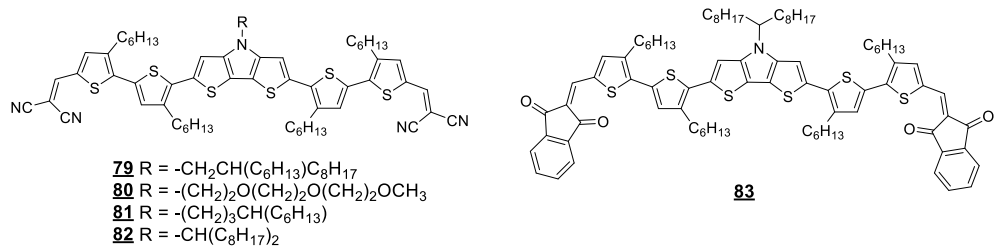


**Figure 2.7.** DTP-based small molecules for OPV

E. Borean et al. have identified the morphological differences in the solar cell active layer containing A-D-A type structure **79**, the PCE of the **79:PC71BM** device has increased noticeably to 7.1 % [99].

**Table 2.5.** Optical and optoelectronic properties and OSC performance of DTP based small molecules

	$\lambda_{\text{max}}$ [nm]	HOMO/LUMO [eV]	$V_{\text{OC}}$ [V]	$J_{\text{sc}}$ [mA $\text{cm}^{-2}$ ]	FF	PCE [%]	Ref.
<b>79</b>	700	-5.30/-3.73	0.83	12.0	0.71	7.1	[99]
<b>80</b>	720	-5.28/-3.74	0.74	12.85	0.70	6.57	[98]
<b>81</b>	707	-5.28/-3.70	0.79	12.46	0.69	7.04	[98]
<b>82</b>	694	-5.31/-3.75	0.84	11.4	0.63	7.63	[100]
<b>83</b>	654	-5.25/-3.78	0.86	14.06	0.68	8.22	[100]

D. Sharma and co-workers have synthesised a novel A-D-A absorber **83** consisting of dithieno[3,2-b:2',3'-d]pyrrole core and two electron accepting 1,3-indanedione groups linked by thiophene units (Figure 2.7) and investigated its optical and electrochemical properties. After the device structure optimization, such as inserting hole transporting CuSCN layer and annealing treatment, the devices constructed using **83:PC71BM** mixture [100] demonstrated PCE up to 8.22 % (Table 2.5).

### 2.3.5. Application of DTP derivatives in PSC

Perovskite solar cells (PSC) have achieved high power conversion efficiency of 25.5 % [2]; however, in order to achieve such results, the hole transporting materials had to be doped with various additives to increase conductivity. Resulting PSC demonstrated unimpressive long-term stability, thus blocking the industrial commercialization of such devices. In this chapter, several new dopant-free HTM containing dithieno[3,2-b:2',3'-d]pyrrole fragment will be discussed.

Y. Yan and W. Tang et al. [101, 102] have synthesized HTM **84** featuring a DTP core and four triphenylamine fragments joined by thiophene moieties (Figure 2.8). Planar n-i-p architecture PSC devices, constructed using dopant-free **84**, yielded PCE of 19.42 %, which is comparable to the result obtained with dopant comparing spiro-MeOTAD (PCE 19.59 %). Later, the same group reported a new smaller molecule with two triphenylamine fragments **50**, which exhibited suitable

ionization potential ( $I_p$ ) of 4.94 eV and good hole mobility of  $4.18 \times 10^{-4} \text{ cm}^2 \times \text{V}^{-1} \times \text{s}^{-1}$ ; consequently, the devices constructed using this dopant-free HTM demonstrated impressive PCE of 21.04 % [82] (Table 2.6).

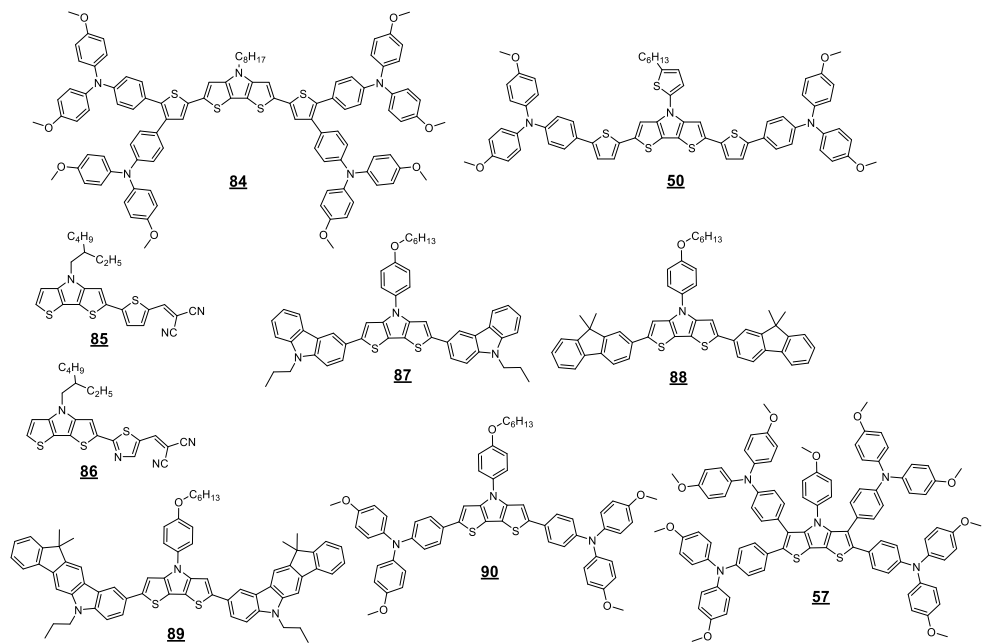


**Figure 2.8.** DTP-based small molecules as HTMs for PSC

S. Pola et al. [103] have synthesized two multichromophoric hybrid small molecules of D- $\pi$ -A architecture (**85** and **86**). The hole mobility characteristics of the newly obtained materials were comparable to that of spiro-OMeTAD. Perovskite solar cells fabricated using **85** and **86** as the hole transporting materials without using any dopants showed PCEs of 17.91 % and 18.75 %, respectively; these characteristics were achieved with the device of active area of  $2.04 \text{ cm}^2$ , and it surpassed the result of spiro-OMeTAD-based devices both in performance (PCE 14.74 %) and active area ( $1.84 \text{ cm}^2$ ).

**Table 2.6.** Optical and optoelectronic properties and PSC performance of DTP-based small molecular HTMs

	$\lambda_{\max}$ [nm]	HOMO/LUMO [eV]	$V_{oc}$ [V]	$J_{sc}$ [mA cm <sup>-2</sup> ]	FF	PCE [%]	Ref.
<b>50</b>		-4.94/-2.94	1.16	22.76	0.80	21.04	[102]
<b>57</b>	407	-4.98/-2.22	1.07	22.2	0.66	15.6	[87]
<b>84</b>		-4.85/-	1.14	23.02	0.74	19.42	[82]
<b>85</b>	525	-5.32/-3.20	1.01	24.56	0.72	17.91	[103]
<b>86</b>	514	-5.41/-3.18	1.03	24.78	0.73	18.75	[103]
<b>87</b>	403	-5.13/-2.3	1.02	20.53	0.59	12.35	[104]
<b>88</b>	420	-5.36/-2.64	1.03	19.40	0.46	9.19	[104]
<b>89</b>	410	-5.15/-2.34	1.08	22.5	0.72	17.5	[104]
<b>90</b>	428	-5.08/-2.42	1.00	20.72	0.69	14.3	[104]

M. Liang et al. have reported HTM series **87–90**, bearing DTP centre and various donoric fragments on the periphery (Figure 2.8), the best photovoltaic performance in PSCs was demonstrated by **89** with the indeno[1,2-b]carbazole moieties. High efficiency and stability were simultaneously realized: the doped **89** exhibited PCE exceeding 20 %, while dopant-free device showed PCE of 17.5 % [104].

M. K. Nazeeruddin et al. have reported novel electron-rich small molecule **57** consisting of DTP aromatic core with four triphenylamine moieties. This material has been successfully demonstrated to function as efficient HTMs in perovskite-based photovoltaic devices. The photovoltaic performance of the PSC was 15.6 %, compared with spiro-MeOTADs 17.7 % [87].

### 2.3.6. Chapter summary

From the information provided in this section, it is evident that DTP-containing derivatives have attracted significant attention in the optoelectronics community, especially in the field of photovoltaics and light emitting devices. A lot of work has been done to improve the synthesis of DTP core itself as well as optimize the synthetic procedures used for the modification or polymerization reactions conducted using DTP moiety. Although, a significant amount of work has been done in this field, only limited DTP modification pathways are available; chief among them are Stille, Suzuki and Sonogashira coupling reactions. Nonetheless, various DTP-based p-type semiconductors have been developed for the application in organic photovoltaics and perovskite solar cells. Some impressive results have been achieved, especially in the PSC field; **50** showed the best performance as dopant-free hole transporting material in perovskite solar cells demonstrating power conversion efficiency of 21.04 %. Overall, it is evident that DTP shows promise for further development of new even more efficient HTMs for application in perovskite solar cells.

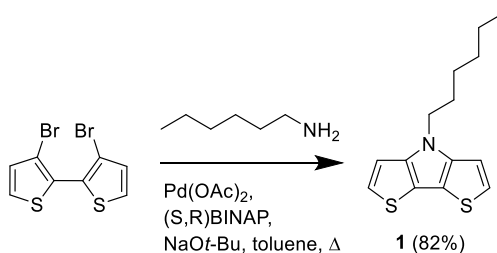
### 3. RESULTS AND DISCUSSION

#### 3.1. Dithieno[3,2-b:2',3'-d]pyrrole-based hole transporting materials

As mentioned in the literature overview, among a wide variety of pyrrole-containing building blocks, dithieno[3,2-b:2',3'-d]pyrrole is among the most studied fragments for optoelectronic applications, especially for organic light emitting diodes [91, 105], organic photovoltaics [60, 106, 107, 108] and organic field effect transistors [60, 109]. The possibility to modify the structure's solubility via *N*-alkylation reactions, relatively low-lying HOMO energy level [110], good to excellent mobility (up to  $4.1 \times 10^{-1} \text{ cm}^2 \times \text{V}^{-1} \times \text{s}^{-1}$ ) [60], symmetry and minimal torsional effects are among the reasons that make DTP moiety quite an attractive option for the above mentioned applications. Interestingly, acceptor–donor–acceptor (A–D–A) molecules containing central DTP fragment, investigated for the application in bulk heterojunction solar cells (BHJ-SC), yield devices with efficiency of over 8 % [100], while BHJ-SC with DTP-containing polymers have managed to achieve only modest result of 5.6 % [97]. Curiously, there is very little research done in the application of the DTP in hole transporting materials for perovskite solar cells. Due to the above-mentioned reasons, it has been decided to synthesize and investigate DTP-based derivatives as possible hole transporting materials for the application in PSC.

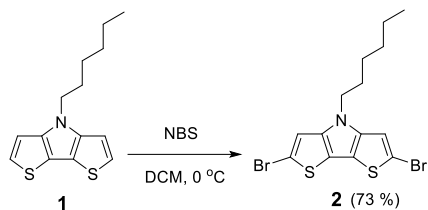
##### 3.1.1. Synthesis of dithieno[3,2-b:2',3'-d]pyrrole-based materials

Pyrrole-containing building block 4-hexyl-4*H*-dithieno[3,2-b:2',3'-d]pyrrole (**1**) was synthesized from 3,3'-dibromo-2,2'-bithiophene via Buchwald–Hartwig amination using palladium (II) acetate and BINAP catalytic system, sodium *tert*-butoxide base and relatively long 1-hexylamine alkyl group for improved solubility (Scheme 3.1) [67].



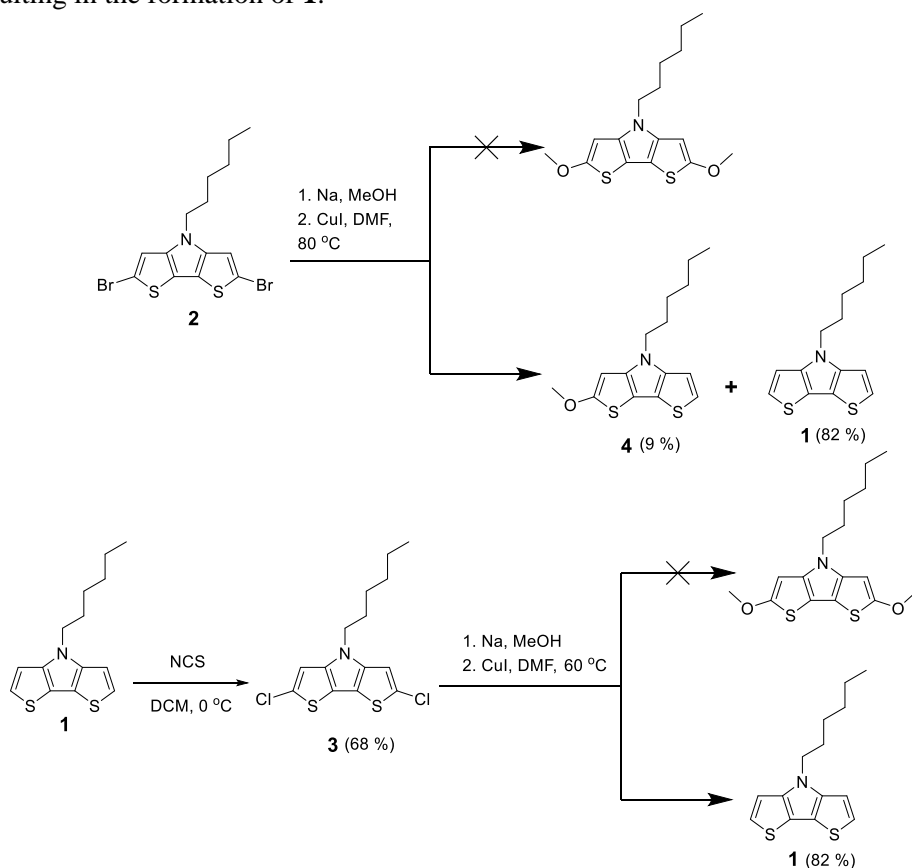
**Scheme 3.1.** Synthesis of dithieno[3,2-b:2',3'-d]pyrrole **1**

Isolated in very good yield, DTP derivative **1** was used in the bromination reaction using NBS as a source of bromine (Scheme 3.2). Dibromo-substituted compound **2** was used as an intermediate in a number of different reactions aimed at the synthesis of goal products containing DTP moiety.



**Scheme 3.2.** Synthesis of dibromo substituted compound **2**

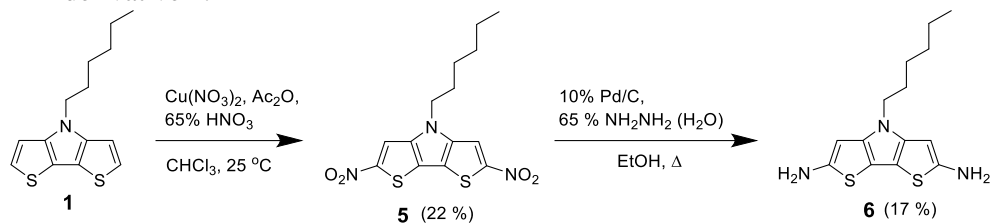
In an effort to synthesize DTP-based small molecules with lower ionization potential, the attempts were made to introduce electron donating groups into the DTP core. Initially, dibromo-substituted derivative **2** was used in methoxylation reaction with sodium methoxide (Scheme 3.3). Unfortunately, the reaction did not proceed as planned, and only a small amount of monosubstituted derivative **4** was isolated; the vast majority of the starting material underwent dehalogenation reaction resulting in the formation of **1**.



**Scheme 3.3.** Synthesis of methoxy-substituted DTP derivatives

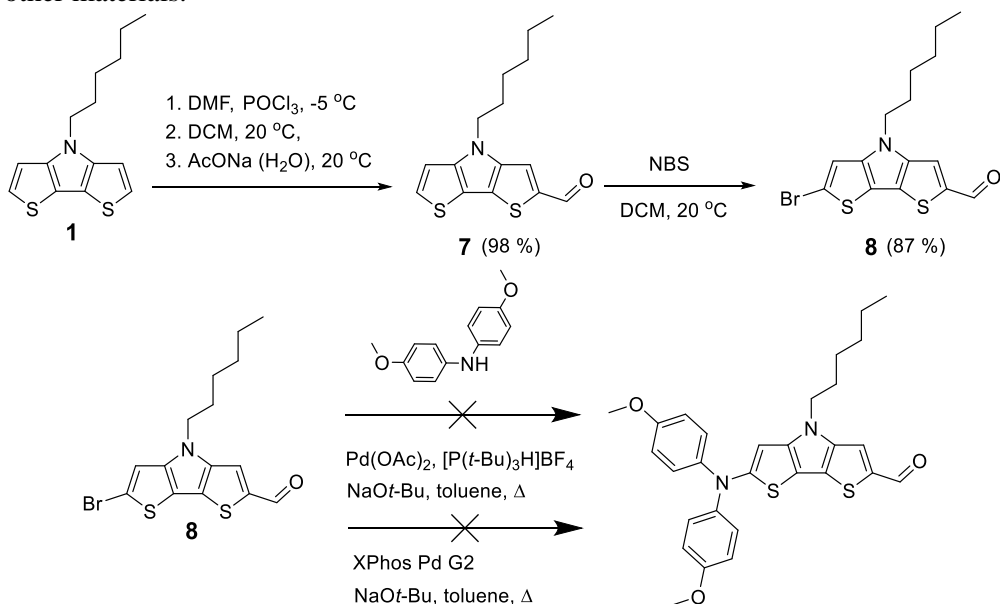
It was decided to use different leaving group, i.e., chlorine atom. *N*-chlorosuccinimide (NCS) was used for chlorination, resulting in dichloro-substituted

compound **3**. As before, **3** was used in methoxylation reaction with sodium methoxide (Scheme 3.3) with the same result, i.e., the formation of dehalogenated DTP derivative **1**.



**Scheme 3.4.** Synthesis of amino-substituted DTP derivative **6**

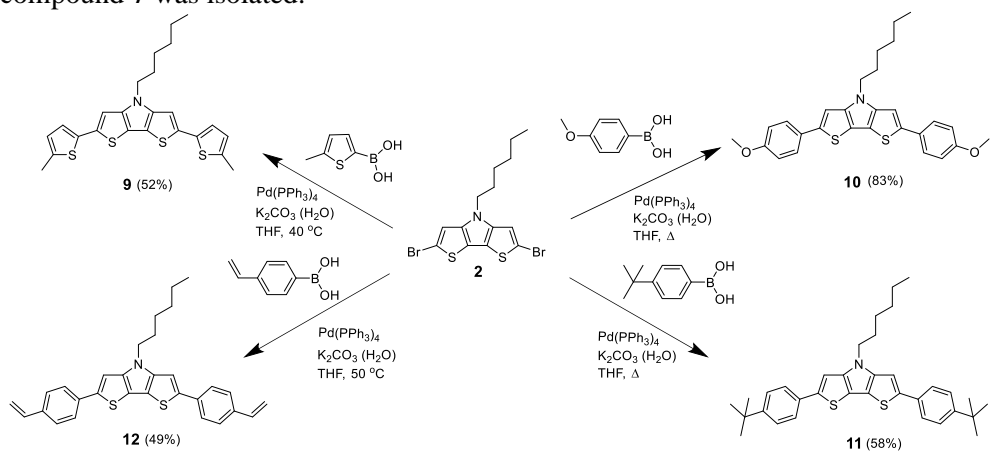
After first unsuccessful attempts to introduce electron donating groups, a different moiety (amine) was selected for the task. Starting DTP derivative **1** was nitrated (Scheme 3.4), and the resulting nitro compound **5** was reduced using palladium on carbon and hydrazine hydrate to appropriate diamino derivative **6**. Unfortunately, DTP with two amine moieties demonstrated very low stability, making purification and further work with it very problematic. As one of the main focuses of the work was the development of HTM with relatively straightforward synthesis suitable for larger scale production, it has been decided to concentrate on other materials.



**Scheme 3.5.** Synthesis of diphenyl amine-substituted DTP derivative

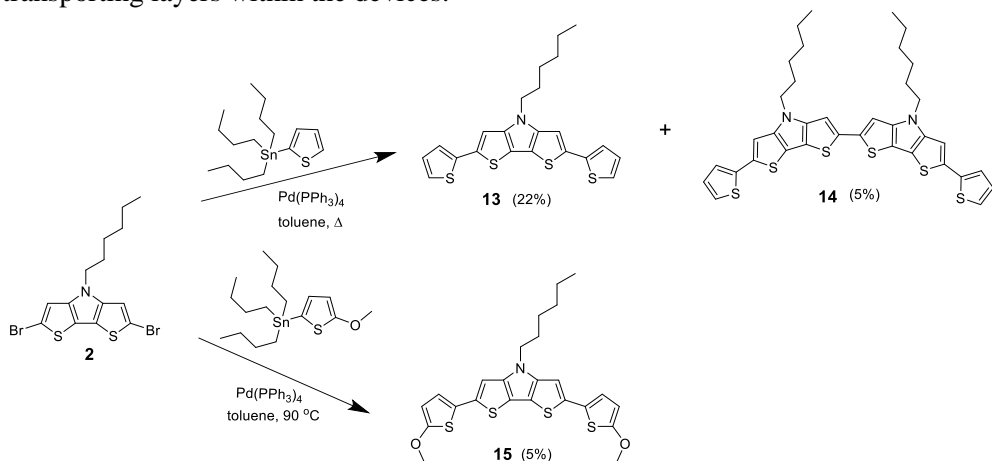
Introduction of 4,4'-dimethoxydiphenylamine into the DTP system was investigated as well. After the introduction of the aldehyde group into the system via Vilsmeier–Haack reaction (Scheme 3.5) and subsequent bromination of obtained

aldehyde **7** using NBS, the obtained bis-substituted compound **8** was used in Buchwald–Hartwig coupling reaction with 4,4'-dimethoxydiphenylamine. Regrettably, the desired product was not obtained, and only dehalogenated compound **7** was isolated.



**Scheme 3.6.** Synthesis of bis-substituted DTP derivatives **9–12**

Evidently, the reactions requiring the usage of stronger bases have resulted in dehalogenation of the starting material; therefore, it was decided to utilize Suzuki coupling reaction, which can be successfully conducted using milder bases. Various boronic acids with electron donating moieties have been utilized to obtain DTP derivatives **9–11** with the enhanced conjugated system, anticipating semiconducting molecules with lower ionization potential (Scheme 3.6). Additionally, the hole transporting material with two reactive vinyl groups **12** has been synthesized; **12** has a potential to be used as a crosslinkable HTM for the production of insoluble hole transporting layers within the devices.



**Scheme 3.7.** Synthesis of compound thiophene-substituted DTP derivatives **13, 14** via Stille coupling reaction



Finally, palladium catalysed Stille coupling reaction using organotin thiophene compounds was utilized to extend the list of possible candidates for the investigation further. Thiophene **13** and 2-methoxythiophene **14** containing derivatives were isolated. The reaction of 2,6-dibromo-4-hexyl-4*H*-bisthieno[3,2-*b*:2',3'-*d*]pyrrole (**2**) with 2-(tributylstannyl)thiophene as well resulted in the formation of dimeric structure **14**, albeit in very low yield. Sadly, thiophene derivatives **13–15** did not demonstrate sufficient stability to be seriously considered as potential candidates for the application in PSC. Most likely, the increased sensitivity of the compounds could be attributed to too shallow HOMO level due to the presence of relatively strong donoric fragments (derivatives **14**, **15**) and unprotected reactive 5-position of the thiophene ring in compound **13**.

### 3.1.2. Thermal properties

The thermal properties of the most promising HTMs have been investigated using thermogravimetric and differential scanning calorimetry analyses (Table 3.1). 4-Hexyl-4*H*-dithieno[3,2-*b*:2',3'-*d*]pyrrole (**1**) demonstrates 5 % weight loss at 202 °C (Table 3.1, Figure 3.1). Looking at the profile of the thermogravimetric analysis (TGA) curve, a sharp drop in weight can be observed, indicating that rapid evaporation of the material takes place. Small molecular weight of the compound as well as relatively long and hydrophobic aliphatic chain allow for easier evaporation. Additional phenyl or thiophene rings, at 2,6-positions of the DTP core in **9** and **10**, increase the molecular weight of the compound and decomposition temperature by more than 110 °C.

**Table 3.1.** Results of TGA<sup>[b]</sup> and differential scanning calorimetry (DSC)<sup>[a]</sup> analysis of **1**, **9–12**

Compound	Thermal decomposition $T_{dec}$ , [°C]	Glass transition $T_g$ , [°C]	Crystallization $T_{crys}$ , [°C]	Melting point $T_m$ , [°C]
<b>1</b>	202 <sup>[c]</sup>	–	7	47
<b>9</b>	316	–	92	117, 119
<b>10</b>	358	–	85	161
<b>11</b>	338 <sup>[c]</sup>	–	181	218
<b>12</b>	412	–	–	–

<sup>[a]</sup> Determined by DSC from second run, heating rate of 10 °C min<sup>-1</sup> under N<sub>2</sub> atmosphere; <sup>[b]</sup> determined by TGA, heating rate 10 °C min<sup>-1</sup> under N<sub>2</sub> atmosphere; <sup>[c]</sup> evaporation.

The substitution of the methoxy moieties to *tert*-butyl ones in **11** weakens the interaction forces between molecules and allows for easier sublimation of the compound while maintaining higher sublimation temperature (Figure 3.1). Finally, the hole transporting material with two reactive vinyl groups **12** demonstrates the highest thermal stability of all materials in this group, although it can be attributed to the thermal polymerization taking place during the heating, and in reality, it demonstrates the thermal stability of the obtained polymer rather than monomer **12** itself.

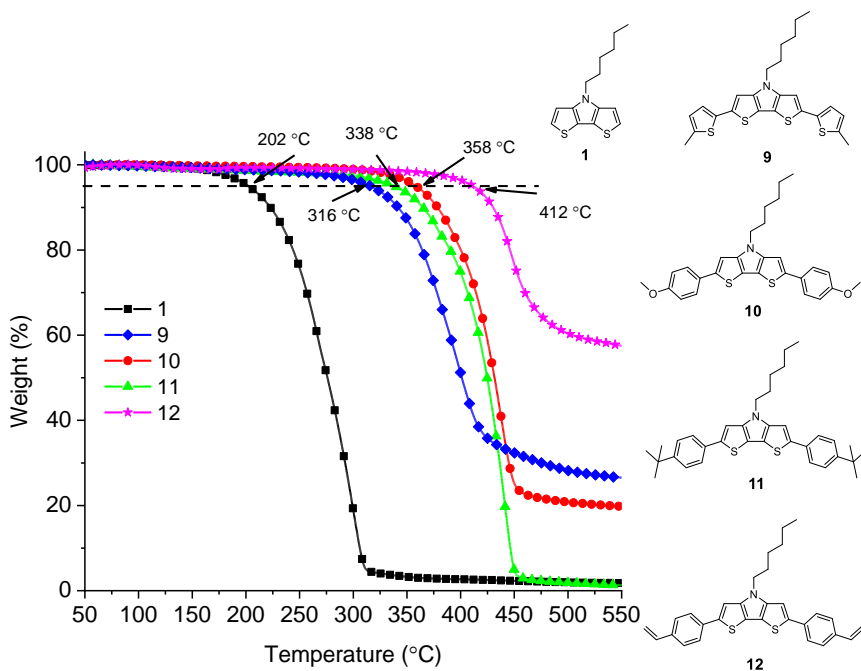


**Figure 3.1.** TGA analysis of DTP derivatives **1**, **9–12**

The analysis of the DTP derivatives **1**, **9–12** using differential scanning calorimetry has revealed that all the investigated compounds are crystalline materials with melting temperatures ranging from 47 to 218 °C (Table 3.1). Comparatively long aliphatic chain in **1** significantly contributes to the low melting temperature of 47 °C, no glass transition is observed throughout the first heating. During the second heating, the crystallization of the materials is observed at 7 °C, followed by the melting of the formed crystals at 47 °C (Figure 3.2).

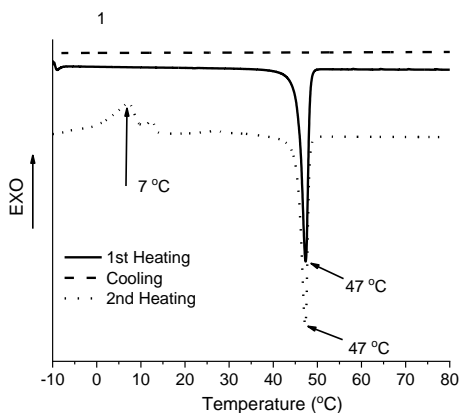


**Figure 3.2.** DSC curves of hole transporting material **1**

Similar picture, i.e., melting of the crystals during the first heating, followed by the crystallization during cooling and melting during the second heating, can be observed for HTMs **9–11** (Figures 3.3a–3.3c). Compared with the starting compound **1**, the addition of the structural bulk in DTP derivatives **9–11** noticeably increases the melting temperature. 5-methylthiophene moieties in **9** increase  $T_m$  by  $\sim 60$  °C, while larger and more rigid 4-methoxyphenyl and 4-*tert*-butylphenyl fragments in **10** and **11** increase it even further by  $\sim 110$  °C and  $\sim 170$  °C, accordingly.

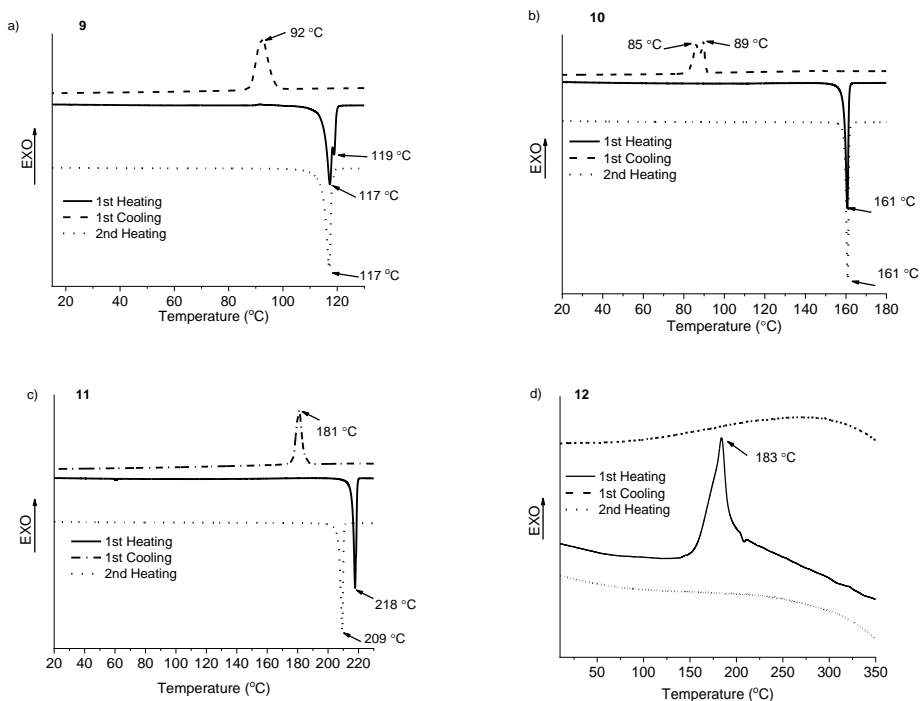


**Figure 3.3.** DSC curves of hole transporting materials **9** (a), **10** (b), **11** (c), **12** (d)

Finally, the hole transporting material with two reactive vinyl groups **12** demonstrates exothermic peak at 183 °C during first heating and no other signals during subsequent cooling and heating cycles, indicating thermal polymerization of the material during the first heating cycle (Figure 3.3d).

### 3.1.3. Optical, electrochemical and photoelectrical properties

In order to investigate the size of the  $\pi$ -conjugated system of the synthesized dithieno[3,2-*b*:2',3'-*d*]pyrrole derivatives, ultraviolet–visible light absorption spectra of the DTP-based compounds were recorded. The DTP core itself absorbs in the UV part of the spectrum with absorption maxima around 300 nm (Figure 3.4).

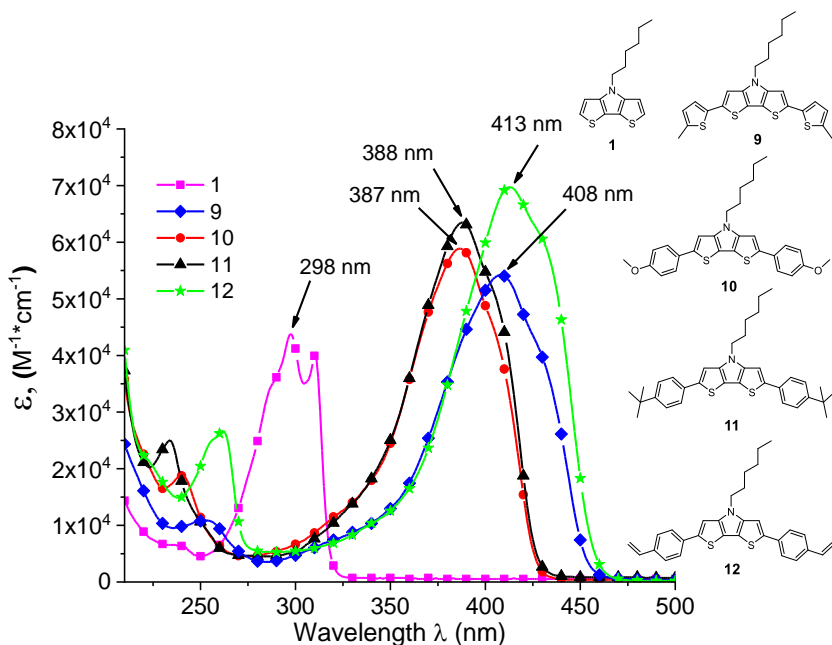


**Figure 3.4.** Light absorption spectra of **1**, **9–12** in THF ( $c = 10^{-4}$  M)

The introduction of two phenyl moieties into the system (**10**, **11**) noticeably increases the size of the  $\pi$ -conjugated system, and a bathochromic shift of  $\sim 80$  nm is observed. Interestingly, additional methoxy groups in DTP derivative **10** did not produce any significant redshift of the spectrum, compared with *tert*-butyl-containing HTM **11**. As it could be expected, stronger electron donating thiophene groups increased the size of the conjugated system resulting in a bathochromic shift of the absorption maximum in UV-Vis spectra of 20 nm, compared with phenyl-bearing analogues **10** and **11**. The most intriguing result was observed for the material with two 4-vinylphenyl groups **12**. It demonstrates the largest  $\pi$ -conjugated system of all investigated compounds and a bathochromic shift of  $\sim 25$  nm, compared with very similar *tert*-butyl and methoxy analogues **10**, **11**. It is quite difficult to rationally explain such differences in UV-vis spectrum, it is speculated that the molecule of **12** adopts a more planar conformation, and vinyl groups contribute to the size of the conjugated system more substantially than it could appear from the first glance.

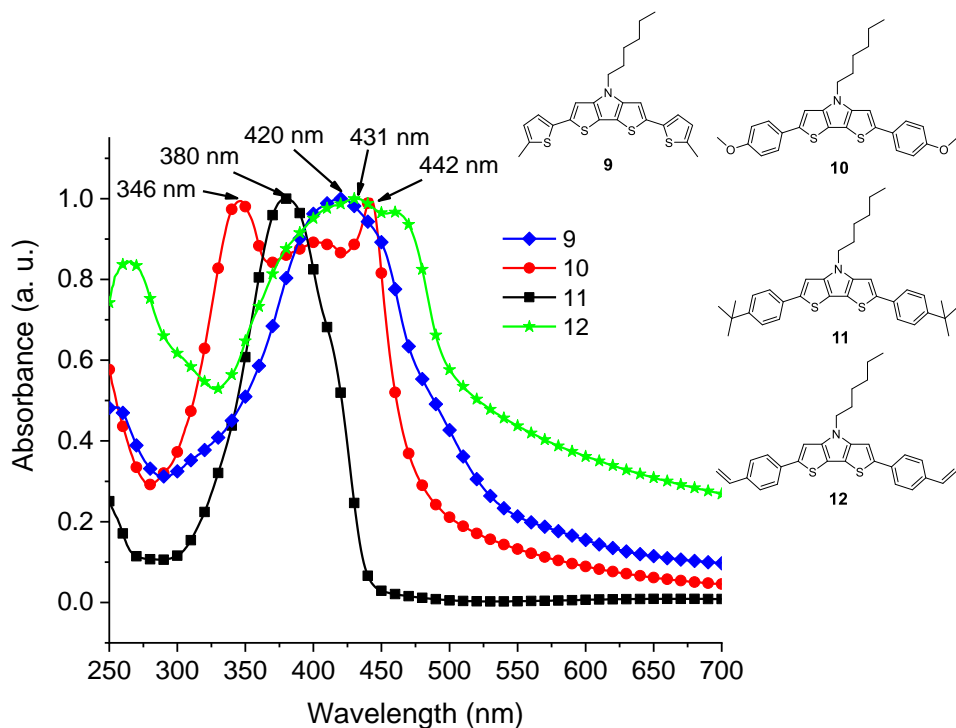


**Figure 3.5.** Light absorption spectra of **9–12** in thin films

Interestingly, UV-vis spectra of the HTMs **9**, **10**, **12** in the solid state demonstrate broadening and redshift characteristic for the formation of the aggregates (Figure 3.5). Vinyl substituted DTP derivative **12** and thiophene substituted HTM **10** display redshifts of approximately 20 nm. The aggregation is especially well pronounced in case of DTP derivative **10** bearing methoxy groups, new redshifted ( $\sim 55$  nm bathochromic shift) and blueshifted ( $\sim 40$  nm hypsochromic shift) absorption maxima, compared with the UV-vis spectrum in the solution, are registered. However, the introduction of branched and sterically bulkier *tert*-butyl groups in **11** results in a suppression of aggregation, and only small changes in shape and position of the spectrum are observed.

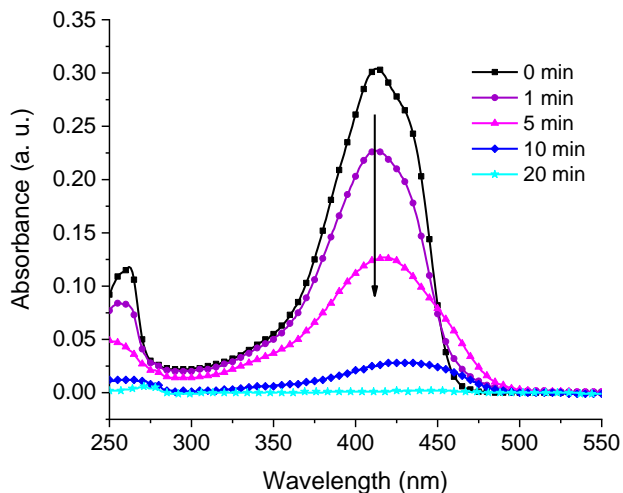


**Figure 3.6.** Light absorption spectra of the THF solvent used for washing of the samples after crosslinking experiments with **12**

The crosslinking of the DTP derivative **12** was further investigated using UV-vis spectroscopy (Figure 3.6). The thin films were heated at 180 °C for various periods of time, washed with THF and their absorption spectra recorded. From the conducted experiments, it is evident that 20 minutes at 180 °C is sufficient for a complete crosslinking of the samples. Looking at the absorption spectra of the solvent used for washing (Figure 3.6), it is evident that the traces of HTM **12** can still be detected in samples heated for 10 min but are practically absent in the samples that are heat treated for 20 minutes.

**Table 3.2.** Electrochemical<sup>[a]</sup> characteristics and  $I_p$  of **1** and **9–12**

Compounds	$E_g^{opt}$ [eV] <sup>[b]</sup>	$E_{HOMO}$ [eV] <sup>[c]</sup>	$E_{LUMO}$ [eV]	$I_p$ [eV]
<b>1</b>	3.87	-5.07	-1.2	5.74
<b>9</b>	2.74	-4.73	-1.99	5.04
<b>10</b>	2.90	-4.83	-1.93	5.09
<b>11</b>	2.89	-4.83	-1.94	4.99
<b>12</b>	2.70	-4.82	-2.12	5.56

<sup>[a]</sup> The cyclic voltammetry (CV) measurements were carried out with a glassy carbon electrode in dichloromethane solutions, 0.1 M tetrabutylammonium hexafluorophosphate as electrolyte and Pt wire as a reference electrode. Potentials measured vs Fc<sup>+</sup>/Fc. <sup>[b]</sup>Optical band gaps  $E_g^{opt}$  estimated from the edges of electronic absorption spectra in solution. <sup>[c]</sup>Conversion factors: Fc in DCM vs SCE 0.46 [111], SCE vs SHE: 0.244 [112], SHE vs. vacuum: 4.43 [113]. <sup>d</sup> $E_{LUMO}$  calculated from the equation  $E_{LUMO} = E_{HOMO} - E_g^{opt}$ .

The oxidation ( $E_{ox}$ ) potentials of the DTP-based HTMs **1**, **9–12** were measured by employing a cyclic voltammetry technique, and the ionization energy ( $E_{HOMO}$ ) as well as electron affinity ( $E_{LUMO}$ ) have been calculated (Table 3.2). These values do not represent any absolute solid-state or gas-phase ionization energies but can be used to compare different compounds that are relative to one another. The cyclic

voltammograms of all synthesized DTP-containing compounds show quasi-reversible oxidation (Figure 3.7). 2,6-Substituted DTP derivatives (**9–12**) demonstrate shallower  $E_{\text{HOMO}}$ , compared with 4-hexyl-4*H*-dithieno[3,2-*b*:2',3'-*d*]-pyrrole (**1**) core (Table 3.2). Larger  $\pi$ -conjugated system of **9–12** ensures a change in  $E_{\text{HOMO}}$  by approximately 0.2 eV, while the presence of the electron donoric thiophene moieties in **9** pushes the ionization energy even further to -4.73 eV.

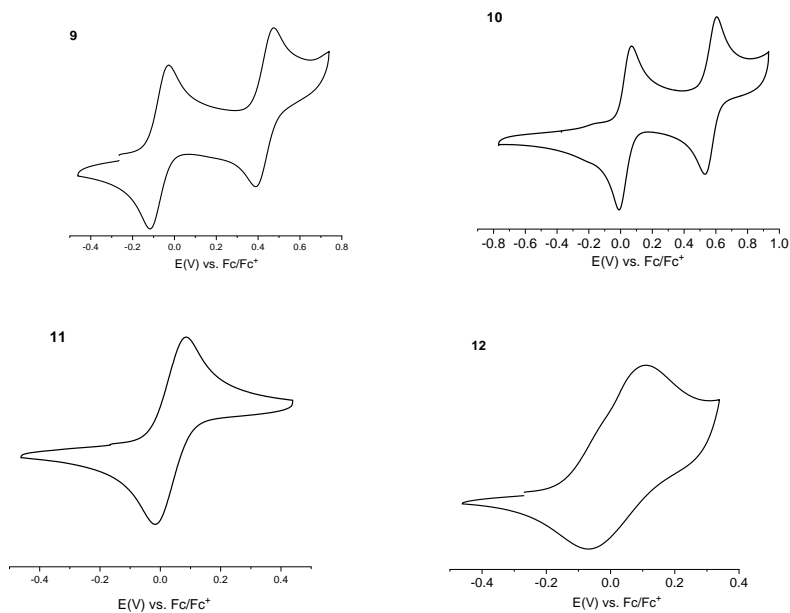


**Figure 3.7.** Cyclic voltammograms of **9–12** (scan rate = 50 mV s<sup>-1</sup>) in argon-purged dichloromethane solutions

The larger size of the  $\pi$ -conjugated system and the presence of additional electron donating moieties as well reduce the energy band gap  $E_g$  and lower  $E_{\text{LUMO}}$  energy level in all four investigated DTP derivatives **9–12**, compared with the starting compound **1**.

The solid-state  $I_p$  is an important parameter for the organic materials that are planned to be used for the optoelectronic applications.  $I_p$  of the HTMs was measured using photoelectron emission in air (PESA) method (Figure 3.8 and Table 3.2). The measurement results indicate that  $I_p$  values of the investigated materials follow the same trend as data obtained from UV-vis and CV, i.e., **1** demonstrates the highest  $I_p$  (5.74 eV), while the increased conjugated system and the presence of stronger electron donating fragments lower  $I_p$  to 5.0–5.1 eV in **9–11**. One noticeable exception is vinyl-containing DTP-derivative **12**: it breaks the trend and demonstrates significantly higher  $I_p$  of 5.56 eV.

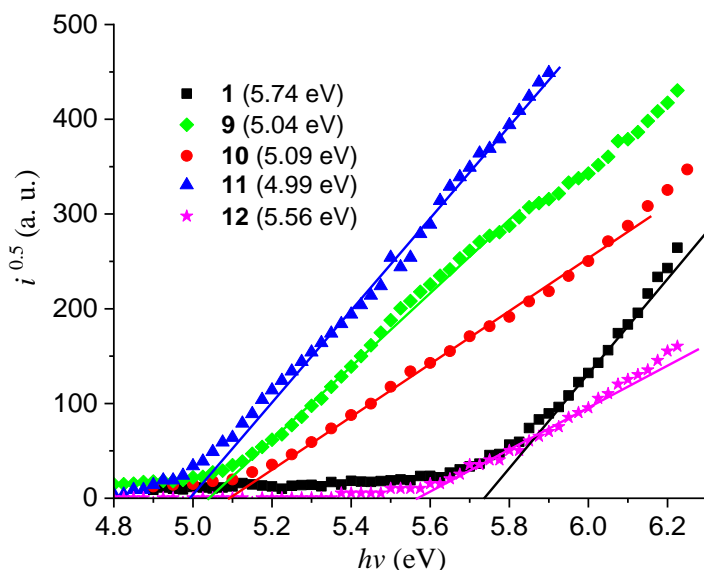


**Figure 3.8.** Photoemission in air spectra of compounds **1**, **9–12**

Generally, absolute values obtained using CV and PESA methods differ, and the main reason for such disagreements are different mediums used for the measurement (solution for CV and thin solid film for PESA). However, the main trends remain very similar using both techniques. In case of **12**, however, the observed differences between results can be explained by different way molecules interact with each other. Cyclic voltammetry is carried out in the solution, and low concentration of **12** in the solution does not allow for any meaningful direct interaction between HTM molecules. However, PESA is measured in the thin films, and intermolecular interaction between HTM molecules is a factor to be considered. Therefore, the interactions between molecules are stronger for **12**, compared with **9–11**, and they influence  $I_p$  significantly, increasing it to 5.56 eV, compared to 4.82 eV measured using CV. In general, for the successful application of the HTMs in perovskite solar cells, their  $I_p$  should ideally be in the range between 4.9–5.4 eV. Purely from the energetic point of view, **9–11** are more promising candidates for the application in PSC.

### 3.1.4. Chapter summary

In conclusion of the chapter, it could be said that the synthesis of the dithieno[3,2-b:2',3'-d] pyrrole-based hole transporting materials is not a straightforward business. Many reactions require substantial optimization, and the materials themselves often lack stability required for the optoelectronic application. Additionally, in the literature related to the synthesis of DTP-derivatives, it can be noticed that the researchers mostly focus on the Suzuki coupling reaction as other types of reactions run into considerable difficulties. The investigation of small



molecule materials that were synthesized in this work reveals some interesting traits of these DTP-derivatives. Most importantly, the energy level of these HTMs is suitable for the application in perovskite solar cells; furthermore, TGA analysis reveals potential for the application of these materials in vacuum deposited devices. In addition, the introduction of reactive functional groups opens a path for thermal crosslinking of these HTMs in the layer, thus simplifying the process of constructing solar cell devices.

### **3.2. Long-term stability of the oxidized hole transporting materials used in perovskite solar cells\***

During the past eight years, perovskite solar cell technology has evolved from a scientific curiosity to a major research subject in the field of photovoltaics and in a short period of time, managed to demonstrate remarkable achievements in the PCE [114]. While significant progress has been made in terms of performance of PSC devices, much less attention has been paid to their long-term stability. Therefore, the next logical step is to address the longevity of the PSC devices. The stability of the PSC depends on a number of potential degradation factors. Some of them are obvious, for example, oxygen and moisture. Others, which are active as well under inert conditions and affect various materials, are harder to determine and eliminate due to the complex, multicomponent nature of the devices. Good examples of such intrinsic instabilities could be gold migration through hole transporting layer [115] and the crystallization of the hole transporting material which reduces the electronic contact between HTM and perovskite [116, 117]. Both these processes are observed at elevated temperatures and are responsible for rapid performance losses. Temperature induced degradation of perovskite solar cells is a particularly interesting and important topic, as temperatures as high as 40–45 °C could be routinely encountered in the field, especially in hot desert environments, which are particularly attractive for photovoltaic energy generation due to the abundance of sunshine and vast unutilized space. Normally, photovoltaic devices operate in direct sunlight, and cell temperature can be up to 45 °C higher than in the environmental one [118]. Therefore, it is important to study in a greater detail the stability of the HTMs at elevated temperatures not only as separate materials but more importantly in combination with various dopants used in the PSC as well as in contact with other components of devices, such as perovskite itself.

#### **3.2.1. Interaction with dopants used in perovskite solar cells**

To this date, a wide variety of hole transporting materials has been developed for use in perovskite solar cells, and vast majority of them require the use of chemical doping as an essential step in the preparation of efficient devices [119]. 4-*tert*-Butylpyridine, lithium bis(trifluoromethanesulfonyl)imide and metalorganic

---

\* E. Kasparavičius investigated the stability of the oxidized HTMs, while A. Magomedov in his PhD thesis focused on a more detailed study of the pyridination reaction with model compound.

oxidants, such as tris(2-(1*H*-pyrazol-1-yl)-4-*tert*-butylpyridine)cobalt(III) tri[bis(trifluoromethane)sulfon-imide], comprise the doping mixture commonly in use for HTMs in perovskite solar cells. During the doping procedure part of the hole transporting material, approximately 10 % of it is oxidized to corresponding cation radical, which is responsible for the improvement in conductivity of the material and subsequently, device efficiency. The combination and the role of each doping component are more a result of the empirical optimizations rather than the application of a thorough design. An increase in HTMs conductivity while keeping charge recombination to a minimum is the most obvious effect observed so far from HTM doping [120, 121].

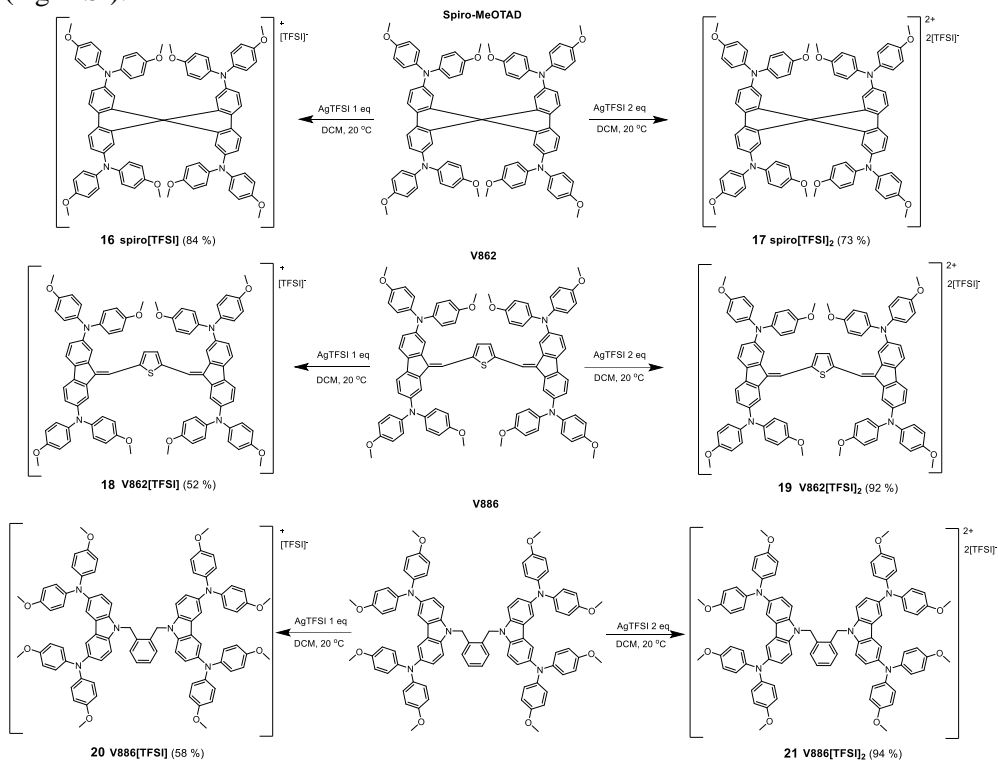
The oxidized organic hole transporting material could be one of the potential weak links in the perovskite solar cell composition. Interestingly, very little investigation has been done concerning the oxidized HTMs applied in the PSC, their properties and the effect of additives [122, 123, 124, 125, 126, 127, 128, 129]. Most importantly, long-term stability, especially under thermal stress, has not been investigated. It is not uncommon for a solar cell to heat up to temperatures exceeding 80 °C under summer sun; therefore, all device components must possess some degree of resistance to repetitive thermal stress [130].

In the current chapter, the thermal stability of a series of oxidized small molecular HTMs under different conditions and with different additives are investigated. In order to maximize the relevance of the research for the photovoltaic community, the hole transporting materials demonstrating very good performance in the PSCs have been chosen for this investigation.

### 3.2.1.1. Synthesis of the oxidized HTMs

A series of experiments with oxidized HTMs in the solid state have been conducted to investigate their long-term stability under different conditions and with different additives, which are routinely used in the hole transporting layers of the perovskite solar cells. Under standard doping conditions, the oxidized HTM comprises relatively small portion of the charge transporting layer composition, the rest being undoped hole transporting material. Hence, it is complicated to monitor its degradation dynamics in the film in real time due to low concentration and difficulties in identifying the oxidized species using such common analysis methods such as nuclear magnetic resonance (NMR) or mass spectrometry (MS) [128, 131]. Fortunately, however, the investigated hole transporting materials demonstrate intense absorption in the visible range of the spectrum in their oxidized state; thus, UV-vis spectroscopy is a very useful tool for monitoring processes that are taking place in the encapsulated films during the extended stability testing. In order to avoid concentration related problems and obtain a clearer picture of the processes taking place during the long-term stability testing, it has been decided to use films comprised of only oxidized material and not a mixture of HTM with a few percent of oxidized HTM in it. The layers of the oxidized HTMs have been prepared with and without the dopants and used in these studies. The oxidized derivatives of spiro-MeOTAD, V886 and V862[132] (Scheme 3.8), used in the study, have been

obtained using chemical oxidation by the silver bis(trifluoromethanesulfonyl)imide (AgTFSI).



**Scheme 3.8.** Synthesis of oxidized spiro-MeOTAD, V886 and V862

The investigation of the synthesized materials was conducted in three steps: analysis of the thermal properties of the oxidized HTMs, study of their stability in the solution and, finally, long-term stability tests in the thin films.

### 3.2.1.2. Thermal properties

Prior to the actual stability tests of the thin films, a number of important parameters of the oxidized HTMs have been investigated. Thermal stability of the HTMs was determined by thermogravimetric analysis of the oxidized and pristine samples (Figure 3.9, Table 3.3). Different materials display somewhat different decomposition dynamics under thermal stress; nonetheless, from the obtained results, it is evident that oxidized HTMs have reduced thermal stability, compared to the pristine materials, and decomposition temperature decreased by more than 100 °C.

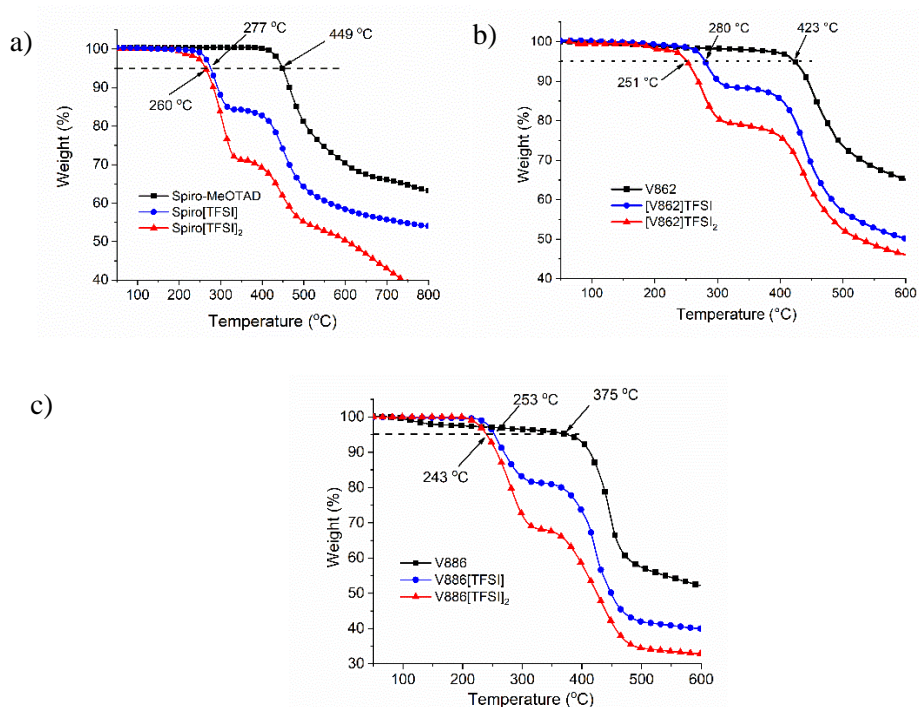


**Figure 3.9.** Thermogravimetric analysis of pristine spiro-OMeTAD (a), V862 (b), V886 (c) and their oxidized derivatives (heating rate  $10\text{ }^{\circ}\text{C min}^{-1}$ )

Two-step patterns can be seen for all of the oxidized HTMs: most likely, the first step is the breakdown of the oxidized salt, and the second one is the decomposition of the HTM structure itself, as the second decomposition temperature is very similar to the one registered for the pristine unoxidized materials.

**Table 3.3.** Thermal properties of spiro-MeOTAD, V862, V886 and their oxidized derivatives

Compound	$T_m$ [ $^{\circ}\text{C}$ ] [a]	$T_g$ [ $^{\circ}\text{C}$ ] [b]	$T_{dec}$ [ $^{\circ}\text{C}$ ] [c]
<b>spiro-MeOTAD</b>	245	126	449
spiro[TFSI] ( <b>16</b> )	213	91	277
spiro[TFSI] <sub>2</sub> ( <b>17</b> )	215	95	260*
<b>V862</b>	–	138	423
V862[TFSI] ( <b>18</b> )	–	97	280
V862[TFSI] <sub>2</sub> ( <b>19</b> )	–	100	251
<b>V886</b>	–	141	375
V886[TFSI] ( <b>20</b> )	217	93	253
V886[TFSI] <sub>2</sub> ( <b>21</b> )	216	99	243

[a] Determined by DSC from the first run, heating rate of  $10\text{ }^{\circ}\text{C min}^{-1}$  under  $\text{N}_2$  atmosphere; [b] determined by DSC from second run, heating rate of  $10\text{ }^{\circ}\text{C min}^{-1}$  under  $\text{N}_2$  atmosphere; [c] determined by TGA, heating rate  $10\text{ }^{\circ}\text{C min}^{-1}$  under  $\text{N}_2$  atmosphere.

Differential scanning calorimetry analysis revealed that oxidized HTMs of spiro-MeOTAD and V886 can exist in both crystalline and amorphous state, whereas derivatives of V862 are fully amorphous (Table 3.3); typical example of the DSC heating and cooling curves are given in Figure 3.10 (remaining DSC analysis curves can be found in Appendix 1, Figures S1–S7).

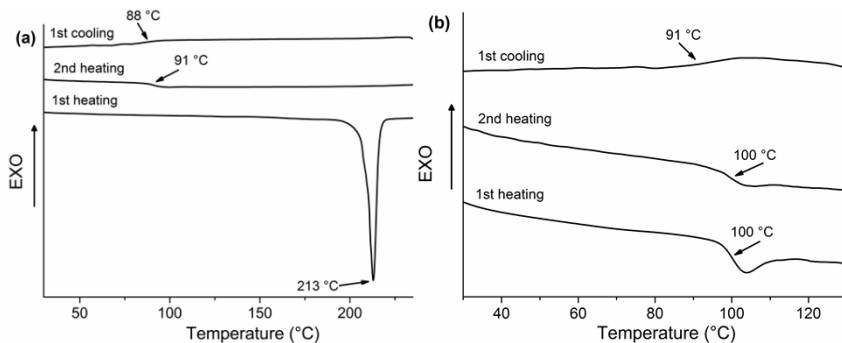


**Figure 3.10.** DSC curves for spiro[TFSI] (a) and V862[TFSI]<sub>2</sub> (b); heating and cooling rates 10 °C min<sup>-1</sup>

Similarly as spiro-MeOTAD, both spiro[TFSI] and spiro[TFSI]<sub>2</sub> are crystalline after the synthesis and form amorphous state only after the melting of crystals and subsequent cooling (Figure 3.10a). In contrast, derivatives of V862, V862[TFSI] and V862[TFSI]<sub>2</sub> remain completely amorphous, and only glass transition is observed (Figure 3.10b). In all of the cases, a drop in glass transition temperature is registered for the oxidized materials compared with the pristine HTMs.

### 3.2.1.3. Long-term stability of the oxidized HTMs in the solution

During the routine procedure of spiro-MeOTAD solution preparation in the air, it was noticed that light purple colour, which is formed after the addition of the bis(trifluoromethane)sulfonimide lithium salt and is associated with generated oxidized species, faded after the addition of 4-*tert*-butylpyridine. The same process, albeit much slower, was observed in the experiments with diluted solutions (10<sup>-4</sup> M) of the oxidized spiro[TFSI], V862[TFSI] and V886[TFSI] after the addition of tBP (Figure 3.11).

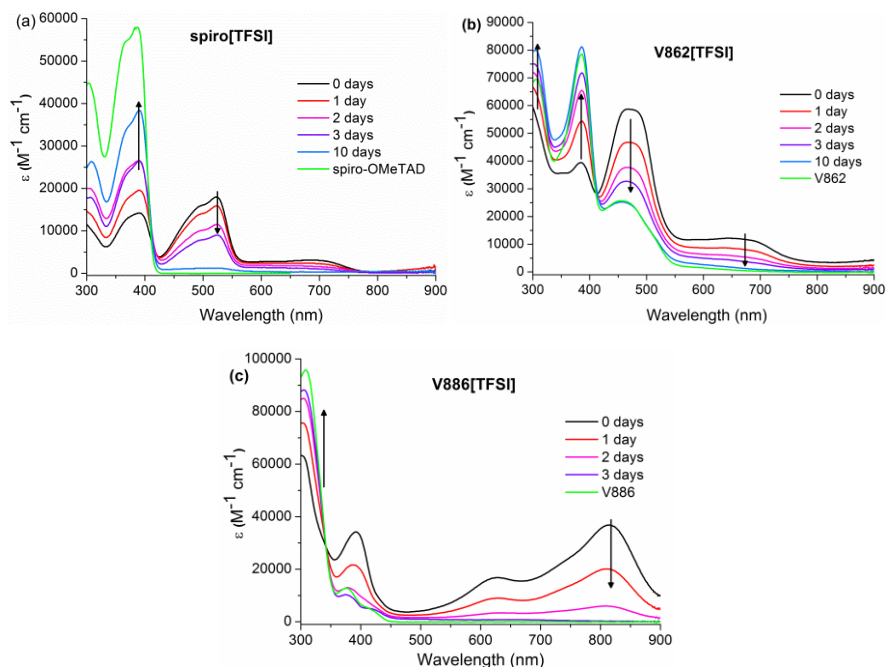
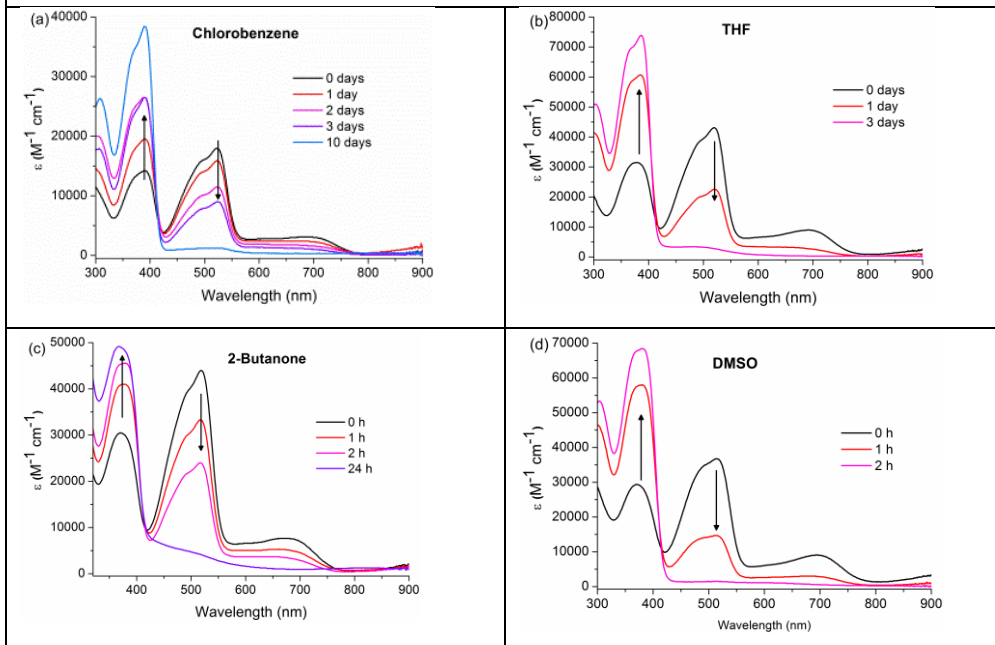


**Figure 3.11.** Stability of the diluted spiro[TFSI], V862[TFSI] and V886[TFSI] solutions ( $10^{-4}$  M) in chlorobenzene upon addition of the tBP at room temperature (RT) under ambient light

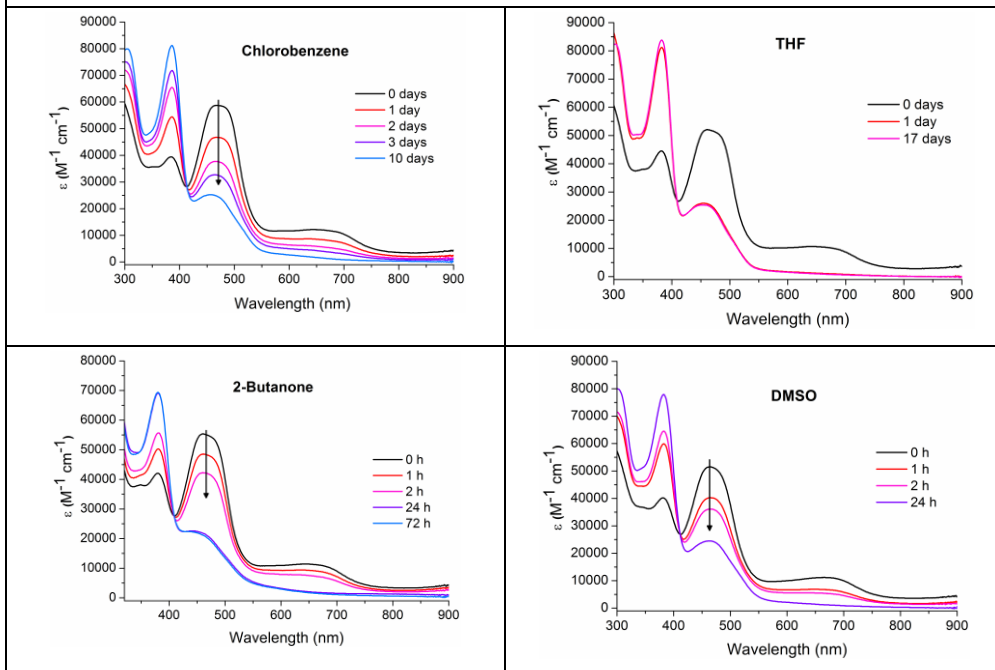
From the UV-vis absorption dynamics, it is evident that the absorption band, attributed to the radical-cation species, diminishes strongly, and the intense colour fades. After several days, the peaks associated with the oxidized HTM disappear completely, and the intensity of the maxima attributed to the pristine HTM increases until the shape and position of the UV-vis absorption spectrum starts to resemble closely that of undoped HTM.

The reaction proceeds more rapidly as the polarity of the solvent increases (Figure 3.12). In chlorobenzene, the whole process can take more than ten days; while in dimethyl sulfoxide (DMSO), it is over in a matter of hours.

### spiro[TFSI]



### V862[TFSI]



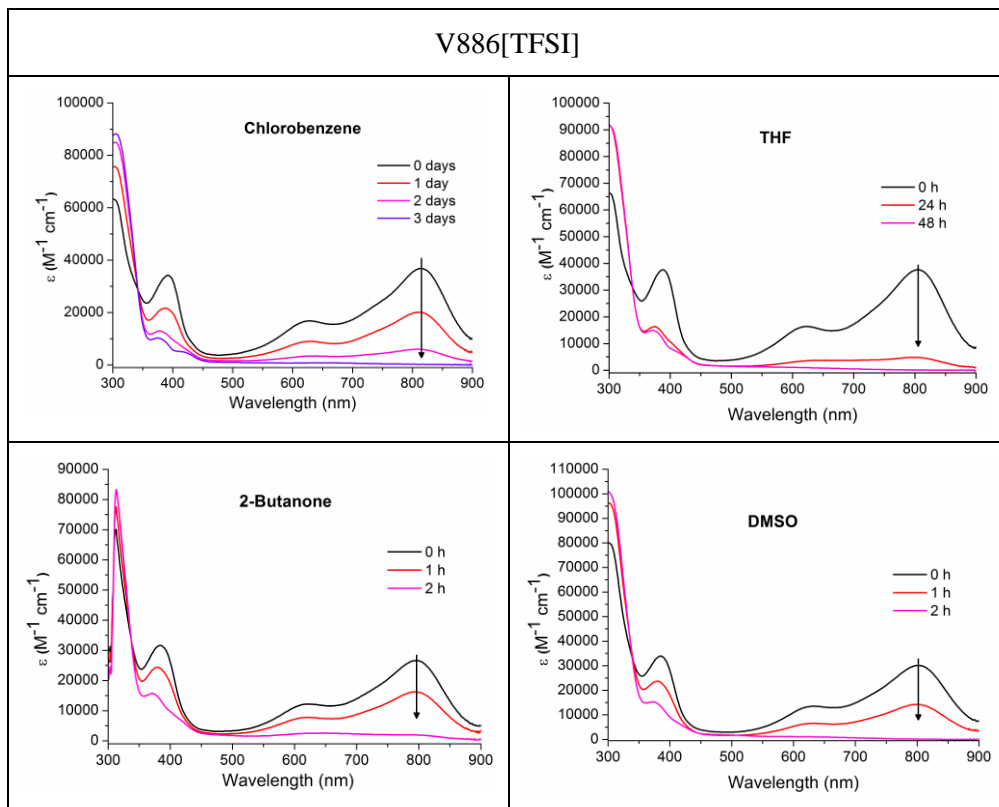
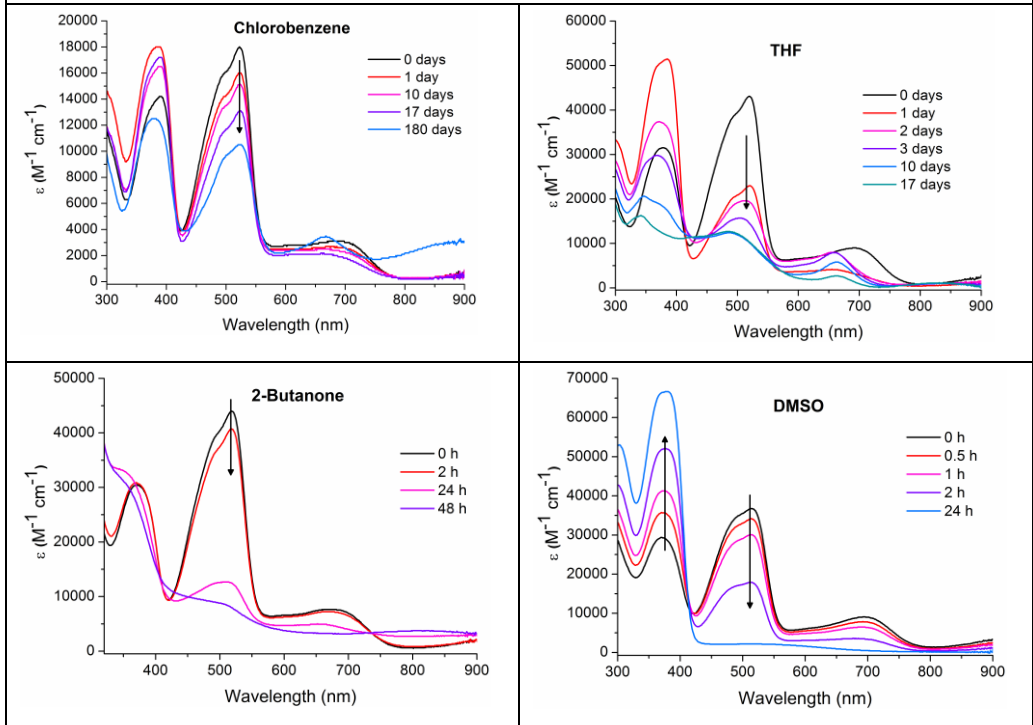


**Figure 3.12.** Stability of the diluted spiro[TFSI], V862[TFSI] and V886[TFSI] solutions ( $10^{-4}$  M) in different solvents upon addition of the tBP at RT under ambient light

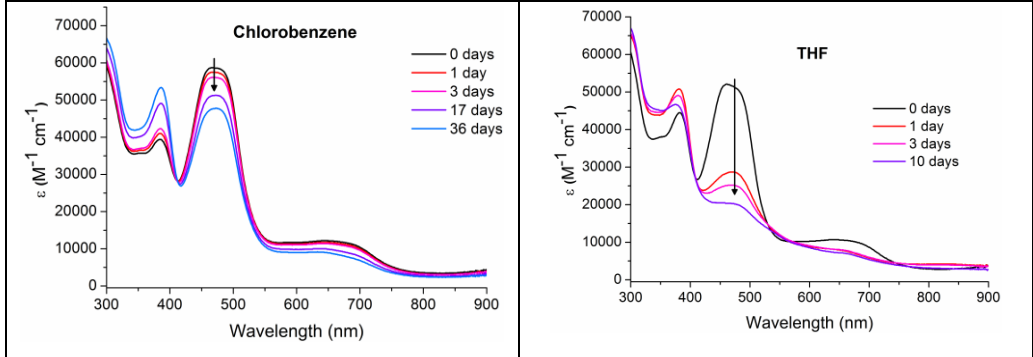
After a more detailed investigation, it has been determined that the irradiation by ambient light is sufficient to promote decomposition of the investigated oxidized HTMs in the solution (Figure 3.13), although without tBP, the process is significantly slower. Even after 180 days, UV-vis spectra of the materials dissolved in less polar chlorobenzene, demonstrated absorption maxima attributed to the oxidized HTMs.

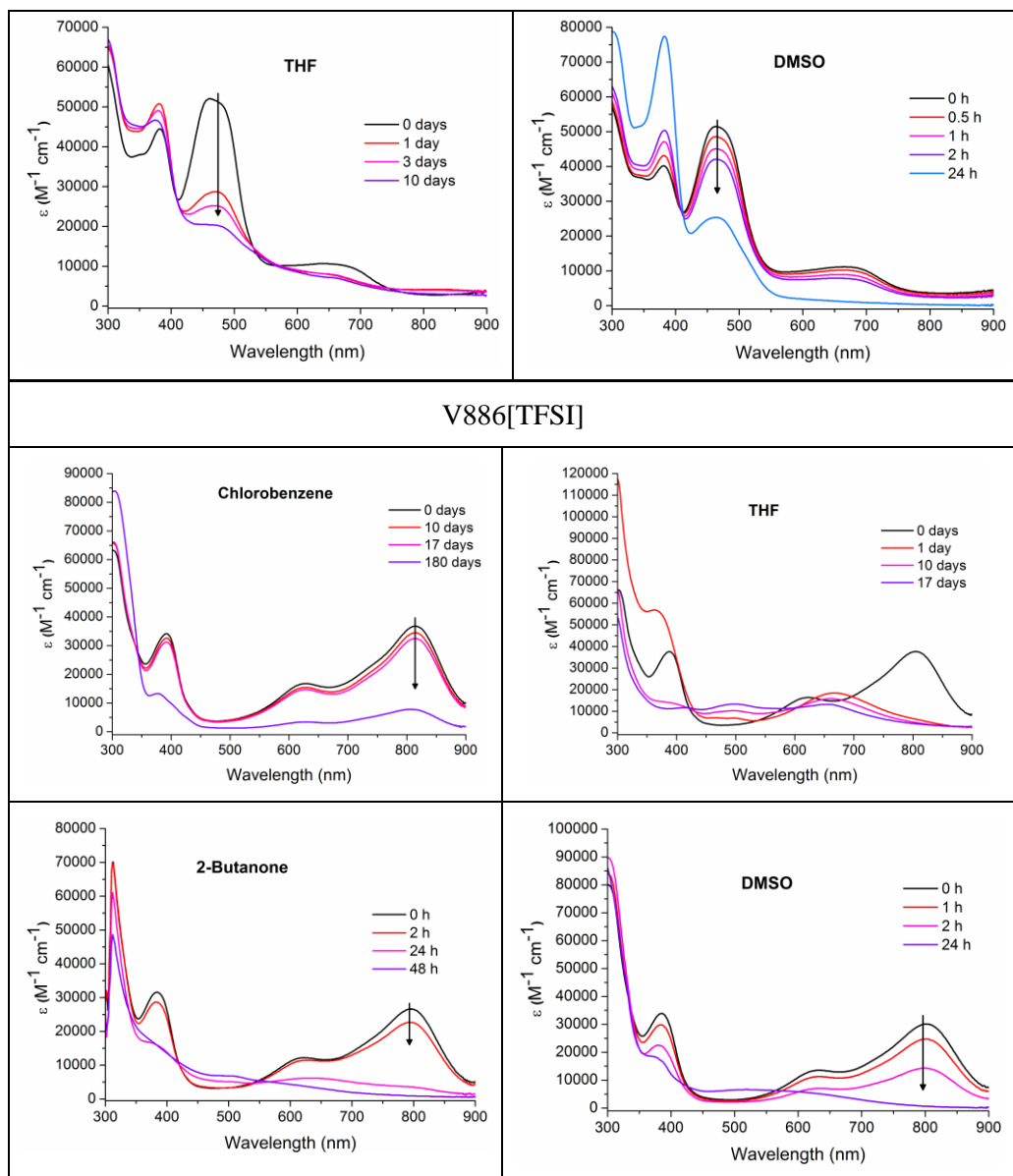


### spiro[TFSI]



### V862[TFSI]

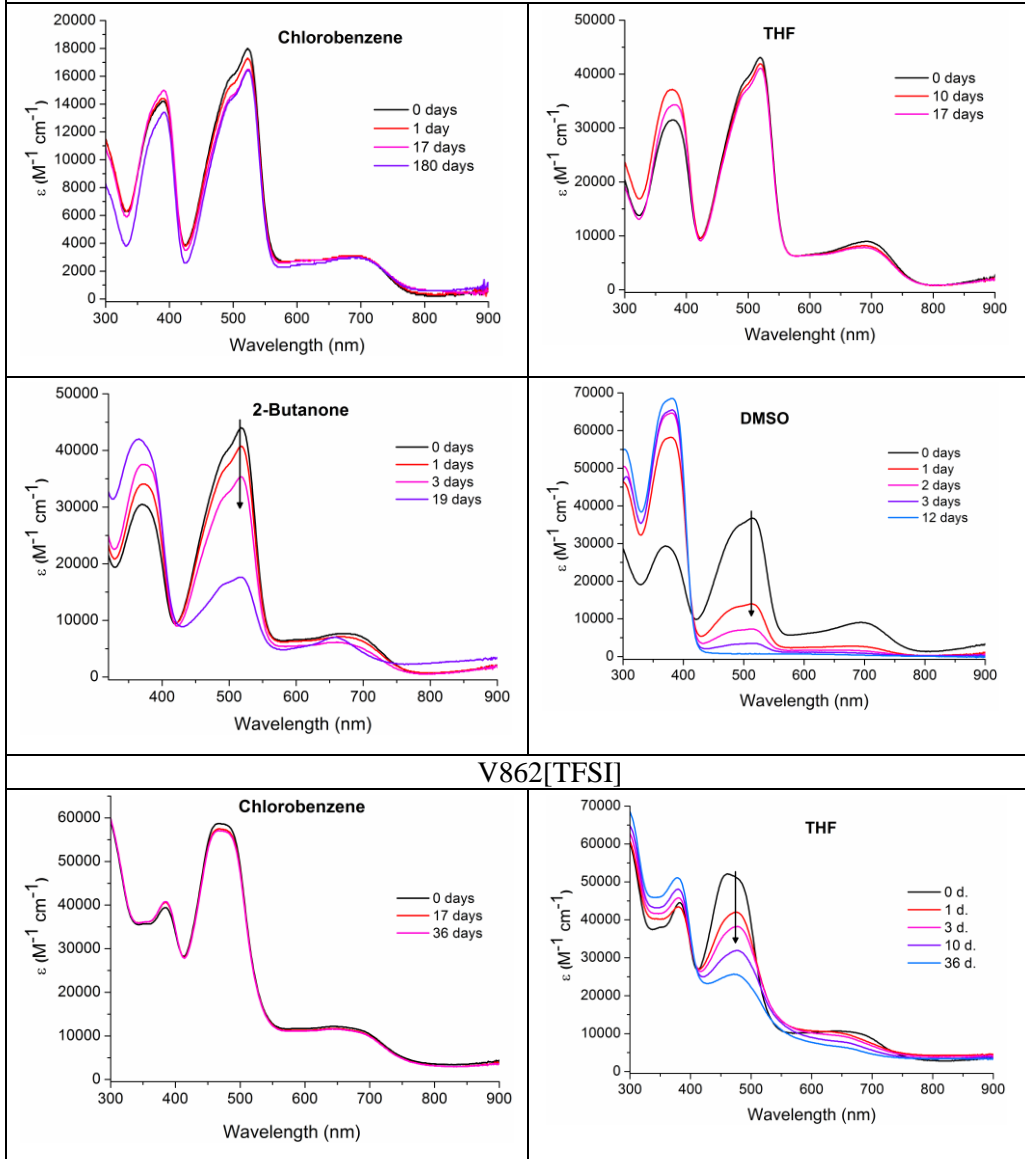




**Figure 3.13.** Stability of the diluted spiro[TFSI], V862[TFSI] and V886[TFSI] solutions ( $10^{-4}$  M) in different solvents at RT under ambient light

In order to determine the role of the light, a series of identical measurements were conducted in the dark using solutions with and without tBP. The samples dissolved in chlorobenzene without tBP demonstrated very good stability, with very little change in absorption after the prolonged periods of time. In more polar solvents, the decomposition was a lot more noticeable but still significantly less rapid compared with the analogues kept under ambient light (Figure 3.14).

### spiro[TFSI]



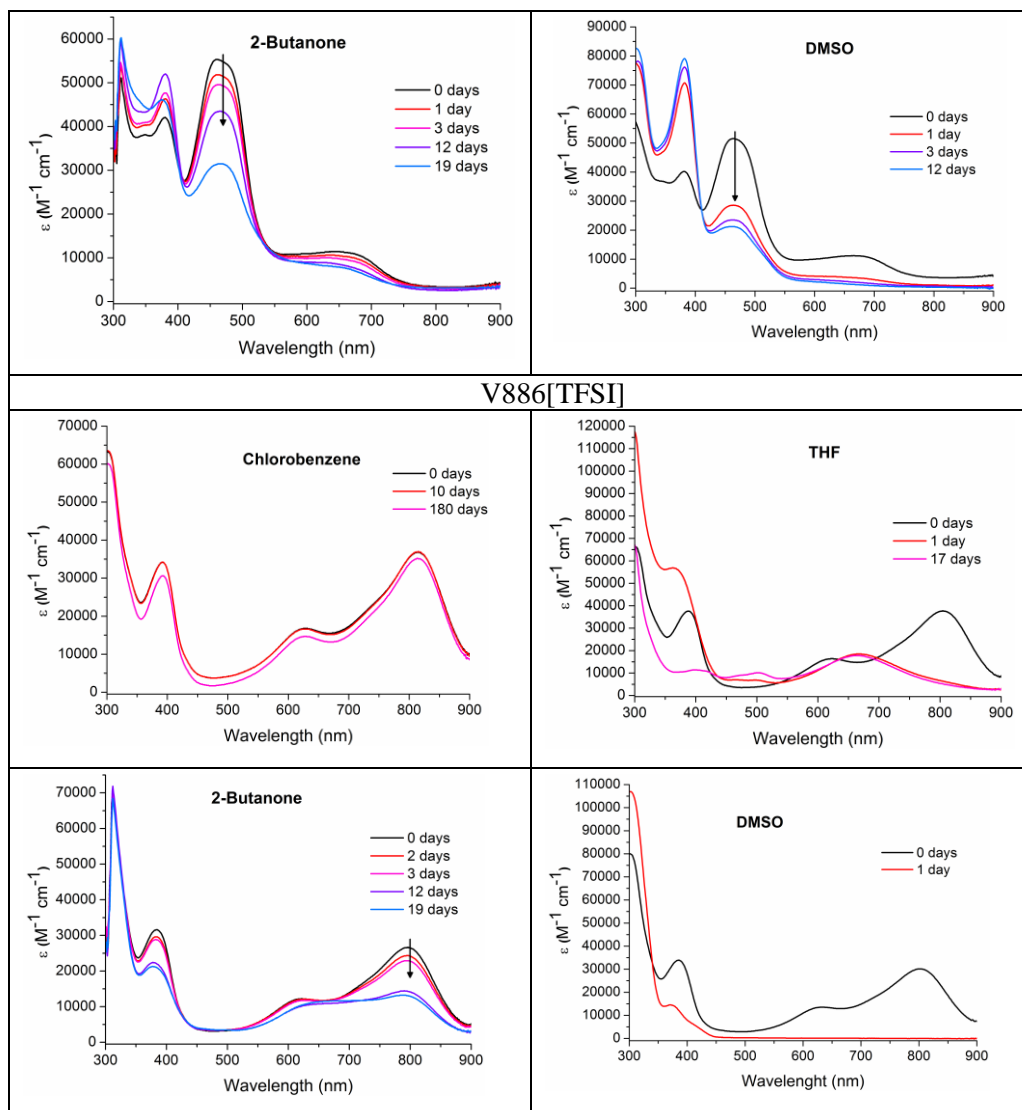
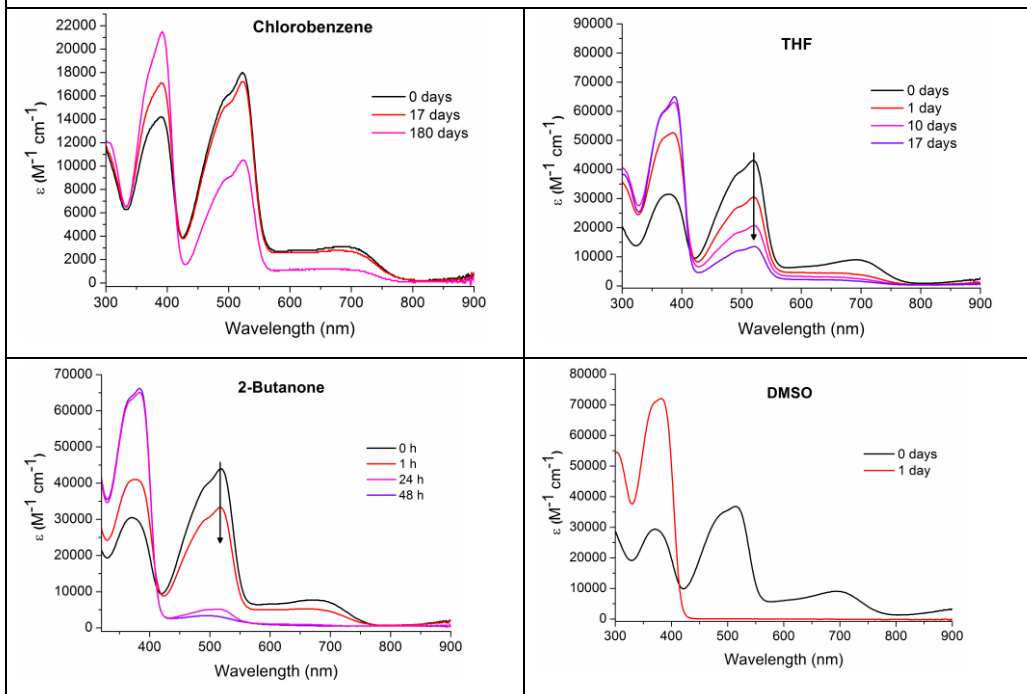


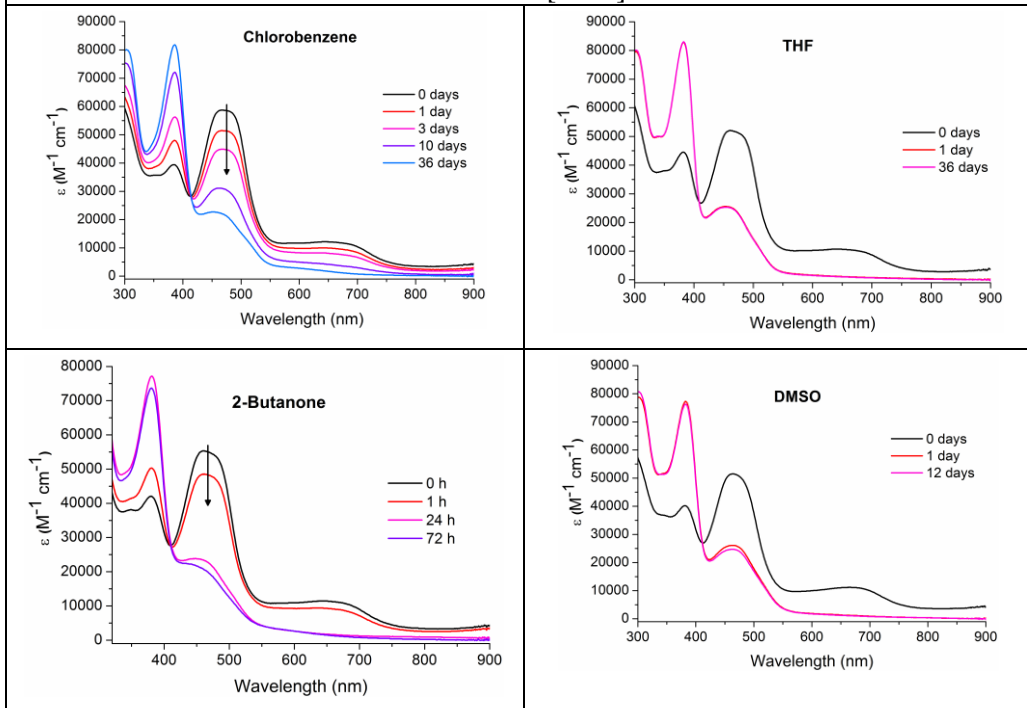
**Figure 3.14.** Stability of the diluted spiro[TFSI], V862[TFSI] and V886[TFSI] solutions ( $10^{-4}$  M) in different solvents at RT in the dark

In the presence of tBP, the decomposition of the investigated materials is accelerated to some extent; however, the effect is strongly dependent on the polarity of the solvent and structure of the investigated molecule (Figure 3.15).

spiro[TFSI]



V862[TFSI]



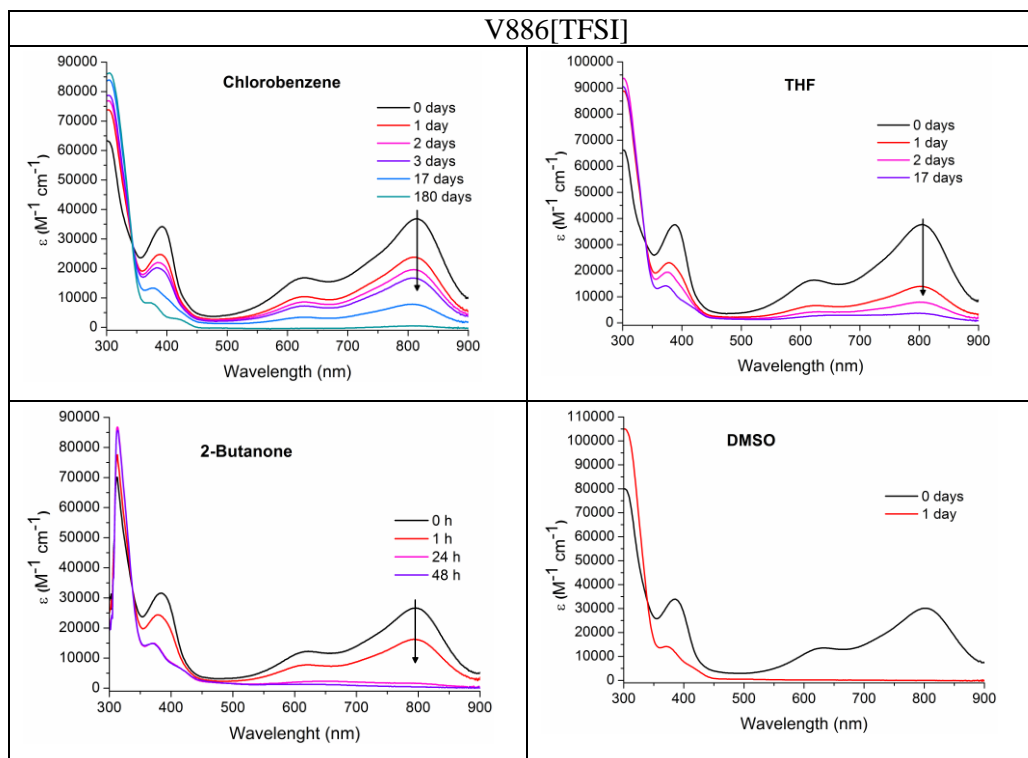
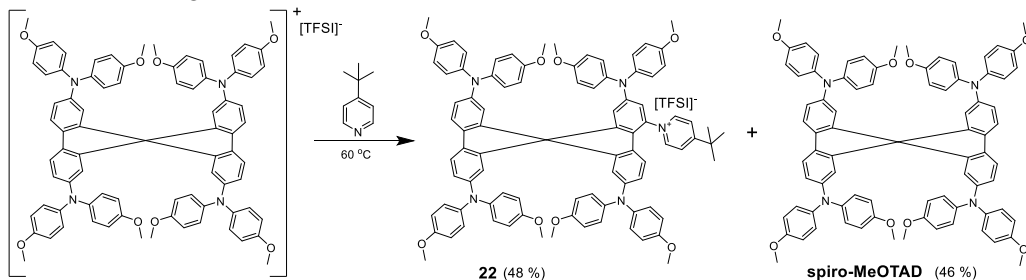


**Figure 3.15.** Stability of the diluted spiro[TFSI], V862[TFSI] and V886[TFSI] solutions ( $10^{-4}$  M) in different solvents upon the addition of the tBP at RT in the dark

Larger scale experiment with spiro[TFSI] and tBP was conducted to investigate the process in more detail and determine the role of tBP, whether it is catalysing the ongoing reaction or does it react with the oxidized HTM. After the reaction, two main products were isolated with an approximate ratio of 1:1. NMR and MS analysis revealed that during the reaction part of the spiro[TFSI] gets reduced back to spiro-MeOTAD, while another part undergoes a pyridination reaction forming derivative **22** (Scheme 3.9).



**Scheme 3.9.** Proposed pathway of the pyridination reaction of the oxidized spiro-MeOTAD

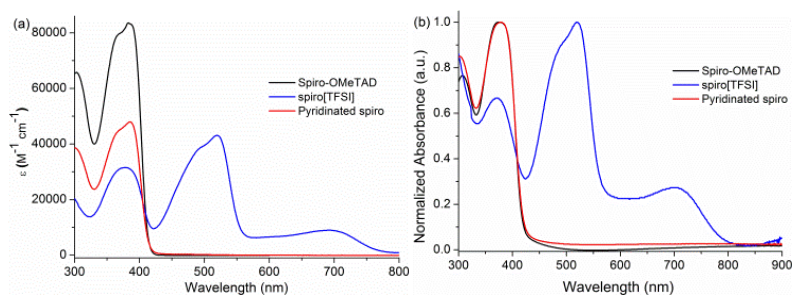


**Figure 3.16.** UV-vis absorption spectra of spiro-MeOTAD, pyridinated spiro-MeOTAD and spiro[TFSI] in the THF solution (a) and film (b)

Both compounds demonstrate very similar UV-vis absorption spectra, albeit in a solution, light absorption intensity is lower for the pyridinated derivative, compared with pristine spiro-MeOTAD (Figure 3.16a), and there is a slight shoulder in the visible range of the spectrum for the pyridinated spiro-MeOTAD in the film (Figure 3.16b). Identical processes taking place in case of V862[TFSI] and V886[TFSI] have been observed.

#### 3.2.1.4. Long-term stability of the oxidized HTMs in the thin films

The processes occurring in the solution will not necessarily take place in the solid state. In the solution, the molecules are much more mobile, and the interaction with solvent or other compounds, for example, tBP, is easier and faster. In order to evaluate the long-term stability of the investigated materials in the solid state under various conditions, a series of experiments with oxidized HTMs has been carried out. HTMs have been deposited as thin films on the glass substrates, encapsulated under inert atmosphere and stored under different conditions for prolonged periods of time.

Long-term thermal stability of the encapsulated films of the synthesized materials was investigated using UV-vis spectroscopy. The thin films of the oxidized HTMs with standard additives: tris(2-(1*H*-pyrazol-1-yl)-4-*tert*-butylpyridine)cobalt(III) tri[bis(trifluoromethane)sulfonimide], 4-*tert*-butylpyridine and bis(trifluoromethane)sulfonimide lithium salt, in different variations have been prepared using spin-coating method. The layers were encapsulated under inert atmosphere and kept at RT or 100 °C for 70 days.

The investigated oxidized HTMs are relatively stable at room temperature over longer periods of time (Appendix 1, Figures S8–S13); even the nonencapsulated material remains largely unchanged. Different additive variations have as well shown very similar results, the only notable exception is a composition containing all three additives (LiTFSI, FK209 and tBP): in this case, a more noticeable degradation takes place (Figure 3.17a). In this case, a decrease of absorption maxima attributed to the oxidized HTM and an increase of peaks related to the unoxidized HTM are observed (Appendix 1, Figure S13).

When samples were kept at 100 °C, however, the degradation process was much more pronounced and rapid. In the UV-vis spectra of the nonencapsulated films of the investigated materials, kept in the air at 100 °C, the peaks associated

with the oxidized HTMs have practically disappeared in less than three weeks (Figure 3.17b). Decomposition dynamics are similar to the ones observed in the previously mentioned example, i.e., a drop in the intensity of the peaks associated with the oxidized species and an increase of maxima attributed to the unoxidized HTM (Appendix 1, Figure S14).

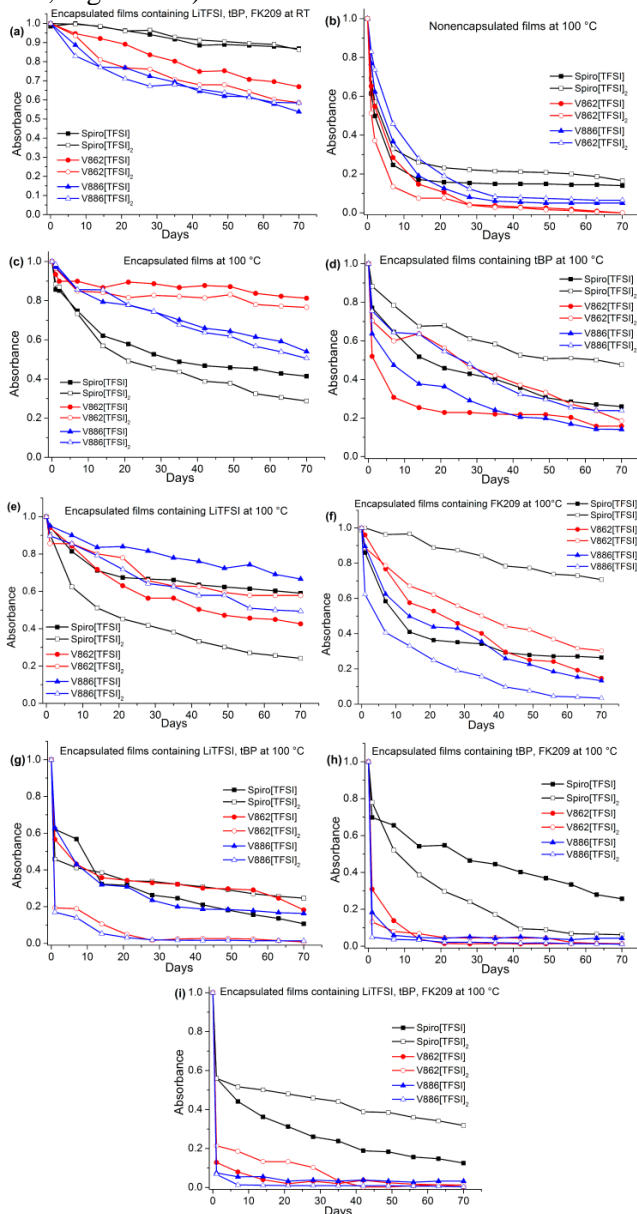


**Figure 3.17.** Light absorption intensity dynamics of the films containing oxidized HTMs; measured at 517 nm for spiro(TFSI) and spiro(TFSI)<sub>2</sub>, 465 nm for V862(TFSI) and V862(TFSI)<sub>2</sub>, 818 nm for V886(TFSI) and V886(TFSI)<sub>2</sub>



Encapsulation slows down the decomposition process to some extent; however, all of the investigated materials degrade at elevated temperature, albeit at different rates (Figure 3.17c, Appendix 1, Figure S15). In most of the cases, the addition of the tBP, with or without other additives, speeds up the reaction quite noticeably (Figure 3.17d, g–i, Appendix 1, Figures S16, S19–21). The decomposition dynamics of the encapsulated films at elevated temperature followed the same pattern observed in the nonencapsulated samples and in the solution, i.e., a drop in intensity of peaks associated with the oxidized species and an increase of maxima attributed to the unoxidized HTM (Appendix 1, Figures S15–21).

Although LiTFSI and FK209 do not play the major role after the initial oxidation of the HTM is done in the solution, prior to the film preparation; nonetheless, the investigation was conducted with these additives to establish if can they restore reduced HTM, formed during the experiment, back to the oxidized form in the film. The presence of the LiTFSI or FK209 in the mixture did not alter the degradation dynamics significantly (Figure 3.17e, f, Appendix 1, Figures S17, S18). Neither LiTFSI nor FK209 seem to be able to regenerate the oxidized species from the pristine HTM formed during the reduction of the investigated materials. The absence of oxygen in the encapsulated samples can explain why LiTFSI did not demonstrate any effect, as it is known that oxygen is required in order for this type of hole transporting material doping to occur [120, 128]. It is somewhat more difficult to explain why FK209 did not work. Possibly, the molecule of the cobalt complex is bigger than tBP and therefore, less mobile in the film of the material, which is just above glass transition temperature. Consequently, the reduction of the oxidized species and pyridination, in case if tBP is present, proceeds faster than the oxidation of the formed reduced products. In case of samples doped only with FK209 (Figure 3.17f), spiro[TFSI]<sub>2</sub> deviates from the general trend; however, it is mostly due to the fact that the material starts to crystallize in the layer. Similarly as pristine spiro-MeOTAD, the oxidized analogues are as well prone to the crystallization, and in a number of samples, the crystallization of material has been observed (Figure 3.18). The crystallization induced changes can as well be observed in the UV-vis spectra; the absorption maxima of the oxidized spiro-MeOTAD starts to be more and more red shifted as the time progresses and crystalline domains grow in size (Figure 3.18d). The red shift of the absorption maxima could be attributed to the formation of more ordered structure inside the crystals. At the same time, the overall intensity of the peak decreases as the degradation process continues. Interestingly, the crystallized parts of the layer showed better resistance to the degradation; these differences can be explained by analysing thermal properties of the materials (Table 3.3). The glass transition temperature of the oxidized spiro-MeOTAD is below 100 °C, and during the thermal test, the materials are essentially in a liquid state, while melting of the crystals occurs well above 200 °C and therefore, crystallized parts of the film are in solid state. The movement of the molecules is severely restricted in the solid state, and the rate of degradation of these crystalline parts of the layer is reduced as well. The materials with higher glass transition temperature or the ones that crystallize during film deposition could potentially improve the stability of the HTM layer at elevated temperatures.

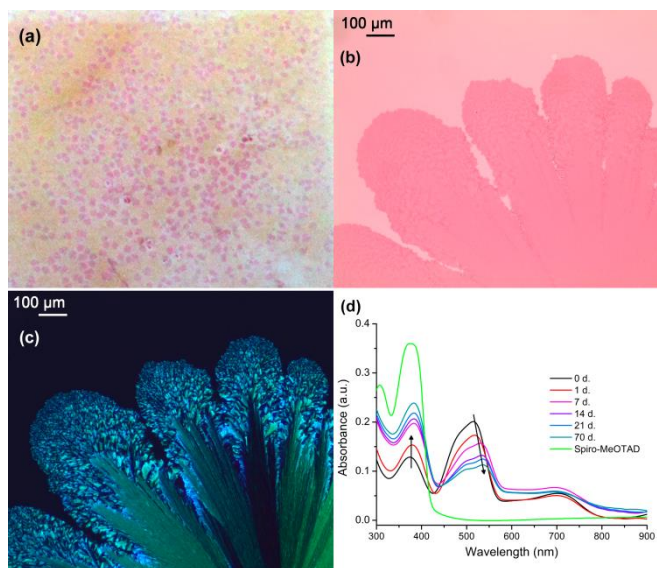


**Figure 18.** Crystallization of the oxidized spiro-MeOTAD films at 100 °C; photograph of the crystallized layer (a), optical micrograph of the film (b), optical micrograph with dark field crossed polarizers (c), UV-vis spectrum of the encapsulated film containing spiro[TFSI] (d)

Overall, the effect of additives on the decomposition dynamics of the oxidized spiro-MeOTAD seems to be less pronounced compared with V862 and V886. It could be due to the structural differences of the investigated molecules, or the above mentioned crystallization effect could be a contributing factor.

Mass spectroscopy analysis of the spiro[TFSI]<sub>2</sub> films, containing LiTFSI, FK209 and tBP kept at 100 °C for 70 days, was performed to confirm the observations made during the analysis of the UV-vis spectra, namely, that films containing oxidized HTMs with additives undergo pyridination and reduction back to the unoxidized hole transporting material during the thermal stability testing.

Identifying the oxidized species is difficult; for example, spiro[TFSI]<sub>2</sub> will only show the parent cation mass in MS [128, 131] and start to revert back to the spiro-MeOTAD in the high-performance liquid chromatography (HPLC) column. However, the reduction of the oxidized spiro back to spiro-MeOTAD is sufficiently slow to register two elution peaks at different retention times in the HPLC chromatogram, one for the spiro-MeOTAD (retention time 7.6 min) and the other for spiro[TFSI]<sub>2</sub> (retention time 6.9 min) (Appendix 1, Figures S25, S26); both of them yield spiro-MeOTAD cation [M+H]<sup>+</sup> of 1225 mass. MS analysis of the spiro[TFSI]<sub>2</sub> films, containing LiTFSI, FK209 and tBP kept at elevated temperatures for 70 days, indicated the presence of the spiro-MeOTAD (retention time 7.6 min), pyridinated spiro (retention time 7.5 min) and spiro[TFSI]<sub>2</sub> (retention time 6.9 min) (Appendix 1, Figures S22–S28). Similarly as in the previous sample, spiro-MeOTAD and spiro[TFSI]<sub>2</sub> yield spiro-MeOTAD cation [M+H]<sup>+</sup> ( $m/z=1225$ ), while pyridinated spiro molecular ion [M+H]<sup>+</sup> can be observed at  $m/z=1359$ .

Since the formation of the oxidized HTMs during the doping process is responsible for the increase in conductivity of the hole transporting materials [120, 128], the observed instability of the oxidized HTMs in the thin films at elevated temperatures could be one of the main causes of drop in the conductivity observed for the doped spiro-MeOTAD [118]. It could potentially be one of the reasons as well why perovskite solar cells lose their efficiency under prolonged thermal stress. A possible solution to this problem could be the substitution of the HTMs that require doping with analogues that do not need it and therefore, do not rely on the oxidized materials to improve conductivity [133, 134]. The development of the efficient technique to regenerate oxidized species in situ in the functioning device could be another more complicated alternative. Perhaps, the pyridination problem could be solved by using a different type of pyridine additive, which would be less prone to the reaction with oxidized HTM: 2-pentylpyridine could be a good candidate. It has been shown that devices constructed using this additive demonstrate better stability [135], and long aliphatic chain at 2-position of the pyridine ring could potentially hamper or at least slow down the pyridination reaction.

### **3.2.1.5. Chapter summary**

In summary, it has been found that the investigated oxidized HTMs can react with 4-*tert*-butylpyridine forming pyridinated derivatives. This process takes place in the solution and in the films kept at elevated temperatures. During the thermal stability testing of the films kept at 100 °C, it has been noticed that the oxidized HTMs start to degrade and partly revert back to the original unoxidized material and partly react with tBP, if it is present in the film. The addition of the LiTFSI and FK209, the additives responsible for the oxidation of the HTMs, do not affect the rate or nature of degradation too significantly (under investigated conditions). Interestingly, a significant number of samples containing films of oxidized spiro-MeOTAD, similarly as pristine spiro-MeOTAD, started to crystallize at elevated temperatures. It is known that the oxidized HTM, formed during doping, is responsible for the increased conductivity and ultimately for better efficiency of the hole extraction process in the PSC device; therefore, the observed instability of the oxidized HTMs in the thin films at elevated temperatures could be one of the causes of the drop in conductivity reported for the doped spiro-MeOTAD. It could potentially be one of the reasons why perovskite solar cells lose their efficiency under prolonged thermal stress. A possible solution to this problem could be the use of HTMs that do not require doping and therefore, do not rely on the oxidized materials to improve conductivity.

### **3.2.2. Interaction with perovskite material**

The diffusion of the mobile ions from perovskite into the charge transporting layers (CTL) is another potential problem magnified at elevated temperatures [136]; it has been shown that the migration of these ions can negatively impact long-term stability of the PSC devices [137, 138, 139, 140, 141]. Halides, such as iodine and bromine, have been reported to be the main culprits in elemental diffusion. The

migration of these mobile ions beyond perovskite/CTL interfaces may result in an undesirable reaction between mobile ions and the CTL materials or metal electrode [140, 142, 143].

Recently, it has been observed that oxidized spiro-MeOTAD reacts readily with I<sup>-</sup> ions, migrating from MAPbI<sub>3</sub> under device operation, resulting in the reduction of the oxidized spiro-MeOTAD and a decrease in conductivity of the transport layer [138]. This diffusion and spiro-MeOTAD dedoping processes were observed to be thermally accelerated in MAPbI<sub>3</sub> and FAPbI<sub>3</sub> at elevated temperatures [118, 138, 142].

It is evident that thermally accelerated ion diffusion processes observed in MAPbI<sub>3</sub> and FAPbI<sub>3</sub> perovskites can cause significant drop in device performance over long-term due to the reduction of the oxidized spiro-MeOTAD. However, during the last few years, a number of improved and more resistant to degradation perovskite compositions, especially the ones incorporating Cs, have been developed. Ion migration into hole transporting spiro-MeOTAD layer under thermal stress has not been investigated in these new perovskites. Therefore, it is important to see if the same problems persist in these cases as well. In the current chapter, the thermal stability of the oxidized spiro-MeOTAD in contact with various most popular perovskite compositions is investigated. Due to the complex nature of the PSC devices and the multitude of possible processes taking place simultaneously, it has been decided to focus on one particular issue involving interaction between perovskite and oxidized spiro-MeOTAD in thin films rather than trying to evaluate the entire system at once. In the previous chapter, it has been established that the stability of different oxidized HTMs and their behaviour was very similar; therefore, for this investigation, it was decided to focus on the most popular and intensively used one, i.e., spiro-MeOTAD.

### **3.2.2.1. Interaction of the oxidized HTM with perovskite forming components**

Initially, it has been decided to investigate in more detail the interaction of the spiro[TFSI]<sub>2</sub> with the perovskite components, namely with methylammonium iodide (MAI), formamidinium iodide (FAI) and methylammonium bromide (MABr). The initial experiments in the solution revealed that the addition of the FAI to the dissolved spiro[TFSI]<sub>2</sub> induced immediate change in colour (Figure 3.19a) as well as disappearance of the absorption maxima associated with the oxidized HTM at around 510 nm and intensification of the maxima associated with neutral spiro-MeOTAD at 380 nm (Figure 3.19b). A similar picture has been observed for MAI (Figure 3.19c, d).

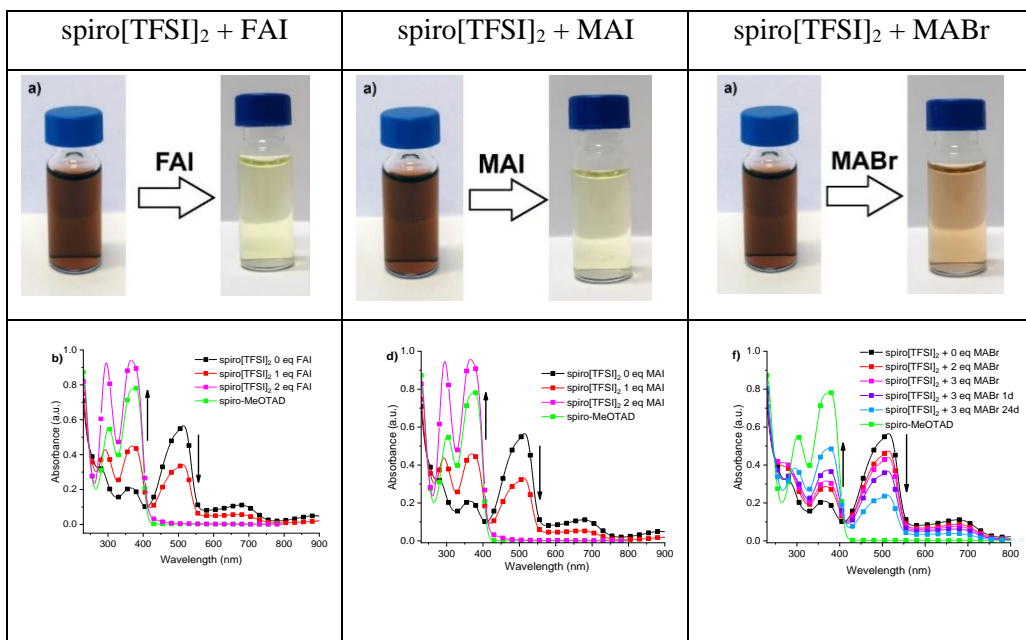


**Figure 3.19.** Spiro[TFSI]<sub>2</sub> stability in acetonitrile solution ( $10^{-4}$  M) at RT after adding FAI, MAI or MABr; photograph (a, c, e) and UV-vis spectrum of the solution (b, d, f)

The processes occurring in the solution will not necessarily take place on the surface of the solid film, as molecules are much more mobile, and the interaction is easier and faster in the solution. Therefore, the interaction between spiro[TFSI]<sub>2</sub> film and solutions of FAI or MAI has been investigated as well. In order to eliminate the possibility of dissolving the film by the solvent, it was specifically selected to dissolve the organic salts but not the spiro[TFSI]<sub>2</sub> (Figure 3.20). In both cases, spin-coating solution of the perovskite precursor on the top of spiro[TFSI]<sub>2</sub> film resulted in discoloration of sample and disappearance of the characteristic absorbance maximum (Figure 3.20).

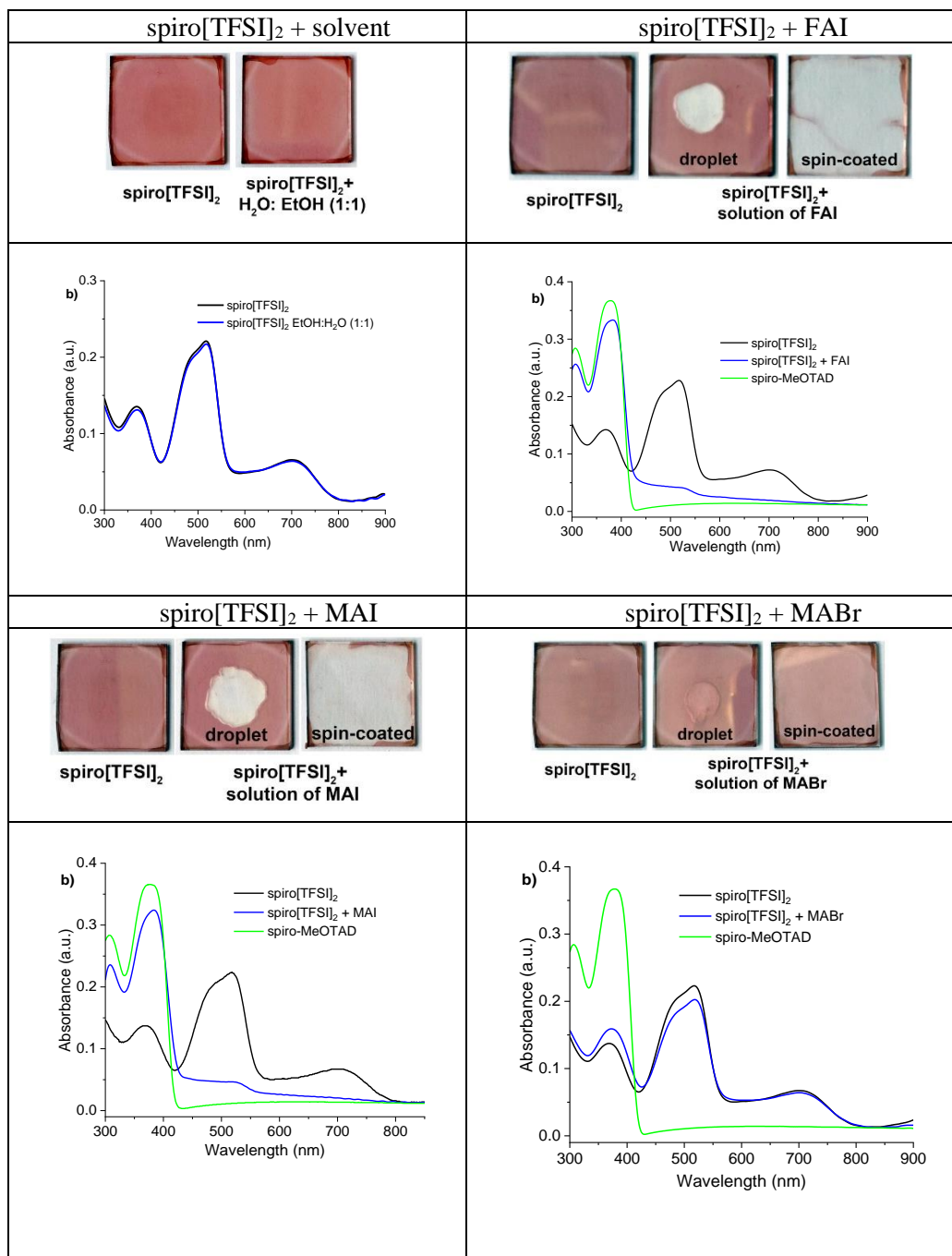


**Figure 3.20.** Photograph and UV-vis spectrum of the spiro[TFSI]<sub>2</sub> film before and after the interaction with solvent, FAI, MAI or MABr solutions

Interestingly, the substitution of iodine with bromine in MABr resulted in a significantly reduced reaction rate (Figures 3.19 e, f, 3.20), the process that took

minutes in case of iodide containing organic salts would not be completed for days when MABr was used. Although, a significant decrease in light absorption intensity at 510 nm can be observed after keeping the sample at 100 °C for 24 hours (under inert conditions), indicating that the reaction does proceed albeit at much slower rate and is accelerated by an increase in temperature.

In order to investigate the process in more detail and establish the final products, the reactions with larger quantities of spiro[TFSI]<sub>2</sub>, MAI and FAI were performed. After the reaction, one main product was isolated in very high yields. The reduction of spiro[TFSI]<sub>2</sub> back to spiro-MeOTAD was confirmed by NMR and MS analysis (Appendix 1, Figures S29–S31). Simple iodine test (Figure 2.21) as well as iodometric titration (for more details, see Experimental section) indicated the formation of iodine during the process (Scheme 2.10).

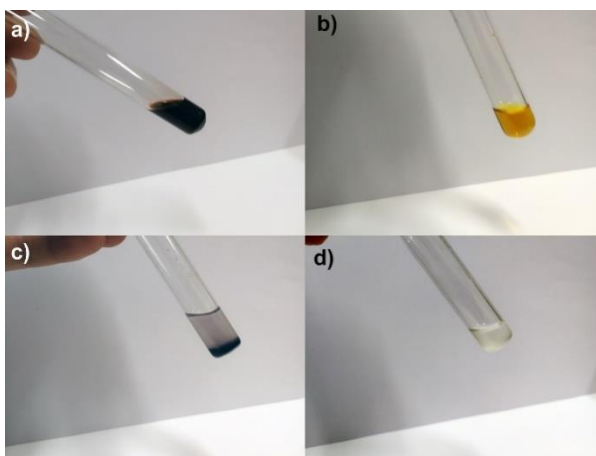
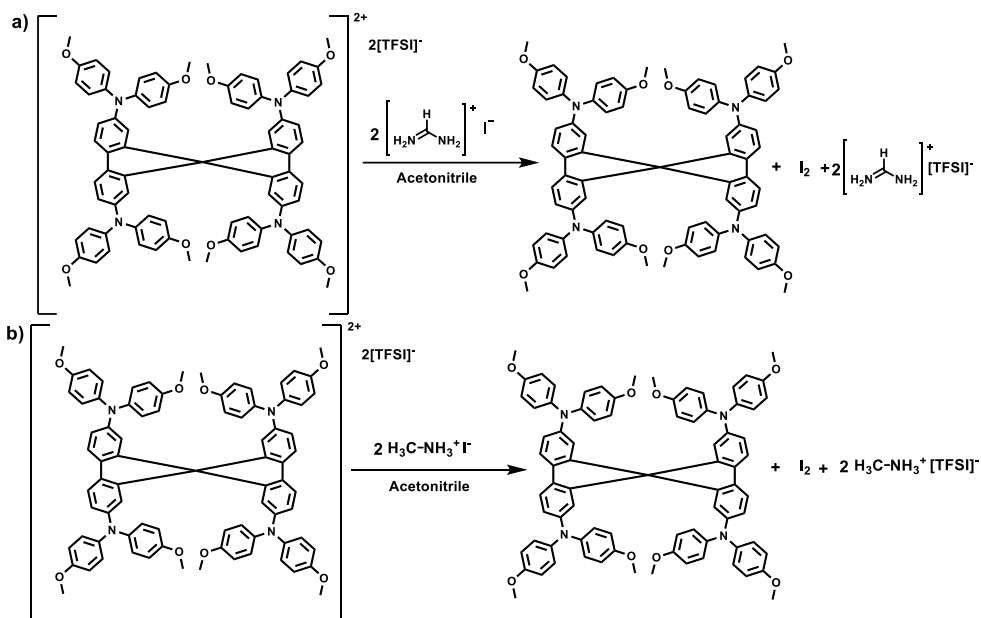


**Figure 3.21.** Detection of the iodine formed during reaction between spiro[TFSI]<sub>2</sub> and FAI, using iodine test; a) spiro[TFSI]<sub>2</sub> solution in acetonitrile, b) spiro[TFSI]<sub>2</sub> solution in acetonitrile after addition of FAI, c) spiro[TFSI]<sub>2</sub> solution in acetonitrile after addition of FAI and starch suspension in water, d) mixture of FAI and starch suspension in water

The MS analysis of the products obtained during the reaction between spiro[TFSI]<sub>2</sub> and MAI, FAI or MABr in the solution has been conducted. The interaction with MAI or FAI resulted only in the reduction product spiro-MeOTAD (Appendix 1, Figures S34, S35), while during slower reaction with MABr, both spiro[TFSI]<sub>2</sub> and spiro-MeOTAD were detected (Appendix 1, Figures S32, S33).

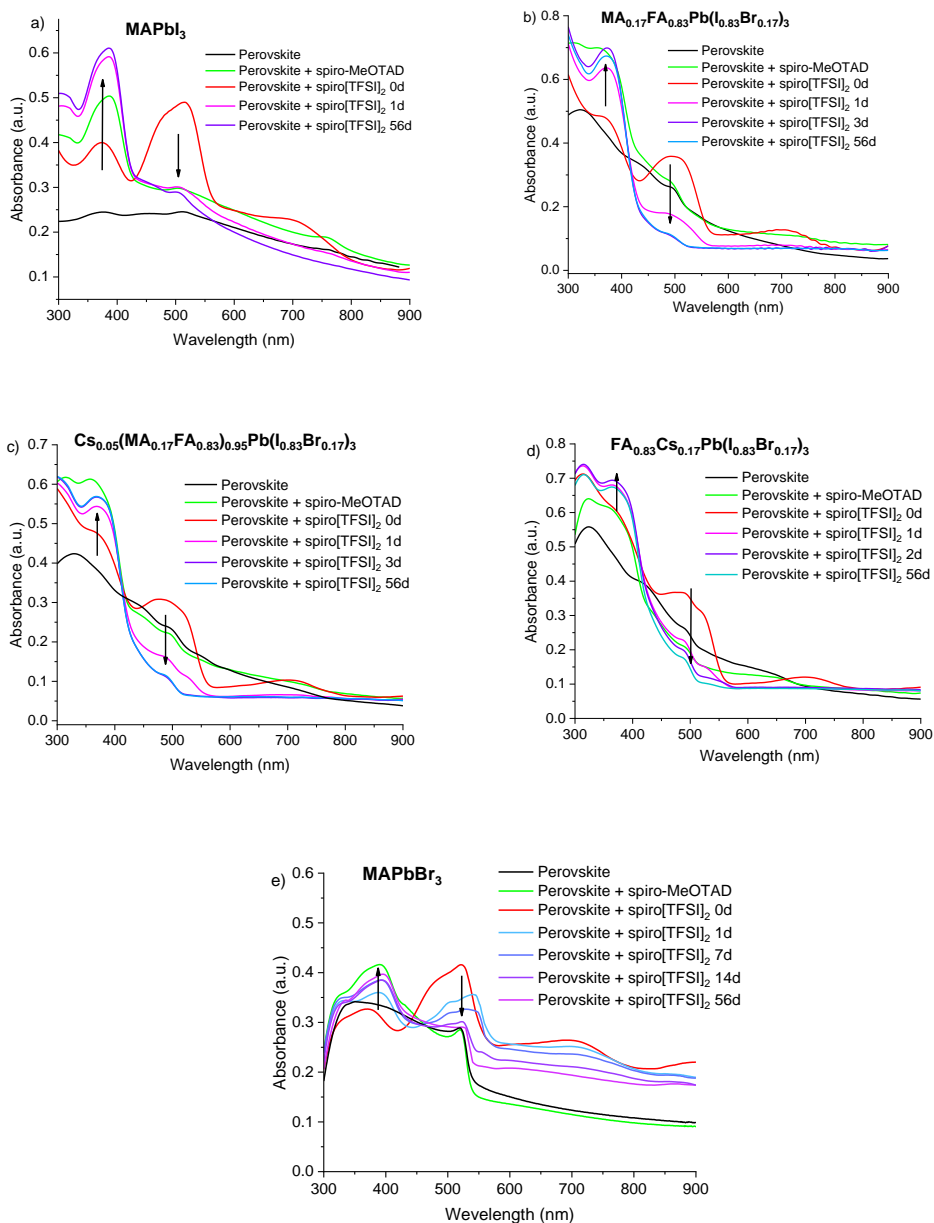


**Scheme 3.10.** Proposed reaction pathway of the oxidized spiro-MeOTAD with FAI (a) and MAI (b)

### 3.2.2.2. Interaction of the oxidized HTM with films of various perovskites

It is interesting that oxidized HTM reacts so easily with perovskite precursors; however, the more important question is whether the same process occurs in the solid-state between the perovskite and spiro[TFSI]<sub>2</sub> films. For this reason, there have been conducted experiments in the solid-state using oxidized spiro-MeOTAD and five different popular perovskite compositions ( $\text{CS}_5(\text{MA}_{0.17}\text{FA}_{0.83})_{95}\text{Pb}(\text{I}_{0.83}\text{Br}_{0.17})_3$ ,  $\text{MA}_{0.17}\text{FA}_{0.83}\text{Pb}(\text{I}_{0.83}\text{Br}_{0.17})_3$ ,  $\text{FA}_{0.83}\text{CS}_{0.17}\text{Pb}(\text{I}_{0.83}\text{Br}_{0.17})_3$ ,  $\text{MAPbI}_3$ ,  $\text{MAPbBr}_3$ ). Due to the complex nature of the PSC devices and the multitude of possible processes taking place simultaneously, rather than trying to evaluate the entire solar cell at once, it has been decided to focus specifically on the stability of oxidized spiro-MeOTAD in contact with the perovskite film. The investigated spiro[TFSI]<sub>2</sub> has been deposited as a thin film on the top of the perovskite. The glass substrate with two deposited layers was encapsulated under inert atmosphere using second class substrate and stored under different conditions for 56 days (for more details, see Experimental section). UV-vis spectra of the investigated samples were recorded periodically during the course of the experiments (Appendix 1, Figures S44–S58), and the results were compared with two different reference samples, i.e., plain perovskite film and spiro-MeOTAD film on top of perovskite. The absorption of the neutral and oxidized spiro-MeOTAD compounds was measured at the appropriate absorption maxima of 380 nm and 510 nm, accordingly. Perovskite absorption was tracked at 590 nm that it would not overlap with the absorption maxima of spiro-MeOTAD and spiro[TFSI]<sub>2</sub>, the only exception being  $\text{MAPbBr}_3$  which has tracked at 510 nm due to the narrower absorption interval.

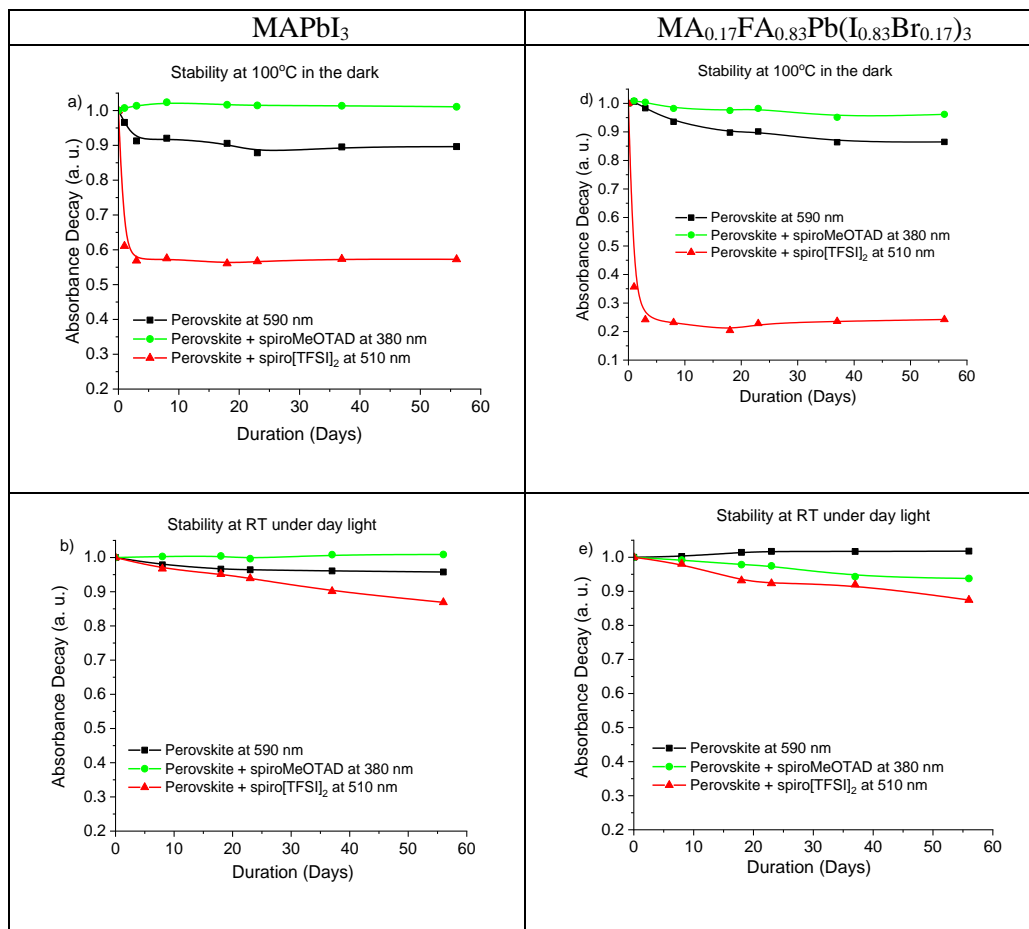


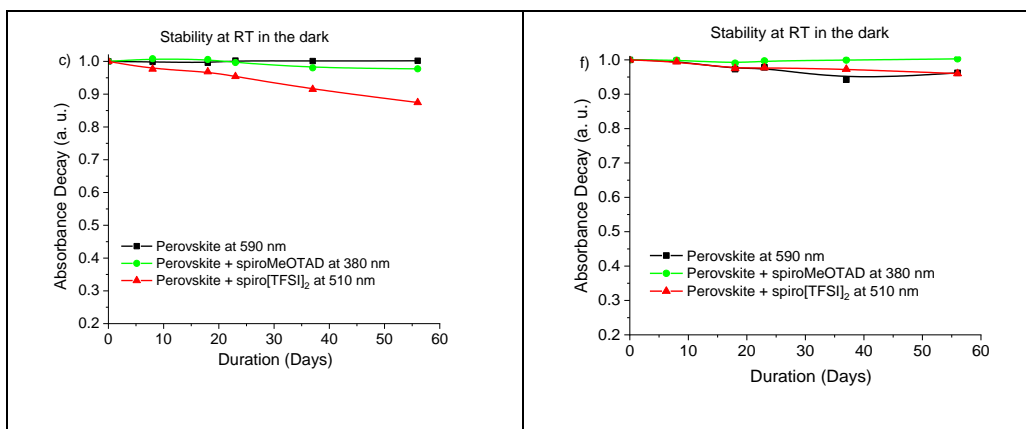


**Figure 3.22.** Stability of the encapsulated spiro[TFSl]<sub>2</sub> films on various perovskites at 100 °C in the dark

The experiments with spiro[TFSl]<sub>2</sub> on MAPbI<sub>3</sub> at 100 °C in the dark have shown that there is a rapid drop in absorption intensity at 510 nm and an increase at 380 nm (Figure 3.22a, Figure 3.23a) indicating the reduction of the oxidized species and the formation of the neutral spiro-MeOTAD. The whole process took less than 1 day, and afterwards, only minor changes in UV-vis spectrum have been observed.

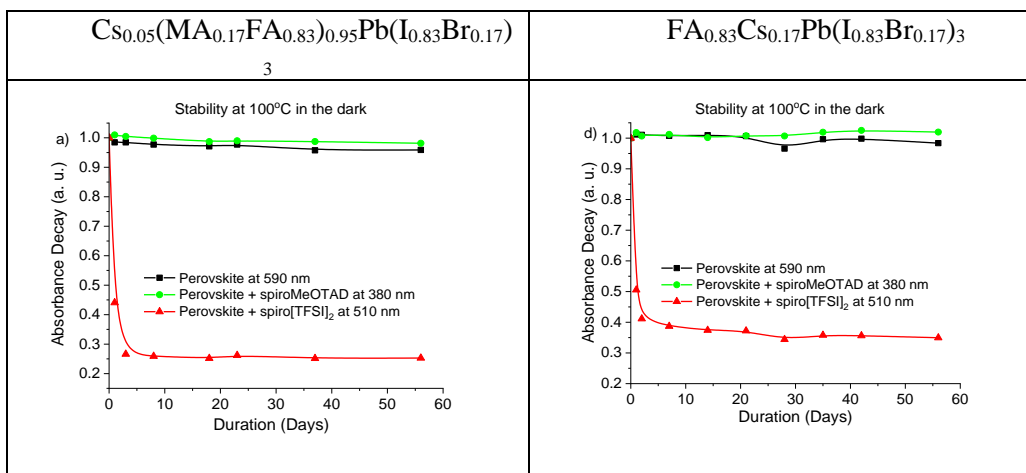
Similar processes, not as intense or rapid, can be observed in samples kept at RT under illumination (Figure 3.23b) and even in the dark (Figure 3.23c). The migration of iodide ions in the solid state at elevated temperature is sufficiently intense to reduce the majority of the spiro[TFSI]<sub>2</sub> to neutral molecule in a matter of hours, and even at RT, the process is noticeable over the extended periods of time. Similarly to the reports in the literature [25, 144], a drop in perovskite absorption intensity at elevated temperatures is observed as well (Figure 3.23a, Appendix 1, Figure S44c), indicating thermal stability related issues with MAPbI<sub>3</sub>.





**Figure 3.23.** Light absorption intensity dynamics of the spiro[TFESI]<sub>2</sub> or spiro-MeOTAD films on MAPbI<sub>3</sub> and MA<sub>0.17</sub>FA<sub>0.83</sub>Pb(I<sub>0.83</sub>Br<sub>0.17</sub>)<sub>3</sub> perovskites

Similar picture can be observed using FA and Cs containing perovskite FA<sub>0.83</sub>Cs<sub>0.17</sub>Pb(I<sub>0.83</sub>Br<sub>0.17</sub>)<sub>3</sub> (Figures 3.22b, 3.23d): the absorption intensity of spiro[TFESI]<sub>2</sub> decreases rapidly under thermal stress and less under direct sunlight at RT. Similarly as with MAPbI<sub>3</sub>, FA containing perovskite as well demonstrates some loss in absorption intensity at elevated temperatures, again indicating sensitivity of material to the elevated temperatures over the extended periods of time (Figure 3.23d, Appendix 1, Figure S47c).



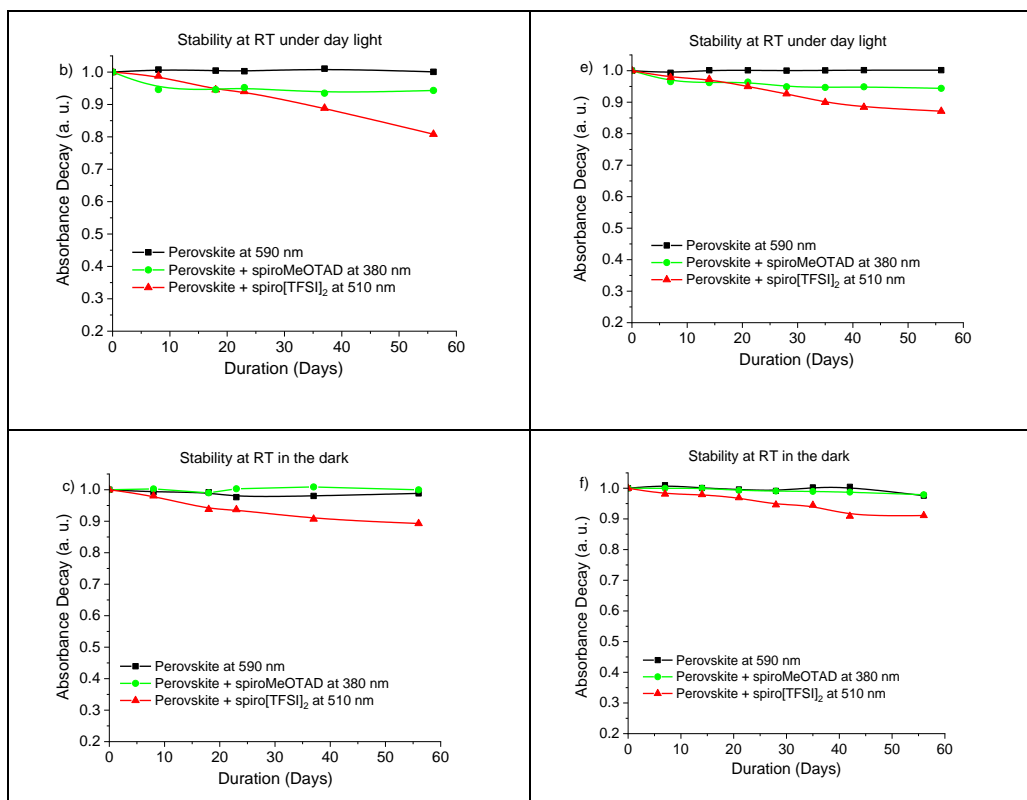


**Figure 3.24.** Light absorption intensity dynamics of the spiro[TFESI]<sub>2</sub> or spiro-MeOTAD films on Cs<sub>0.05</sub>(MA<sub>0.17</sub>FA<sub>0.83</sub>)<sub>0.95</sub>Pb(I<sub>0.83</sub>Br<sub>0.17</sub>)<sub>3</sub> and FA<sub>0.83</sub>Cs<sub>0.17</sub>Pb(I<sub>0.83</sub>Br<sub>0.17</sub>)<sub>3</sub> perovskites

The introduction of the Cs cation to the perovskite compositions Cs<sub>0.05</sub>(MA<sub>0.17</sub>FA<sub>0.83</sub>)<sub>0.95</sub>Pb(I<sub>0.83</sub>Br<sub>0.17</sub>)<sub>3</sub> and FA<sub>0.83</sub>Cs<sub>0.17</sub>Pb(I<sub>0.83</sub>Br<sub>0.17</sub>)<sub>3</sub> results in improved stability of the materials under prolonged thermal stress (Figures 3.24a, 3.24d). However, iodide ions still diffuse in sufficient numbers to adjoining spiro[TFESI]<sub>2</sub> layer to induce relatively rapid reduction of the material at 100 °C (Figures 3.22c, 3.22d, 3.24a, 3.24d). As with other types of perovskites, ion migration does take place at RT, and spiro[TFESI]<sub>2</sub> deteriorates under these milder conditions, as it can be observed by a drop in intensity of the absorption peak at 510 nm (Figures 3.24b, 3.24c, 3.24e, 3.24f).

Interestingly, the samples containing perovskite and spiro-MeOTAD demonstrate very little change during prolonged testing (Figures 3.23, 3.24), indicating that neutral molecule is sufficiently stable under investigated conditions, although a slight loss in absorption intensity under illumination can be detected.

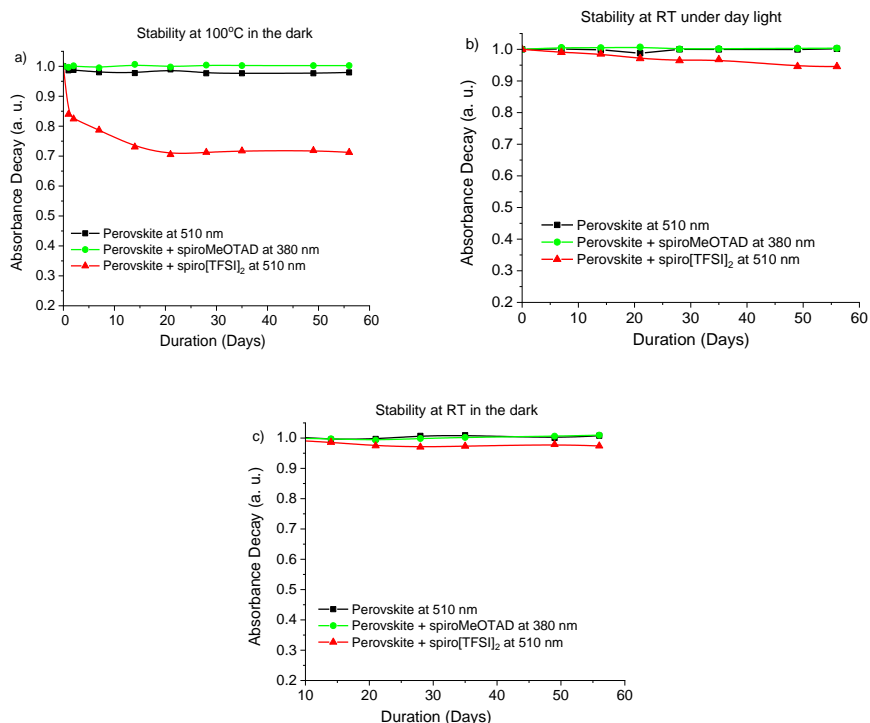


**Figure 3.25.** Light absorption intensity dynamics of the spiro[TFSI]<sub>2</sub> or spiro-MeOTAD films on MAPbBr<sub>3</sub> perovskite

The substitution of iodide with bromide ion in MAPbBr<sub>3</sub> perovskite results in improved resistance of the perovskite material to thermal stress (Figure 3.25a). The lower reactivity of bromide ensures that the reduction of spiro[TFSI]<sub>2</sub> at 100 °C is noticeably slower and takes days and not hours as before (Figures 3.22e, 3.25a), while at RT, only a slight change in absorbance is observed.

In order to confirm that the same reaction takes place in the solid films as in solution, HPLC-MS analysis of the samples was done after the stability experiments. The identification of the oxidized material is problematic: spiro[TFSI]<sub>2</sub> will begin to revert to neutral molecule in HPLC column, and furthermore, only the parent molecular cation mass in MS has been observed [128, 131]. Luckily, the reduction process in the column is slow enough to detect two elution peaks at different retention times: one for the for spiro[TFSI]<sub>2</sub> (retention time 6.9 min) and another for spiro-MeOTAD (retention time 7.6 min) (Appendix 1, Figures S37, S38), both of them yield 1225 mass spiro-MeOTAD molecular cation [M+H]<sup>+</sup>. In all of the samples with spiro[TFSI]<sub>2</sub> on different perovskite compositions, kept at 100 °C for 56 days, only neutral spiro-MeOTAD has been detected (Figures S32–S36). HPLC-MS analysis results correlate well with the data obtained from UV-vis spectroscopy.

Since the presence of oxidized HTM molecules in the charge transporting layer significantly improves conductivity [120, 128], the detected sensitivity of the spiro[TFSI]<sub>2</sub> to ion diffusion from perovskite, especially under thermal stress, could

potentially be one of the main reasons for the conductivity decrease that has been observed in the doped films of spiro-MeOTAD [118] and a subsequent decline in the performance of perovskite solar cells operated under prolonged thermal stress. One possible solution to the problem could be the utilization of the charge transporting materials that do not rely on doping and oxidized molecules to perform effectively in PSC [145]. Alternatively, the suppression of ion migration via blocking layer could be another option [146, 147]. Finally, the application of charge transporting materials capable of forming the self-assembled monolayer could simultaneously solve both doping as well as HTM film quality issues [148, 149].

### 3.2.2.3. Chapter summary

In summary, a series of experiments with oxidized spiro-MeOTAD have been conducted to determine the stability of the material in contact with various most popular perovskite compositions. Particular attention has been paid to long-term stability of the material under thermal stress. It has been determined that oxidized spiro-MeOTAD is readily reduced to neutral molecule during interaction with perovskite precursors MAI and FAI in the solution as well as with all five perovskite compositions in the solid state. It has been established that the presence of iodide ions, either in the solution or via ion migration from perovskite layer, is the main cause for the dedoping process. During the reaction, oxidized spiro-MeOTAD is reduced back to the neutral molecule, and iodine is formed. In the thin films, ion diffusion and consequently reduction of the oxidized spiro-MeOTAD is greatly enhanced at elevated temperatures, leading to a complete disappearance of the spiro[TFSI]<sub>2</sub> in a matter of days. The observed processes take place with all the perovskite compositions, although it has to be mentioned that spiro[TFSI]<sub>2</sub> degrades significantly slower in contact with MAPbBr<sub>3</sub> due to the lower reaction rate with the bromide ion. Since the presence of oxidized HTM molecules in the charge transporting layer significantly improves conductivity, the detected sensitivity of the spiro[TFSI]<sub>2</sub> to ion diffusion from perovskite, especially under thermal stress, could potentially be one of the main reasons for the conductivity decrease, observed in the doped films of spiro-MeOTAD, and a subsequent decline in performance of perovskite solar cells operated at elevated temperatures. Possible solutions to this problem could be the use of materials that do not require doping and therefore, do not rely on oxidized materials to improve conductivity or suppression of interlayer ion diffusion.

### 3.3. Materials capable of forming self-assembled hole transporting monolayer

Recently, the p-i-n configuration (in literature often referred to as “inverted” PSCs), where the hole transporting material is deposited on the TCO before perovskite, gained significant attention [53, 150]. p-i-n PSCs have several advantages in comparison to the n-i-p architecture. Firstly, high temperature annealing, which is required for the TiO<sub>2</sub> layer formation, is avoided. Secondly, much cheaper copper can be used instead of gold as a metal contact layer [150]. Thirdly, no doping is needed for the charge transporting layers, which can improve long-term stability as dopants (for example, the ones used in conjunction with spiro-

MeOTAD) that have been shown to reduce the device stability. Finally, the p-i-n configuration has shown to enable higher tandem efficiency potential due to less parasitic absorption in the front contact [151, 152], and thus, p-i-n PSCs have a great potential for further development.

Currently, most popular hole transporting materials for p-i-n PSC are polymers (e.g., PTAA [53], Poly-TPD [153], PEDOT:PSS [154]) or inorganic metal oxides (e.g., NiO<sub>x</sub> [155]), which are deposited by a spin-coating technique. However, spin-coating is not suitable for a large-scale production due to low throughput and large waste of materials. As an alternative, the vacuum deposition technique can be utilized for the HTM formation (e.g., TaTm [156]); yet, its application is limited to small molecules, which are compatible with sublimation, but usually not with solution-processed perovskites due to their low resistance to the used solvents.

The formation of a self-assembled monolayer on TCO circumvents the disadvantages of spin-coating or vacuum deposition while offering the benefits of uniformly formed layers with minimized thickness [157]. SAM HTMs would have minimal parasitic absorption, very low material consumption, would help to avoid doping procedure and could be adopted for a large area of production of solar cells. Moreover, due to the covalent linking to the substrate surface, these layers are relatively tolerant to perovskite processing and could potentially ensure full coverage of textured surfaces. Therefore, SAM HTMs would be perfect candidates for direct integration of PSCs on top of the textured silicon or rough CIGSe solar cells, thus simplifying tandem device construction.

The molecules with phosphonic acid anchoring groups are known to form densely packed, uniform monolayers on various oxides [157, 158], in particular on ITO by forming strong bidentate/tridentate bonds with the oxide surface [159, 160], which has been shown to occur even at room temperature [161].

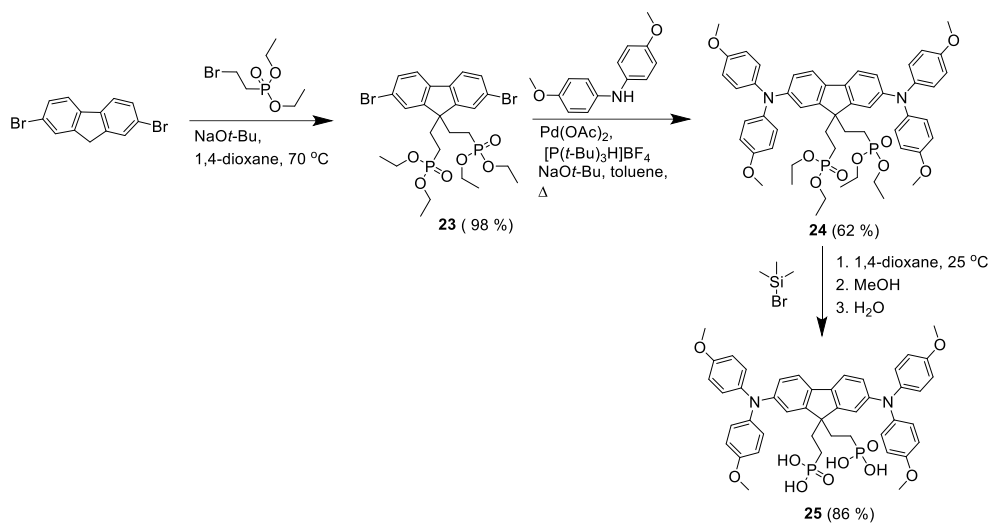
Current section of the work, capitalizes on the information gained in the previous chapter. Herein, the synthesis and characterization of the hole transporting molecules capable of forming SAMs on the surface of the TCO are discussed. As mentioned above, this approach would allow to form extremely thin films, thus ensuring good charge transport without the use of dopants or partially oxidized material, hence improving the device stability, while maintaining good performance. SAM approach as well simplifies the PSC construction procedure, as simpler and upscalable deposition methods (spraying, substrate dipping) could be used.

### **3.3.1. Dimethoxydiphenylamine substituted carbazole and fluorene derivatives**

In this chapter, new carbazole and fluorene-based hole transporting materials containing dimethoxydiphenylamine moiety and phosphonic acid anchoring group were synthesized and used for the formation of a self-assembled hole-transporting monolayer on ITO. PSC devices utilising p-i-n architecture and SAM HTM were constructed and tested.

### 3.3.1.1. Synthesis of the compounds

Dimethoxydiphenylamine-containing derivative **25** having a fluorene central moiety and two diethylphosphonate anchoring groups was obtained by three-step synthesis. Alkylation of dibromofluorene with diethyl 2-bromoethylphosphonate in the presence of the base affords intermediate **23**. Alkylated fluorene and 4,4'-dimethoxydiphenylamine were used in palladium-catalysed Buchwald–Hartwig amination reaction affording dimethoxydiphenylamine-containing derivative **24**. (Scheme 3.11). The resulting phosphonate **24** was hydrolysed in 1,4-dioxane using bromotrimethylsilane to obtain HTM **25** containing two phosphonic acid functional groups.

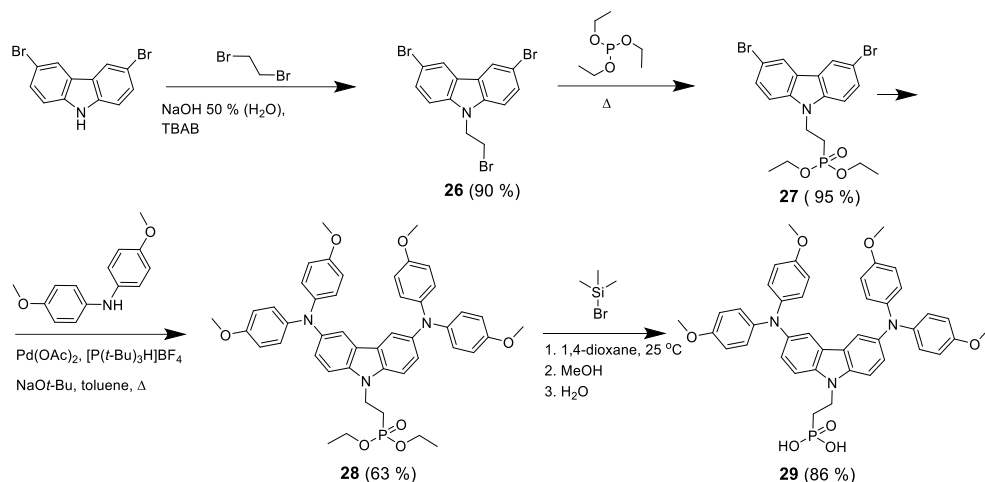


**Scheme 3.11.** Synthesis of fluorene-based HTM **25** with two ethylphosphonic acid anchoring groups

The synthesis of dimethoxydiphenylamine substituted carbazole **29**, functionalized with phosphonic acid, was done in a 4-step synthetic procedure, starting from commercially available materials (Scheme 3.12). 3,6-Dibromocarbazole was alkylated with 1,2-dibromoethane to give intermediate compound **26**. In the next step, by the means of Arbuzov reaction, aliphatic bromide was transformed into phosphonic acid ethyl ester **27**. Dimethoxydiphenylamine fragments were introduced via palladium-catalysed Buchwald–Hartwig amination reaction to yield **28**. Finally, the cleavage of the ester utilising bromotrimethylsilane resulted in phosphonic acid containing carbazole derivative **29**.

The structures of the synthesized compounds were confirmed by means of <sup>1</sup>H and <sup>13</sup>C NMR spectroscopy. A relatively high overall yield of 46 % for the four-step synthesis is achieved due to the simplicity of most of the stages, making **29** a promising material for the practical application from the synthetical point of view.





**Scheme 3.12.** Synthesis of dimethoxydiphenylamine substituted carbazole **29** with phosphonic acid moiety

During Buchwald–Hartwig amination reaction, it has been observed that the yield of the product was significantly influenced by the amount of palladium catalyst used in the reaction; therefore, it has been decided to review it a more detailed way.

**Table 3.4.** Influence of Pd catalyst concentration on Buchwald–Hartwig amination reaction yield

Pd catalyst content [Mol%]	Product yield of <b>28</b> , $\eta$ [%]	Product yield of <b>24</b> , $\eta$ [%]
5	10	11
15	14	16
30	63	62

The investigation showed that using 5 and 15 molar percentages of the palladium catalyst product yield was about 10 %, increasing Pd content to 30 molar percent increased the yield to 62 % (Table 3.4). It can be speculated that phosphonate groups, which tend to form coordination bonds with metal ions, do not allow the coupling reaction to proceed smoothly using lower loadings of the Pd catalyst.

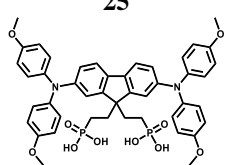
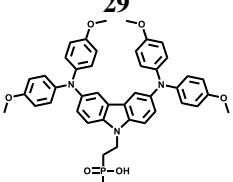
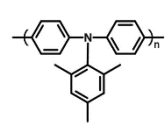
### 3.3.1.2. Thermal and optical properties

Thermal decomposition of **25** and **29** was investigated by the means of thermogravimetric analysis presented in Table 3.5. From the TGA data that has been shown, it is evident that both materials thermally degrade at about 340 °C, although,  $T_{dec}$  is lower than that of commonly used HTM polymer PTAA (500 °C), but it is high enough to make these materials suitable for the practical applications in optoelectronic devices.

From the DSC analysis of HTM **25**, bearing fluorene core, it could be seen that the material is fully amorphous, and only glass transition at 149 °C is registered.

Carbazole-containing compound **29** demonstrates the glass transition temperature of 124 °C. Comparing both semiconductors, it has been observed that the substitution of the fluorene core in **25** to carbazole in **29** and the removal of one phosphonic acid group reduces the glass transition temperature by 25 °C (Table 3.5).

**Table 3.5.** Thermal and optical properties of **25**, **29** and PTAA

	$T_{dec}$ [°C] <sup>[b]</sup>	$T_m$ , [°C]	$T_g$ , [°C] <sup>[a]</sup>	$\lambda_{abs}$ , [nm] <sup>[c]</sup>
<p style="text-align: center;"><b>25</b></p> 	334	–	149	366
<p style="text-align: center;"><b>29</b></p> 	343		124	304
<p style="text-align: center;">PTAA</p> 	500	–	400	383

<sup>[a]</sup> Determined by DSC from the second run, heating rate of 10 °C min<sup>-1</sup> under N<sub>2</sub> atmosphere; <sup>[b]</sup> determined by TGA, heating rate 10 °C min<sup>-1</sup> under N<sub>2</sub> atmosphere; <sup>[c]</sup> UV–vis absorption spectra for 10<sup>-4</sup> M THF solution.

In an inverted PSC, light first passes through the HTM layer when illuminated from the glass-substrate side; thus, it is important to minimize parasitic absorption of this layer. The optical properties of synthesized compounds **25**, **29** were investigated by the means of UV–vis spectroscopy (Figure 3.27). In the UV–vis spectrum of **25**, a  $\pi$ – $\pi^*$  transition is visible at 366 nm, while for **29**, this maximum is hypsochromically shifted by 60 nm to 304 nm, indicating somewhat smaller  $\pi$ –conjugated system for carbazole-based derivative **29**. Weaker n– $\pi^*$  absorption band in the 350–450 nm region is as well observed for **29**, which is characteristic for the carbazole chromophoric system possessing two localized electrons around nitrogen [153]. In comparison, PTAA demonstrates red shifted absorption maximum ( $\lambda_{max} = 387$  nm), which is understandable, bearing in mind conjugated polymeric backbone of the PTAA.

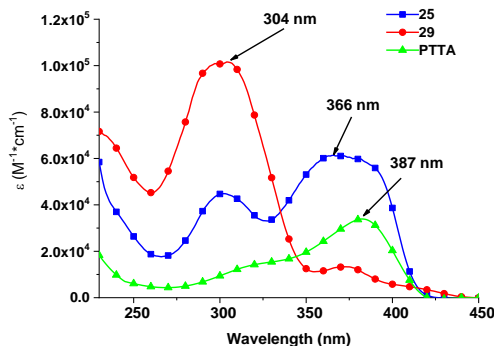


**Figure 27.** UV–vis absorption spectra for  $10^{-4}$  M THF solution of **25** and **29**

From the SAM HTM perspective, it is more beneficial to observe blue shifted absorption, as it would not interfere with the light absorption by perovskite material; therefore, both HTMs look quite promising, as their absorption spectra are mostly located in the UV region of the spectrum.

### 3.3.1.3. Photoelectrical properties and photovoltaic performance in PSC\*

Good matching of the energy levels between the absorber and charge transporting layer is an important requirement for the efficient device operation. The work function of bare ITO was previously measured to be 4.6 eV [162] by the means of ultraviolet photoelectron spectroscopy (UPS). The perovskite valence band edge and conduction band edge energies are measured to be in the range of 5.6–5.8 eV and 3.8–4.2 eV, respectively [163, 164, 165]. A suitable HTM should have  $I_p$  close to the perovskite valence band edge energy and a large energetic offset between the electron affinity (EA) and the perovskite conduction band edge. In order to measure  $I_p$  of the studied SAMs, photoelectron spectroscopy was performed in air measurements of **25**, **29** (Table 3.6).

For a PTAA film, spin-coated from a 2 mg/ml toluene solution on ITO,  $I_p$  value of 5.18 eV was obtained, which is within the measurement uncertainty of  $\approx 0.03$  eV and is very similar to the previously reported value of 5.16 eV [158]. Bulk **25**  $I_p$  measurements showed 5.31 eV (Table 3.6), while bulk **29** showed  $I_p$  of 5.04 eV, which is a typical value for this type of chromophore [159]. For the pure 100 % **25** SAM formed on ITO,  $I_p = 5.26$  eV was obtained, while pure **29** SAM formed on ITO showed  $I_p$  of 4.98 eV, both of which are in good agreement with the bulk material values.

\* PSC devices were constructed by prof. S. Albrecht research group (Helmholtz Zentrum Berlin). The energy level investigation on SAM surface of **29** as well as detailed investigation, optimization and result analysis of the PSC devices containing HTM **29** were reported in A. Magomedov PhD thesis; therefore, they are mentioned just briefly in this work.

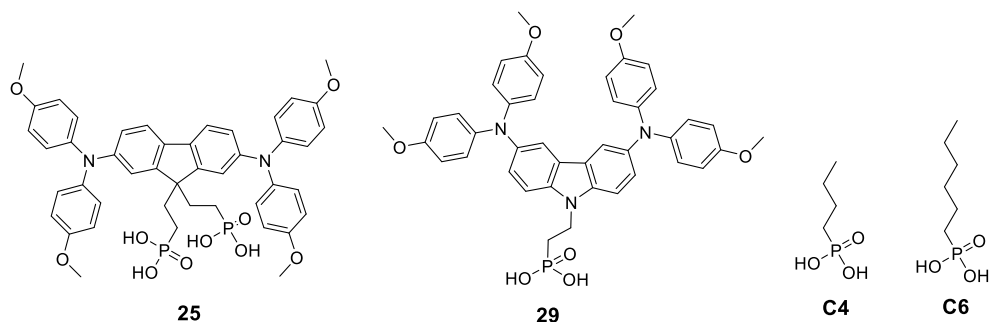


**Figure 3.29.** Structures of the HTM materials and secondary small molecule co-adsorber used in SAM experiments

During the initial device testing, it has been noticed that there are performance issues most likely related to the non-uniform coverage of ITO surface by SAM molecules due to their bulk; therefore, it has been decided to introduce a secondary small molecule co-adsorber to hopefully mitigate this problem (Figure 3.29).

**Table 3.6.**  $I_p$ ,  $E_g^{opt}$  and EA values of the investigated substrates

Material	$I_p$ , [eV]	$E_g^{opt}$ , [eV] <sup>[a]</sup>	EA, [eV] <sup>[c]</sup>
Bulk <b>25</b>	5.31	2.96	2.35
100 % <b>25</b> SAM	5.26	2.96 <sup>b)</sup>	2.30
Bulk <b>29</b>	5.04	2.75	2.29
100 % <b>29</b> SAM	4.98	2.75 <sup>b)</sup>	2.23
PTAA	5.18	2.96	2.22
ITO	4.6 [53] <sup>[d]</sup>	-	-

<sup>[a]</sup> Optical band gap ( $E_g^{opt}$ ) estimated from the edge of absorption spectra; <sup>[b]</sup>for SAMs, the same  $E_g^{opt}$  value as for bulk was used; <sup>[c]</sup>EA calculated using the equation  $EA = I_p - E_g^{opt}$ ; <sup>[d]</sup>ITO work function.

In order to compare **25** SAM HTM performance to a well-established procedure in p-i-n PSC fabrication, solar cells with pristine PTAA as an HTM were constructed. As it can be seen from Figure 3.30, the best-performing SAM devices using fluorene derivative **25** demonstrated PCE of 8.55 %, which is noticeably lower than that of the device with PTAA (17.34 %) as the HTM. The introduction of the co-adsorbers butylphosphonic acid (**C4**) or hexylphosphonic acid (**C6**) did not yield any significant improvement (Table 3.7).

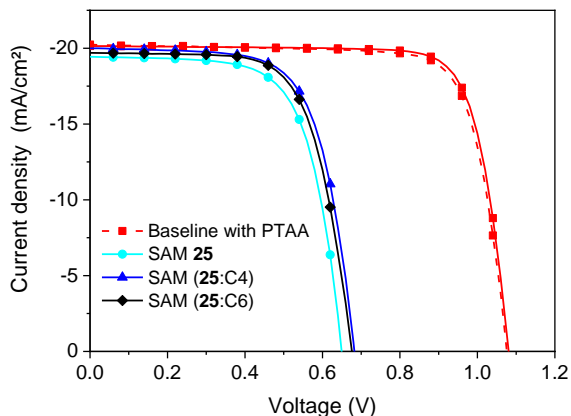


**Figure 3.30.**  $J$ - $V$  characteristics of the best performing PSCs with **25** and PTAA

It is likely that the dimethoxydiphenylamine fragments at 2,7 positions in the fluorene molecule interfere with the packing of the molecules on the ITO surface. Poor monolayer packaging creates "holes" between the ITO and the perovskite through which charge recombination is possible.

**Table 3.7.** Average PSC performance parameters for different SAM HTM compositions of **25**

SAM HTM	$J_{sc}$ , [mA cm <sup>-2</sup> ]	$V_{oc}$ , [V]	FF, [%]	PCE, [%]
<b>25</b>	19.33 ± 0.17 (19.43)	0.63 ± 0.03 (0.64)	66.45 ± 1.65 (67.7)	8.09 ± 0.58 (8.55)
<b>25:C4</b> 1:1	19.81 ± 0.19 (20.14)	0.61 ± 0.06 (0.68)	63.52 ± 3.12 (68.1)	7.67 ± 1.13 (9.32)
<b>25:C6</b> 1:1	19.53 ± 0.18 (19.70)	0.60 ± 0.06 (0.67)	62.84 ± 2.46 (68.1)	7.36 ± 1.02 (8.99)
PTAA	20.09 ± 0.18 (20.24)	1.08 ± 0.01 (1.08)	79.09 ± 0.31 (79.5)	17.12 ± 0.23 (17.34)

<sup>[a]</sup> Data were extracted from  $J$ - $V$  scans, including the standard errors and performance parameters of the best devices (in brackets). The statistics is based on 9–15 cells on different substrates for each SAM HTM composition.

The best PCE achieved with HTM **29** were with the mixed SAM (10 % **29** and 90 % **C4**) (Table 3.8). The better performance of the mixed SAMs compared to the pure **29** SAMs can be rationalized based on the several aspects. The addition of **C4** decreased the wettability of the perovskite solution, and small insulating **C4** molecules could reduce the direct contact of the perovskite with ITO by filling potential gaps left by the larger **29** molecule, thus reducing interfacial recombination.

**Table 3.8.** Average PSCs performance parameters of devices containing **29**, a mixture of 10 % **29**:90 % **C4** and PTAA

HTM	$J_{sc}$ , [mA $\times$ cm $^{-2}$ ]	$V_{oc}$ , [V]	$FF$ , [%]	PCE, [%]
<b>29</b>	21.22 $\pm$ 0.28 (21.8)	0.93 $\pm$ 0.03 (0.96)	66.48 $\pm$ 2.12 (72.8)	13.16 $\pm$ 0.83 (15.3)
<b>29</b> : <b>C4</b> 1:9	21.01 $\pm$ 0.06 (21.9)	1.00 $\pm$ 0.006 (1.09)	78.33 $\pm$ 0.46 (81.0)	16.46 $\pm$ 0.15 (17.8)
PTAA	20.87 $\pm$ 0.06 (21.8)	1.09 $\pm$ 0.002 (1.13)	77.82 $\pm$ 0.28 (81.0)	17.69 $\pm$ 0.08 (19.2)

<sup>[a]</sup> Data, extracted from  $J$ - $V$  scans, including the standard errors and the best performance parameters (in brackets). The statistics is based on 41–68 cells from several batches for **29**, **29**:**C4** 1:9 and PTAA, respectively.

### 3.3.1.4. Chapter summary

In summary, a new and promising hole transporting material concept involving self-assembled monolayers was presented. For this purpose, new molecules **25** and **29**, containing a hole transporting fragment and phosphonic acid anchoring group, were synthesized and used for the formation of functional self-assembled monolayers on ITO surface. It was demonstrated that the addition of a small molecule co-adsorber, resulting in mixed SAM, can potentially have a positive impact on the overall performance of SAM HTM-based devices, although, the structure of the used HTM has a profound importance. Solar cell efficiencies of 9.32 % for fluorene-based material **25** and 17.8 % for carbazole-containing HTM **29** were reached.

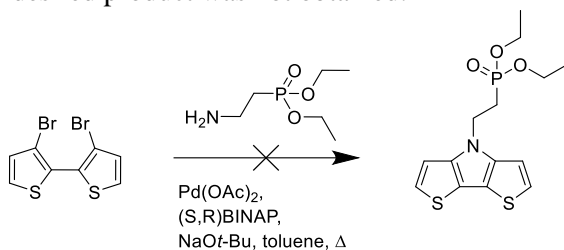
### 3.3.2. Dithieno[3,2-b:2',3'-d]pyrrole based derivatives

In the previous chapter, it has been demonstrated that SAMs formed by larger HTM molecules have uniformity problems, which can be alleviated by the addition of smaller co-adsorbers. Therefore, the next logical step would be to test smaller HTM molecules and hopefully eliminate the need for co-adsorbers, simplifying the deposition procedure even further. In this chapter, a possibility to apply new small molecular weight dithieno[3,2-b:2',3'-d]pyrrole-based hole transporting material, containing phosphonic acid anchoring group as SAM-forming material, is investigated. The HTM was synthesized and tested as self-assembled hole-transporting monolayer in PSC devices utilising p-i-n architecture.

#### 3.3.2.1. Synthesis of dithieno[3,2-b:2',3'-d]pyrrole-based materials containing anchoring group

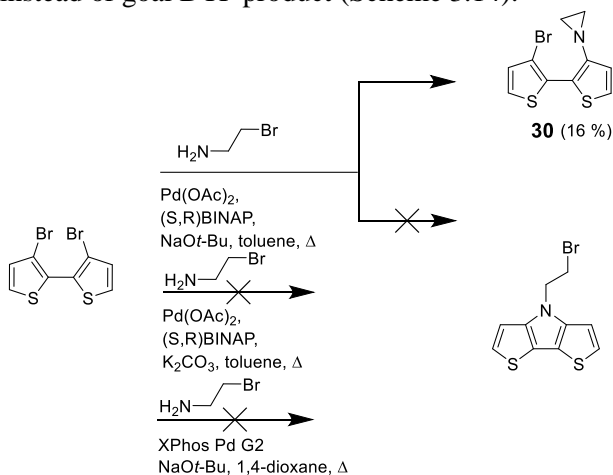
Along the “regular” structure DTP-containing HTMs, it has been decided to additionally synthesize materials containing both hole transporting fragment as well as anchoring moiety. Phosphonic acid was chosen as an anchoring group, as molecules with such groups are known to form densely packed, uniform monolayers on various substrates, for example, oxides, in particular on ITO. They form strong bidentate/tridentate bonds with the surface, which was shown to occur even at room temperature and have been utilized for various applications, e.g., in dye-sensitized solar cells and electrochromic devices.

Initially, it was attempted to synthesize DTP directly via palladium catalysed Buchwald–Hartwig amination employing appropriate amine (Scheme 3.13). Unfortunately, the desired product was not obtained.



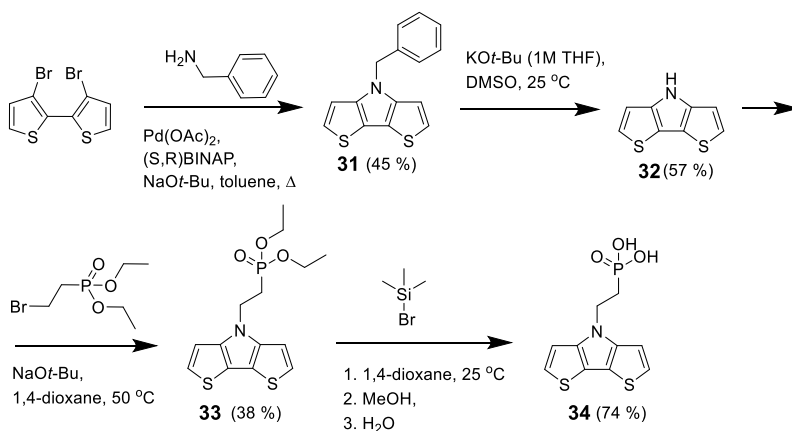
**Scheme 3.13.** Direct synthesis of DTP compound containing phosphonate moiety

A different three-step approach was investigated as well, i.e., palladium catalysed Buchwald–Hartwig amination using 2-bromoethylamine hydrobromide followed by Arbuzov reaction, transforming aliphatic bromide into diethyl phosphonate, which in turn would be hydrolysed to obtain appropriate phosphonic acid. Regrettably, this approach was unsuccessful as well: during the first phase, cyclic aziridine derivative **30** was isolated instead of goal DTP product (Scheme 3.14).



**Scheme 3.14.** Synthesis of DTP compound containing ethylbromide moiety

Finally, the synthesis of target compound containing both hole transporting DTP fragment as well as anchoring moiety was successfully realized via 4-step synthetic procedure (Scheme 3.15). Benzylamine group was introduced by employing palladium catalysed Buchwald–Hartwig amination, yielding DTP derivative **31**. Dithieno[3,2-b:2',3'-d]pyrrole (**32**) has been synthesized by debenylation of **31** with potassium *tert*-butoxide in DMSO.



**Scheme 3.15.** Four-step synthesis of DTP derivative **34** containing phosphonic acid moiety

Dithieno[3,2-*b*:2',3'-*d*]pyrrole (**32**) was alkylated with 2-bromoethylphosphonate to give intermediate compound **33**. Finally, the hydrolysis of the ester groups utilising bromotrimethylsilane resulted in phosphonic acid **34**.

### 3.3.2.2. Optical, photoelectrical properties and photovoltaic performance in PSC

Similarly as with starting DTP derivative **1**, phosphonic acid containing HTM **34** demonstrates absorption maxima around 300 nm and compared with PTAA ( $\lambda_{\text{abs}}=383$  nm), should not have any issues with parasitic absorption when used as self-assembled monolayer in the PSC.

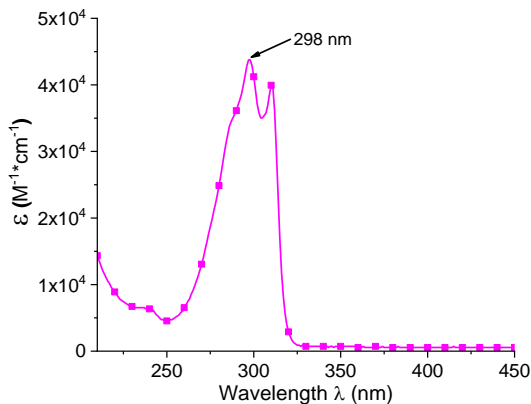


**Figure 3.31.** Light absorption spectra of **34** in THF ( $c = 10^{-4}$  M)

$I_p$  measurements of **34** using PESA technique demonstrated  $I_p$  of 5.74 eV in the bulk and 5.71 eV as self-assembled monolayer on top of the ITO, while EA are 1.86 eV and 1.83 eV, accordingly. The perovskite valence band edge and conduction band edge energies are measured to be in the range of 5.6–5.8 eV and 3.8–4.2 eV,



respectively. From the measurement results, it is evident that DTP derivative **34** has quite high ionization potential, and this energy level mismatch could potentially cause problems with charge transport via the layer, resulting in recombination losses and a drop in device efficiency.

As suspected, the testing of material in the SAM HTM-based PSC devices revealed below average performance (Table 3.9). The best performing solar cells demonstrated efficiency of approximately 10.6 %, which is substantially lower than that of PTAA standard (19.2 %).

**Table 3.9.** Average PSCs performance parameters of **34** and PTAA

HTM	$J_{sc}$ , [mA×cm <sup>-2</sup> ]	$V_{oc}$ , [V]	$FF$ , [%]	PCE, [%]
PTAA	20.87 ± 0.06 (21.8)	1.09 ± 0.002 (1.13)	77.82 ± 0.28 (81.0)	17.69 ± 0.08 (19.2)
<b>34</b>	19.06 ± 0.22 (19.48)	0.71 ± 0.025 (0.74)	74.66 ± 1.83 (77.3)	9.92 ± 0.45 (10.6)

<sup>[a]</sup> Data, extracted from  $J$ - $V$  scans, including the standard errors and the best performance parameters (in brackets). The statistics are based on 20 and 68 cells from several batches for **34** and PTAA, respectively.

The extent of the problem can be clearly observed in EQE spectrum (Figure 3.32). The external quantum efficiency of the devices constructed using SAM of DTP derivative **34** showed approximately 10 % lower photon to electron conversion ratio, compared with the PTAA containing standard. Interestingly, EQE spectrum of the PSC containing **34** demonstrated more or less similar external quantum efficiency along the entire wavelength spectrum, while PTAA has a noticeable drop in EQE at 300–400 nm range associated with parasitic absorbance by HTM.

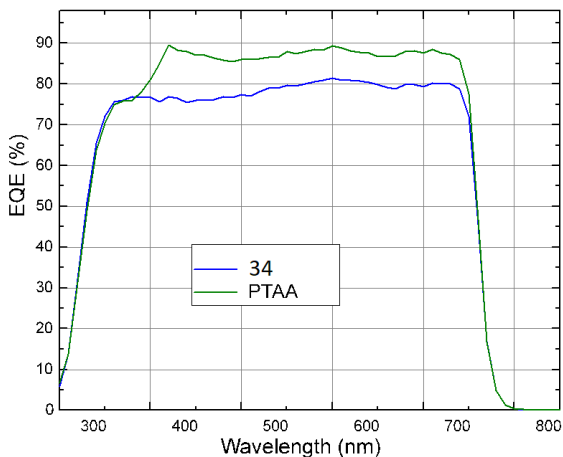


**Figure 3.32.** EQE spectra of **34** and PTAA containing PSC devices

### 3.3.2.3. Chapter summary

In summary, new small molecular weight dithieno[3,2-b:2',3'-d]pyrrole-based hole transporting material, containing phosphonic acid anchoring group, was synthesized and investigated as SAM-forming HTM material in the PSC devices. Unfortunately, mediocre device performance was registered, which could be most likely attributed to the energy level mismatch. On the positive side, it is evident that the application of the small molecule SAM approach allows for the elimination of HTM related parasitic absorbance.

### 3.3.3. Carbazole-based small molecule derivatives

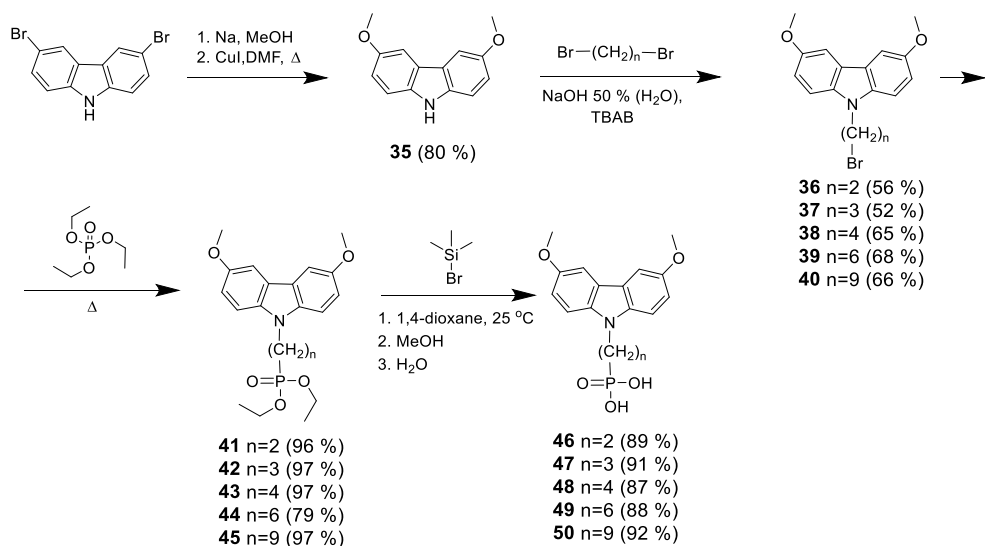
Perovskite-based photovoltaics promises three main benefits: low cost, high efficiency and large versatility. However, combining all three factors into one solar cell design is still a difficult endeavour. In particular, one of the main bottlenecks towards the large-scale production is the available choice of hole transporting materials. The best standards in both architectures, n-i-p (Spiro-MeOTAD) and p-i-n (PTAA), are highly unsuitable for commercial production due to their very high prices and limited processing versatility. Thus, a new generation of self-assembled monolayers as HTM that are intrinsically scalable, simple to process, dopant-free and cheap is a very attractive alternative. Besides minimal material consumption and parasitic absorption, the self-assembly process enables complete coverage of oxide surfaces of different roughness and texture utilising simple to control the process.

The first hole-selective SAMs, discussed in the earlier chapters, demonstrated the ability to covalently bind to the transparent conductive oxide and perform the role of hole-selective contact, i.e., allow the movement of positive charge from perovskite absorber to the electrode while at the same time blocking electrons from going in the same direction. Due to this hole-selectivity, the SAMs demonstrated a potential to replace the classical hole-transporting layer. However, these SAMs did not enable high PCEs that would surpass those reached with the typically used polymeric hole transporting material PTAA.

In this chapter, a second generation of self-assembly capable HTMs is presented. The new molecules are based on simple carbazole core and follow the philosophy of “less is more”. Compared to the previously discussed carbazole and fluorene derivatives **25** and **29**, these molecules are significantly smaller and less complex. The main goal was to reduce the size of the molecule so that the use of co-adsorbents would be unnecessary; furthermore, the synthesis and purification simplicity is of prime importance if a material has to be produced on a large scale. Naturally, proper energetical alignment and HTM/perovskite compatibility could be achieved easier with a system that is easier to modify and faster to synthesize.

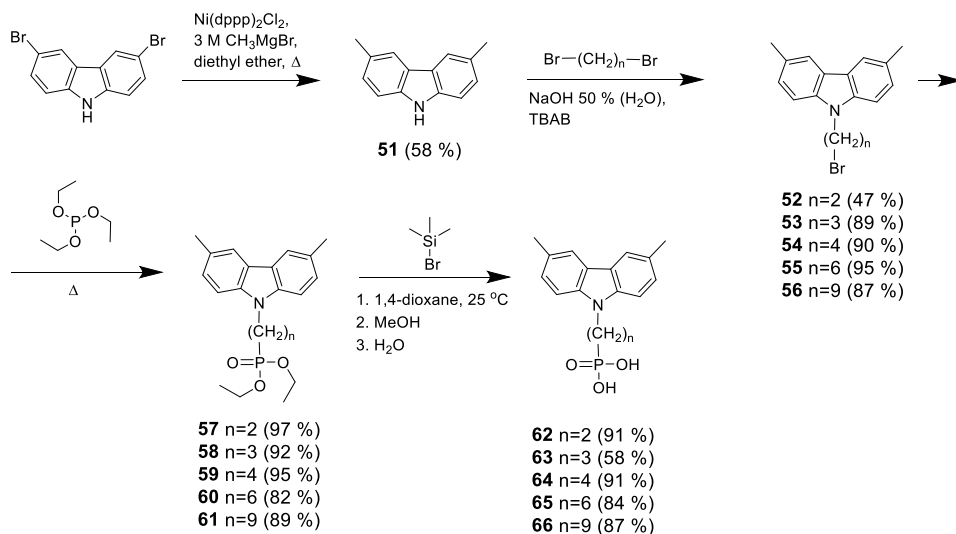
#### 3.3.3.1. Synthesis of carbazole derivatives

The first group of molecules, 3,6-dimethoxy functionalized carbazole with phosphonic acid moiety, was synthesized with the goal of obtaining materials demonstrating lower ionization potential and increased electron donating potential compared with the unsubstituted carbazole molecule.



**Scheme 3.16.** Synthesis of 3,6-dimethoxycarbazole derivatives **46–50**

The synthesis was done in a 4-step synthetic procedure, starting from commercially available materials (Scheme 3.16). 3,6-Dibromocarbazole reacted with sodium methoxide in DMF in the presence of copper iodide to yield 3,6-dimethoxycarbazole **35**. In the next stage, 3,6-dimethoxycarbazole was alkylated with different dibromoalkanes using tetra-*n*-butylammonium bromide as interphase catalyst, aqueous solution of NaOH as a base and alkylating agent as a reagent and solvent to give intermediate compounds **36–40**. In the third step, by the means of Arbuzov reaction, aliphatic bromide was transformed into phosphonic acid ethyl esters **41–45**. Finally, ester hydrolysis utilising bromotrimethylsilane resulted in goal phosphonic acids **46–50**. The demonstrated four-step synthesis procedure is relatively straightforward and inexpensive, making these carbazole-based phosphonic acids **46–50** promising materials for the practical application.



**Scheme 3.17.** Synthesis of 3,6-dimethylcarbazole derivatives **62–66**

The second group of synthesized molecules contained less donoric methyl substituents, and these dimethylcarbazoles **62–66**, functionalized with phosphonic acid anchoring group, were synthesized via similar 4-step procedure (Scheme 3.17). 3,6-Dibromocarbazole reacted with Grignard reagent methylmagnesium bromide to yield 3,6-dimethyl-9H-carbazole (**51**). In the next stage, 3,6-dimethylcarbazole was alkylated with different dibromo alkanes to give intermediate alkylated compounds **52–56**. By the means of Arbuzov reaction, aliphatic bromide in **52–56** was substituted by phosphonic acid ethyl ester **57–61**. Finally, the hydrolysis was conducted utilising bromotrimethylsilane, resulting in 3,6-dimethylcarbazole-based phosphonic acids **62–66**.

### 3.3.3.2. Thermal, optical and photoelectrical properties

DSC measurements of compounds **47–50** revealed that most of the investigated carbazole derivatives with methoxy groups can exist both in amorphous and crystalline states (Figure 3.33, Table 3.10). During the first heating, the melting of crystals was observed; no crystallization takes place during cooling or second heating scans, and only glass transition is registered during the second heating (Figure 3.33, Table 3.10). The only exception being carbazole derivative **47** with the shortest aliphatic chain, which is fully crystalline.

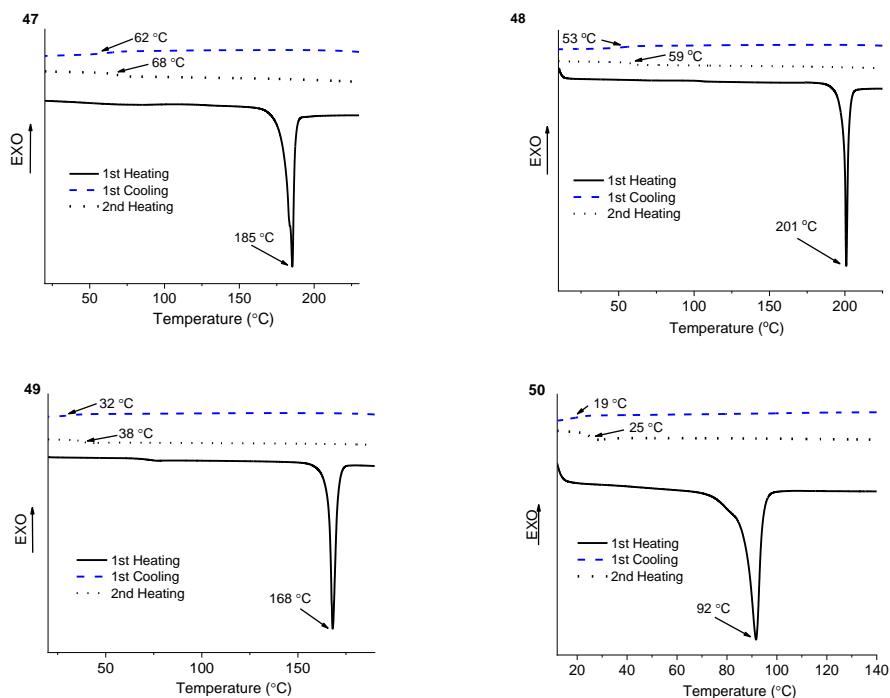


**Figure 3.33.** DSC curves for compounds **47–50**, heating rate 10 °C/min

In general, the lengthening of the aliphatic chain results in a drop of glass transition temperature due to the increased flexibility of molecules.

DSC measurements of the methylcarbazole series **62–66** revealed that the investigated HTM can as well exist both in crystalline and amorphous state (Figure 3.34, Table 3.10), as melting of the crystals and glass transitions are registered. Most of the materials, with the exception of **64**, demonstrate polymorphism, i.e., two or more different melting temperatures, indicating different crystal phases.

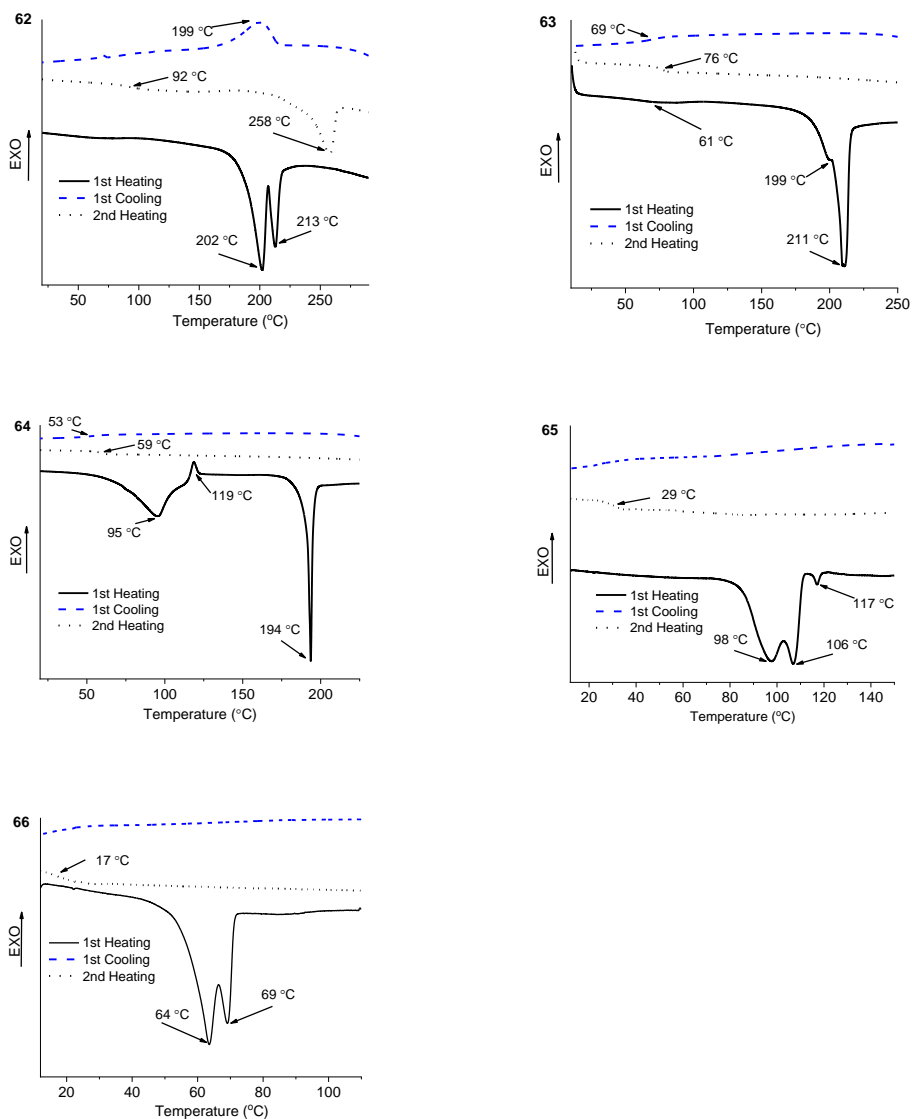


**Figure 3.34.** DSC curves for compounds **62–66**, heating rate 10 °C/min

As with the methoxy analogues, glass transition and melting temperatures decrease with the increasing length of the aliphatic chains. 3,6-Dimethylcarbazole derivative with the shortest aliphatic chain **62**, similarly as with methoxy analogue **46**, has the strongest tendency to crystallize, and the recrystallization is observed at 199 °C during the cooling of the melt. Interestingly, similar, although significantly more subdued, behaviour is observed for butyl analogue **64** containing even number of aliphatic carbons, but not for propyl one **63** containing odd number of aliphatic carbon atoms. Slightly higher tendency of the molecules with an even number of

carbon atoms to organize into orderly structures could be because of the observed differences between compounds **63** and **64**.

**Table 3.10.** Thermal properties of methoxy carbazole derivatives **46–50**, **62–66**

Compound	$T_m$ [°C] <sup>[a]</sup>	$T_g$ [°C] <sup>[b]</sup>	$T_{dec}$ [°C] <sup>[c]</sup>
<b>46</b>	171	-	266
<b>47</b>	185	62	274
<b>48</b>	201	59	281
<b>49</b>	168	38	283
<b>50</b>	92	25	285
<b>62</b>	202, 213, 258	92	294
<b>63</b>	199, 211	76	302
<b>64</b>	194	59	314
<b>65</b>	98, 106, 117	29	327
<b>66</b>	64, 69	17	329

<sup>[a]</sup> Melting point determined by DSC, scan rate 10 °C/min; <sup>[b]</sup> glass transition determined by DSC: scan rate, 10 °C/min, second run; <sup>[c]</sup> onset of decomposition determined by TGA: heating rate, 10 °C/min.

Thermogravimetric analysis of carbazole and methoxycarbazole-based compounds **46–50** (Figure 3.35, Table 3.10) reveals that in general, all the compounds within the series have demonstrated relatively good thermal stability with decomposition temperature (corresponding to 5 % weight loss) in the 260–280 °C range. From the existing result, it should be noted that during the construction of the PSC devices, the temperatures higher than 200 °C are rarely encountered; therefore, thermal stability is sufficient for the practical application.

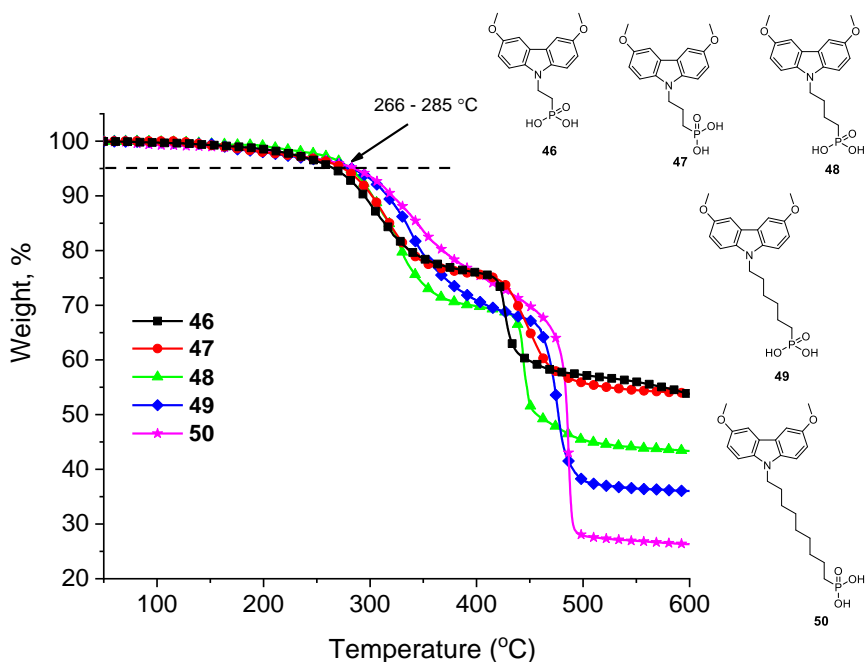


**Figure 3.35.** TGA curves for compounds **46–50**

Thermogravimetric analysis of methyl containing carbazole derivatives **62–66** reveals even higher decomposition temperatures (Figure 3.36, Table 3.10). In general, all the compounds within this series have demonstrated better thermal stability than carbazole derivatives with methoxy groups; initial thermal destruction temperature (corresponding to 5 % weight loss) is higher than 290 °C.

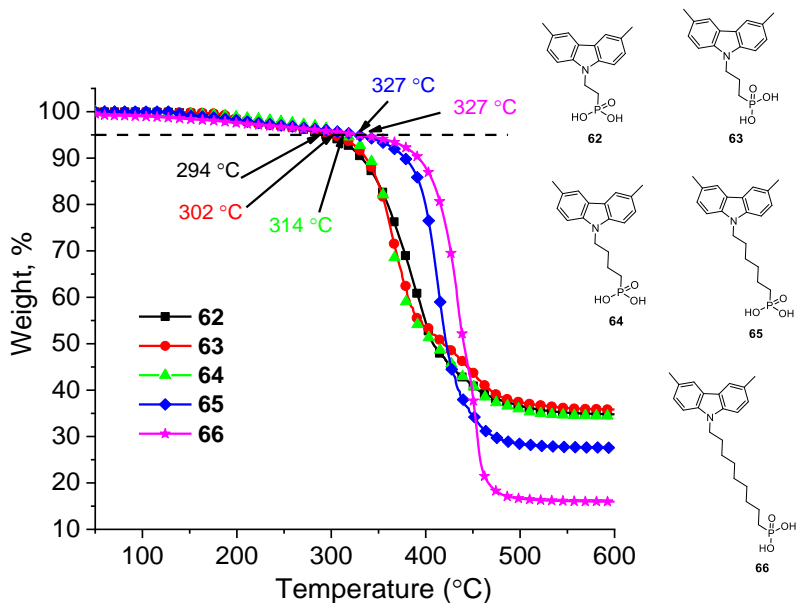


**Figure 3.36.** TGA curves for compounds **62–66**

UV-VIS absorption spectra of carbazole-based derivatives are quite similar; therefore, only the selected spectra are shown (Figure 3.37).



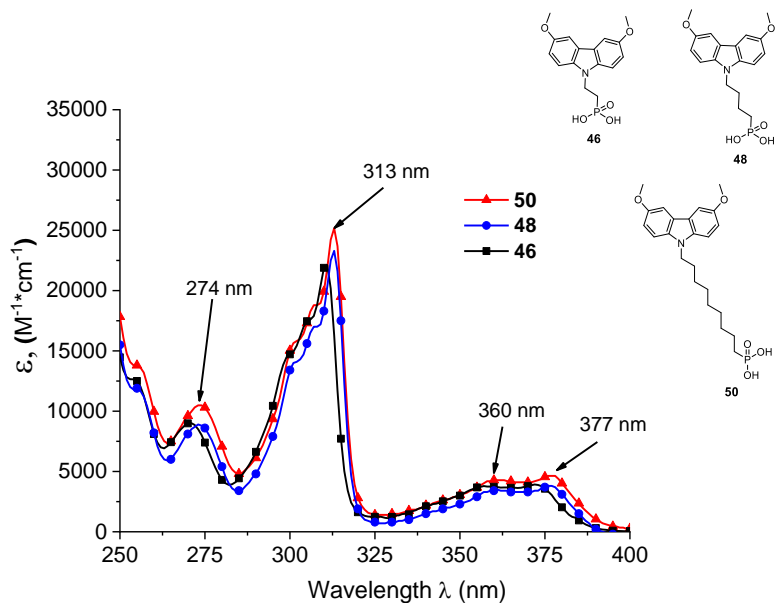


**Figure 3.37.** UV-VIS spectra of compounds **46**, **48**, **50** in THF solution ( $c=10^{-4}$  M)

UV-vis absorption spectra demonstrate that compounds **46**, **48**, **50** have similar absorption peaks.  $\pi$ - $\pi^*$  transition can be seen around 310 nm, while the weak absorption band ascribed to n- $\pi^*$  transition can be seen in the region 320 nm to 390 nm.

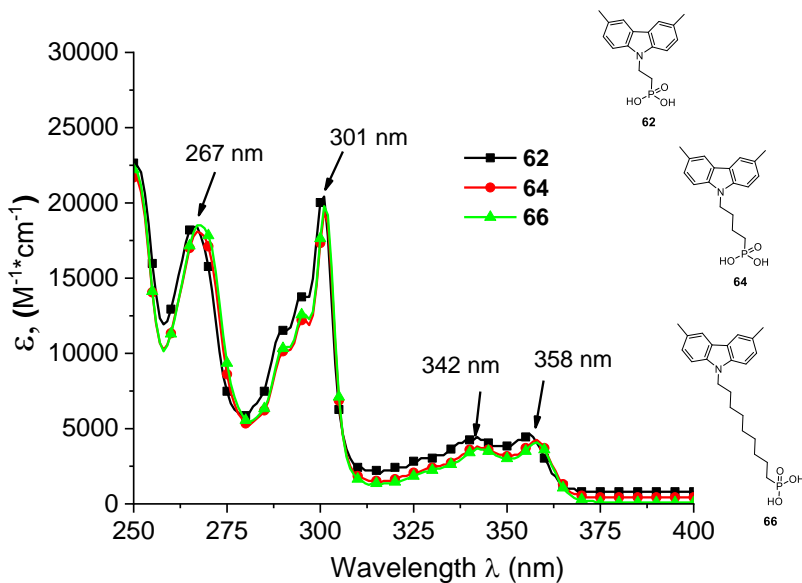


**Figure 3.38.** UV-vis spectra of compounds **62**, **64**, **66** in THF solution ( $c=10^{-4}$  M)

Similarly as in the previous example, UV-vis absorption spectra of 3,6-dimethylcarbazole derivatives **62**, **64**, **66** are quite similar between each other due to the unchanged size of the conjugated system (Figure 3.38). Compared with **46**, methyl groups at the 3,6-carbazole positions have less effect on  $\pi$ -conjugated system, as methoxy groups and the hypsochromic shift of approx. 15 nm can be seen. Most importantly, all of the investigated HTM, due to a relatively small size of the molecule, do not absorb intensively beyond 325 nm, thus ensuring as little parasitic absorption in the device as possible.

The solid-state  $I_p$  is an important parameter for the organic materials that are planned to be used for the optoelectronic applications.  $I_p$  of the HTMs was measured using PESA method (Figure 3.39). Among methyl substituted carbazole derivatives, **63** demonstrates the lowest  $I_p$  (5.41 eV), while HTMs with longer aliphatic chains demonstrate a slightly higher ionization potential, up to 5.58 eV for nonyl derivative **66**.

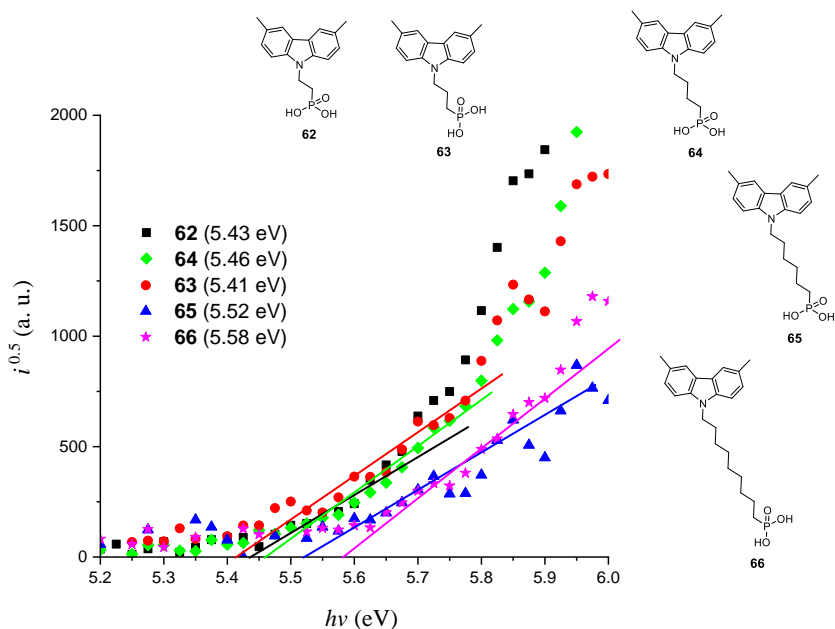


**Figure 3.39.** Photoemission in air spectra of compounds **62–66**

The introduction of stronger electron donating methoxy groups to the 3,6-positions of the carbazole in **46–50** (Figure 3.40) results in the reduction of ionization potential by 0.2–0.3 eV to 5.2–5.3 eV, compared with methyl substituted analogues.

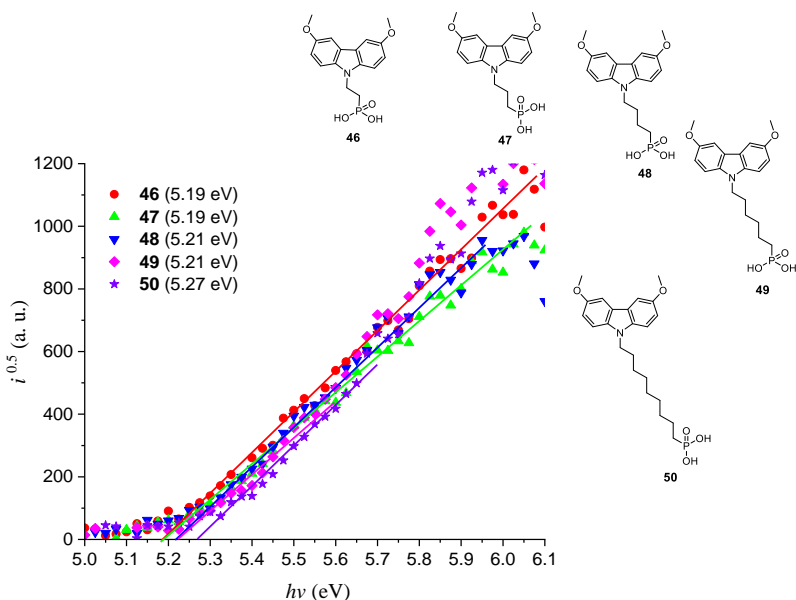


**Figure 3.40.** Photoemission in air spectra of compounds **46–50**

Overall, from the energetical point of view, all of the materials provide a sufficient barrier for the electron migration and should not interfere too significantly with the hole transport from the perovskite to the electrode.

### 3.3.3.3. Performance in perovskite single-junction solar cells

For comparing the performance and device-relevant characteristics of SAM-based solar cells, it has been chosen to focus the analysis on the so called “triple cation” perovskite absorber  $\text{Cs}_5(\text{MA}_{17}\text{-FA}_{83})_{95}\text{Pb}(\text{I}_{83}\text{Br}_{17})_3$  ( $\text{CsMAFA}$ ), which is widely used due to its high reproducibility. Since the polymeric hole transport material PTAA is currently being used in the highest-performing p-i-n PSCs [166, 167, 168], the SAM-based cells have been compared to PTAA-based PSCs and the perovskite film and device properties have been analysed. To keep the devices as simple as possible, the SAM and PTAA cells do not contain any interfacial compatibilizers, additives or doping. As such, the analysed PTAA control cells are comparable to the state-of-the-art ones as found in literature [166, 169].

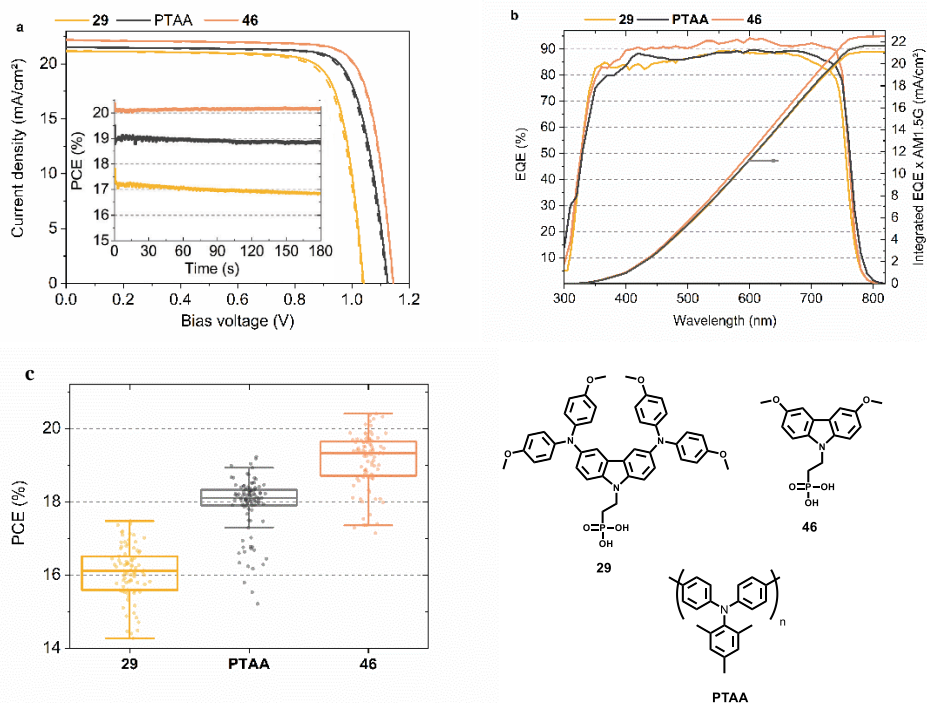


**Figure 3.41.** Device-related analysis of SAM-based solar cells in comparison to the state-of-the-art PTAA solar cells with triple cation perovskite absorber; a)  $J-V$  curves under simulated AM 1.5G illumination at a scan rate of  $250 \text{ mV} \times \text{s}^{-1}$  in forward ( $J_{SC}$  to  $V_{OC}$ , dashed) and reverse scan ( $V_{OC}$  to  $J_{SC}$ , solid) with respective MPP tracks in the inset; (b) external quantum efficiency spectra of the best solar cells and corresponding integration of the product of EQE and AM 1.5G spectrum (right axis); (c) box plot of power conversion efficiency values for 41 (**29**), 53 (PTAA), 47 (**46**) and solar cells

Figure 41a shows  $J-V$  characteristics under simulated AM 1.5G illumination of the best PSCs obtained with methoxy-containing carbazole derivative **46** in forward ( $J_{SC}$  to  $V_{OC}$ ) and reverse scan ( $V_{OC}$  to  $J_{SC}$ ) direction with continuous maximum power point (MPP) tracks in the inset. As a comparison, devices with **29** and standard PTAA are given as well. A full list of the tested materials and their photovoltaic parameters are given in Table 3.11. A statistical comparison of the PCEs is plotted in Figure 3.41c with 41–53 solar cells per HTM. From the  $J-V$  curves, it can be noticed that hysteresis overall is negligible with MPP-tracked efficiencies close to the respective  $J-V$  scan values, and the fill factor is overall comparable at around 80 %. Figure 41b displays the EQE of the best devices as well as the integrated product of EQE and AM 1.5G spectrum. The  $J_{SC}$  values from EQE integration have a negligible difference to the  $J_{SC}$  values obtained from the  $J-V$  scans ( $\sim 1\%$ ). The most noticeable difference between the HTMs is visible in the open circuit voltage with a difference of 20 mV between PTAA and methoxy substituted carbazole SAMs. Overall, the PCE trend resembles an increase in  $V_{OC}$ , and **46–50** series solar cells surpass or are very similar to the efficiency of PTAA

devices with **46**, yielding the highest efficiency of 20.4 % in  $J-V$  scan and 20.2 % in the maximum power point (MPP) track.

**Table 3.11.** Photovoltaic parameters from  $J-V$  scans under illumination in reverse scan direction together with the efficiency of MPP tracking of the best CsMAFA perovskite solar cells based on the different investigated hole selective contacts.

HSC	$J_{sc}$ [mA $\times$ cm $^{-2}$ ]	$V_{oc}$ [V]	FF [%]	PCE ( $J-V$ ) [%]	PCE (MPP) [%]
<b>29</b> [149]	21.2	1.041	79.3	17.5	16.9
<b>PTAA</b>	21.5	1.125	79.3	19.2	18.9
<b>46</b>	22.2	1.144	80.5	20.4	20.2
<b>47</b>	18.4	1.144	77.4	18.4	18.4
<b>48</b>	19.9	1.142	79.9	19.9	19.6
<b>49</b>	20.0	1.145	79.7	19.6	19.5
<b>50</b>	19.0	1.144	76.9	18.9	18.6
<b>62</b>	20.6	1.129	80.4	18.9	–
<b>64</b>	20.3	1.150	84.0	20.0	–
<b>64+</b> C <sub>60</sub> /LiF	20.7	1.224	82.0	20.8	–

As shown in the Table 3.11, the self-assembled hole-transporting monolayers from materials with longer aliphatic chains **48–50**, contrary to the expectations, do not lower the PSC performance very significantly; thus, demonstrating the scope of possible aliphatic chain modifications without severely influencing the device performance.

Compared with PTAA standard, methoxycarbazole **46–50** series enable higher  $V_{oc}$  values in solar cells. The changes in  $V_{oc}$  can have a variety of origins, most importantly, the changes of the bulk properties and of the non-radiative recombination velocities at one or both interfaces. The latter can be caused by either a higher selectivity due to a more favourable energetic alignment and/or less defect states at one or both interfaces to the respective charge-selective contacts.

For the analysis of methylcarbazole-based materials **62–66** on solar cell level, the focus has been placed on the simple single junction device stack glass/ITO/HTM/perovskite/C<sub>60</sub>/SnO<sub>2</sub>/Ag with the SnO<sub>2</sub>, latter serving as a buffer layer for indium zinc oxide (IZO) sputtering, in case the fabrication of tandem solar cells is undertaken [170]. The FF is the major remaining parameter for which PSCs have not yet come close to the values of established solar cell technologies [171, 172], with the ideality factor being one of the main properties that limit high-efficiency PSCs [173]. Combining a low ideality factor with high PCE was considered a significant challenge in the community [174]. Figure 3.42a shows that **46** allow for very good FFs of up to 82 %, while **64** surpasses the other HTMs with FF values of up to 84 % (representing ~ 93 % of the radiative limit). Figure 3.42b shows  $J-V$  curves recorded at simulated AM 1.5G illumination conditions, comparing PTAA to **64** and showing the obvious effect of a lower ideality factor. The ideality factor  $n_{ID}$  for PSCs with the **64** is ~1.26, while it is 1.51 for **46** and 1.55 for PTAA cells (Figure 3.42c). The high FF was accompanied by high  $V_{oc}$  values

(up to 1.16 V) and up to 1.224 V if a LiF interlayer was used between perovskite and C<sub>60</sub> (Figure 3.42d). The combination of high V<sub>OC</sub> with low n<sub>ID</sub> allowed to fabricate a perovskite single junction solar cell with an efficiency of 20.8 % with **64**.

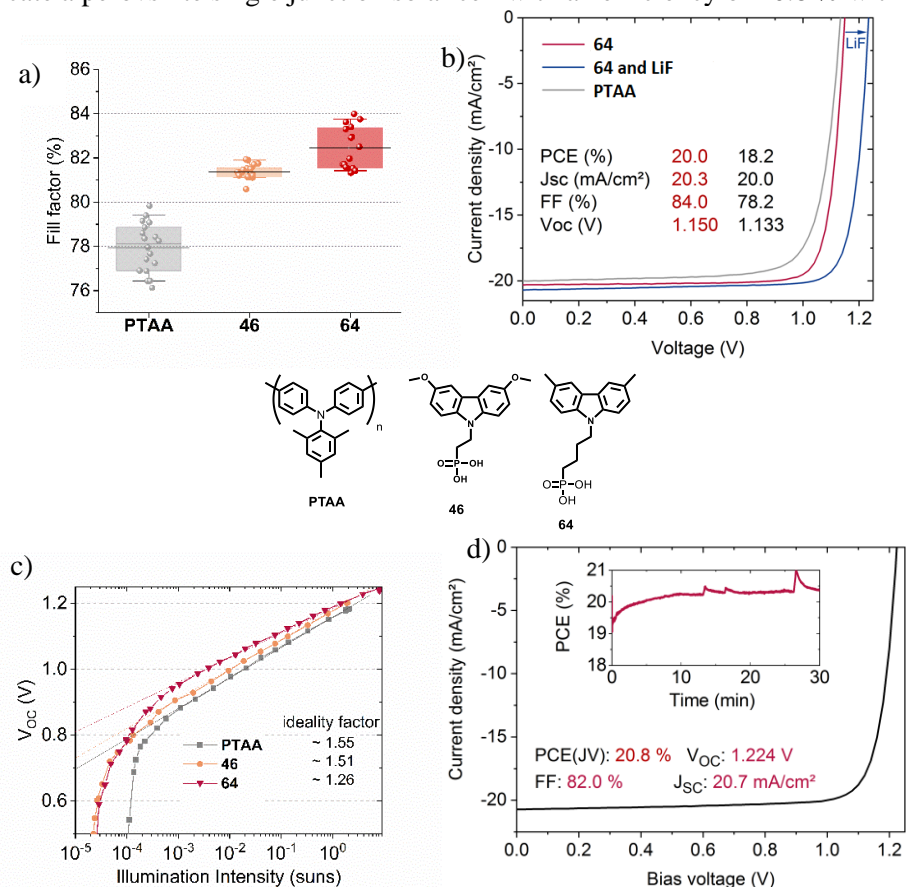


**Figure 3.42.** Analysis of *p-i-n* solar cells, showing of the benefits of **64** as the hole-selective contact: (a) comparison of fill factor values of PSCs with the stack glass/ITO/HTM/perovskite/C<sub>60</sub>/SnO<sub>2</sub>/Ag, triple-cation perovskite absorber with 1.68 eV band gap, all shown cells are made from the same perovskite precursor and contact processing batch; (b) *J-V* curves of the best cells of the batch in (A), and a *J-V* curve of a **64** cell from batch with LiF interlayer between C<sub>60</sub> and perovskite, reaching a V<sub>OC</sub> of 1.234 V; (c) intensity-dependent open-circuit voltage with linear fits (dashed lines); (d) *J-V* curve of the champion single junction cell based on **64** as the hole-selective layer and LiF/C<sub>60</sub>/SnO<sub>2</sub> on the electron-selective side, the inset shows a MPP track of that cell (spikes are from the unstable halogen lamp)

### 3.3.3.4. Versatility of SAM contact and tandem solar cell integration

In order to show the versatility of the new molecules, highly efficient perovskite solar cells with perovskite compositions other than CsMAFA were constructed using SAM approach. In addition to the “triple cation” composition utilized for the analysis above, a “double cation” MA<sub>0.05</sub>FA<sub>0.95</sub>Pb(I<sub>0.95</sub>Br<sub>0.05</sub>)<sub>3</sub>

(MAFA) absorber with a lower band gap of ca. 1.55 eV and a “single cation” (MAPbI<sub>3</sub>) absorber, which is fabricated by direct co-evaporation, were studied (Figure 3.43). Table 3.12 shows the corresponding device performance characteristics.

Perovskite processing by co-evaporation is highly attractive due to the large-area compatibility and absence of potentially harmful solvents for the fabrication. Utilizing **46** as the HTM works well with the co-evaporated MAPbI<sub>3</sub> perovskite absorber. The shown stabilized PCE of 19.6 % with over 1.14 V *V*<sub>OC</sub> is approaching the PCE of the best co-evaporated PSC to date and represents the highest reported value for p–i–n type devices, utilizing co-evaporation for the perovskite absorber [156, 175].

Recently, the highest PSC performances were reported for the MAFA double cation composition [21, 176]. Compared to the CsMAFA solar cells shown before, the MAFA cell has an advantage in higher current density due to the lower band gap of the composition, but still enables a relatively high *V*<sub>OC</sub>. Without detailed optimization, the MAFA absorber enabled a stabilized PCE of 21.1 % when utilizing **46** as the SAM forming HTM.

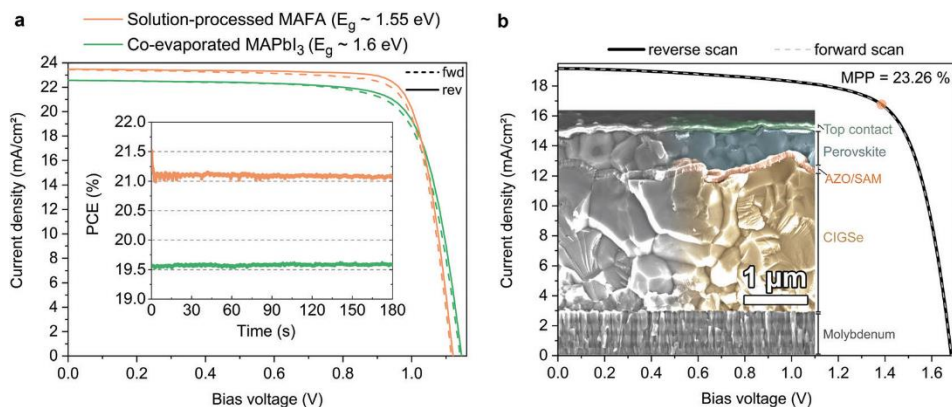


**Figure 3.43.** Display of the versatility of SAM contacts and tandem solar cell integration: (a) *J*-*V* curves under illumination of solar cells based on a solution processed “double cation” perovskite absorber (MAFA, orange line) and co-evaporated perovskite absorber (MAPbI<sub>3</sub>, green line), inset: Continuous MPP tracks of these cells; (b) *J*-*V* curve of a monolithic CIGSe/perovskite tandem solar cell (active area of 1.034 cm<sup>2</sup>) with **46** as HTM conformally covering the rough CIGSe bottom cell; the orange circle indicates the MPP at 23.26 %; inset: SEM image of the cross-section of a representative tandem device; the recombination contact consists of aluminium-doped zinc oxide, sputtered onto the CIGSe surface and covered by **46**

Furthermore, SAM approach is as well suitable for manufacturing PSCs on rough surfaces, which is essential for, e.g., CIGSe/perovskite tandem solar cells (Figure 3.43b). All-thin-film tandem solar cells pose an attractive strategy for cheap, versatile and flexible high-efficiency solar cells and are a promising route for the introduction of halide perovskites into industrial production. CIGSe enables thin-film solar cells with a suitable band gap for the use in perovskite-based tandem solar cells. However, the rough surface of the CIGSe makes it difficult to process the thin

HTM films that currently are used in efficient perovskite top cells. Recently, it has been demonstrated that the use of a  $\text{NiO}_x$  layer processed by atomic layer deposition (ALD) in combination with PTAA represents a CIGSe/perovskite compatible hole-transport layer that prevents shunting caused by the CIGSe roughness, enabling a 21.6 % efficient tandem cell [177]. SAM removes the need for an ALD step, since the self-assembly process works reliably even on rough surfaces by dipping the CIGSe bottom cell into a **46** solution. The perovskite layer was fabricated by solution-processing and the top contact layers by either evaporation or ALD/sputtering. The tandem solar cell prepared in such a way is shown in Figure 3.43b, which demonstrates a stabilized efficiency of 23.26 % on an area of  $1.03 \text{ cm}^2$ . The presented tandem cell surpasses the previous record [168] (22.4 %) in PCE and the area ( $0.04 \text{ cm}^2$  vs.  $1.03 \text{ cm}^2$  in this case). The simplicity of the tandem stack and the use of as-deposited CIGSe additionally suggest that SAM approach could be easily adopted in higher throughput fabrication.

**Table 3.12.** Photovoltaic parameters from  $J$ - $V$  scans under illumination in reverse scan direction as well as continuous MPP tracking; single cells with double cation MAFA and co-evaporated  $\text{MAPbI}_3$  perovskite and a CIGSe/perovskite (triple cation) tandem solar cell are presented; all cells use **46** as the HTM

Perovskite Device type	$J_{sc}$ [ $\text{mA} \times \text{cm}^{-2}$ ]	$V_{oc}$ [V]	FF [%]	PCE ( $J$ - $V$ ) [%]	PCE (MPP) [%]
Co-evaporated $\text{MAPbI}_3$ ; Single	22.6	1.145	76.8	19.8	19.6
Double cation MAFA; Single	23.5	1.120	80.6	21.2	21.1
Triple cation CsMAFA; Monolithic Tandem	19.17 (certified)	1.68 (certified)	71.9 (certified)	23.16	23.26 $\pm$ 0.75 (certified)

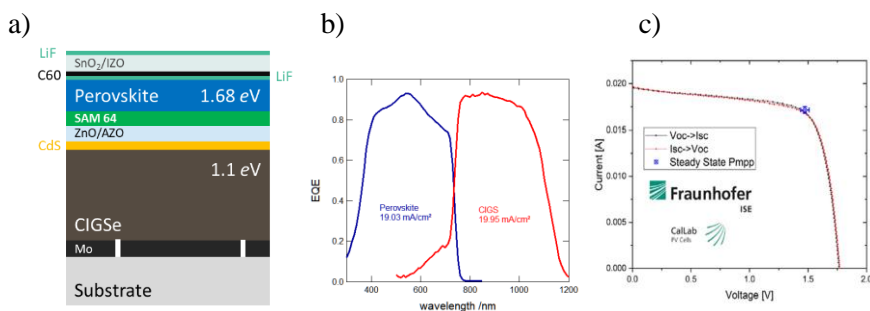


**Figure 3.44.** (a) Schematic stack of the perovskite/CIGSe tandem solar cell; (b) EQE spectrum of the constructed tandem device; (c) certified  $JV$  curve conducted at Fraunhofer ISE including the MPP of the perovskite/CIGSe tandem solar cell with the new HTM **64**



Recently, perovskite/CIGSe tandem devices containing dimethylcarbazole derivative **64** were as well constructed and investigated (Figure 3.44a, b). The tandem device stack is as follows, starting from the bottom: glass/Mo/CIGSe/CdS/i-ZnO/ZnO:Al/SAM **64**/perovskite/LiF/C60/SnO<sub>2</sub>/IZO/LiF+Ag; the perovskite composition used in the device was Cs<sub>0.05</sub>(MA<sub>0.22</sub>FA<sub>0.78</sub>)Pb<sub>1.1</sub>(I<sub>0.78</sub>Br<sub>0.22</sub>)<sub>3</sub>.

The best performing tandem cell with **64** was sent to the Fraunhofer ISE CalLab for independent certification (Figure 3.44c). With a V<sub>OC</sub> of 1.77 V, fill factor of 72 % and J<sub>SC</sub> of 19.6 mA×cm<sup>-2</sup>, the cell has a PCE of 24.98 %, when measuring from J<sub>SC</sub> to V<sub>OC</sub>, and was certified at the MPP with a PCE of 24.16 % with a designated area of 1.04 cm<sup>2</sup>. This PCE surpasses the previously highest certified perovskite/CIGSe tandem record by a cell of HZB [2] by ~1 % absolute and thus, sets a new world record in monolithic CIGSe/perovskite tandem solar cells.

In summary, the compatibility of the SAM with three different perovskite compositions, two different processing techniques (solution and vacuum process), two different oxides (ITO in the single junctions and Al-doped zinc oxide in the tandem) and two different substrate morphologies (rough and flat) strongly suggests that SAM hole-selective contacts represent a universal approach for perovskite-based photovoltaics.

### 3.3.3.5. Integration into monolithic perovskite/silicon tandem solar cells

In the following section, it has been demonstrated that the fast hole extraction capabilities of **64** in perovskite top cells help to achieve significantly higher FF, V<sub>OC</sub> and stability in monolithic tandem solar cells. A schematic stack of this solar cell is shown in Figure 47a. As previously reported [178], silicon hetero junction (SHJ) solar cell as the bottom cell was used, based on a 260 μm thick n-type float-zone Si wafer; the textured rear side enhances the near-infrared absorption, whereas the polished front side enables the deposition of spin-coated perovskite. The 20 nm of ITO serves as a recombination layer as well as the anchoring oxide for the SAMs [149]. The top cell with the Cs<sub>0.05</sub>(FA<sub>0.77</sub>MA<sub>0.23</sub>)<sub>0.95</sub>Pb(I<sub>0.77</sub>Br<sub>0.23</sub>)<sub>3</sub> perovskite absorber resembles the single-junction stack of ITO/HTM/Perovskite/LiF/C<sub>60</sub>/SnO<sub>2</sub>/IZO/Ag/LiF. Figure 3.45b shows a scanning electron microscope cross-section image of a part of the tandem solar cell. As SAM is just a single layer of molecules, it cannot be resolved with the SEM. Furthermore, a columnar growth of the perovskite on **64** is clearly visible.

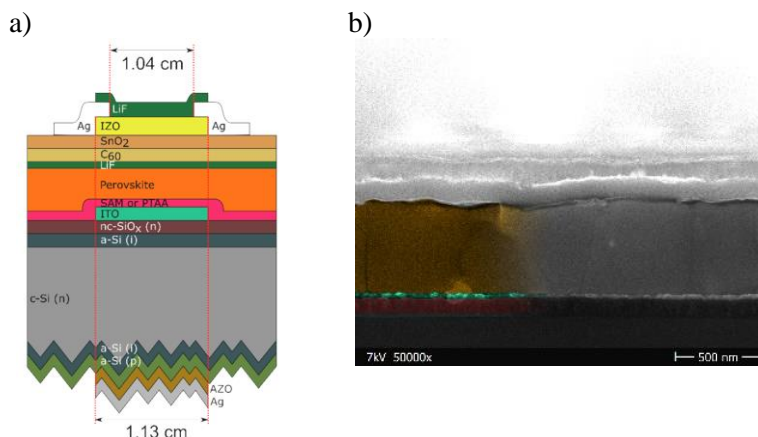


**Figure 3.45.** (a) Schematic stack of the monolithic perovskite/silicon tandem solar cell; (b) scanning electron microscope (SEM) image of a tandem cross-section with **64** as HTM

A comparison of the PCE of tandem solar cells measured by  $J$ - $V$  scans and MPP tracking for PTAA, **46** and **64** can be seen in Figure 3.46a, furthermore, distinguishing between cells with and without a LiF interlayer at the perovskite/ $C_{60}$  interface. Interestingly, with PTAA, the utilization of a LiF interlayer is not advantageous for the constructed PSCs, as it led to rapid degradation of the cells. Although the  $V_{OC}$  has indeed increased, the FF is lower, and together with a rapidly decreasing  $J_{SC}$ , it leads to a lower PCE. Without the interlayer, an average PCE of 25.25 % has been achieved. In contrast, the average efficiency of the tandem device with dimethoxycarbazole **46** was 26.21 %. The utilization of a LiF interlayer for **64** cells increased the  $V_{OC}$  but reduced the FF. Thus, both configurations reached a similar to **46** average PCE of 26.25 % and 26.41 %, respectively. However, with **64**, the number of devices with maximum PCEs of >29 % was higher than with **46**, mainly because of higher FF of up to 81 %. It is necessary to emphasize that these cells with an active area of slightly above 1 cm<sup>2</sup> do not feature a charge-collecting grid on the top contact. Furthermore, the  $V_{OC}$ s of up to 1.92 V (Figure 3.46c) are achieved, which is, to the best of knowledge, the highest  $V_{OC}$  shown for this type of solar cells.

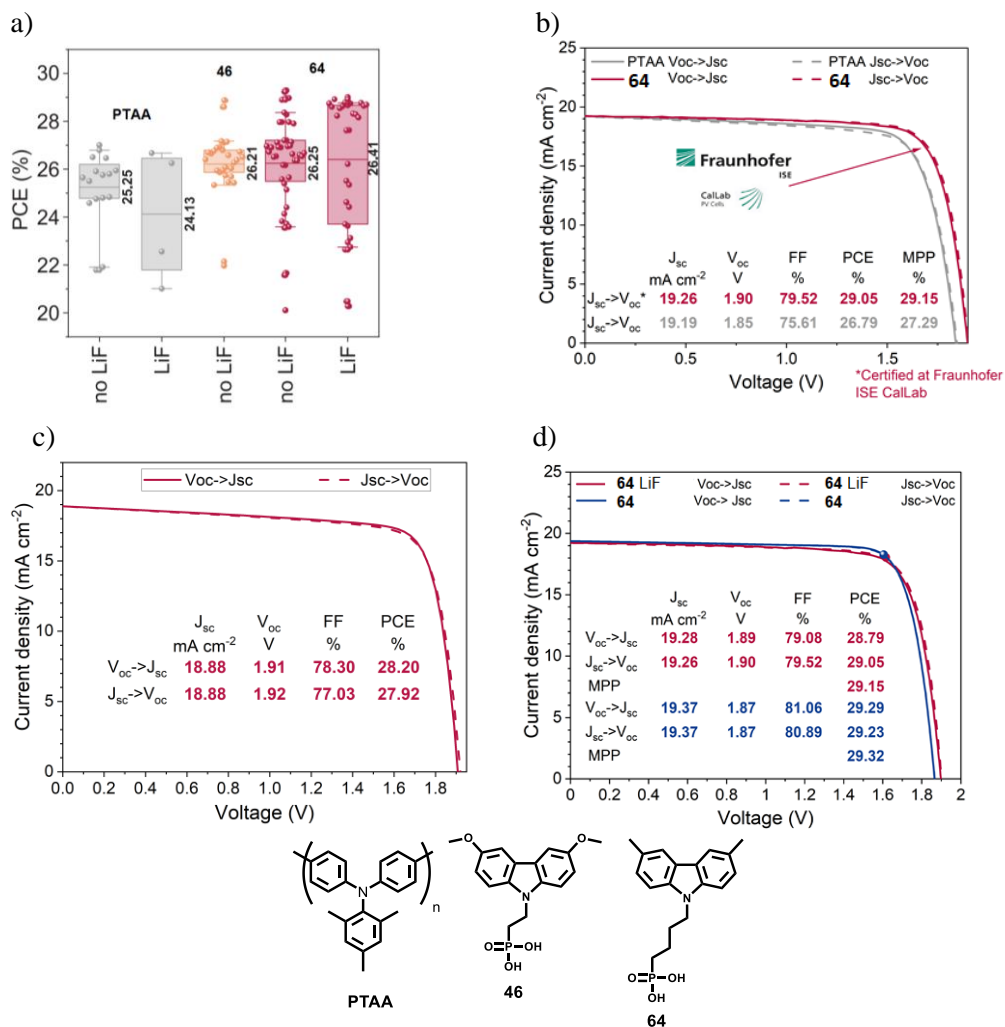


**Figure 3.46.** (a) Statistics of the PCE of several PTAA, **46** and **64** tandem solar cells from  $J$ - $V$ -scan and MPP-tracking; (b) certified  $J$ - $V$  curve conducted at Fraunhofer ISE including the MPP and the device parameters (red) in comparison to a tandem cell with PTAA (gray) as HTM; (c)  $J$ - $V$  of the monolithic perovskite silicon tandem solar cell with the new HTM **64**; to the best of knowledge, this is the highest  $V_{oc}$  for monolithic perovskite silicon tandem solar cells; (d) comparison of champion monolithic perovskite silicon tandem solar cells (**64**) with and without LiF interlayer; the  $J$ - $V$  of the cell with LiF interlayer was certified at Fraunhofer ISE; the higher  $V_{oc}$  but lower FF for cells with LiF interlayer is clearly visible

The best tandem cell with **64** was sent to the Fraunhofer ISE Callab for independent certification (Figure 3.46b). With a  $V_{oc}$  of 1.90 V, fill factor of 79.4 % and  $J_{sc}$  of 19.23 mA $\times$ cm<sup>-2</sup>, the cell has a PCE of 29.01 % when measuring from  $J_{sc}$  to  $V_{oc}$  and was certified at the MPP with a PCE of 29.15 % with a designated area of 1.04 cm<sup>2</sup>. This PCE surpasses the previously highest certified monolithic perovskite/silicon tandem openly reported by Kim et al. in literature by 3 % absolute

[169]. It as well exceeds the previous record of 28 % by a cell of Oxford PV [179] by more than 1 % absolute and thus sets a new world record in monolithic silicon/perovskite tandem solar cells. To date, this monolithic tandem cell additionally outperforms the most efficient four-terminal perovskite-based tandem solar cell [180]. It is on par with the best GaAs single cell at the same active area. Thus, this cell fuels the expectations that the theoretical maximum efficiency for silicon solar cells [181] of 29.43 % will be surpassed in the near future, paving the way towards PCEs over 30 %.

After the certification, more **64** containing tandem solar cells without LiF interlayer were fabricated, which showed similar average performance as with LiF. The champion cell showed a higher FF of 81 % and lower  $V_{oc}$  of 1.87 V than without LiF. Together with a  $J_{sc}$  of  $19.37 \text{ mA} \times \text{cm}^{-2}$ , this led to a PCE of 29.29 % and a stabilized efficiency of 29.32 % (Figure 3.46d).

### 3.3.3.6. Stability assessment

Compositions yielding the most promising results were as well tested for long-term stability under various conditions. In addition to the increased efficiencies of **46** based solar cells compared to PTAA, these devices as well demonstrate an increased stability. Figure 3.47a shows the time evolution of PCE under continuous MPP tracking for the investigated HTMs at simulated 1 sun AM 1.5G illumination without active sample cooling. The samples reach temperatures of at least 40 °C under operation. A slight advantage is evident for the **46** based devices after 11 h of operation (~3 % loss with **46**, ~6 % loss with PTAA and almost 12 % loss for **29**). A stronger difference is visible when increasing the stress on the solar cells, which is done by light soaking at open-circuit condition under 1 sun illumination, a condition in which high average density of charge-carriers is present in the device that can induce a quick degradation of the PSC [167]. The most notable differences occur in the time evolution of  $V_{oc}$ , as displayed in Figure 3.47b. PTAA-based solar cells show a substantial drop (60 mV amplitude) after two hours, while the  $V_{oc}$ s of all SAM-based cells remain virtually stable after an initial drop caused by increasing temperature. Interestingly, light soaking steadily improves the  $V_{oc}$  of **29** based samples. The quick degradation of PTAA-based cells can be attributed to a material-specific characteristic of the CsMAFA/PTAA contact that occurs under conditions with a high number of excess charge carriers and direct illumination of the PTAA, as observed in a recent work [177]. A previous study identified that a large number of excess charge carriers, as under illumination at open-circuit, leads to a lowered energetic threshold of ionic movement [167]. It can be hypothesized that the diffusion of iodine to the PTAA interface leads to the structural damage of PTAA [177]. In contrast, a SAM, being a chemically robust electrode modification with virtually no volume, is neither susceptible to structural damages nor to an accumulation of ions.

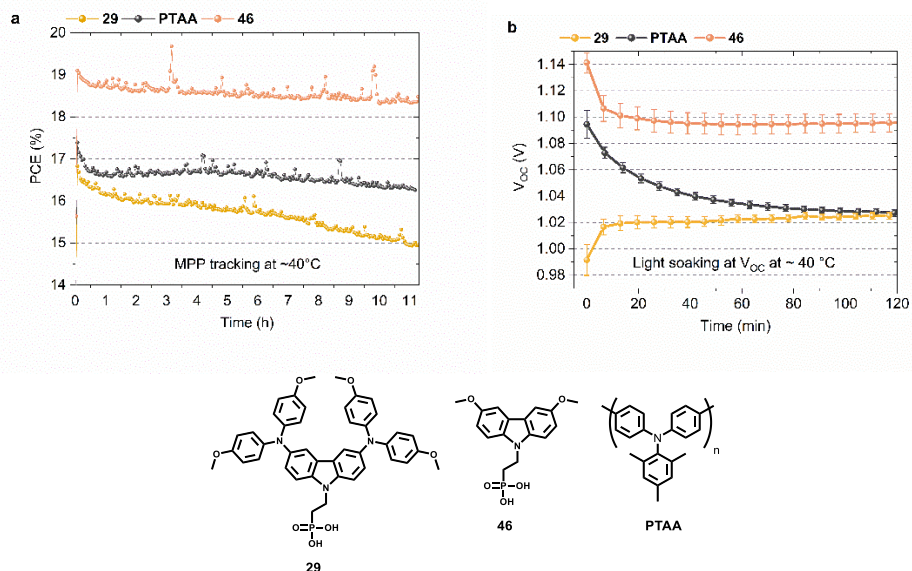


**Figure 3.47.** Stability assessments of PSCs based on the investigated HSCs in  $N_2$  atmosphere: (a) MPP tracking under continuous, simulated 1 sun AM 1.5G illumination of uncooled devices (reaching a temperature of  $\sim 40$  °C in operation); (b) time evolution of  $V_{oc}$  values of solar cells kept at open-circuit conditions under light-soaking at full sun illumination at  $\sim 40$  °C cell temperature (no active cooling); the values were extracted from  $J$ – $V$  scans every 6–8 min; the error bars show the standard deviation of these values across the individual cells (4 devices for **29**, 6 devices for PTAA, 3 devices for **46**)

The stability of different nonencapsulated tandem solar cells was measured as well (Figure 3.48). To track the degradation induced by either the top- or the bottom cell more carefully, a dichromatic LED setup using LEDs with 470 nm and 940 nm centre emission wavelengths and independent intensity calibration and recording was used. The degradation for the champion tandem cell showed 76 % of its initial efficiency (29.13 %) after 300 hours of continuous MPP tracking in ambient atmosphere at 25 °C. Substituting **64** with PTAA, the PCE decreased to 75 % of its initial PCE (25.9 %) after only 90 hours. The fast degradation was attributed to the combination of PTAA with the LiF interlayer.

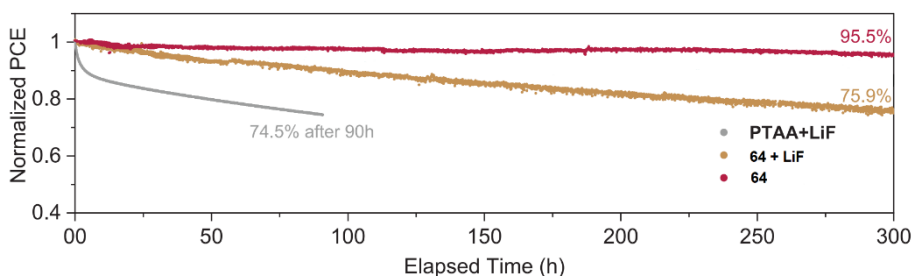


**Figure 3.48.** Long term MPP track using a dichromatic LED illumination of non-encapsulated solar cells in air at a controlled temperature of 25 °C; the data is normalized to the first 60 minutes of each individual track; the legend shows which HTM was used, whether the LiF-interlayer was used and which subcell was limiting

Cell with **64** as HTM without a LiF interlayer was additionally tracked to test the intrinsic stability of the HTM/perovskite combination. After 300 hours, the cell still operated at 95 % of its initial PCE. This result strongly suggested that the utilization of a LiF interlayer (at least in this specific architecture) reduced the stability. Comparing this result to the state-of-the-art stability tests of non-encapsulated tandem solar cells in ambient conditions, where the cells retained 90 % after 61 hours [182] and 92 % after 100 hours [183], the analysed tandem solar cell shows a superior operational stability.

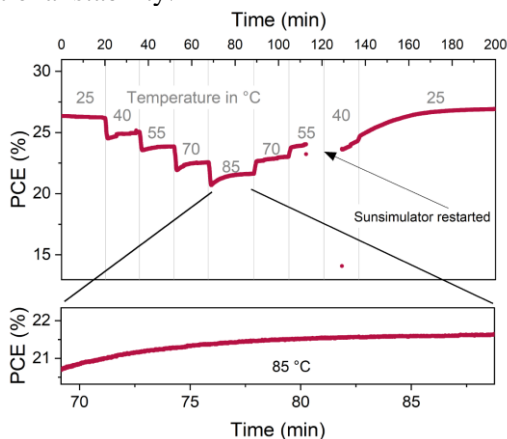


**Figure 3.49.** MPP track of a tandem solar cell with **64** (without LiF interlayer); the cell was illuminated with an AM1.5G spectrum (calibrated with a KG-3 filtered silicon reference cell, certified at Fraunhofer ISE); the cell was held for 15 minutes at 40 °C, 55 °C and 70 °C and for 20 minutes at 85 °C; due to a technical issue, the sun simulator needed to be restarted; however, the cell was still exposed to the elevated temperature

Besides the long-term stability measurements at 25 °C, an MPP track at elevated temperatures was conducted with a tandem cell containing dimethylcarbazole **64** (Figure 3.49). Following the procedure of Jost et al., the temperature was successively increased from 25 °C to 85 °C and back to 25 °C [184], and there was no loss in PCE after this 200 minute procedure.

### 3.3.3.7. Chapter summary

In summary, in this chapter, new simple molecules that form self-assembling monolayers were synthesized and integrated into inverted perovskite solar cells, enabling hole selective contacts with minimized non-radiative losses. The new SAMs can be deposited on transparent conductive oxides via spin-coating or by dipping the substrate into the solution, both yielding layers of comparable properties, combining high reproducibility and ease of fabrication. These SAMs outperform the polymer PTAA, the material that enabled the highest performing p-i-n PSCs to date, in efficiency, stability and versatility. With a standard triple-cation absorber, a maximum power conversion efficiency of 20.8 % and a  $V_{OC}$  of up to 1.15 V were demonstrated using SAM forming methylcarbazole HTM **64**. The results highlight that these carbazole-based compounds can combine all necessary features for lossless interfaces and are thus a compelling material class for future development of high-performance hole-selective contacts. In a light-soaking stress test at open circuit conditions, SAM-based PSCs showed a higher stability compared to PTAA-based cells. Integrating methoxycarbazole **46** as a SAM contact into a monolithic CIGSe/perovskite tandem solar cell demonstrated to create a hole-selective layer on a rough surface. This led to a stabilized, certified PCE of 23.26 % with facile device design on an active area of 1.03 cm<sup>2</sup>, surpassing the values achieved with a complex bilayer or mechanical polishing. Most importantly, the herein demonstrated solar cells are fabricated without additional passivation layers, additives or dopants. Monolithic perovskite/silicon tandem solar cells with an average power conversion efficiency of 28.5 % and a maximum certified PCE of 29.15 %, which sets a new record for this type of solar cells, were constructed using **64** self-assembling monolayer. Besides the increased PCE, a non-encapsulated cell in ambient air with **64** exhibited excellent stability, retaining 95 % of its initial efficiency after 300 h of continuous maximum power point tracking, under LED illumination. With the typical p-i-n hole-selective layer, PTAA, the cell degraded to 76 % of the initial efficiency after just 90 h.

## 4. METHODS AND MATERIAL

### 4.1. General methods

The  $^1\text{H}$  and  $^{13}\text{C}$  NMR spectra were taken on Bruker Avance III 400 (400 MHz for  $^1\text{H}$ , 100 MHz for  $^{13}\text{C}$ ) spectrometer at RT. All the data are given as chemical shifts in  $\delta$  (ppm).

The course of the reactions was monitored by TLC on ALUGRAM SIL G/UV254 plates and developed with UV light. Silica gel (grade 9385, 230–400 mesh, 60 Å, Aldrich) was used for column chromatography.

The elemental analysis was performed with an Exeter Analytical CE-440 elemental analyser, Model 440 C/H/N/.

Differential scanning calorimetry was performed on a Q10 calorimeter (TA Instruments) at a scan rate of  $10\text{ K}\times\text{min}^{-1}$  in the nitrogen atmosphere. The glass transition temperatures for the investigated compounds were determined during the second heating scan.

Thermogravimetric analysis was performed on a Q50 thermogravimetric analyser (TA Instruments) at a scan rate of  $10\text{ K min}^{-1}$  in the nitrogen atmosphere.

UV-Vis spectra were recorded on a Shimadzu UV-2600 spectrophotometer. Microcells with an internal width of 1 mm were used.

Optical microscopy experiments were conducted on Olympus BX-41 equipped with QImaging Go-3 camera.

The thickness of the films was measured using MarSurf WS1 white light interferometer. MS spectroscopy was done using Shimadzu LCMS 2020 SQ LC mass spectrometer.

#### *Photoelectrical measurements*

The solid state ionization potential of layers of the synthesized compounds was measured by the electron photoemission in the air method at the Institute of Chemical Physics, Vilnius University. The samples for the ionization energy measurement were prepared by dissolving materials in THF, and these solutions were coated on Al plates that were pre-coated with  $\sim 0.5\text{ }\mu\text{m}$  thick methylmethacrylate and methacrylic acid copolymers adhesive layer. The thickness of the transporting material layer was  $0.5\text{--}1\text{ }\mu\text{m}$ . Usually, the photoemission experiments are carried out in a vacuum, and high vacuum is one of the main requirements for these measurements. If the vacuum is not high enough, the sample surface oxidation and gas absorption are influencing the measurement results. In this case, however, the organic materials that were investigated were stable enough to oxygen, and the measurements could be carried out in the air. The samples were illuminated with monochromatic light from the quartz monochromator with deuterium lamp. The power of the incident light beam was  $(2\text{--}5)\times 10^{-8}\text{ W}$ . The negative voltage of  $-300\text{ V}$  was supplied to the sample substrate. The counter-electrode with the  $4.5\times 15\text{ mm}^2$  slit for illumination was placed at 8 mm distance from the sample surface. The counter-electrode was connected to the input of the BK2-16 type electrometer, working in the open input regime, for the photocurrent



measurement, the  $10^{-15}$ – $10^{-12}$  A strong photocurrent was flowing in the circuit under illumination. The  $I^{0.5} = f(h\nu)$  dependence was plotted. Usually, the dependence of the photocurrent on incident light quanta energy is well described by a linear relationship between  $I^{0.5}$  and  $h\nu$  near the threshold [185, 186]. The linear part of this dependence was extrapolated to the  $h\nu$  axis,  $I_p$  value was determined as the photon energy at the interception point.

The hole drift mobility was measured by xerographic time of flight of flight technique (XTOF) [187, 188] at the Institute of Chemical Physics, Vilnius University. The samples for the hole mobility measurements were prepared by spin-coating the solutions of the synthesized compounds or compositions of synthesized compounds with bisphenol-Z polycarbonate (Iupilon Z-200 from Mitsubishi Gas Chemical Co.) in weight ratio 1:1 on the polyester films with conductive Al layer. The layer thickness was in the range 5–11  $\mu\text{m}$ . The electric field was created by positive corona charging. The charge carriers were generated at the layer surface by illumination with pulses of nitrogen laser (pulse duration was 2 ns, wavelength 337 nm). The layer surface potential decreases as a result of pulse illumination that was up to 1–5 % of initial potential before the illumination. The capacitance probe that was connected to the wide frequency band electrometer measured the speed of the surface potential decrease  $dU/dt$ . The transit time  $t_t$  was determined by the kink on the curve of the  $dU/dt$  transient in double logarithmic scale. The drift mobility was calculated by the formula  $\mu = d^2/U_0 t_t$ , where  $d$  is the layer thickness,  $U_0$  is the surface potential at the moment of illumination.

XPS measurements were conducted with a non-monochromated Mg Ka excitation source and a ScientaOmicron Argus CU electron analyser in the Energy Materials In-Situ Laboratory (EMIL) of HZB. Core level peak fitting was performed with the free software fityk7. The number of Voigt peaks was determined by fitting all three datasets simultaneously with coupled width and shape parameters and increasing the number of peaks until the residuum was in the order of the background noise of the data. A linear background was included into the fit.

UPS measurements were conducted with the same equipment employing He I (21.22 eV) excitation. For measuring the secondary electron cutoff, a 10 V bias was applied to the substrate. The valence band onset was determined by the leading edge extrapolation method.

### *Device preparation*

Devices for the measurement of compounds **25**, **29**, **34**, **46–50**, **62**, **64** were prepared by the Prof. S. Albrecht Group at Helmholtz-Zentrum, Berlin. Patterned indium tin oxide glass substrates (25x25 mm, resistivity =  $15 \Omega \times \text{sq}^{-1}$ , nominal ITO thickness = 150 nm, patterned by Automatic Research GmbH) were cleaned sequentially for 15 min with a 2 % Mucosol solution in water (Schülke), water, Acetone and Isopropanol at  $\sim 40$  °C in an ultrasonic bath. After that, directly before HTM deposition, the substrates were treated in an UV-ozone cleaner for 15 min. UV treatment seemed crucial for achieving high reproducibility. All subsequent procedures were done in a nitrogen-filled glovebox (MBRAUN). All the spin-coating layer deposition steps were conducted in a nitrogen atmosphere. The hole

transport material PTAA ( $2 \text{ mg} \times \text{ml}^{-1}$  in toluene) was deposited using spin-coating (5000 rpm for 30 s), followed by annealing for 10 min at  $100 \text{ }^\circ\text{C}$ .

SAM powders were dissolved in anhydrous Ethanol at a concentration of  $1 \text{ mmol/l}$  and put into an ultrasonic bath for 15 min ( $30\text{--}40 \text{ }^\circ\text{C}$ ) before using. **46** ( $275.24 \text{ g/mol}$ ) was stored in ambient air, if stored otherwise before dissolving, penalties in performance were observed. The SAMs were prepared either by spincoating or dipping. When spin-coating,  $100 \text{ }\mu\text{l}$  of the solution was uniformly released onto the middle of the substrate, the lid was closed, and after  $\sim 5 \text{ s}$  resting, the spin-coating program (30 s at 3000 rpm) was started. Alternatively, a lower concentration of  $0.1 \text{ mmol/l}$  can be used if dropping the solution 2–3 times dynamically during the spinning program. After spin-coating, the substrates were heated at  $100 \text{ }^\circ\text{C}$  for 10 min. A washing step (with Ethanol) is possible but not necessary. For some perovskites, it might be beneficial to wash the substrates after heating, since it can change the contact angle of the perovskite (no significant performance differences were observed for all used perovskites in this work). SAMs by dipping were prepared by immersing the substrates into a  $0.1 \text{ mmol/l}$  solution for 2–12 h with subsequent heating at  $100 \text{ }^\circ\text{C}$  for 10 min. After heating, the dipped substrates were washed dynamically during a 4000 rpm, 30 s spin-coating program by dripping  $100\text{--}200 \text{ }\mu\text{l}$  of Ethanol 2–3 times onto them.

Triple-cation  $\text{Cs}_{0.05}(\text{MA}_{0.17}\text{FA}_{0.83})_{0.95}\text{Pb}(\text{I}_{0.83}\text{Br}_{0.17})_3$  (CsMAFA) perovskite film was formed according to the previously reported procedure. [128]  $100 \text{ }\mu\text{l}$  of the precursor was dripped onto the PTAA or SAM-covered substrates, and the solution was spread with a pipette tip across the substrate before starting the spinning program (5 s acceleration to 4000 rpm, 35 s steady at 4000 rpm). On PTAA,  $500 \text{ }\mu\text{l}$  of Ethyl Acetate as the antisolvent was dripped onto the perovskite 25 s after starting the spin-coating program (closed spincoater lid). On SAMs, either Ethyl Acetate or, in later optimized stages,  $200 \text{ }\mu\text{l}$  of Chlorobenzene or Anisole [189] were used as the antisolvent (with open lid during the program), dripped 5–7 s before the end of the spinning program (with 3500 instead of 4000 rpm spinning speed). The SAMs are chemically robust and allow the use of more types of antisolvents than PTAA. Further, the perovskite was annealed at  $100 \text{ }^\circ\text{C}$  for 30–60 min.

Double cation  $\text{MA}_5\text{FA}_{95}\text{Pb}(\text{I}_{95}\text{Br}_5)_3$  (MAFA) perovskite was prepared similarly to the CsMAFA perovskite with a respectively changed ratio of mixing the  $\text{MAPbBr}_3$  and  $\text{FAPbI}_3$  precursor solutions and 60 min annealing. The final perovskite solution was mixed just before spin-coating. Additionally,  $1.24 \text{ mol/l}$   $\text{MACl}$  solution in DMSO was mixed with the perovskite solution in a 5:95 volume ratio. The same spin-coating program as for CsMAFA was used with dripping  $300 \text{ }\mu\text{l}$  Chlorobenzene 5 s before the end of the program.

Single cation  $\text{MAPbI}_3$  was prepared by direct co-evaporation using a CreaPhys “PEROVap” deposition tool integrated into the inert glovebox (MBraun). The system includes a cooling shield inside the chamber, whose temperature was set to  $-25 \text{ }^\circ\text{C}$  for the entire process time. The rotation speed of the substrate holder was held constant at 10 rpm. Lead iodide and Methylammonium iodide were filled in two individual crucibles, and the chamber was evacuated. At reaching a base pressure of  $1\text{E-}6 \text{ mbar}$ , the sources were heated to  $240 \text{ }^\circ\text{C}$  ( $\text{PbI}_2$ ) and  $150 \text{ }^\circ\text{C}$  (MAI). Starting

from this point, the temperature was slightly adjusted until a stable rate of  $1.4 \text{ \AA s}^{-1}$  ( $\text{PbI}_2$ ) and  $3.5 \text{ \AA s}^{-1}$  (MAI) were obtained. The ratio was monitored using individual quartz crystal microbalances (QCM, Inficon) for each material.

After perovskite deposition, 23 nm  $\text{C}_{60}$  and 8 nm BCP were thermally evaporated in a MBRAUN ProVap 3G at a base pressure of  $1\text{E-}6$  mbar with an evaporation rate of  $0.1\text{--}0.18 \text{ \AA/s}$ . For completing the device, 100 nm Cu or Ag was thermally evaporated through a shadow mask. The overlap of the substrate's ITO with the Cu stripe defines the active area of  $0.16 \text{ cm}^2$  (cross-checked with an optical microscope).

Some devices, such as the one sent for certification, were encapsulated with a cover glass and a two-component self-curing epoxy glue (5-min epoxy, R&G Faserverbundwerkstoffe GmbH). After encapsulation, an antireflective coating (100 nm NaF) was thermally evaporated onto the glass substrates, which increased the short-circuit current density distinctly more for **46** devices than for PTAA and **29** devices.

#### *CIGSe/perovskite tandem solar cell*

CIGSe devices were prepared in the Prof. S. Albrecht group at Helmholtz-Zentrum, Berlin. The CIGSe bottom cell was fabricated in a multi-step thermal evaporation on a glass substrate with RbF surface treatment. The p-type back contact is made of sputtered Molybdenum. The recombination contact consists of 10 nm sputtered i-ZnO and 140 nm ZnO:Al (AZO). After completion, the surface was rinsed with Ethanol and treated with UV-Ozone for 15 min, before submersing the CIGSe bottom cell into a 0.1 mmol/l **46**, **64**/Ethanol solution overnight. Spin-coating 1 mmol/l **46**, **64** solution once or 0.1 mmol/l solution three times as well yielded  $>20\%$ -efficient tandem cells. Subsequently, the bottom cell was heated at  $100 \text{ }^\circ\text{C}$  for 10 min in a  $\text{N}_2$ -filled glovebox, before proceeding the CsMAFA perovskite processing on top as described above.

After perovskite annealing, 20 nm  $\text{C}_{60}$  was thermally evaporated, and 20 nm of  $\text{SnO}_2$  processed on top at a substrate temperature of  $80 \text{ }^\circ\text{C}$  via atomic layer deposition (ALD, Arradiance GEMStar) to form a buffer layer for the IZO sputtering.  $\text{SnO}_2$  precursors were tetrakis(dimethylamino)tin(IV) (TDMASn) and water. The IZO top electrode was deposited by RF sputtering from 10 % wt ZnO and 90 % wt  $\text{In}_2\text{O}_3$  target. For contacting the electrode, 100 nm thick Ag frame was thermally evaporated through a shadow mask and 100 nm LiF as the anti-reflective coating. After device completion, the tandem cell was manually scribed around the Ag frame, since the AZO recombination and Molybdenum back contact were both processed on the full bottom cell area.

#### *Silicon solar cell preparation*

Silicon solar cell preparation was done in the Prof. S. Albrecht group at Helmholtz-Zentrum, Berlin. The silicon heterojunction-bottom cell was fabricated on a  $260 \text{ }\mu\text{m}$  thick,  $\sim 3 \text{ ohm cm}^{-1}$  polished FZ  $\langle 100 \rangle$  n-type crystalline silicon (c-Si) wafer in a rear junction configuration. The front surface of the wafer was left polished by capping with the plasma enhanced chemical vapour deposition

(PECVD) deposited SiO<sub>2</sub> prior to the wet texturing to obtain random pyramids with <111> facets. After removal of the capping in HF, another final RCA clean and HF dip (1 % dilution in water) were done, and an approx. -5 nm thick, intrinsic (i) amorphous silicon (a-Si:H) layer stack was grown on both sides of the c-Si wafer in order to passivate the c-Si surface. On the textured rear-side, an approx. -5-nm thick, p-doped a-Si:H layer stack was deposited to form the hole contact (junction). On the polished front-side, a 95-nm thick (20-nm thick for single-junction reference cells), n-doped nanocrystalline silicon oxide layer (nc-SiOx:H) with a refractive index, *n*, of 2.7 at 633 nm was used as the electron contact of the SHJ bottom cell and the optical intermediate layer between the top and the bottom cells. The a- and nc-Si layers were deposited with the Applied Materials (AKT1600) plasma enhanced chemical vapour deposition cluster tool. In order to contact the bottom cell, a ZnO:Al/Ag layer stack was deposited on the textured rear-side, and a 20 nm (70-nm thick for single-junction references) thick ITO layer was deposited on the polished front-side on top of the nc-SiOx:H interlayer. Both depositions were DC-sputtered in an in-line sputter tool from Leybold Optics using Ar/O<sub>2</sub> gas mixtures. For the ITO, a tube target with 95/5 doping ratio and for the AZO, a tube target with 1 % Al<sub>2</sub>O<sub>3</sub> in ZnO was used. Both contact-layer stack of the silicon were deposited using aligned shadow masks with an opening of 1.13 x 1.13 cm<sup>2</sup>. For single-junction reference cells, an Ag grid was screen printed on top of the front ITO.

#### *Preparation of tandem solar cells*

Tandem solar cells were prepared in the Prof. S. Albrecht group at Helmholtz-Zentrum, Berlin. The same perovskite deposition as described above was conducted on the silicon bottom cells. As indicated, some cells included a 1 nm LiF interlayer between the 18 nm C<sub>60</sub> and perovskite, deposited via thermal evaporation. Subsequently, 20 nm SnO<sub>2</sub>, 100 nm IZO (Roth&Rau MicroSys 200 PVD) are deposited by ALD and sputtering. For sputtering, the 2 inch ceramic target consisted of 90 % wt. In<sub>2</sub>O<sub>3</sub> and 10 % wt. ZnO. At a RF-power of 70 W, the cells oscillated under the target to have a uniform deposition. 0.2 % vol O<sub>2</sub> was added to the chamber. A 100 nm silver frame was evaporated to collect the charge carriers without the need of grid fingers. Lastly, 100 nm LiF was evaporated as an antireflective coating by thermal evaporation. The active area is defined by the metal frame and is slightly larger than 1 cm<sup>2</sup>.

#### *Solar cell characterization*

Solar cell characterization was done in the Prof. S. Albrecht group at Helmholtz-Zentrum, Berlin. Current-voltage characteristics under 1 sun equivalent illumination were recorded using a Wavelabs Sinus-70 LED class AAA sun simulator in the air, calibrated with a filtered KG3 Silicon reference solar cell certified by Fraunhofer ISE. J-V scans were performed as 2-point measurements with a Keithley 2400 SMU (4-point measurement with Keithley 2600 for the tandem cell), controlled by a measurement control program written in LabView. The single junctions were not masked during measurement (due to small differences between JSC from integrated EQE and J-V). The voltage values are swept in 20 mV steps

with an integration time of 40 ms per point and settling time of 20–40 ms after the voltage application (maximum voltage sweep speed of 250 mV/s). EQE spectra were recorded with an Oriel Instruments QEPVSI-b system with a Newport 300 W xenon arc lamp, controlled by TracQ-Basic software. The white light was filtered into monochromatic light by a Newport Cornerstone 260 monochromator with a 10 nm increment and chopped into a frequency of 78 Hz before being conducted to the solar cell surface via optical fibers. The system is calibrated using a Si reference cell with known spectral response before every measurement. The electrical response of the device under test is measured with a Stanford Research SR830 Lock-In amplifier (time constant of 0.3 s) and evaluated in TracQ. The typical short-circuit current mismatch between integrated external quantum efficiency times AM 1.5G irradiance and values from J-V scans is around 1 %. For the Urbach energy estimation, the monochromator step size is reduced to 2 nm, and Lock-In integration time is increased to 1 s per increment.

The temperature during continuous MPP tracking was measured with a thermocouple attached to the sample's glass surface. A spectral mismatch  $M^6$  for the used solar simulator was calculated with typical CsMAFA and MAFA EQE spectra, the spectral response of the calibrated reference cell and the spectrum of the solar simulator. The small deviations from 1 ( $M = 0.997$  for CsMAFA and 1.005 for MAFA) are within the measurement error margins during J-V characterizations; thus, the measured  $J_{SC}$  values were not corrected by  $1/M$ . No pre-conditioning protocols were applied. For some cells, there has been observed a slight rising trend in  $V_{OC}$  upon multiple J-V scans (or some minutes of light-soaking until thermodynamic stabilization). Typically, the PCE value of the PSCs saturates at higher values a few days after perovskite processing.

The pseudo-JVs were deduced from the intensity-dependent QFLS or  $V_{OC}$  measurements. This was done by calculating the dark-current density from the generated current density at a given light intensity in equivalent suns, e.g., 1 sun corresponds to  $22.0 \text{ mA} \times \text{cm}^{-2}$ , 1 % of a sun to  $0.220 \text{ mA} \times \text{cm}^{-2}$ . The obtained dark current was then plotted against the measured QFLS or  $V_{OC}$  at the given light intensity to create a transport/series resistance-free dark JV-curve. This curve was then shifted to the  $J_{SC}$  in the JV-measurement to create the pseudo-JV curve allowing to read of the pseudo- (or implied) FF and  $V_{OC}$  of the measured partial cell stack (e.g., the neat film or perovskite/transport layer junction) or the complete cell. It should be noted that the implied FF is only impacted by the non-radiative (and radiative) recombination processes in the studied sample but not by charge transport or resistive losses that are induced by the active layer or the transport layers and resistances (e.g., the ITO sheet resistance).

#### **4.2. Film preparation for the long-term stability testing of oxidized HTMs**

Corning Glass 0215 substrates were cleaned by sonication in 2 % Hellmanex water solution for 30 min. After rinsing with deionised water and ethanol, the substrates were further cleaned by sintering at 500 °C for 30 min and left to cool down to room temperature.

The investigated oxidized charge transporting materials with bis(trifluoromethane) sulfonimide lithium salt, 4-*tert*-butylpyridine and tris(2-(1*H*-pyrazol-1-yl)-4-*tert*-butylpyridine)cobalt(III) tri[bis(trifluoromethane)sulfonimide] additives have been dissolved in acetonitrile (spiro[TFSI], spiro[TFSI]<sub>2</sub>) or 2-butanone (V862[TFSI], V862[TFSI]<sub>2</sub>, V886[TFSI] and V886[TFSI]<sub>2</sub>) and immediately spin-coated onto the glass substrates. Chlorobenzene was not used in the spin-coating procedure due to the insufficient solubility of the oxidized materials and poor quality of obtained films on the glass substrates. The concentrations of the additives and spin-coater parameters are identical to those in literature [22]. The thickness of the films was measured to be ~70 nm. The prepared films have been encapsulated under inert atmosphere using a second glass substrate and UV curable epoxy (Ossila Ltd., UK) for edge sealing. Care has been taken to avoid contact between edge sealant and investigated materials, as epoxy dissolves the film of HTM. The samples have been kept at RT and 100 °C for 70 days, and UV-vis spectra were recorded periodically. MS samples of the investigated films, after 70 days at 100 °C, have been prepared by breaking open encapsulated sample and dissolving the films with acetonitrile.

*Preparation of perovskite films containing caesium Cs<sub>0.05</sub>(MA<sub>0.17</sub>FA<sub>0.83</sub>)<sub>0.95</sub>Pb(I<sub>0.83</sub>Br<sub>0.17</sub>)<sub>3</sub> and analogue without caesium MA<sub>0.17</sub>FA<sub>0.83</sub>Pb(I<sub>0.83</sub>Br<sub>0.17</sub>)<sub>3</sub>*

The perovskite precursor films were deposited from a precursor solution containing FAI 0.0017 g (0.1 M), PbI<sub>2</sub> 0.051 g (0.11 M), MABr 0.002 g (0.02 M) and PbBr<sub>2</sub> 0.007 g (0.02 M) in anhydrous DMF:DMSO (4:1 volume ratio) (1 ml). According to the article, this composition contains a lead excess as reported elsewhere [128, 190]. Then, CsI, predissolved as a 0.15 M stock solution in DMSO, was added to the mixed perovskite precursor to achieve the desired triple cation composition [22]; in the samples without Cs this step was omitted.

The perovskite solution was spin coated in a two-step program at 1000 and 6000 rpm for 10 and 25 s, respectively. During the second step, 200 µl of chlorobenzene was poured on the spinning substrate 5 s prior to the end of the program. Films with Cs-containing perovskite turned dark immediately after spin coating. The substrates were then annealed at 100 °C for 1 h in the argon atmosphere.

*Preparation of MAPbI<sub>3</sub> perovskite films*

The MAPbI perovskite precursor solutions were prepared by solubilizing the mixture of PbI<sub>2</sub> 0.092 g (0.1 M) and CH<sub>3</sub>NH<sub>3</sub>I 0.032 g (0.1 M) in DMF 2 ml. The perovskite solution was spin coated in a two-step program at 1000 and 6000 rpm for 10 and 25 s, respectively. Then, the substrates were annealed at 100 °C for 1 h.

*Preparation of FA<sub>0.83</sub>Cs<sub>0.17</sub>Pb(I<sub>0.83</sub>Br<sub>0.17</sub>)<sub>3</sub> perovskite films*

FACs perovskite was made according to the publication [19]. A solution of precursor was prepared with caesium iodide 0.013 g (0.025M), lead bromide 0.021 g (0.028 M), formamadinium iodide 0.041 g (0.12 M) and lead iodide 0.108 g

(0.117 M). Precursors were dissolved in solution (2 ml) of DMF and DMSO (4:1 volume ratio) by stirring at 70 °C for 15 minutes. Precursor solution was spread onto the substrates and spin coated at 1000 rpm for 10 s (1000 rpm $\times$ s<sup>-1</sup> ramp), followed immediately by 6000 rpm for 35 s. 10 seconds before the end of spin coating, the films were solvent quenched with 100  $\mu$ l of anhydrous anisole. Substrates were annealed at 100 °C for 15 minutes. All spin coating occurred at 30–40 % relative humidity.

#### *Preparation of MAPbBr<sub>3</sub> perovskite films*

MAPbBr<sub>3</sub> film was deposited using 1-step deposition method. 0.367 g (0.5 M) PbBr<sub>2</sub> precursor solution was prepared in 2 ml of DMF and DMSO mixture (4:1 volume ratio) without stirring at 80 °C for 20 minutes until completely dissolved. After cooling down at room temperature, this solution was mixed with 0.111 g (0.5 M) of MABr powder to obtain the final solution. The perovskite solution was spin coated in a two-step program at 1000 and 4000 rpm for 10 and 40 s, respectively. The substrates were then annealed at 100 °C for 3 min to obtain shiny and homogenous orange film [191].

#### *HTM film preparation for stability testing with various perovskites*

The investigated oxidized charge transporting material spiro[TFSI]<sub>2</sub> (0.04 g) has been dissolved in acetonitrile (2 ml) and immediately spin-coated at 2000 rpm for 20 s onto the layer formed from different perovskites. Spiro-MeOTAD (0.027 g) has been dissolved in chlorobenzene (2 ml) and immediately spin-coated onto the layer formed from different perovskites via spin coating at 2000 rpm for 20 s.

The thickness of the films was measured to be ~50 nm. All prepared films have been encapsulated under inert atmosphere using a second glass substrate and UV curable epoxy (Ossila Ltd., UK) for edge sealing. Care has been taken to avoid contact between edge sealant and investigated material, as epoxy dissolves the HTM film. The samples have been kept at RT in the dark and under ambient light as well as at 100 °C in the dark for 56 days, and UV-Vis absorption spectra were recorded periodically.

#### *Influence of individual perovskite components on the stability of spiro[TFSI]<sub>2</sub> films*

For the experiments involving interaction between films of oxidized charge transporting material spiro[TFSI]<sub>2</sub> and organic cations, the appropriate organic cation (FAI 0.042 g, 0.5 M or MAI 0.039 g, 0.5 M or MABr 0.028 g, 0.5 M) dissolved in 0.5 ml of the mixture of H<sub>2</sub>O/EtOH (1:1 volume ratio) was deposited on top of HTM via spin coating at 2000 rpm for 20 s. A mixture of ethanol and water was used as a solvent as not to dissolve the layer of spiro[TFSI]<sub>2</sub> that has been already deposited.

#### *Qualitative determination of I<sub>2</sub> in solution*

6 mg of spiro[TFSI]<sub>2</sub> was dissolved in 1 ml of acetonitrile, 3 mg of FAI or MAI were added, and the solution changed colour from dark red to yellow. 0.1 ml of

the prepared sample was added to 1 ml of 4 % starch solution colouring it in purple, indicating that iodine was formed during the reaction.

*Preparation of the solutions for the experiments of spiro[TFSI]<sub>2</sub> reduction with organic cations, monitored via UV-vis absorption spectrometry*

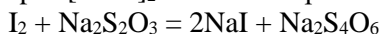
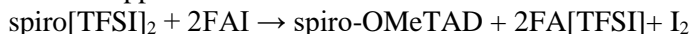
100 ml of 10<sup>-4</sup> M (0.01 mmol) spiro[TFSI]<sub>2</sub> solution in acetonitrile was divided into four 25 ml volumetric flasks. In order for the spiro[TFSI]<sub>2</sub> to react fully, two equivalents of MAI (0.0025 mmol×158.97 g/mol×2= 0.794 mg), FAI (0.0025 mmol×171.97 g/mol×2 = 0.85985 mg) or MABr (0.0025 mmol×111.97 g/mol×2= 0.55985 mg) were calculated. Stock solution with 5-fold excess of appropriate halide was prepared in 1 ml of acetonitrile, and 0.2 ml of the solution was added to the spiro[TFSI]<sub>2</sub> sample; UV-Vis spectra were recorded before and after the addition of the halide solution.

When 0.2 ml of FAI solution was added to the spiro[TFSI]<sub>2</sub> sample, the colour of the sample faded. UV was recorded before and after the reaction.

### **4.3. Determination of iodine content in the mixtures of spiro[TFSI]<sub>2</sub> and FAI by iodometric titration**

#### *General procedure*

0.01 N solution of Na<sub>2</sub>S<sub>2</sub>O<sub>3</sub> in water was prepared using Na<sub>2</sub>S<sub>2</sub>O<sub>3</sub>×5H<sub>2</sub>O fixanal. The sample of spiro[TFSI]<sub>2</sub> is dissolved in 1 ml of acetonitrile (dark red solution), 5 mg (0.029 mol) of FAI is added to the solution, and it changes the colour to yellow. The solution is diluted with 2 ml of H<sub>2</sub>O, and 5 drops of 4 % starch solution are added, turning the starch suspension dark purple. The sample is titrated with the prepared sodium thiosulphate solution until the violet colour of the starch suspension disappears.



#### *Experiment 1*

The violet colour of the sample disappears after 0.71 ml of sodium thiosulphate solution was used for titration.

The amount of sodium thiosulphate in 250 ml of 0.01 N solution was:

$$m = 0.01 \text{ N} \times 124.09 \text{ g/eq} \times 0.25 \text{ l} = 0.310225 \text{ g}$$

0.71 ml of sodium thiosulphate 0.01 N solution used in titration is:

$$m = 310.225 \text{ mg} \times 0.71 \text{ ml} / 250 \text{ ml} = 0.881 \text{ mg} (0.00355 \text{ mmol})$$

According to the reaction equation, 0.00355 mmol of spiro[TFSI]<sub>2</sub> or m=0.00355×1785.77 g/mol= 6.34 mg have reacted with FAI. There has been used 6.45 mg of spiro[TFSI]<sub>2</sub>; therefore, X<sub>1</sub>=6.34 mg×100 %/6.45 mg=98.28 % of the starting material have been used up in the reaction.

#### *Experiment 2*

The violet colour of the sample disappears after 0.7 ml of sodium thiosulphate solution was used for titration. The amount of sodium thiosulphate in 250 ml of 0.01 N solution was:

$$m = 0.01 \text{ N} \times 124.09 \text{ g/eq} \times 0.25 \text{ l} = 0.310225 \text{ g}$$

0.7 ml of sodium thiosulphate 0.01 N solution used in titration is:



$m = 310.225 \text{ mg} \times 0.7 \text{ ml} / 250 \text{ ml} = 0.87 \text{ mg} (0.00349 \text{ mmol})$

According to the reaction equation, 0.00349 mmol of spiro[TFSI]<sub>2</sub> or  $m = 0.00349 \times 1785.77 \text{ g/mol} = 6.25 \text{ mg}$  have reacted with FAI. There has been used 6.34 mg of spiro[TFSI]<sub>2</sub>; therefore,  $X_2 = 6.25 \text{ mg} \times 100 \% / 6.34 \text{ mg} = 98.58 \%$  of the starting material have been used up in the reaction.

#### *Experiment 3*

The violet colour of the sample disappears after 0.72 ml of sodium thiosulphate solution was used for titration. The amount of sodium thiosulphate in 250 ml of 0.01 N solution was:

$m = 0.01 \text{ N} \times 124.09 \text{ g/eq} \times 0.25 \text{ l} = 0.310225 \text{ g}$

0.72 ml of sodium thiosulphate 0.01 N solution used in titration is:

$m = 310.225 \text{ mg} \times 0.72 \text{ ml} / 250 \text{ ml} = 0.89 \text{ mg} (0.0036 \text{ mmol})$

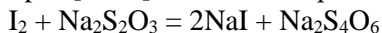
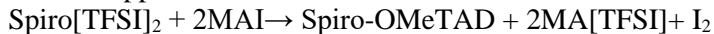
According to the reaction equation, 0.0036 mmol of spiro[TFSI]<sub>2</sub> or  $m = 0.0036 \times 1785.77 \text{ g/mol} = 6.42 \text{ mg}$  have reacted with FAI. There has been used 6.52 mg of spiro[TFSI]<sub>2</sub>; therefore,  $X_3 = 6.42 \text{ mg} \times 100 \% / 6.52 \text{ mg} = 98.6 \%$  of the starting material have been used up in the reaction.

The experiment was repeated 3 times in total and  $X_1 = 98.28 \%$ ;  $X_2 = 98.58 \%$ ,  $X_3 = 98.6 \%$  gives  $X_{\text{average}} = 98.48 \pm 0.18 \%$ , indicating a good correlation between amount of spiro[TFSI]<sub>2</sub> used and iodine produced during reaction as well as proving the validity of the proposed reaction that takes place between spiro[TFSI]<sub>2</sub> and FAI.

#### **4.4. Determination of iodine content in the mixtures of spiro[TFSI]<sub>2</sub> and MAI by iodometric titration**

##### *General procedure*

0.01 N solution of Na<sub>2</sub>S<sub>2</sub>O<sub>3</sub> in water was prepared using Na<sub>2</sub>S<sub>2</sub>O<sub>3</sub> × 5H<sub>2</sub>O fixanal. Sample of spiro[TFSI]<sub>2</sub> is dissolved in 1 ml of acetonitrile (dark red solution), 5 mg (0.031 mol) of MAI are added to the solution, and it changes colour to yellow. The solution is diluted with 2 ml of H<sub>2</sub>O, and 5 drops of 4 % starch solution are added, turning the starch suspension dark purple. The sample is titrated with the prepared sodium thiosulphate solution until the violet colour of the starch suspension disappears.



##### *Experiment 1*

The violet colour of the sample disappears after 0.71 ml of sodium thiosulphate solution was used for titration.

The amount of sodium thiosulphate in 250 ml of 0.01 N solution was:

$m = 0.01 \text{ N} \times 124.09 \text{ g/eq} \times 0.25 \text{ l} = 0.310225 \text{ g}$

The amount of sodium thiosulphate in 0.71 ml of 0.01 N solution was:

$m = 310.225 \text{ mg} \times 0.71 \text{ ml} / 250 \text{ ml} = 0.881 \text{ mg} (0.00355 \text{ mmol})$

According to the reaction equation, 0.00355 mmol of spiro[TFSI]<sub>2</sub> or  $m = 0.00355 \times 1785.77 \text{ g/mol} = 6.34 \text{ mg}$  have reacted with MAI. There has been used

6.37 mg of spiro[TFSI]<sub>2</sub>; therefore,  $X_1 = 6.34 \text{ mg} \times 100 \% / 6.37 \text{ mg} = 99.52 \%$  of the starting material have been used up in the reaction.

#### Experiment 2

The violet colour of the sample disappears after 0.73 ml of sodium thiosulphate solution was used for titration.

The amount of sodium thiosulphate in 250 ml of 0.01 N solution was:

$$m = 0.01 \text{ N} \times 124.09 \text{ g/eq} \times 0.25 \text{ l} = 0.310225 \text{ g}$$

The amount of sodium thiosulphate in 0.73 ml of 0.01 N solution was:

$$m = 310.225 \text{ mg} \times 0.73 \text{ ml} / 250 \text{ ml} = 0.90 \text{ mg} (0.00365 \text{ mmol})$$

According to the reaction equation, 0.00365 mmol of spiro[TFSI]<sub>2</sub> or  $m = 0.00365 \times 1785.77 \text{ g/mol} = 6.51 \text{ mg}$  have reacted with MAI. There has been used 6.62 mg of spiro[TFSI]<sub>2</sub>; therefore,  $X_2 = 6.51 \text{ mg} \times 100 \% / 6.62 \text{ mg} = 98.31 \%$  of the starting material have been used up in the reaction.

#### Experiment 3

The violet colour of the sample disappears after 0.71 ml of sodium thiosulphate solution was used for titration.

The amount of sodium thiosulphate in 250 ml of 0.01 N solution was:

$$m = 0.01 \text{ N} \times 124.09 \text{ g/eq} \times 0.25 \text{ l} = 0.310225 \text{ g}$$

The amount of sodium thiosulphate in 0.71 ml of 0.01 N solution was:

$$m = 310.225 \text{ mg} \times 0.71 \text{ ml} / 250 \text{ ml} = 0.881 \text{ mg} (0.00355 \text{ mmol})$$

According to the reaction equation, 0.00355 mmol of spiro[TFSI]<sub>2</sub> or  $m = 0.00355 \times 1785.77 \text{ g/mol} = 6.34 \text{ mg}$  have reacted with MAI. There has been used 6.49 mg of spiro[TFSI]<sub>2</sub>; therefore,  $X_3 = 6.34 \text{ mg} \times 100 \% / 6.49 \text{ mg} = 97.68 \%$  of the starting material have been used up in the reaction.

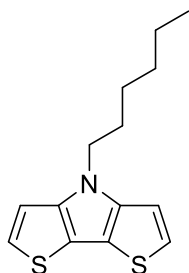
The experiment was repeated 3 times in total and  $X_1 = 99.52 \%$ ;  $X_2 = 98.31 \%$ ,  $X_3 = 97.68 \%$  gives  $X_{\text{average}} = 98.49 \pm 0.91 \%$ , indicating a good correlation between amount of spiro[TFSI]<sub>2</sub> used and iodine produced during the reaction as well as proving the validity of the proposed reaction that takes place between spiro[TFSI]<sub>2</sub> and MAI.

## 4.5. Materials

All reagents were purchased from TCI Europe or Aldrich. The organic cations, methylammonium iodide (MAI), formamidinium iodide (FAI), methylammonium bromide (MABr), were purchased from Dyesol, the lead compounds and 9,9'-(1,2-phenylenebis(methylene))bis[*N*<sup>3</sup>,*N*<sup>3</sup>,*N*<sup>6</sup>,*N*<sup>6</sup>-tetrakis(4-methoxyphenyl)-9*H*-carbazole-3,6-diamine] (V886) from TCI, CsI from abcr GmbH. Diatomaceous earth (Celite 500 fine, Sigma-Aldrich) was used for filtering where mentioned.

Tributyl(5-methoxythiophen-2-yl)stannane was synthesized according to the literature [192]; 9,9'-(thiene-2,5-diylidimethylidene)bis[*N,N,N',N'*-tetrakis(4-methoxyphenyl)-9*H*-fluorene-2,7-diamine] (V862) was synthesized according to the literature [132]. Diethyl (2-(1,3-dioxoisindolin-2-yl)ethyl)phosphonate and Diethyl (2-aminoethyl)phosphonate were synthesized according to the literature [193].

#### 4-hexyl-4*H*-dithieno[3,2-*b*:2',3'-*d*]pyrrole (1)



Under argon atmosphere, a mixture of 3,3'-dibromo-2,2'-bithiophene (4 g, 12.3 mmol), palladium (II) acetate (0.14 g, 0.62 mmol), ( $\pm$ )-BINAP (0.77 g, 1.23 mmol) and sodium *tert*-butoxide (2.93 g, 29.6 mmol) was dissolved in anhydrous toluene (30 ml). After stirring for 10 min, 1-hexylamine (3.4 ml, 13.6 mmol) was added to the reaction mixture, and the solution was stirred for 20 hours at 110 °C temperature (TLC: *n*-hexane). The mixture was extracted with ethyl acetate. The organic layer was washed three times with water, dried over anhydrous Na<sub>2</sub>SO<sub>4</sub>,

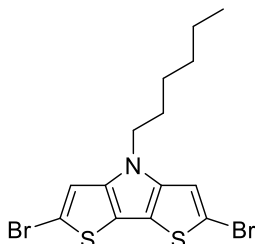
filtered, and the solvent was removed under reduced pressure [67]. The material was purified by column chromatography on silica gel with hexane and dried under vacuum to give a colourless crystal (82 %, 2.67 g). M.p. 45–46 °C

<sup>1</sup>H NMR (400 MHz, CDCl<sub>3</sub>)  $\delta$  7.10 (d,  $J$  = 5.3 Hz, 2H, Ht 2,6-H), 6.97 (d,  $J$  = 5.3 Hz, 2H, Ht 3,5-H), 4.15 (t,  $J$  = 7.1 Hz, 2H, NCH<sub>2</sub>), 1.83 (quin,  $J$  = 7.0 Hz, 2H, CH<sub>2</sub>), 1.35–1.20 (m, 6H, 3 $\times$  CH<sub>2</sub>), 0.85 (t,  $J$  = 6.8 Hz, 3H, CH<sub>3</sub>).

<sup>13</sup>C NMR (100 MHz, CDCl<sub>3</sub>)  $\delta$  145.06, 122.85, 114.72, 111.07, 47.53, 31.54, 30.45, 26.78, 22.63, 14.13.

Anal. calcd. for C<sub>14</sub>H<sub>17</sub>NS<sub>2</sub>, %: C 63.84, H 6.51, N 5.32; found, %: C 63.97, H 6.36, N 5.45.

#### 2,6-dibromo-4-hexyl-4*H*-bisthieno[3,2-*b*:2',3'-*d*]pyrrole (2)



4-hexyl-4*H*-dithieno[3,2-*b*:2',3'-*d*]pyrrole (0.8 g, 3.07 mmol) was dissolved in dichloromethane (12 ml) and cooled in an ice-water bath. Then, *N*-bromosuccinimide (1.16 g, 6.56 mmol) solution in DMF (3 ml) was added dropwise into the reaction mixture, and the solution was stirred for 1 hours in an ice-water bath and 2 hours at 20 °C temperature (TLC: *n*-hexane). The mixture was extracted with dichloromethane. The organic layer was washed three

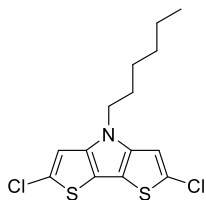
times with water, dried over anhydrous Na<sub>2</sub>SO<sub>4</sub>, filtered, and the solvent was removed under reduced pressure [79]. The material was purified by column chromatography (acetone/ *n*-hexane 1:49 *v/v*) to give a white solid (73 %, 0.94 g). M.p. polymerized by heating.

<sup>1</sup>H NMR (400 MHz, CDCl<sub>3</sub>)  $\delta$  7.01 (s, 2H, Ht 3,5-H), 4.06 (t,  $J$  = 7.1 Hz, 2H, NCH<sub>2</sub>), 1.86–1.74 (m, 2H, CH<sub>2</sub>), 1.34–1.21 (m, 6H, 3 $\times$  CH<sub>2</sub>), 0.87 (t,  $J$  = 6.8 Hz, 3H, CH<sub>3</sub>).

<sup>13</sup>C NMR (100 MHz, CDCl<sub>3</sub>)  $\delta$  141.58, 114.84, 114.36, 109.86, 47.70, 31.49, 30.37, 26.71, 22.61, 14.13.

Anal. calcd. for C<sub>14</sub>H<sub>15</sub>Br<sub>2</sub>NS<sub>2</sub>, %: C 39.92, H 3.59, N 3.33; found, %: C 40.05, H 3.53, N 3.39.

### 2,6-dichloro-4-hexyl-4H-bisthieno[3,2-b:2',3'-d]pyrrole (3)



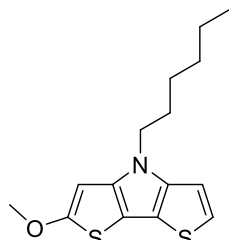
4-hexyl-4H-dithieno[3,2-b:2',3'-d]pyrrole (**1**) (0.5 g, 1.85 mmol) was dissolved in dichloromethane (10 ml) and cooled mixture until 0 °C in an ice-water bath. Then, *N*-chlorosuccinimide (0.530 g, 3.99 mmol) was added into the mixture, and the solution was stirred for 1 hours in an ice-water bath and 2 hours at 20 °C temperature (TLC: *n*-hexane). The mixture was extracted with dichloromethane. The organic layer was washed three times with water, dried over anhydrous Na<sub>2</sub>SO<sub>4</sub>, filtered, and the solvent was removed under reduced pressure. The material was purified by column chromatography with hexane and dried under vacuum to give white crystals (68 %, 0.430 g). M.p. 76–77 °C

<sup>1</sup>H NMR (400 MHz, CDCl<sub>3</sub>) δ 6.90 (s, 2H, Ht 3,5-H), 4.06 (t, *J* = 7.1 Hz, 2H, NCH<sub>2</sub>), 1.79 (quin, *J* = 7.0 Hz, 2H, CH<sub>2</sub>), 1.35–1.21 (m, 6H, 3× CH<sub>2</sub>), 0.92–0.78 (m, 3H, CH<sub>3</sub>).

<sup>13</sup>C NMR (100 MHz, CDCl<sub>3</sub>) δ 140.09, 127.38, 112.13, 111.14, 47.66, 31.50, 30.36, 26.71, 22.61, 14.12.

Anal. calcd. for C<sub>14</sub>H<sub>15</sub>Cl<sub>2</sub>NS<sub>2</sub>, %: C 50.60, H 4.55, N 4.22; found, %: C 50.69, H 4.72, N 4.05.

### 4-hexyl-2-methoxy-4H-bisthieno[3,2-b:2',3'-d]pyrrole (4)



Under argon atmosphere, Na (0.55 g, 23.74 mmol) was dissolved in anhydrous methanol (6.5 ml, 159.3 mmol); afterwards, compound (**2**) (0.5 g, 1.18 mmol) dissolved in anhydrous DMF (3 ml) and CuI (0.926 g 4.838 mmol) were added into the reaction mixture. The solution was stirred for 24 hours at 80 °C temperature under argon atmosphere. After the termination of the reaction (TLC: acetone/ *n*-hexane 4:21 v/v), the mixture was diluted with THF and filtered through

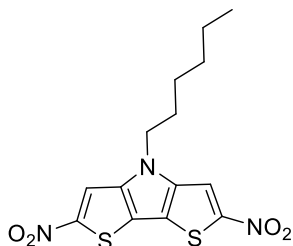
Celite. The solvent was partially removed until ~10 ml of mixture remained. The mixture was extracted with dichloromethane. The organic layer was washed three times with water, dried over anhydrous Na<sub>2</sub>SO<sub>4</sub>, filtered, and the solvent was removed under reduced pressure. The material was purified by column chromatography on silica gel with hexane and dried under vacuum to give a white solid (9 %, 0.03 g).

<sup>1</sup>H NMR (400 MHz, CDCl<sub>3</sub>) δ 6.98 (d, *J* = 5.3 Hz, 1H, Ht), 6.95 (d, *J* = 5.3 Hz, 1H, Ht), 6.26 (s, 1H, Ht H-3), 4.09 (t, *J* = 7.1 Hz, 2H, NCH<sub>2</sub>), 3.94 (s, 3H, OCH<sub>3</sub>), 1.84–1.79 (m, 2H, CH<sub>2</sub>), 1.32–1.26 (m, 6H, 3× CH<sub>2</sub>), 0.88–0.84 (m, 3H, CH<sub>3</sub>).

<sup>13</sup>C NMR (100 MHz, CDCl<sub>3</sub>) δ 165.06, 141.99, 139.90, 122.88, 120.65, 111.08, 110.89, 91.00, 60.84, 47.45, 31.56, 30.46, 26.77, 22.65, 14.15.

Anal. calcd. for C<sub>15</sub>H<sub>19</sub>NOS<sub>2</sub>, %: C 61.40, H 6.53, N 4.77; found, %: C 61.28, H 6.42, N 4.93.

**4-hexyl-2,6-dinitro-4H-bisthieno[3,2-b:2',3'-d]pyrrole (5)**



4-hexyl-4H-dithieno[3,2-b:2',3'-d]pyrrole (**1**) (1 g, 3.8 mmol) was dissolved in chloroform (10 ml); then, acetic anhydride (10ml) and copper(II) nitrate (0.66 g, 7.6 mmol) were added. After 10 minutes, 65 % HNO<sub>3</sub> (0.1 ml, 1.42 mmol) was added, and the solution was stirred at 20 °C for 1 hour (TLC: acetone/ *n*-hexane 3:22 *v/v*). The mixture was neutralized with 20 % K<sub>2</sub>CO<sub>3</sub> solution (50 ml) and extracted with chloroform. The

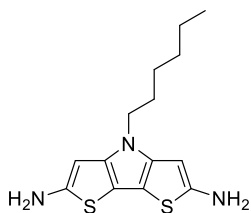
organic layer was washed three times with water, dried over anhydrous Na<sub>2</sub>SO<sub>4</sub>, filtered, and the solvent was removed under reduced pressure. The material was purified by column chromatography (acetone/ *n*-hexane 2:23 *v/v*) to give a yellowish powder (22 %, 0.3 g).

<sup>1</sup>H NMR (400 MHz, CDCl<sub>3</sub>) δ 7.99 (s, 2H, Ht 3,5-H), 4.27 (t, *J* = 7.1 Hz, 2H, NCH<sub>2</sub>), 1.91 (quin, *J* = 7.1 Hz, 2H, CH<sub>2</sub>), 1.38–1.27 (m, 6H, 3× CH<sub>2</sub>), 0.88 (t, *J* = 6.8 Hz, 3H, CH<sub>3</sub>).

<sup>13</sup>C NMR (100 MHz, CDCl<sub>3</sub>) δ 151.98, 143.38, 118.71, 112.73, 48.10, 31.37, 30.30, 26.75, 22.56, 14.07.

Anal. calcd. for C<sub>14</sub>H<sub>15</sub>N<sub>3</sub>O<sub>4</sub>S<sub>2</sub>, %: C 47.58, H 4.28, N 11.98; found, %: C 47.65, H 4.36, N 12.07.

**4-hexyl-4H-bisthieno[3,2-b:2',3'-d]pyrrole-2,6-diamine (6)**



4-hexyl-2,6-dinitro-4H-bisthieno[3,2-b:2',3'-d]pyrrole (**5**) (0.28 g 0.79 mmol) and 10 % Pd/C (0.08 g 0.08 mmol) were mixed in 25 ml ethanol under argon atmosphere. 65 % Hydrazine hydrate (0.5 ml 10.37 mmol) was then added dropwise, and the resulting mixture was refluxed for 3 hours (TLC: acetone/ *n*-hexane 1:4 *v/v*). After cooling to room temperature, the mixture was diluted with THF and filtered

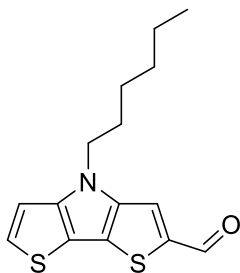
through Celite, the solvent was removed under reduced pressure. The material was purified by column chromatography (acetone/ *n*-hexane 1:4 *v/v*) to give a brown resin (17 %, 0.04 g).

<sup>1</sup>H NMR (400 MHz, DMSO-*d*<sub>6</sub>) δ 7.02 (s, 2H, Ht 3,5-H), 4.30–3.94 (s, 4H, 2× NH<sub>2</sub>), 3.86 (t, *J* = 8.1 Hz, 2H, NCH<sub>2</sub>), 1.51–1.42 (m, 2H, CH<sub>2</sub>), 0.93–0.78 (m, 6H, 3× CH<sub>2</sub>), 0.66 (t, *J* = 7.1 Hz, 3H, CH<sub>3</sub>).

<sup>13</sup>C NMR (100 MHz, DMSO-*d*<sub>6</sub>) δ 142.91, 131.59, 114.18, 107.87, 46.24, 31.23, 24.57, 22.65, 21.27, 14.91.

Anal. calcd. for C<sub>14</sub>H<sub>15</sub>N<sub>3</sub>O<sub>4</sub>S<sub>2</sub>, %: C 57.30, H 6.53, N 14.32; found, %: C 57.46, H 6.68, N 14.43.

4-hexyl-4*H*-bisthieno[3,2-*b*:2',3'-*d*]pyrrole-2-carbaldehyde (**7**)



To a cooled (-5 °C) *N,N*-dimethylformide (1.17 ml, 15.18 mmol), phosphorus(V) oxychloride (1.05 ml, 11.38 mmol) was added dropwise. After the mixture was diluted with dichloromethane (50 ml), 4-hexyl-4*H*-dithieno[3,2-*b*:2',3'-*d*]pyrrole (2 g, 7.59 mmol) was added, and the solution was stirred for 1 hour in an ice-water bath and 1 hour at 20 °C temperature. Subsequently, saturated sodium acetate aqueous solution (20 ml) was added. The mixture was further stirred at room temperature for 2 h

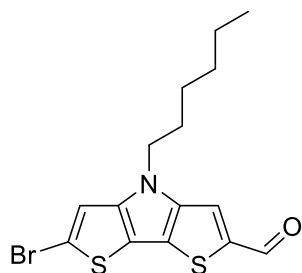
(TLC: acetone/ *n*-hexane 1:24 *v/v*), extracted with dichloromethane. The organic layer was washed three times with water and dried over anhydrous Na<sub>2</sub>SO<sub>4</sub>, filtered, and the solvent was removed under reduced pressure. The material was purified by column chromatography (acetone/ *n*-hexane 2:23 *v/v*) to give yellowish solid (98 %, 2.16 g).

<sup>1</sup>H NMR (400 MHz, CDCl<sub>3</sub>) δ 9.86 (s, 1H, CHO), 7.64 (s, 1H, Ht H-3), 7.37 (d, *J* = 5.3 Hz, 1H, Ht), 7.01 (d, *J* = 5.3 Hz, 1H, Ht), 4.21 (t, *J* = 7.1 Hz, 2H, NCH<sub>2</sub>), 1.88 (quin, *J* = 7.1 Hz, 2H, CH<sub>2</sub>), 1.33–1.26 (m, 6H, 3× CH<sub>2</sub>), 0.90–0.82 (m, 3H, CH<sub>3</sub>).

<sup>13</sup>C NMR (100 MHz, CDCl<sub>3</sub>) δ 183.13, 149.32, 144.40, 140.17, 128.63, 123.38, 119.55, 115.07, 111.01, 47.64, 31.47, 30.36, 26.77, 22.60, 14.10.

Anal. calcd. for C<sub>15</sub>H<sub>17</sub>NOS<sub>2</sub>, %: C 61.82, H 5.88, N 4.81; found, %: C 61.69, H 5.95, N 4.94.

6-bromo-4-hexyl-4*H*-bisthieno[3,2-*b*:2',3'-*d*]pyrrole-2-carbaldehyde (**8**)



4-hexyl-4*H*-bisthieno[3,2-*b*:2',3'-*d*]pyrrole-2-carbaldehyde (**7**) (2 g, 6.87 mmol) was dissolved in dichloromethane (100 ml), and the mixture was cooled to 0 °C in an ice-water bath. Then, NBS (1.28 g, 7.21 mmol) was added into the reaction mixture in proportions, and the solution was stirred for 1 hour in an ice-water bath and 1 hour at 20 °C temperature (TLC: acetone/ *n*-hexane 2:23 *v/v*). The mixture was diluted with dichloromethane and extracted with water. The

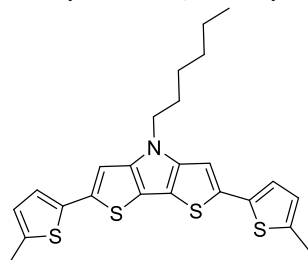
organic layer was washed three times with water and dried over anhydrous Na<sub>2</sub>SO<sub>4</sub>, filtered, and the solvent was removed under reduced pressure. The material was purified by column chromatography (acetone/ *n*-hexane 1:9 *v/v*) to give yellowish oil (87 %, 2.21 g).

<sup>1</sup>H NMR (400 MHz, CDCl<sub>3</sub>) δ 9.85 (s, 1H, CHO), 7.61 (s, 1H, Ht), 7.06 (s, 1H, Ht), 4.15 (t, *J* = 7.1 Hz, 2H, NCH<sub>2</sub>), 1.90–1.79 (m, 2H, CH<sub>2</sub>), 1.34–1.25 (m, 6H, 3× CH<sub>2</sub>), 0.87 (t, *J* = 6.8 Hz, 3H, CH<sub>3</sub>).

<sup>13</sup>C NMR (100 MHz, CDCl<sub>3</sub>) δ 183.06, 146.73, 143.35, 140.47, 122.95, 119.41, 115.65, 115.07, 114.39, 47.72, 31.44, 30.31, 26.73, 22.58, 14.09.

Anal. calcd. for C<sub>15</sub>H<sub>16</sub>BrNOS<sub>2</sub>, %: C 48.65, H 4.36, N 3.78; found, %: C 48.69, H 4.51, N 3.86.

**4-hexyl-2,6-bis(5-methylthiophen-2-yl)-4H-bisthieno[3,2-b:2',3'-d]pyrrole (9)**



A solution of 2,6-dibromo-4-hexyl-4H-bisthieno[3,2-b:2',3'-d]pyrrole (**2**) (0.5 g, 1.19 mmol) and 5-methyl-2-thienylboronic acid (0.51 g, 3.56 mmol) in THF (10 ml) was mixed with argon-purged 2°N aqueous K<sub>2</sub>CO<sub>3</sub> solution (2.7 ml) and stirred under argon atmosphere. After 10 min, Pd(PPh<sub>3</sub>)<sub>4</sub> (0.06 g, 0.30 mmol) was added, and the solution was stirred at 40 °C temperature overnight (TLC: acetone/ *n*-hexane 1:49 *v/v*). The

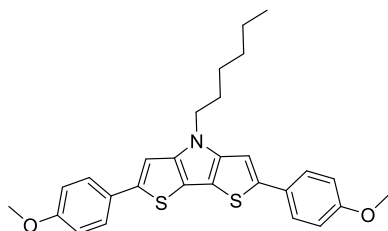
solution was allowed to cool to room temperature; the mixture was filtered through Celite. The solvent was partially removed under reduced pressure until ~10 ml of mixture remained. The mixture was extracted with dichloromethane. The organic layer was washed three times with water and dried over anhydrous Na<sub>2</sub>SO<sub>4</sub>, filtered; the solvent was removed under reduced pressure. The material was purified by column chromatography on silica gel with hexane to give a yellow solid (52 %, 0.28 g). M.p 115–116 °C

<sup>1</sup>H NMR (400 MHz, DMSO-*d*<sub>6</sub>) δ 7.39 (s, 2H, Ht 3,5-H), 7.07 (d, *J* = 3.5 Hz, 2H, Ht Thio), 6.77 (d, *J* = 3.5 Hz, 2H, Ht Thio), 4.26 (t, *J* = 7.0 Hz, 2H, NCH<sub>2</sub>), 2.45 (s, 6H, 2× CH<sub>3</sub>), 1.77 (quin, *J* = 7.0 Hz, 2H, CH<sub>2</sub>), 1.32–1.13 (m, 6H, 3× CH<sub>2</sub>), 0.82 (t, *J* = 6.7 Hz, 3H, CH<sub>3</sub>).

<sup>13</sup>C NMR (100 MHz, DMSO-*d*<sub>6</sub>) δ 144.34, 138.25, 135.78, 134.18, 126.51, 122.89, 112.33, 107.82, 46.39, 30.78, 29.80, 25.85, 22.06, 14.99, 13.86.

Anal. calcd. for C<sub>24</sub>H<sub>25</sub>NS<sub>4</sub>, %: C 63.26, H 5.53, N 3.07; found, %: C 63.09, H 5.65, N 3.19.

**4-hexyl-2,6-bis(4-methoxyphenyl)-4H-bisthieno[3,2-b:2',3'-d]pyrrole (10)**



A solution of 2,6-dibromo-4-hexyl-4H-bisthieno[3,2-b:2',3'-d]pyrrole (**2**) (0.3 g, 0.71 mmol) and 4-methoxyphenylboronic acid (0.32 g, 2.14 mmol) in THF (10 ml) was mixed with argon-purged 2N aqueous K<sub>2</sub>CO<sub>3</sub> solution (2.7 ml) and stirred under argon atmosphere. After 10 min, Pd(PPh<sub>3</sub>)<sub>4</sub> (0.04 g, 0.18 mmol) was added, and the solution was refluxed overnight

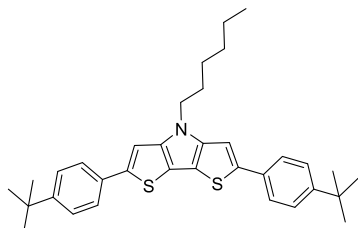
(TLC: acetone/ *n*-hexane 3:22 *v/v*). The solution was allowed to cool to room temperature; the mixture was filtered through Celite. The solvent was partially removed under reduced pressure until ~10 ml of mixture remained. The mixture was extracted with dichloromethane. The organic layer was washed three times with water, dried over anhydrous Na<sub>2</sub>SO<sub>4</sub>, filtered, and the solvent was removed under reduced pressure. The material was purified by column chromatography (acetone/ *n*-hexane 1:24 *v/v*) to give a yellow solid (83 %, 0.28 g). M.p 160–161 °C

<sup>1</sup>H NMR (400 MHz, CDCl<sub>3</sub>) δ 7.55 (d, *J* = 8.0 Hz, 4H, Ar), 7.09 (s, 2H, Ht 3,5-H), 6.91 (d, *J* = 8.8 Hz, 4H, Ar), 4.15 (t, *J* = 7.1 Hz, 2H, NCH<sub>2</sub>), 3.83 (s, 6H, 2× OCH<sub>3</sub>), 1.94–1.80 (m, 2H, CH<sub>2</sub>), 1.41–1.23 (m, 6H, 3× CH<sub>2</sub>), 0.87 (t, *J* = 6.8 Hz, 3H, CH<sub>3</sub>).

$^{13}\text{C}$  NMR (100 MHz,  $\text{CDCl}_3$ )  $\delta$  159.11, 128.83, 128.70, 126.75, 114.48, 113.87, 106.10, 105.82, 55.51, 47.45, 31.60, 30.52, 26.85, 22.67, 14.17.

Anal. calcd. for  $\text{C}_{28}\text{H}_{29}\text{NO}_2\text{S}_2$ , %: C 70.70, H 6.15, N 2.94; found, %: C 70.79, H 6.22, N 2.79.

### 2,6-bis(4-*tert*-butylphenyl)-4-hexyl-4*H*-bisthieno[3,2-*b*:2',3'-*d*]pyrrole (**11**)



A solution of 2,6-dibromo-4-hexyl-4*H*-bisthieno[3,2-*b*:2',3'-*d*]pyrrole (**2**) (0.5 g, 1.19 mmol) and 4-*tert*-butylphenylboronic acid (0.63 g, 3.56 mmol) in THF (10 ml) was mixed with argon-purged 2*N* aqueous  $\text{K}_2\text{CO}_3$  solution (2.7 ml) and stirred under argon atmosphere. After 10 min,  $\text{Pd}(\text{PPh}_3)_4$  (0.06 g, 0.30 mmol) was added, and the solution was refluxed overnight (TLC: acetone/ *n*-

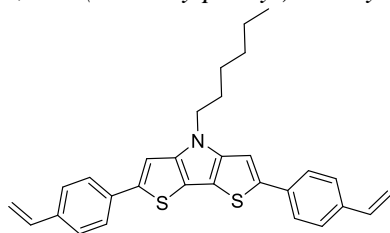
hexane 1:24 *v/v*). The solution was allowed to cool to room temperature; the mixture was filtered through Celite. The solvent was partially removed under reduced pressure until ~10 ml of mixture remained. The mixture was extracted with dichloromethane. The organic layer was washed three times with water, dried over anhydrous  $\text{Na}_2\text{SO}_4$ , filtered, and the solvent was removed under reduced pressure. The material was purified by column chromatography on silica gel with hexane to give a yellow solid (58 %, 0.36 g) M.p. 216–218 °C

$^1\text{H}$  NMR (400 MHz,  $\text{CDCl}_3$ )  $\delta$  7.57 (d,  $J = 8.0$  Hz, 4H, Ar), 7.40 (d,  $J = 8.1$  Hz, 4H, Ar), 7.17 (s, 2H, Ht 3,5-H), 4.15 (t,  $J = 7.1$  Hz, 2H,  $\text{NCH}_2$ ), 1.87 (quin,  $J = 7.1$  Hz, 2H,  $\text{CH}_2$ ), 1.34 (s, 18H,  $6 \times \text{CH}_3$ ), 1.31–1.22 (m, 6H,  $3 \times \text{CH}_2$ ), 0.90–0.82 (m, 3H,  $\text{CH}_3$ ).

$^{13}\text{C}$  NMR (100 MHz,  $\text{CDCl}_3$ )  $\delta$  150.35, 144.97, 141.91, 133.03, 125.97, 125.20, 114.32, 106.63, 47.43, 34.73, 31.60, 31.43, 30.51, 26.85, 22.66, 14.18.

Anal. calcd. for  $\text{C}_{34}\text{H}_{41}\text{NS}_2$ , %: C 77.37, H 7.83, N 2.65; found, %: C 77.54, H 7.70, N 2.51.

### 2,6-bis(4-ethenylphenyl)-4-hexyl-4*H*-bisthieno[3,2-*b*:2',3'-*d*]pyrrole (**12**)



A solution of 2,6-dibromo-4-hexyl-4*H*-bisthieno[3,2-*b*:2',3'-*d*]pyrrole (**2**) (0.5 g, 1.19 mmol) and 4-vinylphenylboronic acid (0.53 g, 3.56 mmol) in THF (10 ml) was mixed with argon-purged 2 *N* aqueous  $\text{K}_2\text{CO}_3$  solution (2.7 ml) and stirred under argon atmosphere. After 10 min,  $\text{Pd}(\text{PPh}_3)_4$  (0.06 g, 0.30 mmol) was added, and the solution was stirred at 50 °C

temperature for 5 h (TLC: acetone/ *n*-hexane 1:49 *v/v*). The solution was allowed to cool to room temperature; the mixture was filtered through Celite. The solvent was partially removed under reduced pressure until ~10 ml of mixture remained. The mixture was extracted with dichloromethane. The organic layer was washed three times with water, dried over anhydrous  $\text{Na}_2\text{SO}_4$ , filtered, and the solvent was removed under reduced pressure. The material was purified by column



chromatography on silica gel with hexane to give a yellow solid (49 %, 0.26 g). M.p. 179–181 °C

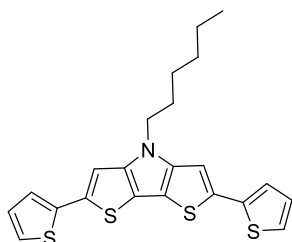
$^1\text{H}$  NMR (400 MHz, DMSO- $d_6$ )  $\delta$  7.82 (s, 2H, Ht 3,5-H), 7.67 (d,  $J$  = 8.1 Hz, 4H, Ar), 7.52 (d,  $J$  = 8.2 Hz, 4H, Ar), 6.75 (dd,  $J$  = 17.6, 10.9 Hz, 2H, 2 $\times$  CH), 5.86 (d,  $J$  = 17.6 Hz, 2H, CH<sub>2</sub>), 5.28 (d,  $J$  = 11.0 Hz, 2H, CH<sub>2</sub>), 4.32 (t,  $J$  = 7.0 Hz, 2H, NCH<sub>2</sub>), 1.84 (quin,  $J$  = 7.0 Hz, 2H, CH<sub>2</sub>), 1.32–1.17 (m, 6H, 3 $\times$  CH<sub>2</sub>), 0.82 (t,  $J$  = 6.9 Hz, 3H, CH<sub>3</sub>).

$^{13}\text{C}$  NMR (100 MHz, DMSO- $d_6$ )  $\delta$  145.31, 140.49, 136.09, 135.93, 134.52, 126.86, 124.79, 114.14, 113.33, 108.62, 46.53, 30.83, 29.81, 25.94, 22.07, 13.87.

Anal. calcd. for C<sub>30</sub>H<sub>29</sub>NS<sub>2</sub>, %: C 77.04, H 6.25, N 2.99; found, %: C 77.21, H 6.11, N 3.15.

Under argon atmosphere, a mixture of 2,6-dibromo-4-hexyl-4*H*-bisthieno[3,2-*b*:2',3'-*d*]pyrrole (**2**) (0.5 g, 1.19 mmol), 2-(tributylstannyl)thiophene (0.95 ml, 2.97 mmol) and Pd(PPh<sub>3</sub>)<sub>4</sub> (0.025 g, 0.12 mmol) was dissolved in anhydrous toluene (10 ml), and the solution was refluxed overnight. The solution was allowed to cool to room temperature; the mixture was filtered through Celite; the solvent was removed under reduced pressure. The mixture was purified by column chromatography on silica gel with hexane and dried under vacuum to give two main products: **13** (22 %, 0.11 g) yellow solids and **14** (5 %, 0.04 g) yellow solids.

#### 4-hexyl-2,6-di(thiophen-2-yl)-4*H*-bisthieno[3,2-*b*:2',3'-*d*]pyrrole (**13**)



M.p. 105–107 °C

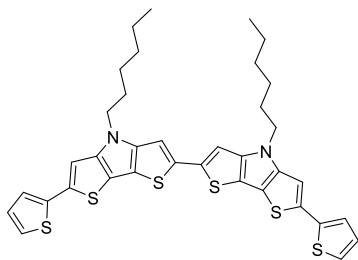
$^1\text{H}$  NMR (400 MHz, CDCl<sub>3</sub>)  $\delta$  7.11 (t,  $J$  = 3.6 Hz, 4H, Ht Thio), 6.98 (s, 2H, Ht 3,5-H), 6.94 (dd,  $J$  = 4.9, 3.8 Hz, 2H, Ht Thio), 4.07 (t,  $J$  = 7.1 Hz, 2H, NCH<sub>2</sub>), 1.79 (quin,  $J$  = 7.1 Hz, 2H, CH<sub>2</sub>), 1.30–1.19 (m, 6H, 3 $\times$  CH<sub>2</sub>), 0.80 (t,  $J$  = 7.0 Hz, 3H, CH<sub>3</sub>).

$^{13}\text{C}$  NMR (100 MHz, CDCl<sub>3</sub>)  $\delta$  144.62, 138.99, 135.06, 128.02, 123.99, 123.11, 114.08, 107.59, 47.52, 31.57,

30.48, 26.80, 22.68, 14.17.

Anal. calcd. for C<sub>22</sub>H<sub>21</sub>NS<sub>4</sub>, %: C 61.79, H 4.95, N 3.28; found, %: C 61.75, H 5.09, N 3.14.

#### 4,4'-dihexyl-6,6'-di(thiophen-2-yl)-4*H*,4'*H*-2,2'-bibisthieno[3,2-*b*:2',3'-*d*]pyrrole (**14**)



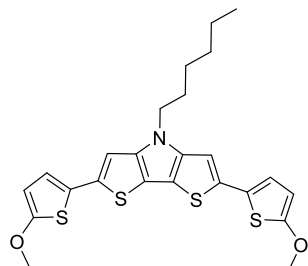
$^1\text{H}$  NMR (400 MHz, CDCl<sub>3</sub>)  $\delta$  7.20 (d,  $J$  = 4.9 Hz, 4H, Ht Thio), 7.07 (s, 4H, Ht), 7.03 (dd,  $J$  = 5.0, 3.7 Hz, 2H, Ht Thio), 4.18 (t,  $J$  = 7.1 Hz, 4H, 2 $\times$  NCH<sub>2</sub>), 1.90 (quin,  $J$  = 7.1 Hz, 4H, 2 $\times$ CH<sub>2</sub>), 1.42–1.28 (m, 12H, 6 $\times$  CH<sub>2</sub>), 0.93–0.85 (m, 6H, 2 $\times$  CH<sub>3</sub>).

$^{13}\text{C}$  NMR (100 MHz, CDCl<sub>3</sub>)  $\delta$  179.09, 149.42, 144.80, 137.74, 131.63, 128.05, 126.92, 125.54, 123.99, 123.08, 118.60, 106.72, 47.56, 31.59,

30.50, 26.82, 22.70, 14.19.

Anal. calcd. for  $C_{36}H_{36}N_2S_6$ , %: C 62.75, H 5.2, N 4.07; found, %: C 62.86, H 5.42, N 4.01.

*4-hexyl-2,6-bis(5-methoxythiophen-2-yl)-4H-bisthieno[3,2-b:2',3'-d]pyrrole (15)*



Under argon atmosphere, a mixture of 2,6-dibromo-4-hexyl-4*H*-bisthieno[3,2-*b*:2',3'-*d*]pyrrole (**2**) (0.99 g, 2.36 mmol), tributyl(5-methoxythiophen-2-yl)stannane (1.8 g) and  $Pd(PPh_3)_4$  (0.053 g, 0.24 mmol) was dissolved in anhydrous toluene (35 ml), and the solution was stirred for 10 hours at 90 °C (TLC: acetone/ *n*-hexane 1:49 *v/v*). The solution was allowed to cool to room temperature; the mixture was filtered through Celite; the solvent was removed under reduced pressure.

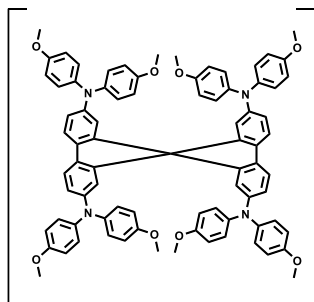
The material was purified by column chromatography (acetone/ *n*-hexane 1:24 *v/v*) to give a brown solid (5 %, 0.06 g).

$^1H$  NMR (400 MHz,  $CDCl_3$ )  $\delta$  7.26 (s, 2H, Ht 3,5-H), 7.11 (d,  $J = 3.5$  Hz, 2H, Ht Thio), 6.86 (d,  $J = 3.5$  Hz, 2H, Ht Thio), 4.09 (t,  $J = 7.1$  Hz, 2H,  $NCH_2$ ), 3.89 (s, 6H,  $2 \times OCH_3$ ), 1.78 (quin,  $J = 7.1$  Hz, 2H,  $CH_2$ ), 1.29–1.20 (m, 6H,  $3 \times CH_2$ ), 0.82 (t,  $J = 7.0$  Hz, 3H,  $CH_3$ ).

$^{13}C$  NMR (100 MHz,  $CDCl_3$ )  $\delta$  143.96, 138.56, 134.89, 125.68, 121.98, 121.12, 111.91, 107.34, 58.21, 31.27, 30.28, 26.33, 22.54, 15.47, 14.34.

Anal. calcd. for  $C_{24}H_{25}NO_2S_4$ , %: C 59.11, H 5.17, N 2.87; found, %: C 58.94, H 5.28, N 2.95.

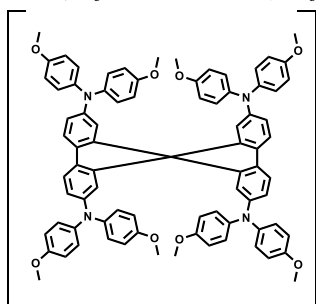
*2,2',7,7'-Tetrakis[N,N-di(4-methoxyphenyl)amino]-9,9'-spirobifluorene bis(trifluoromethane)sulfonimide salt (Spiro[TFSI]) (16)*



The compound was synthesized according to the literature [109] [131].

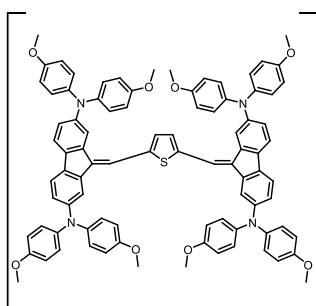
M.p. 217–219 °C

*2,2',7,7'-Tetrakis[N,N-di(4-methoxyphenyl)amino]-9,9'-spirobifluorene dibis(trifluoromethane)sulfonimide salt (Spiro[TFSI]<sub>2</sub>) (17)*



The compound was synthesized according to the literature [128].  
M.p. 213–215 °C

*9,9'-(thiene-2,5-diylidimethylidene)bis[N,N,N',N'-tetrakis(4-methoxyphenyl)-9H-fluorene-2,7- diamine] bis(trifluoromethane)sulfonimide salt (V862[TFSI]) (18)*

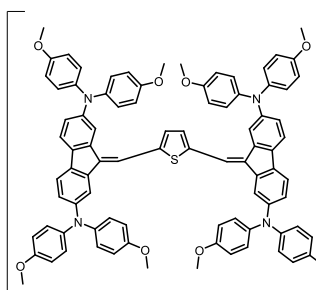


The V862 (0.4 g, 0.297 mmol) was dissolved in chlorobenzene (23 ml). Silver trifluoromethylsulfonylamide (0.115 g, 0.297 mmol) was dissolved in 1 ml of methanol and added to the reaction. The mixture was stirred overnight, after which it was filtered through Celite. The solvent was partially removed under reduced pressure until ~10 ml of the mixture remained. The remaining solution was diluted in Toluene (100 ml) and kept at 0 °C overnight. A

fine black powder was collected via filtration and washed with cold toluene. Then, the resulting powder was dissolved in warm methanol (20 mg/ml), placed in the refrigerator overnight; the resulting black precipitate was collected via filtration and washed with cold methanol. The powder was dried at 35 °C overnight to give dark yellow crystals (52 %, 0.250 g). M.p. 128–130 °C

Anal. calcd for C<sub>90</sub>H<sub>72</sub>F<sub>6</sub>N<sub>5</sub>O<sub>12</sub>S<sub>3</sub>, %: C 66.49, H 4.46, N 4.31, found, %: C 66.32, H 4.52, N 4.45.

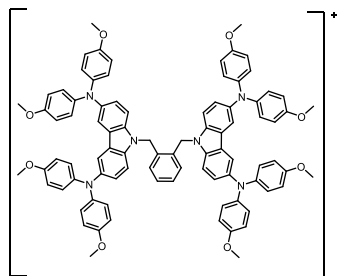
*9,9'-(thiene-2,5-diylidimethylidene)bis[N,N,N',N'-tetrakis(4-methoxyphenyl)-9H-fluorene-2,7- diamine] dibis(trifluoromethane)sulfonimide salt (V862[TFSI]<sub>2</sub>) (19)*



The V862 (0.4 g, 0.297 mmol) was dissolved in chlorobenzene (23 ml). Silver trifluoromethylsulfonylamide (0.330 g, 0.594 mmol) was added to the reaction. The mixture was stirred overnight, after which it was filtered through Celite. The solvent was removed under reduced pressure. The powder was dried at 35 °C overnight to give dark yellow crystals (92 %, 0.52 g). M.p. 106–108 °C

Anal. calcd for C<sub>92</sub>H<sub>72</sub>F<sub>12</sub>N<sub>6</sub>O<sub>16</sub>S<sub>5</sub>, %: C 57.98, H 3.81, N 4.41, found, %: C 58.13, H 3.76, N 4.63.

*1,2-Bis[3,6-(4,4'-dimethoxydiphenylamino)-9H-carbazol-9-methyl]benzene bis(trifluoromethane)sulfonimide salt (V886[TFSI]) (20)*

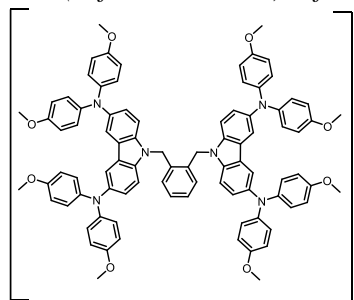


The V886 (0.4 g, 0.297 mmol) was dissolved in chlorobenzene (23 ml). Silver trifluoromethylsulfonamide (0.115 g, 0.297 mmol) was dissolved in 1 ml of methanol and added to the reaction. The mixture was stirred overnight, after which it was filtered through Celite. The solvent was partially removed under reduced pressure until ~10 ml of the mixture remained. The remaining solution was diluted

with toluene (100 ml) and kept at 0 °C overnight. A fine black powder was collected via filtration and washed with cold toluene. The resulting powder was then dissolved in warm methanol (20 mg/ml), placed in the refrigerator overnight; the resulting black precipitate was collected via filtration and washed with cold methanol. The powder was dried at 35 °C overnight to give dark pink crystals (58 %, 0.280 g). M.p. 198–199 °C

Anal. calcd for C<sub>90</sub>H<sub>76</sub>F<sub>6</sub>N<sub>7</sub>O<sub>12</sub>S<sub>2</sub>, %: C 66.49, H 4.71, N 6.03, found, %: C 66.58, H 4.86, N 5.98.

*1,2-Bis[3,6-(4,4'-dimethoxydiphenylamino)-9H-carbazol-9-methyl]benzene dibis(trifluoromethane)sulfonimide salt (V886[TFSI]<sub>2</sub>) (21)*



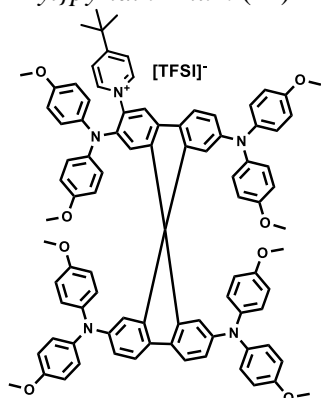
The V886 (0.4 g, 0.297 mmol) was dissolved in chlorobenzene (23 ml). Silver trifluoromethylsulfonamide (0.330 g, 0.594 mmol) was added to the reaction. The mixture was stirred overnight, after which it was filtered through Celite. The solvent was removed under reduced pressure. The powder was dried at 35 °C overnight to give dark blue crystals (94 %, 0.530 g). M.p. 96–98 °C

Anal. calcd for C<sub>92</sub>H<sub>72</sub>F<sub>12</sub>N<sub>6</sub>O<sub>16</sub>S<sub>4</sub>, %: C 57.98, H 4.02, N 5.88, found, %: C 57.76, H 4.17, N 5.95.

### Pyridination of oxidized spiro-MeOTAD

Spiro[TFSI]<sub>2</sub> (0.5 g, 0.28 mmol) was dissolved in 4-*tert*-butylpyridine (3 ml) and stirred at 60 °C for 24 h. After the reaction has ended (TLC acetone/ *n*-hexane, 2:3 v/v), 4-*tert*-butylpyridine was removed under vacuum, and residue was purified by column chromatography (acetone/ *n*-hexane, 8:17 v/v) yielding 0.18 g (48 %) of pyridinated spiro-MeOTAD and 0.16 g (46 %) of spiro-MeOTAD.

4-*tert*-butyl-1-{2,2',7,7'-tetrakis[bis(4-methoxyphenyl)amino]-9,9'-spirobifluoren]-4-yl}pyridin-1-ium (22)



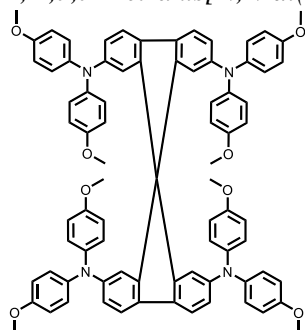
$^1\text{H NMR}$  (400 MHz,  $\text{DMSO-}d_6$ )  $\delta$  9.04 (d,  $J = 6.9$  Hz, 2H, Ht), 8.21 (d,  $J = 7.0$  Hz, 2H, Ht), 7.58–7.46 (m, 4H, Ar), 7.34 (d,  $J = 2.7$  Hz, 1H, Ar), 7.24 (d,  $J = 9.2$  Hz, 1H, Ar), 7.10 (dd,  $J = 9.0, 2.7$  Hz, 1H, Ar), 6.98–6.75 (m, 29H, Ar), 6.70 (dd,  $J = 8.3, 2.0$  Hz, 3H, Ar), 6.30 (d,  $J = 1.8$  Hz, 1H, Ar), 6.19 (d,  $J = 1.6$  Hz, 3H, Ar), 3.84–3.62 (m, 24H,  $8 \times \text{OCH}_3$ ), 1.36 (s, 9H,  $3 \times \text{CH}_3$ ).

$^{13}\text{C NMR}$  (100 MHz,  $\text{DMSO-}d_6$ )  $\delta$  171.40, 155.92, 155.35, 155.28, 149.60, 149.20, 147.53, 147.15, 146.08, 145.72, 141.04, 140.34, 140.32, 139.58, 135.32, 133.96, 133.52, 131.14, 126.32, 126.30, 126.26, 126.23, 125.67, 125.56, 124.71, 121.32, 121.30, 120.85, 120.52, 120.30, 115.52, 114.91, 114.70, 65.03, 56.57, 55.24, 55.20, 40.19, 36.53, 29.40.

MS (APCI)  $m/z$   $[\text{M}+\text{H}]^+ = 1359$ .

Anal. calcd for  $\text{C}_9\text{H}_{80}\text{F}_6\text{N}_6\text{O}_{12}\text{S}_2$ , %: C 67.39, H 4.92, N 5.13, found, %: C 67.22, H 5.05, N 4.91.

2,2',7,7'-Tetrakis[*N,N*-di(4-methoxyphenyl)amino]-9,9'-spirobifluorene



$^1\text{H NMR}$  (400 MHz,  $\text{DMSO-}d_6$ )  $\delta$  7.41 (d,  $J = 8.3$  Hz, 4H, Ar), 6.81 (dd,  $J = 9.0$  Hz, 32H, Ar), 6.67 (d,  $J = 8.5$ , 4H, Ar), 6.20 (s, 4H, Ar), 3.69 (s, 24H,  $8 \times \text{OCH}_3$ ).

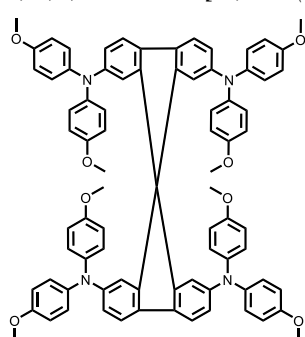
$^{13}\text{C NMR}$  (100 MHz,  $\text{DMSO-}d_6$ )  $\delta$  155.72, 149.87, 147.63, 140.89, 134.44, 126.00, 121.35, 120.71, 116.14, 115.14, 65.44, 55.63.

MS (APCI)  $m/z$   $[\text{M}+\text{H}]^+ = 1225$ .

Anal. calcd for  $\text{C}_{81}\text{H}_{68}\text{N}_4\text{O}_8$ , %: C 79.39, H 5.59, N 4.57, found, %: C 79.15, H 5.40, N 4.71.

**Reduction of oxidized spiro-MeOTAD with FAI**

2,2',7,7'-Tetrakis[*N,N*-di(4-methoxyphenyl)amino]-9,9'-spirobifluorene



Spiro[TFSI] $_2$  (0.1 g, 0.056 mmol) was dissolved in acetonitrile (5 ml); formamidine iodide (0.05 g, 0.29 mmol) was added, and the reaction mixture was stirred at room temperature for 10 min. After the reaction has ended (TLC acetone: *n*-hexane, 2:3), the precipitate was collected and purified by column chromatography (acetone/ *n*-hexane, 1:4 v/v), yielding 0.067 g (98 %) of spiro-MeOTAD.

$^1\text{H NMR}$  (400 MHz,  $\text{DMSO-}d_6$ )  $\delta$  7.41 (d,  $J = 8.3$  Hz, 4H, Ar), 6.81 (dd,  $J = 9.0$  Hz, 32H, Ar), 6.67 (d,  $J = 8.5$ , 4H, Ar), 6.20 (s, 4H, Ar), 3.69 (s, 24H,  $8 \times \text{OCH}_3$ ).

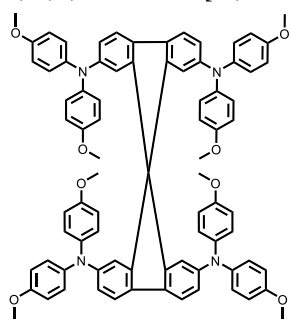
$^{13}\text{C}$  NMR (100 MHz, DMSO- $d_6$ )  $\delta$  155.72, 149.87, 147.63, 140.89, 134.44, 126.00, 121.35, 120.71, 116.14, 115.14, 65.45, 55.63.

MS (APCI)  $m/z$   $[\text{M}+\text{H}]^+ = 1225$ .

Anal. calcd for  $\text{C}_{81}\text{H}_{68}\text{N}_4\text{O}_8$ , %: C 79.39, H 5.59, N 4.57, found, %: C 79.21, H 5.47, N 4.65.

### Reduction of oxidized spiro-MeOTAD with MAI

#### 2,2',7,7'-Tetrakis[*N,N*-di(4-methoxyphenyl)amino]-9,9'-spirobifluorene



Spiro[TFSI] $_2$  (0.1 g, 0.056 mmol) was dissolved in acetonitrile (5 ml); methylammonium iodide (0.09 g, 0.56 mmol) was added, and the reaction mixture was stirred at room temperature for 10 min. After the reaction has ended (TLC acetone: *n*-hexane, 2:3 *v/v*), the precipitate was collected and purified by column chromatography (acetone/ *n*-hexane, 1:4 *v/v*), yielding 0.062 g (90 %) of spiro-MeOTAD.

$^1\text{H}$  NMR (400 MHz, DMSO- $d_6$ )  $\delta$  7.41 (d,  $J = 8.3$  Hz, 4H, Ar), 6.81 (d,  $J = 9.0$  Hz, 32H, Ar), 6.67 (d,  $J = 8.5$  Hz,

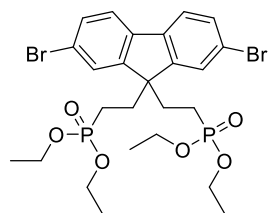
4H, Ar), 6.20 (s, 4H, Ar), 3.69 (s, 24H, 8 $\times$  OCH $_3$ ).

$^{13}\text{C}$  NMR (100 MHz, DMSO- $d_6$ )  $\delta$  155.72, 149.87, 147.63, 140.89, 134.44, 126.00, 121.35, 120.71, 116.14, 115.14, 65.45, 55.63.

MS (APCI)  $m/z$   $[\text{M}+\text{H}]^+ = 1225$ .

Anal. calcd for  $\text{C}_{81}\text{H}_{68}\text{N}_4\text{O}_8$ , %: C 79.39, H 5.59, N 4.57, found, %: C 79.56, H 5.51, N 4.72.

#### Tetraethyl [(2,7-dibromo-9H-fluorene-9,9-diyl)di(ethane-2,1-diyl)]bis(phosphonate) (**23**)



2,7-dibromo-9H-fluorene (1 g, 3.08 mmol) was dissolved in anhydrous 1,4-dioxane (30 ml); diethyl 2-bromoethylphosphonate (1.55 ml, 9.25 mmol) was added dropwise; finally, sodium *tert*-butoxide (1.18 g, 12.34 mmol) was added in three proportions every 10 min. The reaction was stirred for 3 hours, raising the temperature every hour by 20 degrees from 30 to 70  $^\circ\text{C}$ . After

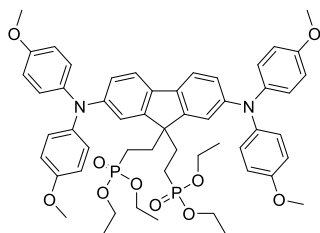
completion (TLC, acetone: *n*-hexane, 7:18, *v/v*), the mixture was extracted with diethyl ether; the organic layer was washed three times with water, dried over anhydrous  $\text{Na}_2\text{SO}_4$ , filtered, and the solvent was removed under reduced pressure. The material was purified by column chromatography (acetone/ *n*-hexane 7:18 *v/v*) to give a white resin (98 %, 2.16 g).

$^1\text{H}$  BMR (400 MHz,  $\text{CDCl}_3$ )  $\delta$  7.53 (s, 2H, Ar), 7.52 (d,  $J = 1.6$  Hz, 2H, Ar), 7.46 (d,  $J = 1.3$  Hz, 2H, Ar), 4.08–3.87 (m, 8H, 4 $\times$  OCH $_2$ ), 2.32–2.20 (m, 4H, 2 $\times$  CH $_2$ ), 1.26 (t,  $J = 7.1$  Hz, 12H, 4 $\times$  CH $_3$ ), 1.02–0.88 (m, 4H, 2 $\times$  CH $_2$ ).

$^{13}\text{C}$  BMR (100 MHz,  $\text{CDCl}_3$ )  $\delta$  138.64, 129.24, 123.70, 123.35, 112.49, 110.29, 61.97 (d,  $^2J_{\text{C,P}} = 6.5$  Hz), 37.24 (d,  $^2J_{\text{C,P}} = 1.6$  Hz), 25.19 (d,  $^1J_{\text{C,P}} = 139.0$  Hz), 16.34 (d,  $^3J_{\text{C,P}} = 6.0$  Hz).

Anal. calcd for  $C_{25}H_{34}Br_2O_6P_2$ , %: C 46.03, H 5.25, found, %: C 45.87, H 5.12.

*Tetraethyl [(2,7-bis(bis(4-methoxyphenyl)amino)-9H-fluorene-9,9-diyl)bis(ethane-2,1-diyl)]bis(phosphonate) (24)*



A solution of tetraethyl [(2,7-dibromo-9H-fluorene-9,9-diyl)di(ethane-2,1-diyl)]bis(phosphonate) (**23**) (1 g, 1.53 mmol) and 4,4'-dimethoxydiphenylamine (1.05 g, 4.59 mmol) in anhydrous toluene (50 ml) was purged with argon for 20 min. Afterwards, palladium(II) acetate (0.10 g, 0.46 mmol), tri-*tert*-butylphosphonium tetrafluoroborate (0.28 g, 0.95 mmol) and sodium *tert*-butoxide (0.44 g, 4.59 mmol) were added, and the

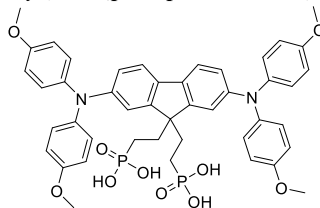
solution was refluxed under argon atmosphere for 6 h. After completion (TLC, acetone: *n*-hexane, 2:3, *v/v*), the reaction mixture was filtered through Celite. The solvent was removed under reduced pressure, and the crude product was purified by column chromatography (acetone/ *n*-hexane 7:18 *v/v*) to give 0.9 g (62 %) of yellow resin.

$^1H$  BMR (700 MHz,  $CDCl_3$ )  $\delta$  7.30 (dd,  $J = 16.8, 9.4$  Hz, 2H, Ar), 7.24–6.71 (m, 20H, Ar), 3.96 (p,  $J = 7.2$  Hz, 8H, 4  $\times$   $OCH_2$ ), 3.80 (s, 12H, 4  $\times$   $OCH_3$ ), 1.99 (dd,  $J = 16.6, 7.1$  Hz, 4H, 2  $\times$   $CH_2$ ), 1.25 (t,  $J = 7.1$  Hz, 12H, 4  $\times$   $CH_3$ ), 1.13–1.05 (m, 4H, 2  $\times$   $CH_2$ ).

$^{13}C$  BMR (100 MHz,  $CDCl_3$ )  $\delta$  155.85, 146.59, 141.60, 141.04, 127.85, 126.38, 122.47, 120.62, 119.17, 114.76, 61.41, (d,  $^2J_{(C,P)} = 6.5$  Hz), 54.85, 32.21, (d,  $^2J_{(C,P)} = 1.6$  Hz), 29.70, 20.84(d,  $^1J_{(C,P)} = 139.0$  Hz), 16.43 (d,  $^3J_{(C,P)} = 6.0$  Hz).

Anal. calcd for  $C_{53}H_{62}N_2O_{10}P_2$ , %: C 67.08, H 6.58, N 2.95, found, %: C 67.31, H 7.09, N 2.79.

*[[{2,7-bis[bis(4-methoxyphenyl)amino]-9H-fluorene-9,9-diyl}di(ethane-2,1-diyl)]bis(phosphonic acid) (25)*



Tetraethyl [[{2,7-bis(bis(4-methoxyphenyl)amino)-9H-fluorene-9,9-diyl}bis(ethane-2,1-diyl)]bis(phosphonate) (**24**) (0.88 g, 0.93 mmol) was dissolved in anhydrous 1,4-dioxane (20 ml) under argon followed by dropwise addition of bromotrimethylsilane (1.96 ml, 14.88 mmol). The reaction was stirred for 20 h at 25 °C under argon

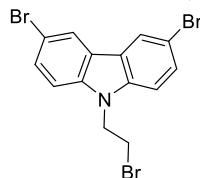
atmosphere. Afterwards, the solvent was distilled off under reduced pressure; solid residue was dissolved in methanol (10 ml), and distilled water was added dropwise (20 ml), until the solution became opaque, and was stirred for 3 h. The product was filtered off and washed with water to give 0.671 g (86 %) of reddish powder.

$^1H$  BMR (400 MHz,  $d_8$ -THF)  $\delta$  7.34 (d,  $J = 8.3$  Hz, 2H, Ar), 7.19 (d,  $J = 1.2$  Hz, 2H, Ar), 7.02 (d,  $J = 8.9$  Hz, 8H, Ar), 6.80 (d,  $J = 8.9$  Hz, 8H, Ar), 6.74 (dd,  $J = 8.2, 1.7$  Hz, 2H, Ar), 3.71 (s, 12H, 4  $\times$   $OCH_3$ ), 2.09 (d,  $J = 7.5$  Hz, 4H, 2  $\times$   $CH_2$ ), 0.99–0.85 (m, 4H, 2  $\times$   $CH_2$ ).

$^{13}\text{C}$  BMR (100 MHz,  $d_8$ -THF)  $\delta$  155.78, 148.68, 147.61, 141.09, 134.71, 125.67, 120.66, 118.88, 115.96, 114.59, 54.65, 31.70, 28.37.

Anal. calcd for  $\text{C}_{45}\text{H}_{46}\text{N}_2\text{O}_{10}\text{P}_2$ , %: C 64.59, H 5.54, N 3.35, found, %: C 64.56, H 5.67, N 3.35.

### 3,6-dibromo-9-(2-bromoethyl)-9H-carbazole (**26**)



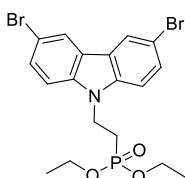
3,6-dibromo-9H-carbazole (2 g, 6.15 mmol) was dissolved in 1,2-dibromoethane (40 ml), and tetrabutylammonium bromide (0.198 g, 0.62 mmol) with 50 % KOH aqueous solution (1.72 ml, 30.77 mmol) were added subsequently. The reaction was stirred at 60 °C for three days (TLC, acetone:*n*-hexane, 1:23, *v/v*) after each 24 h adding 0.198 g of tetrabutylammonium bromide and 1.72 ml of 50 % aqueous KOH solution. After completion of the reaction, the extraction was done with dichloromethane. The organic layer was dried over anhydrous  $\text{Na}_2\text{SO}_4$ , and the solvent was distilled off under reduced pressure. The crude product was purified by column chromatography (acetone/*n*-hexane 3:22 *v/v*) to give 2.4 g (90 %) of the white crystalline material. M.p.=153–155 °C

$^1\text{H}$  NMR (400 MHz,  $\text{CDCl}_3$ )  $\delta$  8.07 (d,  $J = 1.8$  Hz, 2H, Ht); 7.54 (dd,  $J = 8.7, 1.8$  Hz, 2H, Ht), 7.25 (d,  $J = 8.7$  Hz, 2H, Ht); 4.59 (t,  $J = 7.2$  Hz, 2H,  $\text{NCH}_2$ ); 3.62 (t,  $J = 7.2$  Hz, 2H,  $\text{CH}_2$ ).

$^{13}\text{C}$  NMR (100 MHz,  $\text{CDCl}_3$ )  $\delta$  138.98, 129.43, 123.80, 123.53, 112.86, 110.31, 44.90, 28.09.

Anal. calcd for  $\text{C}_{14}\text{H}_{10}\text{NBr}_3$ , %: C 38.93, H 2.33, N 3.24, found, %: C 38.78, H 2.42, N 3.11.

### Diethyl [2-(3,6-dibromo-9H-carbazol-9-yl)ethyl]phosphonate (**27**)



Compound 3,6-dibromo-9-(2-bromoethyl)-9H-carbazole (**26**) (2.4 g, 5.55 mmol) was dissolved in triethylphosphite (20 ml), and the reaction mixture was heated at reflux for 18 h. After reaction completion (TLC, acetone: *n*-hexane, 2:3, *v/v*), the triethylphosphite was distilled off under reduced pressure. The crude product was purified by column chromatography (acetone/*n*-hexane 7:18 *v/v*) to give 2.56 g (95 %) of white crystalline material (M.p.=118–119 °C)

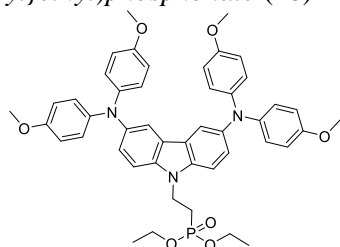
$^1\text{H}$  NMR (400 MHz,  $\text{CDCl}_3$ )  $\delta$  8.11 (d,  $J = 1.8$  Hz, 2H, Ht); 7.56 (dd,  $J = 8.7, 1.8$  Hz, 2H, Ht); 7.30 (d,  $J = 8.7$  Hz, 2H, Ht); 4.60–4.49 (m, 2H,  $\text{NCH}_2$ ); 4.04 (dq,  $J = 14.2, 7.1$  Hz, 4H,  $2 \times \text{OCH}_2$ ); 2.28–2.16 (m, 2H,  $\text{PCH}_2$ ); 1.24 (t,  $J = 7.1$  Hz, 6H,  $2 \times \text{CH}_3$ ).

$^{13}\text{C}$  NMR (100 MHz,  $\text{CDCl}_3$ )  $\delta$  138.65; 129.25; 123.71; 123.37; 112.50; 110.30;  $\delta$  61.99 (d,  $^3J_{\text{C,P}} = 6.6$  Hz), 37.26 (d,  $^2J_{\text{C,P}} = 1.7$  Hz), 25.20 (d,  $^1J_{\text{C,P}} = 139.0$  Hz), 16.35 (d,  $^2J_{\text{C,P}} = 6.0$  Hz).

Anal. calcd for  $\text{C}_{18}\text{H}_{20}\text{NBr}_2\text{O}_3\text{P}$ , %: C 44.20, H 4.12, N 2.86, found, %: C 44.09, H 4.26, N 3.02.



Diethyl  
yl}ethyl)phosphonate (28)



(2-{3,6-bis[bis(4-methoxyphenyl)amino]-9H-carbazol-9-

yl}ethyl)phosphonate (27) (1 g, 2.04 mmol) and 4,4'-dimethoxydiphenylamine (1.37 g, 6.13 mmol) in anhydrous toluene (50 ml) was purged with argon for 20 min. Afterwards, palladium(II) acetate (0.137 g, 0.613 mmol), tri-*tert*-butylphosphonium tetrafluoroborate (0.35 g, 1.23 mmol) and sodium *tert*-butoxide (0.59 g, 6.13 mmol) were added, and

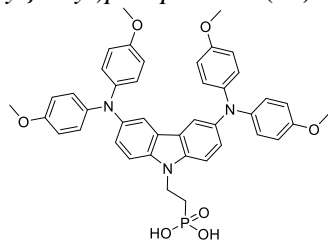
the solution was refluxed under argon atmosphere for 5 h. After completion (TLC, acetone: *n*-hexane, 2:3, *v/v*), the reaction mixture was filtered through Celite. The solvent was removed under reduced pressure, and the crude product was purified by column chromatography (acetone/ *n*-hexane 7:18 *v/v*) to give 1 g (63 %) of greenish powder.

<sup>1</sup>H NMR (400 MHz, DMSO-*d*<sub>6</sub>) δ 7.64 (d, *J* = 2.2 Hz, 2H, Ht), 7.46 (d, *J* = 8.7 Hz, 2H, Ht), 7.11 (dd, *J* = 8.7, 2.2 Hz, 2H, Ht), 6.86–6.74 (m, 16H, Ar), 4.50 (dt, *J* = 13.8, 7.3 Hz, 2H, NCH<sub>2</sub>), 3.92 (p, *J* = 7.2 Hz, 4H, 2× OCH<sub>2</sub>), 3.67 (s, 12H, 4× OCH<sub>3</sub>), 2.26 (dt, *J* = 18.2, 7.3 Hz, 2H, PCH<sub>2</sub>), 1.12 (t, *J* = 7.0 Hz, 6H, 2× CH<sub>3</sub>).

<sup>13</sup>C NMR (100 MHz, DMSO-*d*<sub>6</sub>) δ 154.16, 142.08, 140.25, 136.67, 124.39, 123.67, 122.90, 116.94, 114.60, 110.28, 61.90 (d, <sup>2</sup>*J*<sub>(C,P)</sub> = 6.5 Hz), 55.15, 30.22, 28.30 (d, <sup>1</sup>*J*<sub>(C,P)</sub> = 280.3 Hz), 16.45 (d, <sup>3</sup>*J*<sub>(C,P)</sub> = 6.1 Hz).

Anal. calcd for C<sub>46</sub>H<sub>48</sub>N<sub>3</sub>O<sub>7</sub>P, %: C 70.30; H 6.16; N 5.35, found, %: C 70.14; H 6.29; N 5.56.

Diethyl  
yl}ethyl)phosphonate (29)



(2-{3,6-bis[bis(4-methoxyphenyl)amino]-9H-carbazol-9-

yl}ethyl)phosphonate (28) (0.4 g, 0.51 mmol) was dissolved in anhydrous 1,4-dioxane (15 ml) under argon. Afterwards, bromotrimethylsilane (0.67 ml, 5.08 mmol) was added dropwise. The reaction was stirred for 24 h at 25 °C under argon atmosphere. Afterwards, the solvent was distilled off under reduced pressure; the solid residue

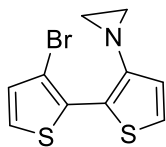
was dissolved in methanol (10 ml), and distilled water was added dropwise (10 ml), until the solution became opaque, and was stirred for 15 h. The product was filtered and washed with water to give 0.321 g (86 %) of greenish powder.

<sup>1</sup>H NMR (400 MHz, DMSO-*d*<sub>6</sub>) δ 7.64 (s, 2H, Ht), 7.42 (d, *J* = 8.8 Hz, 2H, Ht), 7.15–7.07 (m, 2H, Ht), 6.87–6.74 (m, 16H, Ar), 4.50–4.44 (m, 2H, NCH<sub>2</sub>), 3.67 (s, 12H, 4×OCH<sub>3</sub>), 2.02 (dt, *J* = 17.3, 8.0 Hz, 2H, PCH<sub>2</sub>).

<sup>13</sup>C NMR (100 MHz, DMSO-*d*<sub>6</sub>) δ 154.16, 142.09, 140.22, 136.6, 124.60, 123.66, 122.88, 117.15, 114.63, 110.01, 66.36, 55.16, 30.51 (d, <sup>1</sup>*J*<sub>(C,P)</sub> = 180.5 Hz).

Anal. calcd for C<sub>42</sub>H<sub>40</sub>N<sub>3</sub>O<sub>7</sub>P, %: C 69.13, H 5.52, N 5.76, found, %: C 68.89, H 5.38, N 5.53.

#### 1-(3'-bromo[2,2'-bithiophen]-3-yl)aziridine (**30**)



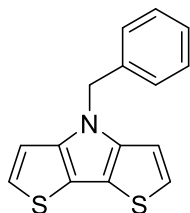
Under argon atmosphere, a mixture of 3,3'-dibromo-2,2'-bithiophene (0.5 g, 1.54 mmol), palladium (II) acetate (0.017 g, 0.077 mmol), ( $\pm$ )-BINAP (0.096 g, 0.154 mmol) and sodium *tert*-butoxide (0.355 g, 3.69 mmol) was mixed in anhydrous toluene (15 ml). After stirring for 10 min, 2-bromoethylamine hydrobromide (0.34 g, 1.69 mmol) was added to the reaction mixture, and the solution was stirred overnight at 110 °C temperature (TLC: *n*-hexane). The mixture was extracted with ethyl acetate. The organic layer was washed three times with water, dried over anhydrous Na<sub>2</sub>SO<sub>4</sub>, filtered, and the solvent was removed under reduced pressure. The material was purified by column chromatography on silica gel with hexane and dried under vacuum to give a white solid (16 %, 0.07 g).

<sup>1</sup>H NMR (400 MHz, DMSO-*d*<sub>6</sub>)  $\delta$  7.72 (d, *J* = 5.4 Hz, 1H, Ht), 7.52 (d, *J* = 5.4 Hz, 1H, Ht), 7.17 (d, *J* = 5.4 Hz, 1H, Ht), 6.91 (d, *J* = 5.4 Hz, 1H, Ht), 2.03 (s, 4H, 2  $\times$  CH<sub>2</sub>).

<sup>13</sup>C NMR (100 MHz, DMSO-*d*<sub>6</sub>)  $\delta$  152.45, 130.43, 129.80, 127.41, 125.62, 123.32, 116.32, 108.59, 29.49.

Anal. calcd. for C<sub>10</sub>H<sub>8</sub>BrNS<sub>2</sub>, %: C 41.97, H 2.82, N 4.89; found, %: C 42.08, H 2.85, N 4.76.

#### 4-benzyl-4H-bisthieno[3,2-*b*:2',3'-*d*]pyrrole (**31**)



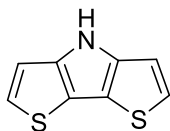
Under argon atmosphere, a mixture of 3,3'-dibromo-2,2'-bithiophene (4 g, 12.3 mmol), palladium (II) acetate (0.14 g, 0.62 mmol), ( $\pm$ )-BINAP (0.77 g, 1.23 mmol) and sodium *tert*-butoxide (2.93 g, 29.6 mmol) was mixed in anhydrous toluene (280 ml). After stirring for 30 min, benzylamine (1.4 ml, 12.96 mmol) was added to the reaction mixture, and the solution was refluxed for 20 hours (TLC: acetone/ *n*-hexane 1:24 *v/v*). The mixture was extracted with ethyl acetate. The organic layer was washed three times with water, dried over anhydrous Na<sub>2</sub>SO<sub>4</sub>, filtered, and the solvent was removed under reduced pressure. The material was purified by column chromatography (acetone/ *n*-hexane 1:249 *v/v*) to give a white powder (45 %, 1.5 g).

<sup>1</sup>H NMR (400 MHz, CDCl<sub>3</sub>)  $\delta$  7.33–7.23 (m, 3H, Ar), 7.17 (d, *J* = 6.4 Hz, 2H, Ar), 7.08 (d, *J* = 5.3 Hz, 2H, Ht), 6.86 (d, *J* = 5.3 Hz, 2H, Ht), 5.35 (s, 2H, NCH<sub>2</sub>).

<sup>13</sup>C NMR (100 MHz, CDCl<sub>3</sub>)  $\delta$  145.27, 137.19, 128.93, 127.93, 127.12, 123.14, 115.41, 111.28, 51.09.

Anal. calcd. for C<sub>15</sub>H<sub>11</sub>NS<sub>2</sub>, %: C 66.88, H 4.12, N 5.20; found, %: C 66.97, H 4.06, N 5.38.

#### 4H-bisthieno[3,2-*b*:2',3'-*d*]pyrrole (**32**)



4-benzyl-4H-bisthieno[3,2-*b*:2',3'-*d*]pyrrole (**31**) (0.5 g, 1.86 mmol) was dissolved in dimethyl sulfoxide (15 ml); 1 M tetrahydrofuran solution of potassium *tert*-butoxide was added (18 ml, 18.6 mol), and the reaction was stirred at 20 °C overnight (TLC: acetone/ *n*-

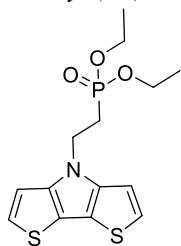
hexane 3:22 *v/v*). The mixture was quenched with water (150 ml), and the precipitate was filtered off. The material was purified by column chromatography (acetone: *n*-hexane 2:23 *v/v*) to give white powder (57 %, 0.190 g). M.p. 164 °C

<sup>1</sup>H NMR (400 MHz, CDCl<sub>3</sub>) δ 8.28 (s, 1H, NH), 7.16 (d, *J* = 5.3 Hz, 2H, Ht 2,6-H), 6.95 (d, *J* = 5.3 Hz, 2H, Ht 3,5-H).

<sup>13</sup>C NMR (100 MHz, CDCl<sub>3</sub>) δ 144.25, 123.69, 115.35, 112.43.

Anal. calcd. for C<sub>8</sub>H<sub>5</sub>NS<sub>2</sub>, %: C 53.60, H 2.81, N 7.81; found, %: C 53.74, H 2.76, N 7.95.

### Diethyl (2-(4*H*-bisthieno[3,2-*b*:2',3'-*d*]pyrrol-4-yl)ethyl)phosphonate (**33**)



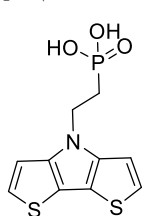
A mixture of 4*H*-bisthieno[3,2-*b*:2',3'-*d*]pyrrole (**32**) (0.65 g, 3.62 mmol), diethyl 2-bromoethylphosphonate (1.22 ml, 7.25 mmol) and sodium *tert*-butoxide (0.873 g, 9.07 mmol) was mixed in anhydrous 1,4-dioxane (15 ml), and the solution was stirred overnight at 50 °C under argon atmosphere (TLC: acetone/*n*-hexane 3:22 *v/v*). The mixture was extracted with ethyl acetate. The organic layer was washed three times with water, dried over anhydrous Na<sub>2</sub>SO<sub>4</sub>, filtered, and the solvent was removed under reduced pressure. The material was purified by column chromatography (acetone/*n*-hexane 13:37 *v/v*) to give a colourless resin (38 %, 0.47 g).

<sup>1</sup>H NMR (400 MHz, DMSO-*d*<sub>6</sub>) δ 7.34 (d, *J* = 5.4 Hz, 2H, Ht 2,6-H), 7.26 (d, *J* = 5.4 Hz, 2H, Ht 3,5-H), 4.48 (dt, <sup>3</sup>*J*<sub>(H,P)</sub> = 14.3, 7.2 Hz, 2H, NCH<sub>2</sub>), 3.92–3.82 (m, 4H, 2 × OCH<sub>2</sub>), 2.32 (dt, <sup>2</sup>*J*<sub>(H,P)</sub> = 18.0, 7.2 Hz, 2H, PCH<sub>2</sub>), 1.10 (t, *J* = 7.1 Hz, 6H, 2 × CH<sub>3</sub>).

<sup>13</sup>C NMR (100 MHz, DMSO-*d*<sub>6</sub>) δ 144.44, 123.37, 113.90, 112.09, 61.09 (d, <sup>2</sup>*J*<sub>(C,P)</sub> = 6.2 Hz), 40.86 (d, <sup>2</sup>*J*<sub>(C,P)</sub> = 3.1 Hz), 25.71 (d, <sup>1</sup>*J*<sub>(C,P)</sub> = 136.4 Hz), 16.02 (d, <sup>3</sup>*J*<sub>(C,P)</sub> = 6.0 Hz).

Anal. calcd. For C<sub>14</sub>H<sub>18</sub>NO<sub>3</sub>PS<sub>2</sub>, %: C 48.97, H 5.28, N 4.08; found, %: C 49.14, H 5.13, N 4.19.

### [2-(4*H*-bisthieno[3,2-*b*:2',3'-*d*]pyrrol-4-yl)ethyl]phosphonic acid (**34**)



Diethyl (2-(4*H*-bisthieno[3,2-*b*:2',3'-*d*]pyrrol-4-yl)ethyl)phosphonate (**33**) (0.3 g, 0.87 mmol) was dissolved in anhydrous 1,4-dioxane (10 ml) under argon atmosphere followed by dropwise addition of bromotrimethylsilane (1.15 ml, 8.73 mmol); the reaction was stirred for 24 h at 25 °C under argon atmosphere. Afterwards, methanol (0.5 ml) was added and stirring continued for 3 h. Finally, distilled water was added dropwise (10 ml), until the solution became opaque,

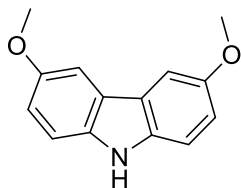
and it was stirred overnight. The product was filtered off and washed with water to give 0.185 g (74 %) of white powder.

<sup>1</sup>H NMR (400 MHz, DMSO-*d*<sub>6</sub>) δ 7.20 (d, *J* = 5.4 Hz, 2H, Ht 2,6-H), 7.09 (d, *J* = 5.4 Hz, 2H, Ht 3,5-H), 4.39 (dt, *J* = 14.3, 7.2 Hz, 2H, NCH<sub>2</sub>), 2.10–1.91 (m, 2H, PCH<sub>2</sub>).

<sup>13</sup>C NMR (101 MHz, DMSO) δ 145.08, 123.63, 114.58, 112.66, 41.55 (d, <sup>2</sup>*J*<sub>(C,P)</sub> = 3.1 Hz) 28.46(d, <sup>1</sup>*J*<sub>(C,P)</sub> = 30.1 Hz).

Anal. calcd. For C<sub>10</sub>H<sub>10</sub>NO<sub>3</sub>PS<sub>2</sub>, %: C 41.81, H 3.51, N 4.88; found, %: C 41.95, H 3.72, N 4.71.

### 3,6-dimethoxy-9H-carbazole (**35**)



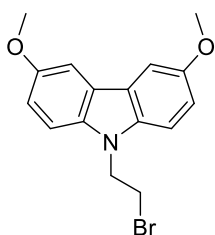
Sodium (10 g, 434.98 mmol) was dissolved in anhydrous methanol (170 ml) and 3,6-dibromocarbazole (10 g, 30.76 mmol), copper(I)-iodide (24.61 g, 129.23 mmol) and anhydrous DMF (80 ml) were added and refluxed for 6 h (TLC, acetone: *n*-hexane 4:21, *v/v*). Afterwards, tetrahydrofuran (100 ml) was added; the mixture was filtered over Celite; half of the solvent was removed under reduced pressure, and the mixture was extracted with dichloromethane. The organic layer was washed three times with water, dried over anhydrous Na<sub>2</sub>SO<sub>4</sub>, filtered, and the solvent was removed under reduced pressure. The material was purified by column chromatography (tetrahydrofuran *n*-hexane 3:22 *v/v*) to give 5.62 g (80 %) as a white solid. M.p. 110–112 °C

<sup>1</sup>H NMR (400 MHz, CDCl<sub>3</sub>) δ 7.77 (s, H, NH), 7.47 (s, 2H, Ht), 7.30–7.20 (m, 2H, Ht), 7.04 (dd, *J* = 8.8, 2.5 Hz, 2H, Ht), 3.91 (s, 6H, 2 × OCH<sub>3</sub>).

<sup>13</sup>C NMR (100 MHz, CDCl<sub>3</sub>) δ 128.52, 123.83, 116.19, 112.30, 111.71, 103.00, 56.20.

Anal. calcd for C<sub>14</sub>H<sub>13</sub>NO<sub>2</sub>, %: C 73.99, H 5.77, N 6.16, found, %: C 73.86, H 5.92, N 6.23.

### 9-(2-bromoethyl)-3,6-dimethoxy-9H-carbazole (**36**)



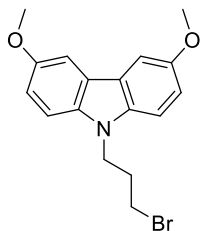
3,6-dimethoxy-9H-carbazole (**35**) (0.534 g, 2.35 mmol) was dissolved in 1,2-dibromoethane (8 ml, 92.4 mmol); tetrabutylammonium bromide (0.08 g, 0.25 mmol) and 50 % KOH aqueous solution (0.62 ml, 11.00 mmol) were added subsequently. The reaction was stirred at 50 °C for two days (TLC, acetone: *n*-hexane 2:23, *v/v*); after each 24 h, 0.03 g (0.09 mmol) of tetrabutylammonium bromide and 0.3 ml of 50 % aqueous KOH solution were added. After completion of the reaction, the extraction was done with dichloromethane. The organic layer was dried over anhydrous Na<sub>2</sub>SO<sub>4</sub>, and the solvent was distilled off under reduced pressure. The crude product was purified by column chromatography (acetone *n*-hexane 1:49 *v/v*) to give 0.352 g (60 %) of colourless solid.

<sup>1</sup>H NMR (400 MHz, CDCl<sub>3</sub>) δ 7.51 (d, *J* = 2.5 Hz, 2H, Ht), 7.29 (d, *J* = 8.8 Hz, 2H, Ht), 7.10 (dd, *J* = 8.8, 2.5 Hz, 2H, Ht), 4.62 (t, *J* = 7.5 Hz, 2H, NCH<sub>2</sub>), 3.93 (s, 6H, 2 × OCH<sub>3</sub>), 3.62 (t, *J* = 7.5 Hz, 2H, CH<sub>2</sub>).

<sup>13</sup>C NMR (100 MHz, CDCl<sub>3</sub>) δ 153.85, 135.65, 123.39, 115.30, 109.41, 103.45, 56.27, 45.07, 28.55.

Anal. calcd for C<sub>16</sub>H<sub>16</sub>O<sub>2</sub>NBr, %: C 57.50, H 4.83, N 4.19, found, %: C 57.39, H 4.86, N 4.15.

**9-(3-bromopropyl)-3,6-dimethoxy-9H-carbazole (37)**



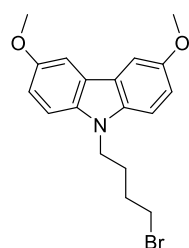
3,6-dimethoxy-9H-carbazole (**35**) (0.5 g, 2.20 mmol) was dissolved in 1,3-dibromopropane (5.6 ml, 55 mmol); tetrabutylammonium bromide (0.071 g, 0.22 mmol) and 50 % KOH aqueous solution (0.62 ml, 11.00 mmol) were added subsequently. The reaction was stirred at 50 °C for two days (TLC, acetone: *n*-hexane 2:23, *v/v*); after each 24 h, 0.03 g (0.09 mmol) of tetrabutylammonium bromide and 0.3 ml of 50 % aqueous KOH solution were added. After completion of the reaction, the extraction was done with dichloromethane. The organic layer was dried over anhydrous Na<sub>2</sub>SO<sub>4</sub>, and the solvent was distilled off under reduced pressure. The crude product was purified by column chromatography (acetone *n*-hexane 1:49 *v/v*) to give 0.48 g (52 %) of colourless solid.

<sup>1</sup>H NMR (400 MHz, CDCl<sub>3</sub>) δ 7.52 (d, *J* = 2.5 Hz, 2H, Ht), 7.34 (d, *J* = 8.8 Hz, 2H, Ht), 7.10 (dd, *J* = 8.9, 2.5 Hz, 2H, Ht), 4.41 (t, *J* = 6.5 Hz, 2H, NCH<sub>2</sub>), 3.93 (s, 6H, 2 × OCH<sub>3</sub>), 3.34 (t, *J* = 6.1 Hz, 2H, CH<sub>2</sub>), 2.38 (p, *J* = 6.3 Hz, 2H, CH<sub>2</sub>).

<sup>13</sup>C NMR (100 MHz, CDCl<sub>3</sub>) δ 153.45, 136.00, 123.02, 115.14, 109.48, 103.21, 56.17, 41.09, 32.14, 30.94.

Anal. calcd for C<sub>17</sub>H<sub>18</sub>BrNO<sub>2</sub>, %: C 58.63, H 5.21, N 4.02, found, %: C 58.38, H 5.39, N 4.25.

**9-(4-bromobutyl)-3,6-dimethoxy-9H-carbazole (38)**



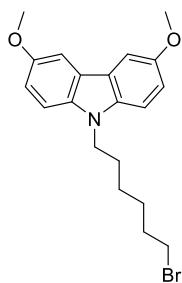
3,6-dimethoxy-9H-carbazole (**35**) (0.5 g, 2.20 mmol) was dissolved in 1,4-dibromobutane (6 ml, 55 mmol); tetrabutylammonium bromide (0.071 g, 0.22 mmol) and 50 % KOH aqueous solution (0.62 ml, 11.00 mmol) were added subsequently. The reaction was stirred at 50 °C for two days (TLC, acetone: *n*-hexane 2:23, *v/v*); after each 24 h, 0.03 g (0.09 mmol) of tetrabutylammonium bromide and 0.3 ml of 50 % aqueous KOH solution were added. After completion of the reaction, the extraction was done with dichloromethane. The organic layer was dried over anhydrous Na<sub>2</sub>SO<sub>4</sub>, and the solvent was distilled off under reduced pressure. The crude product was purified by column chromatography (acetone: *n*-hexane 1:49 *v/v*) to give 0.52 g (65 %) of white powder.

<sup>1</sup>H NMR (400 MHz, CDCl<sub>3</sub>) δ 7.52 (d, *J* = 2.5 Hz, 2H, Ht), 7.25 (d, *J* = 8.7 Hz, 2H, Ht), 7.09 (dd, *J* = 8.8, 2.5 Hz, 2H, Ht), 4.25 (t, *J* = 6.9 Hz, 2H, NCH<sub>2</sub>), 3.92 (s, 6H, 2 × OCH<sub>3</sub>), 3.34 (t, *J* = 6.5 Hz, 2H, CH<sub>2</sub>), 2.00 (quin, *J* = 6.9 Hz, 2H, CH<sub>2</sub>), 1.91–1.79 (m, 2H, CH<sub>2</sub>).

<sup>13</sup>C NMR (100 MHz, CDCl<sub>3</sub>) δ 153.31, 135.94, 122.91, 115.10, 109.40, 103.19, 56.17, 42.38, 33.21, 30.25, 27.82.

Anal. calcd for C<sub>18</sub>H<sub>20</sub>BrNO<sub>2</sub>, %: C 59.68, H 5.56, N 3.87, found, %: C 59.92, H 5.43, N 4.12.

9-(6-bromohexyl)-3,6-dimethoxy-9H-carbazole (**39**)



3,6-dimethoxy-9H-carbazole (**35**) (0.5 g, 2.20 mmol) was dissolved in 1,6-dibromohexane (8.5 ml, 55 mmol); tetrabutylammonium bromide (0.071 g, 0.22 mmol) and 50 % KOH aqueous solution (0.62 ml, 11.00 mmol) were added subsequently. The reaction was stirred at 60 °C for 24 h (TLC, acetone: *n*-hexane 2:23, *v/v*). After completion of the reaction, the extraction was done with dichloromethane. The organic layer was dried over anhydrous Na<sub>2</sub>SO<sub>4</sub>, and the solvent was distilled off under reduced pressure. The crude product was purified by

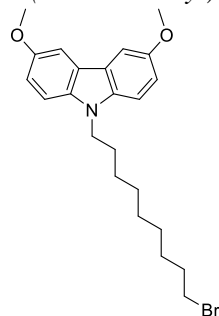
column chromatography (acetone: *n*-hexane 1:24 *v/v*) to give 0.58 g (68 %) of white powder.

<sup>1</sup>H NMR (400 MHz, CDCl<sub>3</sub>) δ 7.53 (s, 2H, Ht), 7.26 (d, *J* = 8.9 Hz, 2H, Ht), 7.09 (dd, *J* = 8.9, 2.6 Hz, 2H, Ht), 4.23 (t, *J* = 7.0 Hz, 2H, NCH<sub>2</sub>), 3.93 (s, 6H, 2× OCH<sub>3</sub>), 3.34 (t, *J* = 6.7 Hz, 2H, CH<sub>2</sub>), 1.90–1.73 (m, 4H, 2× CH<sub>2</sub>), 1.51–1.40 (m, 2H, CH<sub>2</sub>), 1.35 (quin, *J* = 7.9 Hz, 2H, CH<sub>2</sub>).

<sup>13</sup>C NMR (100 MHz, CDCl<sub>3</sub>) δ 153.32, 136.18, 122.92, 115.15, 109.58, 103.23, 56.30, 43.19, 33.88, 32.70, 29.13, 28.05, 26.58.

Anal. calcd for C<sub>20</sub>H<sub>24</sub>BrNO<sub>2</sub>, %: C 61.54, H 6.20, N 3.59, found, %: C 61.75, H 6.02, N 3.73.

9-(9-bromononyl)-3,6-dimethoxy-9H-carbazole (**40**)



3,6-dimethoxy-9H-carbazole (**35**) (0.5 g, 2.20 mmol) was dissolved in 1,9-dibromononane (11.2 ml, 55 mmol); tetrabutylammonium bromide (0.071 g, 0.22 mmol) and 50 % KOH aqueous solution (0.62 ml, 11.00 mmol) were added subsequently. The reaction was stirred at 70 °C for 24 h (TLC, acetone: *n*-hexane 2:23, *v/v*). After completion of the reaction, the extraction was done with dichloromethane. The organic layer was dried over anhydrous Na<sub>2</sub>SO<sub>4</sub>, and the solvent was distilled off under reduced pressure. The crude product was purified by column chromatography (acetone: *n*-hexane 1:24

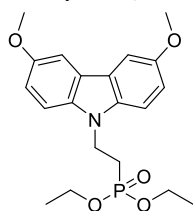
*v/v*) to give 0.63 g (66 %) of white powder.

<sup>1</sup>H NMR (400 MHz, CDCl<sub>3</sub>) δ 7.52 (s, 2H, Ht), 7.26 (d, *J* = 8.8 Hz, 2H, Ht), 7.09 (dd, *J* = 9.0, 2.5 Hz, 2H, Ht), 4.21 (t, *J* = 7.1 Hz, 2H, NCH<sub>2</sub>), 3.93 (s, 6H, 2× OCH<sub>3</sub>), 3.36 (t, *J* = 6.9 Hz, 2H, CH<sub>2</sub>), 1.87–1.75 (m, 4H, 2× CH<sub>2</sub>), 1.43–1.19 (m, 10H, 5× CH<sub>2</sub>).

<sup>13</sup>C NMR (100 MHz, CDCl<sub>3</sub>) δ 153.24, 136.20, 122.86, 115.09, 109.60, 103.16, 56.27, 43.35, 34.11, 32.86, 29.38, 29.36, 29.23, 28.73, 28.19, 27.33.

Anal. calcd for C<sub>23</sub>H<sub>30</sub>BrNO<sub>2</sub>, %: C 63.89, H 6.99, N 3.24, found, %: C 63.67, H 7.28, N 3.49.

**Diethyl [2-(3,6-dimethoxy-9H-carbazol-9-yl)ethyl]phosphonate (41)**



9-(2-bromoethyl)-3,6-dimethoxy-9H-carbazole (**36**) (0.316 g, 0.95 mmol) was dissolved in triethylphosphite (2.7 ml, 15.74 mmol), and the reaction mixture was heated at reflux for 18 h. After reaction completion (TLC, acetone: *n*-hexane 1:4, *v/v*), the triethylphosphite was distilled off under reduced pressure. The crude product was purified by column chromatography (acetone/ *n*-hexane 1:1 *v/v*) to give 0.353 g

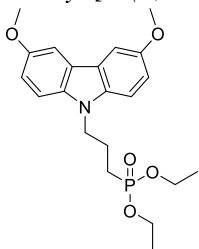
(95 %) of clear liquid.

$^1\text{H NMR}$  (400 MHz,  $\text{CDCl}_3$ )  $\delta$  7.52 (d,  $J = 2.5$  Hz, 2H, Ht), 7.30 (d,  $J = 8.8$  Hz, 2H, Ht), 7.10 (dd,  $J = 8.8, 2.5$  Hz, 2H, Ht), 4.60–4.49 (m, 2H,  $\text{NCH}_2$ ), 4.09–4.03 (m, 4H,  $2 \times \text{OCH}_2$ ), 3.93 (s, 6H,  $2 \times \text{OCH}_3$ ), 2.29–2.15 (m, 2H,  $\text{CH}_2$ ), 1.28 (t,  $J = 7.1$  Hz, 6H,  $2 \times \text{CH}_3$ ).

$^{13}\text{C NMR}$  (100 MHz,  $\text{CDCl}_3$ )  $\delta$  153.67, 135.46, 123.37, 115.20, 109.49, 103.46, 61.93 (d,  $^2J_{\text{C,P}} = 6.1$  Hz), 56.28, 37.31, 25.47 (d,  $^1J_{\text{C,P}} = 136.2$  Hz), 16.53 (d,  $^3J_{\text{C,P}} = 6.1$  Hz).

Anal. calcd for  $\text{C}_{20}\text{H}_{26}\text{NO}_5\text{P}$ , %: C 61.37, H 6.70, N 3.58, found, %: C 61.32, H 6.73, N 3.55.

**Diethyl [3-(3,6-dimethoxy-9H-carbazol-9-yl)propyl]phosphonate (42)**



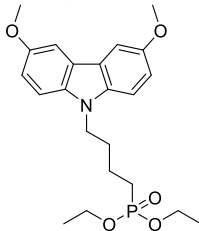
9-(3-bromopropyl)-3,6-dimethoxy-9H-carbazole (**37**) (0.4 g, 1.15 mmol) was dissolved in triethylphosphite (8 ml, 47.2 mmol), and the reaction mixture was heated at reflux for 19 h. After reaction completion (TLC, acetone: *n*-hexane 8:17, *v/v*), the triethylphosphite was distilled off under reduced pressure. The crude product was purified by column chromatography (acetone/ *n*-hexane 15:35 *v/v*) to give 0.45 g (97 %) of yellowish resin.

$^1\text{H NMR}$  (400 MHz,  $\text{CDCl}_3$ )  $\delta$  7.52 (d,  $J = 2.5$  Hz, 2H, Ht), 7.30 (d,  $J = 8.8$  Hz, 2H, Ht), 7.09 (dd,  $J = 8.8, 2.5$  Hz, 2H, Ht), 4.34 (t,  $J = 6.9$  Hz, 2H,  $\text{NCH}_2$ ), 4.04 (pd,  $J = 7.3, 2.3$  Hz, 4H,  $2 \times \text{OCH}_2$ ), 3.93 (s, 6H,  $2 \times \text{OCH}_3$ ), 2.15 (dp,  $J = 14.6, 7.2$  Hz, 2H,  $\text{CH}_2$ ), 1.71 (dt,  $J = 18.6, 7.8$  Hz, 2H,  $\text{CH}_2$ ), 1.27 (t,  $J = 7.0$  Hz, 6H,  $2 \times \text{CH}_3$ ).

$^{13}\text{C NMR}$  (100 MHz,  $\text{CDCl}_3$ )  $\delta$  153.46, 136.07, 123.04, 115.22, 109.59, 103.26, 61.77 (d,  $^2J_{\text{C,P}} = 6.5$  Hz), 56.27, 43.23 (d,  $^3J_{\text{C,P}} = 15.5$  Hz), 23.16 (d,  $^1J_{\text{C,P}} = 142.4$  Hz), 22.40 (d,  $^2J_{\text{C,P}} = 4.9$  Hz), 16.54 (d,  $^3J_{\text{C,P}} = 5.9$  Hz).

Anal. calcd for  $\text{C}_{21}\text{H}_{28}\text{NO}_5\text{P}$ , %: C 62.21, H 6.96, N 3.45, found, %: C 62.39, H 6.77, N 3.69.

**Diethyl [4-(3,6-dimethoxy-9H-carbazol-9-yl)butyl]phosphonate (43)**



9-(4-bromobutyl)-3,6-dimethoxy-9H-carbazole (**38**) (0.48 g, 1.32 mmol) was dissolved in triethylphosphite (9 ml, 53 mmol), and the reaction mixture was refluxed overnight. After reaction completion (TLC, acetone: *n*-hexane 7:18, *v/v*), the triethylphosphite was distilled off under reduced pressure. The

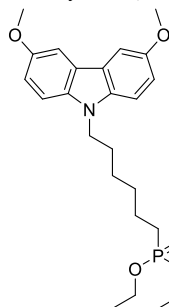
crude product was purified by column chromatography (acetone: *n*-hexane 7:18 *v/v*) to give 0.54 g (97 %) of yellowish resin.

$^1\text{H}$  NMR (400 MHz,  $\text{CDCl}_3$ )  $\delta$  7.52 (d,  $J = 2.5$  Hz, 2H, Ar), 7.26 (d,  $J = 8.9$  Hz, 2H, Ar), 7.08 (dd,  $J = 8.8, 2.5$  Hz, 2H, Ar), 4.24 (t,  $J = 7.0$  Hz, 2H,  $\text{NCH}_2$ ), 4.06–3.97 (m, 4H,  $2 \times \text{OCH}_2$ ), 3.93 (s, 6H,  $2 \times \text{OCH}_3$ ), 1.99–1.89 (m, 2H,  $\text{CH}_2$ ), 1.76–1.57 (m, 4H,  $2 \times \text{CH}_2$ ), 1.25 (t,  $J = 7.1$  Hz, 6H,  $2 \times \text{CH}_3$ ).

$^{13}\text{C}$  NMR (100 MHz,  $\text{CDCl}_3$ )  $\delta$  153.36, 136.08, 122.97, 115.14, 109.52, 103.26, 61.63 (d,  $^2J_{\text{C,P}} = 6.5$  Hz), 56.28, 42.86, 30.02 (d,  $^3J_{\text{C,P}} = 15.2$  Hz), 25.56 (d,  $^1J_{\text{C,P}} = 141.4$  Hz), 20.54 (d,  $^2J_{\text{C,P}} = 5.1$  Hz), 16.52 (d,  $^3J_{\text{C,P}} = 6.0$  Hz).

Anal. calcd for  $\text{C}_{22}\text{H}_{30}\text{NO}_5\text{P}$ , %: C 63.00, H 7.21, N 3.34, found, %: C 62.83, H 6.95, N 3.59.

**Diethyl [6-(3,6-dimethoxy-9H-carbazol-9-yl)hexyl]phosphonate (44)**



9-(6-bromohexyl)-3,6-dimethoxy-9H-carbazole (**39**) (0.5 g, 1.28 mmol) was dissolved in triethylphosphite (9 ml, 52 mmol), and the reaction mixture was refluxed for 19 h. After reaction completion (TLC, acetone: *n*-hexane 7:18, *v/v*), the triethylphosphite was distilled off under reduced pressure. The crude product was purified by column chromatography (acetone: *n*-hexane 7:18 *v/v*) to give 0.45 g (79 %) of yellowish resin.

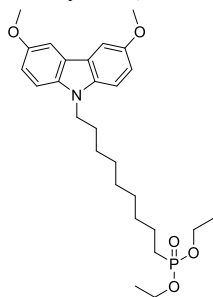
$^1\text{H}$  NMR (400 MHz,  $\text{CDCl}_3$ )  $\delta$  7.52 (d,  $J = 2.4$  Hz, 2H, Ht), 7.26 (d,  $J = 8.9$  Hz, 2H, Ht), 7.09 (dd,  $J = 8.8, 2.5$  Hz, 2H, Ht), 4.22 (t,  $J = 7.1$  Hz, 2H,  $\text{NCH}_2$ ), 4.11–4.00 (m, 4H,  $2 \times \text{OCH}_2$ ), 3.93 (s, 6H,

$2 \times \text{OCH}_3$ ), 1.83 (p,  $J = 7.1$  Hz, 2H,  $\text{CH}_2$ ), 1.71–1.60 (m, 2H,  $\text{CH}_2$ ), 1.60–1.49 (m, 2H,  $\text{CH}_2$ ), 1.43–1.33 (m, 4H,  $2 \times \text{CH}_2$ ), 1.29 (t,  $J = 7.0$  Hz, 6H,  $2 \times \text{CH}_3$ ).

$^{13}\text{C}$  NMR (100 MHz,  $\text{CDCl}_3$ )  $\delta$  153.27, 136.15, 122.87, 115.10, 109.56, 103.19, 61.52 (d,  $^2J_{\text{C,P}} = 6.5$  Hz), 56.27, 43.24, 30.45 (d,  $^3J_{\text{C,P}} = 16.7$  Hz), 29.05, 26.93, 25.67 (d,  $^1J_{\text{C,P}} = 140.6$  Hz), 22.44 (d,  $^2J_{\text{C,P}} = 5.2$  Hz), 16.58 (d,  $^3J_{\text{C,P}} = 6.0$  Hz).

Anal. calcd for  $\text{C}_{24}\text{H}_{34}\text{NO}_5\text{P}$ , %: C 64.41, H 7.66, N 3.13, found, %: C 64.18, H 7.85, N 2.98.

**Diethyl [9-(3,6-dimethoxy-9H-carbazol-9-yl)nonyl]phosphonate (45)**



9-(9-bromononyl)-3,6-dimethoxy-9H-carbazole (**40**) (0.58 g, 1.34 mmol) was dissolved in triethylphosphite (9 ml, 51 mmol), and the reaction mixture was refluxed overnight. After reaction completion (TLC, acetone: *n*-hexane 7:18, *v/v*), the triethylphosphite was distilled off under reduced pressure. The crude product was purified by column chromatography (acetone: *n*-hexane 7:18 *v/v*) to give 0.64 g (97 %) of yellowish resin.

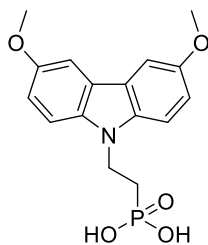
$^1\text{H}$  NMR (400 MHz,  $\text{CDCl}_3$ )  $\delta$  7.52 (d,  $J = 2.5$  Hz, 2H, Ht), 7.26 (d,  $J = 8.8$  Hz, 2H, Ht), 7.09 (dd,  $J = 8.8, 2.5$  Hz, 2H, Ht), 4.21 (t,  $J = 7.2$  Hz, 2H,  $\text{NCH}_2$ ), 4.13–4.01 (m, 4H,  $2 \times \text{OCH}_2$ ), 3.93 (s, 6H,  $2 \times \text{OCH}_3$ ), 1.81 (p,  $J = 7.3$  Hz, 2H,  $\text{CH}_2$ ), 1.75–1.63 (m, 2H,  $\text{CH}_2$ ), 1.62–1.49 (m, 2H,  $\text{CH}_2$ ), 1.36–1.20 (m, 16H, Aliph).



$^{13}\text{C}$  NMR (100 MHz,  $\text{CDCl}_3$ )  $\delta$  153.23, 136.18, 122.84, 115.07, 109.58, 103.15, 61.49 (d,  $^2J_{\text{C,P}} = 6.5$  Hz), 56.26, 43.36, 30.64 (d,  $^3J_{\text{C,P}} = 16.9$  Hz), 29.45, 29.33, 29.25, 29.11, 27.37, 25.77 (d,  $^1J_{\text{C,P}} = 140.4$  Hz), 22.47 (d,  $^2J_{\text{C,P}} = 5.2$  Hz), 16.59 (d,  $^3J_{\text{C,P}} = 6.0$  Hz).

Anal. calcd for  $\text{C}_{27}\text{H}_{40}\text{NO}_5\text{P}$ , %: C 66.24, H 8.24, N 2.86, found, %: C 65.95, H 8.53, N 2.92.

*[2-(3,6-dimethoxy-9H-carbazol-9-yl)ethyl]phosphonic acid (46)*



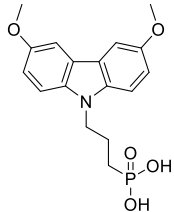
Diethyl [2-(3,6-dimethoxy-9H-carbazol-9-yl)ethyl]phosphonate (**41**) (0.335 g, 0.86 mmol) was dissolved in dry 1,4-dioxane (25 ml) under argon. Afterwards, bromotrimethylsilane (1.12 ml, 8.48 mmol) was added dropwise. The reaction was kept for 24 h at 25 °C under argon atmosphere. Afterwards, the solvent was distilled off under reduced pressure; the solid residue was dissolved in methanol (15 ml), and distilled water was added dropwise (30 ml), until the solution became opaque and was stirred for 15 h. The product was filtered off and washed with water to give 0.230 g (80 %) of beige solid – **46**.

$^1\text{H}$  NMR (400 MHz, MeOD)  $\delta$  7.57 (d,  $J = 2.5$  Hz, 2H, Ht), 7.34 (d,  $J = 8.8$  Hz, 2H, Ht), 7.05 (dd,  $J = 8.8, 2.5$  Hz, 2H, Ht), 4.58–4.48 (m, 2H,  $\text{NCH}_2$ ), 3.87 (s, 6H,  $2 \times \text{OCH}_3$ ), 2.20–2.06 (m, 2H,  $\text{CH}_2$ ).

$^{13}\text{C}$  NMR (100 MHz, MeOD)  $\delta$  154.97, 136.71, 124.61, 116.03, 110.37, 104.29, 56.46, 38.47 (d,  $^2J_{\text{C,P}} = 16.9$  Hz), 26.02 (d,  $^1J_{\text{C,P}} = 132.0$  Hz).

Anal. calculated for  $\text{C}_{16}\text{H}_{18}\text{NO}_5\text{P}$ , %: C 57.32, H 5.41, N 4.18, found, %: C 57.19, H 5.53, N 4.11.

*[3-(3,6-dimethoxy-9H-carbazol-9-yl)propyl]phosphonic acid (47)*



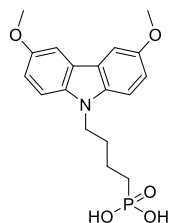
Diethyl [3-(3,6-dimethoxy-9H-carbazol-9-yl)propyl]phosphonate (**42**) (0.43 g, 1.06 mmol) was dissolved in anhydrous 1,4-dioxane (15 ml) under argon atmosphere followed by dropwise addition of bromotrimethylsilane (1.45 ml, 10.6 mmol). The reaction was stirred for 22 h at 25 °C under argon atmosphere. Afterwards methanol (2 ml) was added, and stirring continued for 3 h. Finally, distilled water was added dropwise (15 ml), until the solution became opaque, and it was stirred overnight. The product was filtered off, washed with water and dissolved in tetrahydrofuran (1ml) and precipitated into *n*-hexane (12 ml). The precipitate was filtered off and washed with *n*-hexane to give 0.350 g (91 %) of white powder. M.p. 176–178 °C

$^1\text{H}$  NMR (400 MHz,  $\text{DMSO}-d_6$ )  $\delta$  9.49–7.88 (m, 2H,  $2 \times \text{OH}$ ), 7.72 (d,  $J = 2.5$  Hz, 2H, Ht), 7.50 (d,  $J = 8.9$  Hz, 2H, Ht), 7.05 (dd,  $J = 8.9, 2.5$  Hz, 2H, Ht), 4.38 (t,  $J = 6.9$  Hz, 2H,  $\text{NCH}_2$ ), 3.85 (s, 6H,  $2 \times \text{OCH}_3$ ), 1.99–1.84 (m, 2H,  $\text{CH}_2$ ), 1.49 (dt,  $J = 16.7, 8.0$  Hz, 2H,  $\text{CH}_2$ ).

$^{13}\text{C}$  NMR (100 MHz,  $\text{DMSO}-d_6$ )  $\delta$  152.82, 135.52, 122.26, 114.90, 110.06, 103.19, 55.65, 42.63 (d,  $^3J_{\text{C,P}} = 17.7$  Hz), 25.02 (d,  $^1J_{\text{C,P}} = 136.0$  Hz), 22.80 (d,  $^2J_{\text{C,P}} = 2.7$  Hz).

Anal. calcd for C<sub>17</sub>H<sub>20</sub>NO<sub>5</sub>P, %: C 58.45, H 5.77, N 4.01, found, %: C 58.73, H 5.51, N 4.27.

[4-(3,6-dimethoxy-9H-carbazol-9-yl)butyl]phosphonic acid (**48**)



Diethyl [4-(3,6-dimethoxy-9H-carbazol-9-yl)butyl]phosphonate (**43**) (0.49 g, 1.17 mmol) was dissolved in anhydrous 1,4-dioxane (15 ml) under argon atmosphere followed by dropwise addition of bromotrimethylsilane (1.55 ml, 11.67 mmol). The reaction was stirred for 22 h at 25 °C under argon atmosphere. Afterwards, methanol (3 ml) was added, and stirring continued for 3 h. Finally, distilled water was added dropwise (12 ml), until the solution became opaque, and it was stirred overnight. The product was

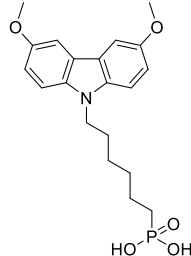
filtered off, washed with water dissolved in tetrahydrofuran (1 ml) and precipitated into *n*-hexane (12 ml). The precipitate was filtered off and washed with *n*-hexane to give 0.370 g (87 %) of white powder. M.p. 193–194 °C

<sup>1</sup>H NMR (400 MHz, DMSO-*d*<sub>6</sub>) δ 9.35–8.28 (s, 2H, 2× OH), 7.71 (d, *J* = 2.5 Hz, 2H, Ht), 7.46 (d, *J* = 8.8 Hz, 2H, Ht), 7.04 (dd, *J* = 8.9, 2.5 Hz, 2H, Ht), 4.30 (t, *J* = 7.0 Hz, 2H, NCH<sub>2</sub>), 3.85 (s, 6H, 2× OCH<sub>3</sub>), 1.79 (quin, *J* = 6.9 Hz, 2H, CH<sub>2</sub>), 1.60–1.42 (m, 4H, 2× CH<sub>2</sub>).

<sup>13</sup>C NMR (100 MHz, DMSO-*d*<sub>6</sub>) δ 153.20, 135.96, 122.68, 115.32, 110.50, 103.59, 56.10, 42.63, 30.22 (d, <sup>3</sup>*J*<sub>(C,P)</sub> = 15.1 Hz), 27.84 (d, <sup>1</sup>*J*<sub>(C,P)</sub> = 136.7 Hz), 20.90 (d, <sup>2</sup>*J*<sub>(C,P)</sub> = 4.5 Hz).

Anal. calcd for C<sub>18</sub>H<sub>22</sub>NO<sub>5</sub>P, %: C 59.50, H 6.10, N 3.85, found, %: C 59.36, H 5.89, N 3.51.

[6-(3,6-dimethoxy-9H-carbazol-9-yl)hexyl]phosphonic acid (**49**)



Diethyl [6-(3,6-dimethoxy-9H-carbazol-9-yl)hexyl]phosphonate (**44**) (0.3 g, 0.67 mmol) was dissolved in anhydrous 1,4-dioxane (10 ml) under argon atmosphere followed by dropwise addition of bromotrimethylsilane (0.91 ml, 6.7 mmol). The reaction was stirred for 22 h at 25 °C under argon atmosphere. Afterwards, methanol (2 ml) was added, and stirring continued for 3 h. Finally, distilled water was added dropwise (11 ml), until the solution became opaque, and it was stirred overnight. The product was

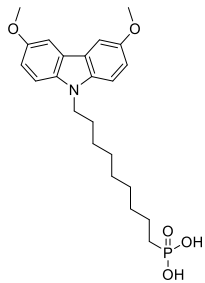
filtered off, washed with water dissolved in tetrahydrofuran (1.5 ml) and precipitated into *n*-hexane (18 ml). The precipitate was filtered off and washed with *n*-hexane to give 0.23 g (88 %) of white powder. M.p 165–167 °C

<sup>1</sup>H NMR (400 MHz, DMSO-*d*<sub>6</sub>) δ 8.73 (s, 2H, 2× OH), 7.53 (d, *J* = 2.5 Hz, 2H, Ht), 7.25 (d, *J* = 8.8 Hz, 2H, Ht), 6.86 (dd, *J* = 8.8, 2.5 Hz, 2H, Ht), 4.10 (t, *J* = 7.0 Hz, 2H, NCH<sub>2</sub>), 3.66 (s, 6H, 2× OCH<sub>3</sub>), 1.51 (t, *J* = 7.4 Hz, 2H, CH<sub>2</sub>), 1.36–0.96 (m, 8H, 4× CH<sub>2</sub>).

<sup>13</sup>C NMR (100 MHz, DMSO-*d*<sub>6</sub>) δ 152.72, 135.51, 122.21, 114.85, 109.96, 103.14, 55.63, 42.30, 29.72 (d, <sup>3</sup>*J*<sub>(C,P)</sub> = 15.8 Hz), 28.50, 27.44 (d, <sup>1</sup>*J*<sub>(C,P)</sub> = 134.8 Hz), 26.13, 22.67 (d, <sup>2</sup>*J*<sub>(C,P)</sub> = 4.2 Hz).

Anal. calcd for C<sub>20</sub>H<sub>26</sub>NO<sub>5</sub>P, %: C 61.37, H 6.70, N 3.58, found, %: C 61.59, H 6.93, N 3.36.

*[9-(3,6-dimethoxy-9H-carbazol-9-yl)nonyl]phosphonic acid (50)*



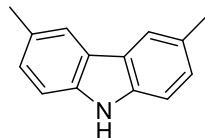
Diethyl [9-(3,6-dimethoxy-9H-carbazol-9-yl)nonyl]phosphonate (**45**) (0.6 g, 1.23 mmol) was dissolved in anhydrous 1,4-dioxane (15 ml) under argon atmosphere followed by dropwise addition of bromotrimethylsilane (1.86 ml, 12.26 mmol). The reaction was stirred for 22 h at 20 °C under argon atmosphere. Afterwards, methanol (3 ml) was added, and stirring continued for 3 h. Finally, distilled water was added dropwise (16 ml), until the solution became opaque, and it was stirred overnight. The product was filtered off, washed with water dissolved in tetrahydrofuran (2 ml) and precipitated into *n*-hexane (24 ml). The precipitate was filtered off and washed with *n*-hexane to give 0.490 g (92 %) of white powder. M.p. 90–92 °C

<sup>1</sup>H NMR (400 MHz, DMSO-*d*<sub>6</sub>) δ 7.71 (d, *J* = 2.6 Hz, 2H, Ht), 7.42 (d, *J* = 8.9 Hz, 2H, Ht), 7.04 (dd, *J* = 8.9, 2.5 Hz, 2H, Ht), 4.27 (t, *J* = 7.0 Hz, 2H, NCH<sub>2</sub>), 3.85 (s, 6H, 2 × OCH<sub>3</sub>), 1.69 (p, *J* = 6.7 Hz, 2H, CH<sub>2</sub>), 1.55–1.34 (m, 4H, 2 × CH<sub>2</sub>), 1.33–1.06 (m, 10H, 5 × CH<sub>2</sub>).

<sup>13</sup>C NMR (100 MHz, DMSO-*d*<sub>6</sub>) δ 152.72, 135.51, 122.21, 114.83, 109.95, 103.13, 55.62, 42.34, 30.10, 29.95, 28.81, 28.75, 28.65, 28.60, 26.47, 22.72.

Anal. calcd for C<sub>23</sub>H<sub>32</sub>NO<sub>5</sub>P, %: C 63.73, H 7.44, N 3.23, found, %: C 63.97, H 7.25, N 3.01.

*3,6-dimethyl-9H-carbazole (51)*



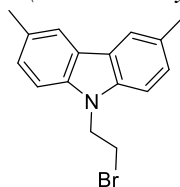
3,6-dibromo-9H-carbazole (10 g, 30.77 mmol) and 1,3-bis-(diphenylphosphino)dichloronickel(II) (Ni(dppp)<sub>2</sub>Cl<sub>2</sub>) (2.5 g, 4.62 mmol) were dissolved in 700 ml of absolute diethyl ether under argon atmosphere. After 15 min, to the purple red suspension, 40.9 ml of 3 M CH<sub>3</sub>MgBr solution in diethyl ether (123.08 mmol) over a period of 60 min was added, yielding a brown and clear solution. Afterwards, the reaction mixture was refluxed for 5 h (TLC, acetone: *n*-hexane 1:24 *v/v*), cooled to room temperature and quenched with 100 ml of saturated aqueous NH<sub>4</sub>Cl solution. The organic phase was extracted three times with 200 ml of saturated aqueous Na<sub>2</sub>CO<sub>3</sub> solution, three times with 200 ml of water and finally, three times with 200 ml of saturated aqueous NaCl solution. The organic layer was dried over anhydrous Na<sub>2</sub>SO<sub>4</sub>, and the solvent was distilled off under reduced pressure. The crude product was purified by column chromatography (acetone: *n*-hexane 1:24 *v/v*) to give 3.5 g (58 %) of white crystals. M.p. 218–219 °C

<sup>1</sup>H NMR (400 MHz, DMSO-*d*<sub>6</sub>) δ 10.95 (s, 1H, NH), 7.84 (s, 2H, Ht), 7.35 (d, *J* = 8.1 Hz, 2H, Ht), 7.18 (d, *J* = 8.0 Hz, 2H, Ht), 2.46 (s, 6H, 2 × CH<sub>3</sub>).

<sup>13</sup>C NMR (100 MHz, DMSO-*d*<sub>6</sub>) δ 138.27, 126.79, 126.64, 122.40, 119.79, 110.58, 21.12.

Anal. calcd for C<sub>14</sub>H<sub>13</sub>N, %: C 86.12, H 6.71, N 7.17, found, %: C 85.91, H 6.82, N 7.27.

**9-(2-bromoethyl)-3,6-dimethyl-9H-carbazole (52)**



3,6-dimethyl-9H-carbazole (0.6 g, 3.07 mmol) was dissolved in 1,3-dibromoethane (7 ml, 81.23 mmol); tetrabutylammonium bromide (0.148 g, 0.46 mmol) and 50 % KOH aqueous solution (0.86 ml, 15.35 mmol) were added subsequently. The reaction was stirred at 50 °C for two days (TLC, acetone: *n*-hexane 2:23 *v/v*); after each 24 h, tetrabutylammonium bromide (0.1 g, 0.31 mmol)

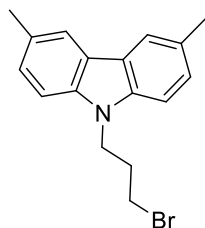
and 0.5 ml of 50 % aqueous KOH solution were added. After completion of the reaction, the extraction was done with dichloromethane. The organic layer was dried over anhydrous Na<sub>2</sub>SO<sub>4</sub>, and the solvent was distilled off under reduced pressure. The crude product was purified by column chromatography (acetone: *n*-hexane 1:23 *v/v*) to give 0.52 g (47 %) of colourless solid.

<sup>1</sup>H NMR (400 MHz, CDCl<sub>3</sub>) δ 7.82 (s, 2H, Ht), 7.27–7.22 (m, 4H, Ht), 4.57 (t, *J* = 7.5 Hz, 2H, NCH<sub>2</sub>), 3.58 (t, *J* = 7.5 Hz, 2H, CH<sub>2</sub>), 2.50 (s, 6H, HtCH<sub>3</sub>).

<sup>13</sup>C NMR (100 MHz, CDCl<sub>3</sub>) δ 138.58, 128.75, 127.16, 123.21, 120.57, 108.16, 44.82, 28.41, 21.50.

Anal. calcd for C<sub>16</sub>H<sub>16</sub>BrN, %: C 63.59, H 5.34, N 4.63, found, %: C 63.72, H 5.52, N 4.77.

**9-(3-bromopropyl)-3,6-dimethyl-9H-carbazole (53)**



3,6-dimethyl-9H-carbazole (51) (0.6 g, 3.07 mmol) was dissolved in 1,3-dibromopropane (8 ml, 78.46 mmol); tetrabutylammonium bromide (0.148 g, 0.46 mmol) and 50 % KOH aqueous solution (0.86 ml, 15.35 mmol) were added subsequently. The reaction was stirred at 55 °C overnight (TLC, acetone: *n*-hexane 2:23 *v/v*). After completion of the reaction, the extraction was done with dichloromethane. The organic layer was dried over anhydrous Na<sub>2</sub>SO<sub>4</sub>, and the solvent was distilled

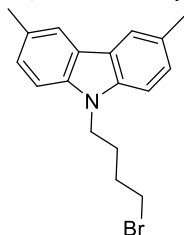
off under reduced pressure. The crude product was purified by column chromatography (acetone *n*-hexane 1:49 *v/v*) to give 0.85 g (89 %) of white powder.

<sup>1</sup>H NMR (400 MHz, CDCl<sub>3</sub>) δ 7.84 (s, 2H, Ht), 7.32 (d, *J* = 8.3 Hz, 2H, Ht), 7.25 (d, *J* = 8.3 Hz, 2H, Ht), 4.41 (t, *J* = 6.4 Hz, 2H, NCH<sub>2</sub>), 3.33 (t, *J* = 6.2 Hz, 2H, CH<sub>2</sub>), 2.52 (s, 6H, 2× CH<sub>3</sub>), 2.38 (quin, *J* = 6.3 Hz, 2H, CH<sub>2</sub>).

<sup>13</sup>C NMR (100 MHz, CDCl<sub>3</sub>) δ 139.03, 128.29, 127.08, 123.05, 120.46, 108.38, 41.04, 32.16, 31.06, 21.49.

Anal. calcd for C<sub>17</sub>H<sub>18</sub>BrN, %: C 64.57, H 5.74, N 4.43, found, %: C 64.72, H 5.95, N 4.26.

**9-(4-bromobutyl)-3,6-dimethyl-9H-carbazole (54)**



3,6-dimethyl-9H-carbazole (**51**) (0.6 g, 3.07 mmol) was dissolved in 1,4-dibromobutane (9.1 ml, 76.75 mmol), and tetrabutylammonium bromide (0.148 g, 0.46 mmol) and 50 % KOH aqueous solution (0.86 ml, 15.35 mmol) were added subsequently. The reaction was stirred at 60 °C overnight (TLC, acetone: *n*-hexane 1:24 *v/v*). After completion of the reaction, the extraction was done with dichloromethane. The organic layer was dried over anhydrous Na<sub>2</sub>SO<sub>4</sub>, and the solvent was distilled off

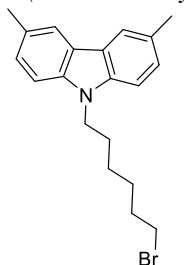
under reduced pressure. The crude product was purified by column chromatography (acetone *n*-hexane 1:124 *v/v*) to give 0.91 g (90 %) of white powder.

<sup>1</sup>H NMR (400 MHz, CDCl<sub>3</sub>) δ 7.85 (s, 2H, Ht), 7.29–7.20 (m, 4H, Ht), 4.27 (t, *J* = 6.8 Hz, 2H, NCH<sub>2</sub>), 3.33 (t, *J* = 6.5 Hz, 2H, CH<sub>2</sub>), 2.52 (s, 6H, 2× CH<sub>3</sub>), 2.01 (p, *J* = 7.1 Hz, 2H, CH<sub>2</sub>), 1.92–1.80 (m, 2H, CH<sub>2</sub>).

<sup>13</sup>C NMR (100 MHz, CDCl<sub>3</sub>) δ 138.88, 127.98, 126.88, 122.88, 120.37, 108.20, 42.21, 33.26, 30.27, 27.71, 21.40.

Anal. calcd for C<sub>18</sub>H<sub>20</sub>BrN, %: C 65.46, H 6.10, N 4.24, found, %: C 65.31, H 6.34, N 4.39.

**9-(6-bromohexyl)-3,6-dimethyl-9H-carbazole (55)**



3,6-dimethyl-9H-carbazole (**51**) (0.6 g, 3.07 mmol) was dissolved in 1,6-dibromohexane (9 ml, 58.51 mmol); tetrabutylammonium bromide (0.148 g, 0.46 mmol) and 50 % KOH aqueous solution (0.86 ml, 15.35 mmol) were added subsequently. The reaction was stirred at 60 °C overnight (TLC, acetone: *n*-hexane 1:24 *v/v*). After completion of the reaction, the extraction was done with dichloromethane. The organic layer was dried over anhydrous Na<sub>2</sub>SO<sub>4</sub>, and the solvent was distilled off under reduced pressure.

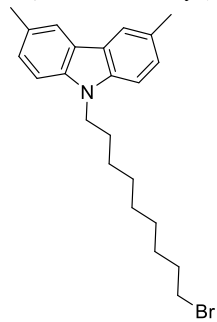
The crude product was purified by column chromatography (acetone: *n*-hexane 1:249 *v/v*) to give 1.04 g (95 %) of colourless compound.

<sup>1</sup>H NMR (400 MHz, CDCl<sub>3</sub>) δ 7.85 (s, 2H, Ht), 7.25–7.23 (m, 4H, Ht), 4.22 (t, *J* = 7.0 Hz, 2H, NCH<sub>2</sub>), 3.32 (t, *J* = 6.7 Hz, 2H, CH<sub>2</sub>), 2.52 (s, 6H, 2× CH<sub>3</sub>), 1.88–1.80 (m, 2H, CH<sub>2</sub>), 1.80–1.72 (m, 2H, CH<sub>2</sub>), 1.47–1.39 (m, 2H, CH<sub>2</sub>), 1.38–1.29 (m, 2H, CH<sub>2</sub>).

<sup>13</sup>C NMR (100 MHz, CDCl<sub>3</sub>) δ 139.08, 127.86, 126.87, 122.89, 120.40, 108.35, 42.99, 33.88, 32.70, 28.97, 28.06, 26.56, 21.50.

Anal. calcd for C<sub>20</sub>H<sub>24</sub>BrN, %: C 67.04, H 6.75, N 3.91, found, %: C 67.18, H 6.62, N 4.10.

9-(9-bromononyl)-3,6-dimethyl-9H-carbazole (**56**)



3,6-dimethyl-9H-carbazole (**51**) (0.6 g, 3.07 mmol) was dissolved in 1,9-dibromononane (9 ml, 44.27 mmol); tetrabutylammonium bromide (0.148 g, 0.46 mmol) and 50 % KOH aqueous solution (0.86 ml, 15.35 mmol) were added subsequently. The reaction was stirred at 60 °C overnight (TLC, acetone: *n*-hexane 1:24 *v/v*). After completion of the reaction, the extraction was done with dichloromethane. The organic layer was dried over anhydrous Na<sub>2</sub>SO<sub>4</sub>, and the solvent was distilled off under reduced pressure. The crude product was purified by column chromatography (acetone *n*-hexane 1:249

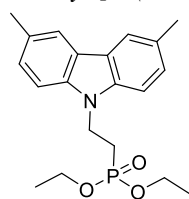
*v/v*) to give 1.08 g (87 %) of white material.

<sup>1</sup>H NMR (400 MHz, CDCl<sub>3</sub>) δ 7.85 (s, 2H, Ht), 7.25–7.23 (m, 4H, Ht), 4.21 (t, *J* = 7.1 Hz, 2H, NCH<sub>2</sub>), 3.36 (t, *J* = 6.8 Hz, 2H, CH<sub>2</sub>), 2.52 (s, 6H, 2× CH<sub>3</sub>), 1.86–1.74 (m, 4H, 2× CH<sub>2</sub>), 1.39–1.20 (m, 10H, 5× CH<sub>2</sub>).

<sup>13</sup>C NMR (100 MHz, CDCl<sub>3</sub>) δ 139.12, 127.77, 126.82, 122.87, 120.36, 108.39, 43.19, 34.11, 32.88, 29.40, 29.36, 29.08, 28.76, 28.20, 27.34, 21.51.

Anal. calcd for C<sub>23</sub>H<sub>30</sub>BrN, %: C 68.99, H 7.55, N 3.50, found, %: C 69.15, H 7.38, N 3.69.

Diethyl [2-(3,6-dimethyl-9H-carbazol-9-yl)ethyl]phosphonate (**57**)



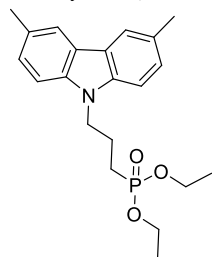
9-(2-bromoethyl)-3,6-dimethyl-9H-carbazole (**52**) (0.4 g, 1.32 mmol) was dissolved in triethylphosphite (6 ml, 34.99 mmol), and the reaction mixture was refluxed for 19 h. After reaction completion (TLC, acetone: *n*-hexane 8:17 *v/v*), the triethylphosphite was distilled off under reduced pressure. The crude product was purified by column chromatography (acetone: *n*-hexane 1:4 *v/v*) to give 0.46 g (97 %) of yellowish resin.

<sup>1</sup>H NMR (400 MHz, CDCl<sub>3</sub>) δ 7.84 (s, 2H, Ht), 7.30–7.23 (m, 4H, Ht), 4.55 (quin, *J* = 8.5 Hz, 2H, NCH<sub>2</sub>), 4.08 (quin, *J* = 7.1 Hz, 4H, 2× OCH<sub>2</sub>), 2.52 (s, 6H, 2× HtCH<sub>3</sub>), 2.28–2.16 (m, 2H, CH<sub>2</sub>), 1.28 (t, *J* = 7.0 Hz, 6H, 2× CH<sub>3</sub>).

<sup>13</sup>C NMR (100 MHz, CDCl<sub>3</sub>) δ 138.34, 128.42, 127.06, 123.23, 120.49, 108.21, 61.95(d, <sup>2</sup>*J*<sub>(C,P)</sub> = 6.5 Hz), 37.08, 25.30 (d, <sup>1</sup>*J*<sub>(C,P)</sub> = 137.2 Hz), 21.47, 16.51 (d, <sup>3</sup>*J*<sub>(C,P)</sub> = 6.1 Hz).

Anal. calcd for C<sub>20</sub>H<sub>26</sub>NO<sub>3</sub>P, %: C 66.84, H 7.29, N 3.90, found, %: C 67.01, H 7.09, N 4.08.

Diethyl [3-(3,6-dimethyl-9H-carbazol-9-yl)propyl]phosphonate (**58**)



9-(3-bromopropyl)-3,6-dimethyl-9H-carbazole (**53**) (0.6 g, 1.90 mmol) was dissolved in triethylphosphite (9 ml, 52.49 mmol), and the reaction mixture was refluxed overnight. After reaction completion (TLC, acetone: *n*-hexane 6:19, *v/v*), the triethylphosphite was distilled off under reduced pressure. The crude product was purified by column chromatography

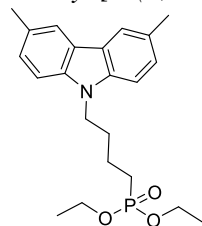
(acetone/ *n*-hexane 1:4 v/v) to give 0.65 g (92 %) of yellowish resin.

$^1\text{H}$  NMR (400 MHz,  $\text{CDCl}_3$ )  $\delta$  7.84 (s, 2H, Ht), 7.30–7.22 (m, 4H, Ht), 4.34 (t,  $J = 7.0$  Hz, 2H,  $\text{NCH}_2$ ), 4.06–4.01 (m, 4H,  $2 \times \text{OCH}_2$ ), 2.52 (s, 6H,  $2 \times \text{HtCH}_3$ ), 2.22–2.09 (m, 2H,  $\text{CH}_2$ ), 1.72 (dt,  $J = 18.6, 7.8$  Hz, 2H,  $\text{CH}_2$ ), 1.26 (t,  $J = 7.1$  Hz, 6H,  $2 \times \text{CH}_3$ ).

$^{13}\text{C}$  NMR (100 MHz,  $\text{CDCl}_3$ )  $\delta$  138.99, 128.11, 126.99, 122.97, 120.40, 108.35, 61.73 (d,  $^2J_{(\text{C,P})} = 6.5$  Hz), 43.11 (d,  $^3J_{(\text{C,P})} = 15.9$  Hz), 23.22 (d,  $^1J_{(\text{C,P})} = 142.4$  Hz), 22.26 (d,  $^2J_{(\text{C,P})} = 4.9$  Hz), 21.46, 16.53 (d,  $^3J_{(\text{C,P})} = 5.9$  Hz).

Anal. calcd for  $\text{C}_{21}\text{H}_{28}\text{NO}_3\text{P}$ , %: C 67.54, H 7.56, N 3.75, found, %: C 67.41, H 7.52, N 3.63.

**Diethyl [4-(3,6-dimethyl-9H-carbazol-9-yl)butyl]phosphonate (59)**



9-(4-bromobutyl)-3,6-dimethyl-9H-carbazole (**54**) (0.8 g, 2.42 mmol) was dissolved in triethylphosphite (9 ml, 52.49 mmol), and the reaction mixture was refluxed overnight. After reaction completion (TLC, acetone: *n*-hexane 6:19 v/v), the triethylphosphite was distilled off under reduced pressure. The crude product was purified by column chromatography (acetone:*n*-hexane 1:4 v/v) to give 0.89 g (95 %) of yellowish

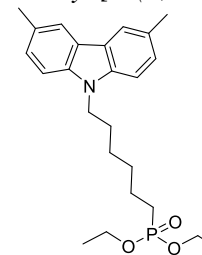
resin.

$^1\text{H}$  NMR (400 MHz,  $\text{CDCl}_3$ )  $\delta$  7.84 (s, 2H, Ht), 7.25–7.22 (m, 4H, Ht), 4.24 (t,  $J = 7.0$  Hz, 2H,  $\text{NCH}_2$ ), 4.00 (quin,  $J = 7.3$  Hz, 4H,  $2 \times \text{OCH}_2$ ), 2.51 (s, 6H,  $2 \times \text{HtCH}_3$ ), 1.93 (p,  $J = 7.5$  Hz, 2H,  $\text{CH}_2$ ), 1.75–1.58 (m, 4H,  $2 \times \text{CH}_2$ ), 1.24 (t,  $J = 7.0$  Hz, 6H,  $2 \times \text{CH}_3$ ).

$^{13}\text{C}$  NMR (100 MHz,  $\text{CDCl}_3$ )  $\delta$  138.97, 127.94, 126.89, 122.91, 120.37, 108.30, 61.59 (d,  $^2J_{(\text{C,P})} = 6.5$  Hz), 42.64, 29.84 (d,  $^3J_{(\text{C,P})} = 15.3$  Hz), 25.54 (d,  $^1J_{(\text{C,P})} = 141.2$  Hz), 21.45, 20.51 (d,  $^2J_{(\text{C,P})} = 5.0$  Hz), 16.50 (d,  $^3J_{(\text{C,P})} = 6.0$  Hz).

Anal. calcd for  $\text{C}_{22}\text{H}_{30}\text{NO}_3\text{P}$ , %: C 68.20, H 7.80, N 3.62, found, %: C 68.03, H 7.98, N 3.79.

**Diethyl [6-(3,6-dimethyl-9H-carbazol-9-yl)hexyl]phosphonate (60)**

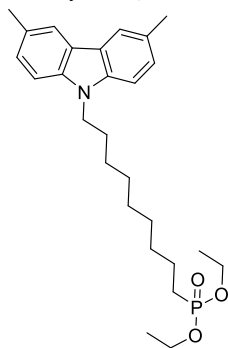


9-(6-bromohexyl)-3,6-dimethyl-9H-carbazole (**55**) (1 g, 2.79 mmol) was dissolved in triethylphosphite (10 ml, 58.32 mmol), and the reaction mixture was refluxed overnight. After reaction completion (TLC, acetone: *n*-hexane 6:19 v/v), the triethylphosphite was distilled off under reduced pressure. The crude product was purified by column chromatography (acetone: *n*-hexane 4:21 v/v) to give 0.96 g (82 %) of yellowish resin.

$^1\text{H}$  NMR (400 MHz,  $\text{CDCl}_3$ )  $\delta$  7.84 (s, 2H, Ht), 7.25–7.22 (m, 4H, Ht), 4.22 (t,  $J = 7.0$  Hz, 2H,  $\text{NCH}_2$ ), 4.10–3.99 (m, 4H,  $2 \times \text{OCH}_2$ ), 2.52 (s, 6H,  $2 \times \text{HtCH}_3$ ), 1.82 (p,  $J = 7.0$  Hz, 2H,  $\text{CH}_2$ ), 1.70–1.59 (m, 2H,  $\text{CH}_2$ ), 1.59–1.48 (m, 2H,  $\text{CH}_2$ ), 1.40–1.31 (m, 4H,  $2 \times \text{CH}_2$ ), 1.28 (t,  $J = 7.0$  Hz, 6H,  $2 \times \text{CH}_3$ ).

$^{13}\text{C}$  NMR (100 MHz,  $\text{CDCl}_3$ )  $\delta$  139.04, 127.79, 126.82, 122.84, 120.33, 108.33, 61.47 (d,  $^2J_{\text{C,P}} = 6.5$  Hz), 43.03, 30.44 (d,  $^3J_{\text{C,P}} = 16.7$  Hz), 28.88, 26.89, 25.65 (d,  $^1J_{\text{C,P}} = 140.5$  Hz), 22.42 (d,  $^2J_{\text{C,P}} = 5.2$  Hz), 21.45, 16.55 (d,  $^3J_{\text{C,P}} = 6.0$  Hz).  
 Anal. calcd for  $\text{C}_{24}\text{H}_{34}\text{NO}_3\text{P}$ , %: C 69.38, H 8.25, N 3.37, found, %: C 69.56, H 8.13, N 3.50.

**Diethyl [9-(3,6-dimethyl-9H-carbazol-9-yl)nonyl]phosphonate (61)**



9-(9-bromononyl)-3,6-dimethyl-9H-carbazole (**56**) (1 g, 2.50 mmol) was dissolved in triethylphosphite (10 ml, 58.32 mmol), and the reaction mixture was refluxed overnight. After reaction completion (TLC, acetone: *n*-hexane 6:19 *v/v*), the triethylphosphite was distilled off under reduced pressure. The crude product was purified by column chromatography (acetone: *n*-hexane 4:21 *v/v*) to give 1.02 g (89 %) of yellowish resin.

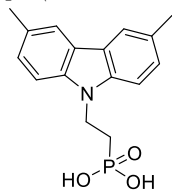
$^1\text{H}$  NMR (400 MHz,  $\text{CDCl}_3$ )  $\delta$  7.85 (s, 2H, Ht), 7.26–7.22 (m, 4H, Ht), 4.22 (t,  $J = 7.2$  Hz, 2H,  $\text{NCH}_2$ ), 4.13–4.02 (m, 4H,  $2 \times \text{OCH}_2$ ), 2.52 (s, 6H,  $2 \times \text{HtCH}_3$ ), 1.82 (p,  $J = 7.2$  Hz, 2H,  $\text{CH}_2$ ),

1.74–1.63 (m, 2H,  $\text{CH}_2$ ), 1.61–1.51 (m, 2H,  $\text{CH}_2$ ), 1.35–1.28 (m, 12H, Aliph), 1.26–1.19 (m, 4H,  $2 \times \text{CH}_2$ ).

$^{13}\text{C}$  NMR (100 MHz,  $\text{CDCl}_3$ )  $\delta$  139.10, 127.74, 126.80, 122.85, 120.34, 108.37, 61.47 (d,  $^2J_{\text{C,P}} = 6.5$  Hz), 43.19, 30.65 (d,  $^3J_{\text{C,P}} = 16.9$  Hz), 29.47, 29.34, 29.13, 29.10, 27.37, 25.79 (d,  $^1J_{\text{C,P}} = 140.3$  Hz), 22.49 (d,  $^2J_{\text{C,P}} = 5.2$  Hz), 21.48, 16.60 (d,  $^3J_{\text{C,P}} = 6.0$  Hz).

Anal. calcd for  $\text{C}_{27}\text{H}_{40}\text{NO}_3\text{P}$ , %: C 70.87, H 8.81, N 3.06, found, %: C 71.11, H 8.98, N 2.95.

**[2-(3,6-dimethyl-9H-carbazol-9-yl)ethyl]phosphonic acid (62)**



Diethyl [2-(3,6-dimethyl-9H-carbazol-9-yl)ethyl]phosphonate (**57**) (0.47 g, 1.31 mmol) was dissolved in anhydrous 1,4-dioxane (15 ml) under argon atmosphere, followed by dropwise addition of bromotrimethylsilane (1.73 ml, 13.07 mmol). The reaction was stirred for 22 h at 25 °C under argon atmosphere. Afterwards, methanol (3 ml) was added, and stirring continued for 3h. Finally,

distilled water was added dropwise (10 ml), until the solution became opaque, and it was stirred overnight. The product was filtered off, washed with water dissolved in tetrahydrofuran (1ml) and precipitated into *n*-hexane (12 ml). The precipitate was filtered off and washed with *n*-hexane to give 0.360 g (91 %) of white powder. M.p 195–196 °C

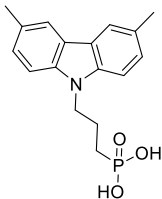
$^1\text{H}$  NMR (400 MHz,  $\text{DMSO}-d_6$ )  $\delta$  9.59 (s, 2H,  $2 \times \text{OH}$ ), 7.88 (s, 2H, Ht), 7.38 (d,  $J = 8.3$  Hz, 2H, Ht), 7.25 (d,  $J = 8.3$  Hz, 2H, Ht), 4.59–4.40 (m, 2H,  $\text{NCH}_2$ ), 2.46 (s, 6H,  $2 \times \text{CH}_3$ ), 2.09–1.90 (m, 2H,  $\text{CH}_2$ ).

$^{13}\text{C}$  NMR (100 MHz,  $\text{DMSO}-d_6$ )  $\delta$  137.99, 127.43, 126.94, 122.27, 120.15, 108.58, 37.43, 27.33 (d,  $^1J_{\text{C,P}} = 128.2$  Hz), 21.04.



Anal. calcd for C<sub>16</sub>H<sub>18</sub>NO<sub>3</sub>P, %: C 63.36, H 5.98, N 4.62, found, %: C 63.53, H 5.81, N 4.76.

*[3-(3,6-dimethyl-9H-carbazol-9-yl)propyl]phosphonic acid (63)*



Diethyl [3-(3,6-dimethyl-9H-carbazol-9-yl)propyl]phosphonate (**58**) (0.6 g, 1.61 mmol) was dissolved in anhydrous 1,4-dioxane (20 ml) under argon atmosphere, followed by dropwise addition of bromotrimethylsilane (2.12 ml, 16.07 mmol). The reaction was stirred for 22 h at 25 °C under argon atmosphere. Afterwards, methanol (3 ml) was added, and stirring continued for 3 h. Finally, distilled water was added dropwise (15 ml), until the solution

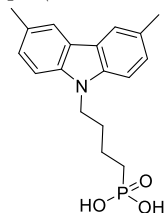
became opaque, and it was stirred overnight. The product was filtered off and washed with water dissolved in tetrahydrofuran (1 ml) and precipitated into *n*-hexane (15 ml); the precipitate was filtered off and washed with *n*-hexane to give 0.430 g (85 %) of white powder. M.p. 201–203 °C

<sup>1</sup>H NMR (400 MHz, DMSO-*d*<sub>6</sub>) δ 7.89 (s, 2H, Ht), 7.48 (d, *J* = 8.3 Hz, 2H, Ht), 7.24 (d, *J* = 8.3 Hz, 2H, Ht), 4.39 (t, *J* = 7.0 Hz, 2H, NCH<sub>2</sub>), 2.47 (s, 6H, 2× CH<sub>3</sub>), 2.01–1.86 (m, 2H, CH<sub>2</sub>), 1.56–1.43 (m, 2H, CH<sub>2</sub>).

<sup>13</sup>C NMR (100 MHz, DMSO-*d*<sub>6</sub>) δ 138.60, 127.17, 126.83, 121.98, 120.00, 108.98, 42.52 (d, <sup>3</sup>*J*<sub>(C,P)</sub> = 17.2 Hz), 25.05 (d, <sup>1</sup>*J*<sub>(C,P)</sub> = 137.8 Hz), 22.67 (d, <sup>2</sup>*J*<sub>(C,P)</sub> = 3.6 Hz), 21.05.

Anal. calcd for C<sub>17</sub>H<sub>20</sub>NO<sub>3</sub>P, %: C 64.35, H 6.35, N 4.41, found, %: C 64.18, H 6.47, N 4.55.

*[4-(3,6-Dimethyl-9H-carbazol-9-yl)butyl]phosphonic acid (64)*



Diethyl [4-(3,6-dimethyl-9H-carbazol-9-yl)butyl]phosphonate (**59**) (0.6 g, 1.55 mmol) was dissolved in anhydrous 1,4-dioxane (20 ml) under argon atmosphere followed by dropwise addition of bromotrimethylsilane (2.12 ml, 15.59 mmol). The reaction was stirred for 22 h at 25 °C under argon atmosphere. Afterwards methanol (3 ml) was added, and stirring continued for 3 h. Finally, distilled water was added dropwise (15 ml), until the solution

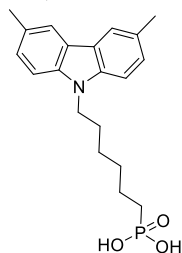
became opaque, and it was stirred overnight. The product was filtered off, washed with water dissolved in tetrahydrofuran (1 ml) and precipitated into *n*-hexane (15 ml). The precipitate was filtered off and washed with *n*-hexane, to give 0.460 g (91 %) of white powder. M.p. 187–188 °C

<sup>1</sup>H NMR (400 MHz, DMSO-*d*<sub>6</sub>) δ 7.88 (s, 2H, Ht), 7.45 (d, *J* = 8.3 Hz, 2H, Ht), 7.23 (d, *J* = 8.3 Hz, 2H, Ht), 4.34–4.27 (m, 2H, NCH<sub>2</sub>), 2.47 (s, 6H, 2× HtCH<sub>3</sub>), 1.85–1.76 (m, 2H, CH<sub>2</sub>), 1.58–1.45 (m, 4H, 2× CH<sub>2</sub>).

<sup>13</sup>C NMR (100 MHz, DMSO-*d*<sub>6</sub>) δ 138.57, 127.03, 126.78, 121.95, 119.95, 108.95, 42.05, 29.64 (d, <sup>3</sup>*J*<sub>(C,P)</sub> = 15.6 Hz), 27.42 (d, <sup>1</sup>*J*<sub>(C,P)</sub> = 136.7 Hz), 21.05, 20.47 (d, <sup>2</sup>*J*<sub>(C,N)</sub> = 4.2 Hz).

Anal. calcd for C<sub>18</sub>H<sub>22</sub>NO<sub>3</sub>P, %: C 65.25, H 6.69, N 4.23, found, %: C 65.38, H 6.51, N 4.29.

[6-(3,6-Dimethyl-9H-carbazol-9-yl)hexyl]phosphonic acid (**65**)



Diethyl [6-(3,6-dimethyl-9H-carbazol-9-yl)hexyl]phosphonate (**60**) (0.8 g, 1.92 mmol) was dissolved in anhydrous 1,4-dioxane (20 ml) under argon atmosphere, followed by dropwise addition of bromotrimethylsilane (2.5 ml, 19.25 mmol). The reaction was stirred for 22 h at 25 °C under argon atmosphere. Afterwards, methanol (3 ml) was added, and stirring continued for 3h. Finally, distilled water was added dropwise (15 ml), until the solution became opaque, and it was stirred overnight. The product was

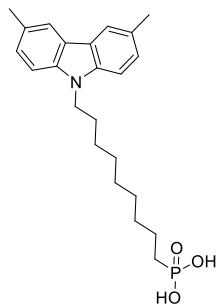
filtered off, washed with water dissolved in tetrahydrofuran (2 ml) and precipitated into *n*-hexane (25 ml). The precipitate was filtered off and washed with *n*-hexane to give 0.580 g (84 %) of white powder. M.p. 109–111 °C

<sup>1</sup>H NMR (400 MHz, DMSO-*d*<sub>6</sub>) δ 8.98–8.00 (m, 2H, 2× OH), 7.84 (s, 2H, Ht), 7.38 (d, *J* = 8.4 Hz, 2H, Ht), 7.20 (d, *J* = 8.2 Hz, 2H, Ht), 4.25 (t, *J* = 6.9 Hz, 2H, NCH<sub>2</sub>), 2.43 (s, 6H, 2× HtCH<sub>3</sub>), 1.72–1.63 (m, 2H, CH<sub>2</sub>), 1.46–1.17 (m, 6H, 3× CH<sub>2</sub>), 0.87–0.78 (m, 2H, CH<sub>2</sub>).

<sup>13</sup>C NMR (100 MHz, DMSO-*d*<sub>6</sub>) δ 138.57, 127.00, 126.76, 121.95, 119.96, 108.84, 42.17, 30.98, 29.79 (d, <sup>3</sup>*J*<sub>(C,P)</sub> = 16.1 Hz), 27.51 (d, <sup>1</sup>*J*<sub>(C,P)</sub> = 138.1 Hz), 26.17, 22.71 (d, <sup>2</sup>*J*<sub>(C,P)</sub> = 4.7 Hz), 21.04.

Anal. calcd for C<sub>20</sub>H<sub>26</sub>NO<sub>3</sub>P, %: C 66.84, H 7.29, N 3.90, found, %: C 66.73, H 7.47, N 3.76.

[9-(3,6-dimethyl-9H-carbazol-9-yl)nonyl]phosphonic acid (**66**)



Diethyl [9-(3,6-dimethyl-9H-carbazol-9-yl)nonyl]phosphonate (**61**) (0.8 g, 1.75 mmol) was dissolved in anhydrous 1,4-dioxane (25 ml) under argon atmosphere, followed by dropwise addition of bromotrimethylsilane (2.3 ml, 17.48 mmol). The reaction was stirred for 22 h at 25 °C under argon atmosphere. Afterwards, methanol (3 ml) was added, and stirring continued for 3 h. Finally, distilled water was added dropwise (20 ml), until the solution became opaque, and it was stirred overnight. The product was filtered off and washed with water dissolved in tetrahydrofuran (2 ml) and precipitated into *n*-hexane (25 ml);

the precipitate was filtered off and washed with *n*-hexane to give 0.610 g (87 %) of white powder. M.p. 63–65 °C

<sup>1</sup>H NMR (400 MHz, DMSO-*d*<sub>6</sub>) δ 7.86 (s, 2H, Ht), 7.39 (d, *J* = 8.3 Hz, 2H, Ht), 7.21 (d, *J* = 8.2 Hz, 2H, Ht), 4.26 (t, *J* = 7.1 Hz, 2H, NCH<sub>2</sub>), 2.45 (s, 6H, 2× HtCH<sub>3</sub>), 1.78–1.61 (m, 2H, CH<sub>2</sub>), 1.53–1.35 (m, 4H, 2× CH<sub>2</sub>), 1.29–1.07 (m, 10H, 5× CH<sub>2</sub>).

<sup>13</sup>C NMR (100 MHz, DMSO-*d*<sub>6</sub>) δ 138.56, 126.97, 126.73, 121.94, 119.94, 108.82, 42.18, 30.18, 28.84, 28.77, 28.64, 28.49, 26.93, 26.47, 22.76, 21.03.

Anal. calcd for C<sub>23</sub>H<sub>32</sub>NO<sub>3</sub>P, %: C 68.81, H 8.03, N 3.49, found, %: C 68.98, H 7.89, N 3.65.

## 5. CONCLUSIONS

1. DTP-based HTMs were successfully synthesised and investigated; it has been determined that:

- Energy levels of the DTP-based HTMs are suitable for the application in perovskite solar cells.
- TGA analysis revealed potential for the application of these materials in vacuum deposited devices, especially DTP derivatives **10**, **11**.
- The introduction of reactive functional groups to **12** opens a path for thermal crosslinking of these HTMs in the layer, thus simplifying the process of constructing solar cell devices.

2. A series of experiments with oxidized hole transporting materials have been conducted to determine the stability of the materials in contact with various most popular additives and perovskite compositions; it has been determined that:

- Investigated oxidized HTMs **16–21** can react with 4-*tert*-butylpyridine forming pyridinated derivatives. This process takes place in the solution and in the films kept at the elevated temperatures.
- LiTFSI and FK209, additives responsible for the oxidation of HTMs, do not affect the rate or nature of degradation too significantly under the investigated conditions.
- The presence of iodide ions, either in the solution or via ion migration from perovskite layer at elevated temperatures, is among the main causes for the dedoping process. During the reaction, oxidized spiro-OMeTAD (**17**) is reduced back to the neutral molecule, and iodine is formed.
- The observed processes take place with all the perovskite compositions, although it has to be mentioned that spiro[TFSI]<sub>2</sub> degrades significantly slower in contact with MAPbBr<sub>3</sub> due to the slower reaction rate with the bromide ion.
- The observed instability of the oxidized HTMs in the thin films at elevated temperatures could be one of the causes of the drop in conductivity reported for the doped spiro-OMeTAD and could as well potentially be one of the reasons why perovskite solar cells lose their efficiency under prolonged thermal stress. A possible solution to this problem could be the use of HTMs that do not require doping and therefore, do not rely on oxidized materials to improve conductivity.

3. New simple molecules that form self-assembling monolayers (**46–50**, **62–66**) were synthesized and integrated into the inverted perovskite solar cells, enabling hole selective contacts with minimized non-radiative losses. It has been determined that:

- These SAMs can be deposited on transparent conductive oxides via spin-coating or by dipping the substrate into the solution, both yielding layers of

comparable properties, combining high reproducibility and ease of fabrication.

- SAM-based solar cells can be fabricated without additional passivation layers, additives or dopants.
- They outperform the polymer PTAA, the material that enabled the highest performing p-i-n PSCs to date, in efficiency, stability and versatility. The maximum power conversion efficiency of 20.8 % and a  $V_{OC}$  of up to 1.15 V were demonstrated using dimethylcarbazole HTM **64**.
- In a light-soaking stress test at open circuit conditions, SAM-based PSCs containing showed a higher stability compared to the PTAA-based cells.
- By integrating **46** SAM layer into a monolithic CIGSe/perovskite tandem solar cell, the ability of conformally creating a hole-selective layer on a rough surface was demonstrated. This led to a stabilized, certified PCE of 23.26 % with facile device design on an active area of 1.03 cm<sup>2</sup>, surpassing the values achieved with a complex bilayer or mechanical polishing.

4. Monolithic perovskite/silicon tandem solar cells with maximum certified PCE of 29.15 % and monolithic perovskite/CIGSe tandem solar cells with maximum certified PCE of 24.16 %, both constructed using dimethylcarbazole **64** self-assembling monolayers, set new records for appropriate types of solar cells; thus, demonstrating viability of the SAM approach for the construction of the tandem devices of various architectures.

5. Superior stability of the PSC devices was achieved by utilizing new materials and SAM approach. For instance, non-encapsulated c-Si/perovskite tandem cell with dimethylcarbazole HTM **64** in ambient air exhibited excellent stability, retaining 95 % of its initial efficiency after 300 h of continuous maximum power point tracking, under illumination. With the typical *p-i-n* hole-selective layer, PTAA, the cell degraded to 76 % of the initial efficiency after just 90 h.

## 6. REFERENCES

1. KOJIMA, A., TESHIMA, K., SHIRAI, Y. and MIYASAKA, T. Organometal Halide Perovskites as Visible-Light Sensitizers for Photovoltaic Cells. *Journal of the American Chemical Society*, 2009, vol. 131, no. 17. pp. 6050-6051. Available from: <https://doi.org/10.1021/ja809598r> ISSN 0002-7863. DOI 10.1021/ja809598r.
2. *Best Research-Cell Efficiency Chart*. [viewed Nov 25, 2020]. Available from: <https://www.nrel.gov/pv/cell-efficiency.html>.
3. STOUUMPOS, C.C. and KANATZIDIS, M.G. The Renaissance of Halide Perovskites and their Evolution as Emerging Semiconductors. *Accounts of Chemical Research*, 2015, vol. 48, no. 10. pp. 2791-2802. Available from: <https://doi.org/10.1021/acs.accounts.5b00229> ISSN 0001-4842. DOI 10.1021/acs.accounts.5b00229.
4. SALIBA, M., et al. How to make Over 20% Efficient Perovskite Solar Cells in Regular (N-i-p) and Inverted (P-i-n) Architectures. *Chemistry of Materials*, 2018, vol. 30, no. 13. pp. 4193-4201. Available from: <https://doi.org/10.1021/acs.chemmater.8b00136> ISSN 0897-4756. DOI 10.1021/acs.chemmater.8b00136.
5. JUNG, E.H., et al. Efficient, Stable and Scalable Perovskite Solar Cells using Poly(3-Hexylthiophene). *Nature*, 2019, vol. 567, no. 7749. pp. 511-515. Available from: <https://doi.org/10.1038/s41586-019-1036-3> ISSN 1476-4687. DOI 10.1038/s41586-019-1036-3.
6. GREEN, M.A., et al. Solar Cell Efficiency Tables (Version 54). *Progress in Photovoltaics: Research and Applications*, 2019, vol. 27, no. 7. pp. 565-575. Available from: <https://doi.org/10.1002/pip.3171> ISSN 1062-7995. DOI <https://doi.org/10.1002/pip.3171>.
7. JIANG, Q., et al. Planar-Structure Perovskite Solar Cells with Efficiency Beyond 21%. *Advanced Materials*, 2017, vol. 29, no. 46. pp. 1703852. Available from: <https://doi.org/10.1002/adma.201703852> ISSN 0935-9648. DOI <https://doi.org/10.1002/adma.201703852>.
8. LUO, D., et al. Enhanced Photovoltage for Inverted Planar Heterojunction Perovskite Solar Cells. *Science*, 2018, vol. 360, no. 6396. pp. 1442-1446. Available from: <http://science.sciencemag.org/content/360/6396/1442.abstract> DOI 10.1126/science.aap9282.
9. CHEN, W., et al. Stabilizing N-Type Hetero-Junctions for NiOx Based Inverted Planar Perovskite Solar Cells with an Efficiency of 21.6%. *Journal of Materials Chemistry A*, 2020, vol. 8, no. 4. pp. 1865-1874. Available from: <http://dx.doi.org/10.1039/C9TA12368G> ISSN 2050-7488. DOI 10.1039/C9TA12368G.
10. BAIKIE, T., et al. Synthesis and Crystal Chemistry of the Hybrid Perovskite (CH<sub>3</sub>NH<sub>3</sub>)PbI<sub>3</sub> for Solid-State Sensitised Solar Cell Applications. *Journal of Materials Chemistry A*, 2013, vol. 1, no. 18. pp. 5628-5641. Available from:

<http://dx.doi.org/10.1039/C3TA10518K> ISSN 2050-7488. DOI 10.1039/C3TA10518K.

11. WANG, T., et al. Indirect to Direct Bandgap Transition in Methylammonium Lead Halide Perovskite. *Energy & Environmental Science*, 2017, vol. 10, no. 2. pp. 509-515. Available from: <http://dx.doi.org/10.1039/C6EE03474H> ISSN 1754-5692. DOI 10.1039/C6EE03474H.

12. AMAT, A., et al. Cation-Induced Band-Gap Tuning in Organohalide Perovskites: Interplay of Spin–Orbit Coupling and Octahedra Tilting. *Nano Letters*, 2014, vol. 14, no. 6. pp. 3608-3616. Available from: <https://doi.org/10.1021/nl5012992> ISSN 1530-6984. DOI 10.1021/nl5012992.

13. AVA, T.T., AL MAMUN, A., MARSILLAC, S. and NAMKOONG, G. A Review: Thermal Stability of Methylammonium Lead Halide Based Perovskite Solar Cells. *Applied Sciences*, 2019, vol. 9, no. 1. pp. 188.

14. KOH, T.M., et al. Formamidinium-Containing Metal-Halide: An Alternative Material for Near-IR Absorption Perovskite Solar Cells. *The Journal of Physical Chemistry C*, 2014, vol. 118, no. 30. pp. 16458-16462. Available from: <https://doi.org/10.1021/jp411112k> ISSN 1932-7447. DOI 10.1021/jp411112k.

15. LU, H., et al. Vapor-Assisted Deposition of Highly Efficient, Stable Black-Phase FAPbI<sub>3</sub> Perovskite Solar Cells. *Science*, 2020, vol. 370, no. 6512. pp. eabb8985. Available from: <http://science.sciencemag.org/content/370/6512/eabb8985.abstract> DOI 10.1126/science.abb8985.

16. SHENG, R., et al. Methylammonium Lead Bromide Perovskite-Based Solar Cells by Vapor-Assisted Deposition. *The Journal of Physical Chemistry C*, 2015, vol. 119, no. 7. pp. 3545-3549. Available from: <https://doi.org/10.1021/jp512936z> ISSN 1932-7447. DOI 10.1021/jp512936z.

17. ARANDA, C., GUERRERO, A. and BISQUERT, J. Ionic Effect Enhances Light Emission and the Photovoltage of Methylammonium Lead Bromide Perovskite Solar Cells by Reduced Surface Recombination. *ACS Energy Letters*, 2019, vol. 4, no. 3. pp. 741-746. Available from: <https://doi.org/10.1021/acseenergylett.9b00186> DOI 10.1021/acseenergylett.9b00186.

18. LEE, J., et al. Formamidinium and Cesium Hybridization for Photo- and Moisture-Stable Perovskite Solar Cell. *Advanced Energy Materials*, 2015, vol. 5, no. 20. pp. 1501310. Available from: <https://doi.org/10.1002/aenm.201501310> ISSN 1614-6832. DOI <https://doi.org/10.1002/aenm.201501310>.

19. SCHUTT, K., et al. Overcoming Zinc Oxide Interface Instability with a Methylammonium-Free Perovskite for High-Performance Solar Cells. *Advanced Functional Materials*, 2019, vol. 29, no. 47. pp. 1900466. Available from: <https://doi.org/10.1002/adfm.201900466> ISSN 1616-301X. DOI <https://doi.org/10.1002/adfm.201900466>.

20. JEON, N.J., et al. Compositional Engineering of Perovskite Materials for High-Performance Solar Cells. *Nature*, 2015, vol. 517, no. 7535. pp. 476-480. Available from: <https://doi.org/10.1038/nature14133> ISSN 1476-4687. DOI 10.1038/nature14133.

21. JIANG, Q., et al. Surface Passivation of Perovskite Film for Efficient Solar Cells. *Nature Photonics*, 2019, vol. 13, no. 7. pp. 460-466. Available from: <https://doi.org/10.1038/s41566-019-0398-2> ISSN 1749-4893. DOI 10.1038/s41566-019-0398-2.
22. SALIBA, M., et al. Cesium-Containing Triple Cation Perovskite Solar Cells: Improved Stability, Reproducibility and High Efficiency. *Energy & Environmental Science*, 2016, vol. 9, no. 6. pp. 1989-1997. Available from: <http://dx.doi.org/10.1039/C5EE03874J> ISSN 1754-5692. DOI 10.1039/C5EE03874J.
23. AITOLA, K., et al. High Temperature-Stable Perovskite Solar Cell Based on Low-Cost Carbon Nanotube Hole Contact. *Advanced Materials*, 2017, vol. 29, no. 17. pp. 1606398. Available from: <https://doi.org/10.1002/adma.201606398> ISSN 0935-9648. DOI <https://doi.org/10.1002/adma.201606398>.
24. YANG, J., SIEMPELKAMP, B.D., LIU, D. and KELLY, T.L. Investigation of CH<sub>3</sub>NH<sub>3</sub>PbI<sub>3</sub> Degradation Rates and Mechanisms in Controlled Humidity Environments using in Situ Techniques. *ACS Nano*, 2015, vol. 9, no. 2. pp. 1955-1963. Available from: <https://doi.org/10.1021/nn506864k> ISSN 1936-0851. DOI 10.1021/nn506864k.
25. CONINGS, B., et al. Intrinsic Thermal Instability of Methylammonium Lead Trihalide Perovskite. *Advanced Energy Materials*, 2015, vol. 5, no. 15. pp. 1500477. Available from: <https://doi.org/10.1002/aenm.201500477> ISSN 1614-6832. DOI <https://doi.org/10.1002/aenm.201500477>.
26. CHRISTIANS, J.A., MIRANDA HERRERA, P.A. and KAMAT, P.V. Transformation of the Excited State and Photovoltaic Efficiency of CH<sub>3</sub>NH<sub>3</sub>PbI<sub>3</sub> Perovskite upon Controlled Exposure to Humidified Air. *Journal of the American Chemical Society*, 2015, vol. 137, no. 4. pp. 1530-1538. Available from: <https://doi.org/10.1021/ja511132a> ISSN 0002-7863. DOI 10.1021/ja511132a.
27. PHILIPPE, B., et al. Chemical and Electronic Structure Characterization of Lead Halide Perovskites and Stability Behavior Under Different Exposures—A Photoelectron Spectroscopy Investigation. *Chemistry of Materials*, 2015, vol. 27, no. 5. pp. 1720-1731. Available from: <https://doi.org/10.1021/acs.chemmater.5b00348> ISSN 0897-4756. DOI 10.1021/acs.chemmater.5b00348.
28. ARISTIDOU, N., et al. The Role of Oxygen in the Degradation of Methylammonium Lead Trihalide Perovskite Photoactive Layers. *Angewandte Chemie International Edition*, 2015, vol. 54, no. 28. pp. 8208-8212. Available from: <https://doi.org/10.1002/anie.201503153> ISSN 1433-7851. DOI <https://doi.org/10.1002/anie.201503153>.
29. TURREN-CRUZ, S., HAGFELDT, A. and SALIBA, M. Methylammonium-Free, High-Performance, and Stable Perovskite Solar Cells on a Planar Architecture. *Science*, 2018, vol. 362, no. 6413. pp. 449. Available from: <http://science.sciencemag.org/content/362/6413/449.abstract> DOI 10.1126/science.aat3583.

30. BERHE, T.A., et al. Organometal Halide Perovskite Solar Cells: Degradation and Stability. *Energy & Environmental Science*, 2016, vol. 9, no. 2. pp. 323-356. Available from: <http://dx.doi.org/10.1039/C5EE02733K> ISSN 1754-5692. DOI 10.1039/C5EE02733K.
31. BINEK, A., HANUSCH, F.C., DOCAMPO, P. and BEIN, T. Stabilization of the Trigonal High-Temperature Phase of Formamidinium Lead Iodide. *The Journal of Physical Chemistry Letters*, 2015, vol. 6, no. 7. pp. 1249-1253. Available from: <https://doi.org/10.1021/acs.jpcclett.5b00380> DOI 10.1021/acs.jpcclett.5b00380.
32. WANG, Z., et al. Stability of Perovskite Solar Cells: A Prospective on the Substitution of the A Cation and X Anion. *Angewandte Chemie International Edition*, 2017, vol. 56, no. 5. pp. 1190-1212. Available from: <https://doi.org/10.1002/anie.201603694> ISSN 1433-7851. DOI <https://doi.org/10.1002/anie.201603694>.
33. ANARAKI, E.H., et al. Highly Efficient and Stable Planar Perovskite Solar Cells by Solution-Processed Tin Oxide. *Energy & Environmental Science*, 2016, vol. 9, no. 10. pp. 3128-3134. Available from: <http://dx.doi.org/10.1039/C6EE02390H> ISSN 1754-5692. DOI 10.1039/C6EE02390H.
34. POPLAVSKYY, D. and NELSON, J. Nondispersive Hole Transport in Amorphous Films of Methoxy-Spirofluorene-Arylamine Organic Compound. *Journal of Applied Physics*, 2003, vol. 93, no. 1. pp. 341-346. Available from: <https://doi.org/10.1063/1.1525866> ISSN 0021-8979. DOI 10.1063/1.1525866.
35. KANG, M.S., et al. Novel Carbazole-Based Hole-Transporting Materials with Star-Shaped Chemical Structures for Perovskite-Sensitized Solar Cells. *ACS Applied Materials & Interfaces*, 2015, vol. 7, no. 40. pp. 22213-22217. Available from: <https://doi.org/10.1021/acsami.5b04662> ISSN 1944-8244. DOI 10.1021/acsami.5b04662.
36. WANG, X., et al. Lowering Molecular Symmetry to Improve the Morphological Properties of the Hole-Transport Layer for Stable Perovskite Solar Cells. *Angewandte Chemie International Edition*, 2018, vol. 57, no. 38. pp. 12529-12533. Available from: <https://doi.org/10.1002/anie.201807402> ISSN 1433-7851. DOI <https://doi.org/10.1002/anie.201807402>.
37. LU, C., CHOI, I.T., KIM, J. and KIM, H.K. Simple Synthesis and Molecular Engineering of Low-Cost and Star-Shaped Carbazole-Based Hole Transporting Materials for Highly Efficient Perovskite Solar Cells. *Journal of Materials Chemistry A*, 2017, vol. 5, no. 38. pp. 20263-20276. Available from: <http://dx.doi.org/10.1039/C7TA04762B> ISSN 2050-7488. DOI 10.1039/C7TA04762B.
38. LI, D., et al. New Hole Transporting Materials for Planar Perovskite Solar Cells. *Chemical Communications*, 2018, vol. 54, no. 13. pp. 1651-1654. Available from: <http://dx.doi.org/10.1039/C7CC08985F> ISSN 1359-7345. DOI 10.1039/C7CC08985F.



39. MAGOMEDOV, A., et al. Diphenylamine-Substituted Carbazole-Based Hole Transporting Materials for Perovskite Solar Cells: Influence of Isomeric Derivatives. *Advanced Functional Materials*, 2018, vol. 28, no. 9. pp. 1704351. Available from: <https://doi.org/10.1002/adfm.201704351> ISSN 1616-301X. DOI <https://doi.org/10.1002/adfm.201704351>.
40. DASKEVICIENE, M., et al. Carbazole-Based Enamine: Low-Cost and Efficient Hole Transporting Material for Perovskite Solar Cells. *Nano Energy*, 2017, vol. 32. pp. 551-557. Available from: <http://www.sciencedirect.com/science/article/pii/S2211285517300150> ISSN 2211-2855. DOI <https://doi.org/10.1016/j.nanoen.2017.01.015>.
41. YIN, X., et al. One-Step Facile Synthesis of a Simple Carbazole-Cored Hole Transport Material for High-Performance Perovskite Solar Cells. *Nano Energy*, 2017, vol. 40. pp. 163-169. Available from: <http://www.sciencedirect.com/science/article/pii/S2211285517304834> ISSN 2211-2855. DOI <https://doi.org/10.1016/j.nanoen.2017.08.016>.
42. CHRISTIANS, J.A., et al. Tailored Interfaces of Unencapsulated Perovskite Solar Cells for >1,000 Hour Operational Stability. *Nature Energy*, 2018, vol. 3, no. 1. pp. 68-74. Available from: <https://doi.org/10.1038/s41560-017-0067-y> ISSN 2058-7546. DOI 10.1038/s41560-017-0067-y.
43. LIU, X., et al. A Star-Shaped Carbazole-Based Hole-Transporting Material with Triphenylamine Side Arms for Perovskite Solar Cells. *Journal of Materials Chemistry C*, 2018, vol. 6, no. 47. pp. 12912-12918. Available from: <http://dx.doi.org/10.1039/C8TC04191A> ISSN 2050-7526. DOI 10.1039/C8TC04191A.
44. MAGOMEDOV, A., et al. "Click-Chemistry" Inspired Synthesis of Hydrazone-Based Molecular Glasses. *RSC Advances*, 2016, vol. 6, no. 11. pp. 8701-8704. Available from: <http://dx.doi.org/10.1039/C5RA24211H> DOI 10.1039/C5RA24211H.
45. HUANG, C., et al. Dopant-Free Hole-Transporting Material with a C<sub>3h</sub> Symmetrical Truxene Core for Highly Efficient Perovskite Solar Cells. *Journal of the American Chemical Society*, 2016, vol. 138, no. 8. pp. 2528-2531. Available from: <https://doi.org/10.1021/jacs.6b00039> ISSN 0002-7863. DOI 10.1021/jacs.6b00039.
46. RAKSTYS, K., et al. Molecular Engineering of Face-on Oriented Dopant-Free Hole Transporting Material for Perovskite Solar Cells with 19% PCE. *Journal of Materials Chemistry A*, 2017, vol. 5, no. 17. pp. 7811-7815. Available from: <http://dx.doi.org/10.1039/C7TA01718A> ISSN 2050-7488. DOI 10.1039/C7TA01718A.
47. AZMI, R., et al. High-Performance Dopant-Free Conjugated Small Molecule-Based Hole-Transport Materials for Perovskite Solar Cells. *Nano Energy*, 2018, vol. 44. pp. 191-198. Available from: <http://www.sciencedirect.com/science/article/pii/S2211285517307693> ISSN 2211-2855. DOI <https://doi.org/10.1016/j.nanoen.2017.12.002>.

48. CHENG, M., et al. Efficient Perovskite Solar Cells Based on a Solution Processable Nickel(II) Phthalocyanine and Vanadium Oxide Integrated Hole Transport Layer. *Advanced Energy Materials*, 2017, vol. 7, no. 14. pp. 1602556. Available from: <https://doi.org/10.1002/aenm.201602556> ISSN 1614-6832. DOI <https://doi.org/10.1002/aenm.201602556>.
49. YIN, C., et al. Low-Cost N,N'-Bicarbazole-Based Dopant-Free Hole-Transporting Materials for Large-Area Perovskite Solar Cells. *Advanced Energy Materials*, 2018, vol. 8, no. 21. pp. 1800538. Available from: <https://doi.org/10.1002/aenm.201800538> ISSN 1614-6832. DOI <https://doi.org/10.1002/aenm.201800538>.
50. QIU, J., et al. Impact of 9-(4-Methoxyphenyl) Carbazole and Benzodithiophene Cores on Performance and Stability for Perovskite Solar Cells Based on Dopant-Free Hole-Transporting Materials. *Solar RRL*, 2019, vol. 3, no. 10. pp. 1900202. Available from: <https://doi.org/10.1002/solr.201900202> ISSN 2367-198X. DOI <https://doi.org/10.1002/solr.201900202>.
51. SHEN, C., et al. Semi-Locked Tetrathienylethene as a Building Block for Hole-Transporting Materials: Toward Efficient and Stable Perovskite Solar Cells. *Angewandte Chemie International Edition*, 2019, vol. 58, no. 12. pp. 3784-3789. Available from: <https://doi.org/10.1002/anie.201811593> ISSN 1433-7851. DOI <https://doi.org/10.1002/anie.201811593>.
52. WANG, Y., et al. Dopant-Free Small-Molecule Hole-Transporting Material for Inverted Perovskite Solar Cells with Efficiency Exceeding 21%. *Advanced Materials*, 2019, vol. 31, no. 35. pp. 1902781. Available from: <https://doi.org/10.1002/adma.201902781> ISSN 0935-9648. DOI <https://doi.org/10.1002/adma.201902781>.
53. STOLTERFOHT, M., et al. Approaching the Fill Factor Shockley–Queisser Limit in Stable, Dopant-Free Triple Cation Perovskite Solar Cells. *Energy & Environmental Science*, 2017, vol. 10, no. 6. pp. 1530-1539. Available from: <http://dx.doi.org/10.1039/C7EE00899F> ISSN 1754-5692. DOI 10.1039/C7EE00899F.
54. YANG, W.S., et al. Iodide Management in Formamidinium-Lead-Halide-based Perovskite Layers for Efficient Solar Cells. *Science*, 2017, vol. 356, no. 6345. pp. 1376-1379. Available from: <http://science.sciencemag.org/content/356/6345/1376.abstract> DOI 10.1126/science.aan2301.
55. LI, X., et al. Improving Efficiency and Reproducibility of Perovskite Solar Cells through Aggregation Control in Polyelectrolytes Hole Transport Layer. *ACS Applied Materials & Interfaces*, 2017, vol. 9, no. 37. pp. 31357-31361. Available from: <https://doi.org/10.1021/acsami.7b11977> ISSN 1944-8244. DOI 10.1021/acsami.7b11977.
56. HOU, Y., et al. A Generic Interface to Reduce the Efficiency-Stability-Cost Gap of Perovskite Solar Cells. *Science*, 2017, vol. 358, no. 6367. pp. 1192-1197.

Available from: <http://science.sciencemag.org/content/358/6367/1192.abstract> DOI 10.1126/science.aao5561.

57. CAI, F., et al. Molecular Engineering of Conjugated Polymers for Efficient Hole Transport and Defect Passivation in Perovskite Solar Cells. *Nano Energy*, 2018, vol. 45. pp. 28-36. Available from:

<http://www.sciencedirect.com/science/article/pii/S2211285517308030> ISSN 2211-2855. DOI <https://doi.org/10.1016/j.nanoen.2017.12.028>.

58. WU, J., et al. Side-Chain Polymers as Dopant-Free Hole-Transporting Materials for Perovskite Solar Cells—The Impact of Substituents' Positions in Carbazole on Device Performance. *ACS Applied Materials & Interfaces*, 2019, vol. 11, no. 30. pp. 26928-26937. Available from: <https://doi.org/10.1021/acsami.9b07859> ISSN 1944-8244. DOI 10.1021/acsami.9b07859.

59. GENG, Y., et al. Conjugated Materials Containing Dithieno[3,2-B:2',3'-D]Pyrrole and its Derivatives for Organic and Hybrid Solar Cell Applications. *Journal of Materials Chemistry A*, 2019, vol. 7, no. 1. pp. 64-96. Available from: <http://dx.doi.org/10.1039/C8TA09383K> ISSN 2050-7488. DOI 10.1039/C8TA09383K.

60. BULUMULLA, C., et al. Pyrrole-Containing Semiconducting Materials: Synthesis and Applications in Organic Photovoltaics and Organic Field-Effect Transistors. *ACS Applied Materials & Interfaces*, 2020, vol. 12, no. 29. pp. 32209-32232. Available from: <https://doi.org/10.1021/acsami.0c07161> ISSN 1944-8244. DOI 10.1021/acsami.0c07161.

61. ZHANG, L., et al. A Review on Solution-Processable Dopant-Free Small Molecules as Hole-Transporting Materials for Efficient Perovskite Solar Cells. *Small Methods*, 2020, vol. 4, no. 9. pp. 2000254. Available from: <https://doi.org/10.1002/smt.202000254> ISSN 2366-9608. DOI <https://doi.org/10.1002/smt.202000254>.

62. ZANIRATO, P., SPAGNOLO, P. and ZANARDI, G. Thermal Decomposition of O-Azidobithienyls. *Journal of the Chemical Society, Perkin Transactions 1*, 1983. pp. 2551-2554 CrossRef. ISSN 0300-922X. DOI 10.1039/P19830002551.

63. GRONOWITZ, S. Halogen-Metal Interconversion with Dibromobithienyls, 1961, vol. 15. pp. 1393-1395.

64. KOSER, G.F., et al. One-Step .Alpha.-Tosyloxylation of Ketones with [Hydroxy(Tosyloxy)Iodo]Benzene. *The Journal of Organic Chemistry*, 1982, vol. 47, no. 12. pp. 2487-2489. Available from: <https://doi.org/10.1021/jo00133a053> ISSN 0022-3263. DOI 10.1021/jo00133a053.

65. BERLIN, A., PAGANI, G., ZOTTI, G. and SCHIAVON, G. Electrochemical Polymerization of 1H,7H-Pyrrolo[2',3':4,5]-Thieno[3,2-B]Pyrrole and 4H-Dithieno[3,2-B;2',3'-D]Pyrrole. *Die Makromolekulare Chemie*, 1992, vol. 193, no. 2. pp. 399-409. Available from: <https://doi.org/10.1002/macp.1992.021930212> ISSN 0025-116X. DOI <https://doi.org/10.1002/macp.1992.021930212>.

66. ZHANG, W., LI, J., ZHANG, B. and QIN, J. Highly Fluorescent Conjugated Copolymers Containing Dithieno[3,2-B:2',3'-D]Pyrrole. *Macromolecular Rapid*

*Communications*, 2008, vol. 29, no. 19. pp. 1603-1608. Available from:

<https://doi.org/10.1002/marc.200800336> ISSN 1022-1336. DOI

<https://doi.org/10.1002/marc.200800336>.

67. FÖRTSCH, S., VOGT, A. and BÄUERLE, P. New Methods for the Synthesis of 4H-Dithieno[3,2-B:2',3'-D]Pyrrole. *Journal of Physical Organic Chemistry*, 2017, vol. 30, no. 9. pp. e3743. Available from: <https://doi.org/10.1002/poc.3743> ISSN 0894-3230. DOI <https://doi.org/10.1002/poc.3743>.

68. SONE, T., ABE, Y., SATO, N. and EBINA, M. The use of N, N-Dimethylformamide-Sulfonyl Chloride Complex for the Preparation of Thiophenesulfonyl Chlorides. *Bulletin of the Chemical Society of Japan*, 1985, vol. 58, no. 3. pp. 1063-1064.

69. CARPANELLI, C. and LEANDRI, G. Studies on the Chemistry of Dithienyls and Arylthienyls. I. Nitration of 2,2'-Dithienyl. *Annali Di Chimica (Rome)*, 1961, vol. 51. pp. 181-194.

70. OGAWA, K. and RASMUSSEN, S.C. A Simple and Efficient Route to N-Functionalized Dithieno[3,2-B:2',3'-D]Pyrroles: Fused-Ring Building Blocks for New Conjugated Polymeric Systems. *The Journal of Organic Chemistry*, 2003, vol. 68, no. 7. pp. 2921-2928. Available from: <https://doi.org/10.1021/jo034078k> ISSN 0022-3263. DOI 10.1021/jo034078k.

71. OGAWA, K., RADKE, K.R., ROTHSTEIN, S.D. and RASMUSSEN, S.C. Synthesis of Secondary and Tertiary Aminothiophenes Via Palladium-Catalyzed Amination. *The Journal of Organic Chemistry*, 2001, vol. 66, no. 26. pp. 9067-9070. Available from: <https://doi.org/10.1021/jo016195q> ISSN 0022-3263. DOI 10.1021/jo016195q.

72. OGAWA, K. and RASMUSSEN, S.C. N-Functionalized Poly(Dithieno[3,2-B:2',3'-D]Pyrrole)s: Highly Fluorescent Materials with Reduced Band Gaps. *Macromolecules*, 2006, vol. 39, no. 5. pp. 1771-1778. Available from: <https://doi.org/10.1021/ma052490r> ISSN 0024-9297. DOI 10.1021/ma052490r.

73. NOZAKI, K., et al. The Double N-Arylation of Primary Amines: Toward Multisubstituted Carbazoles with Unique Optical Properties. *Angewandte Chemie International Edition*, 2003, vol. 42, no. 18. pp. 2051-2053. Available from: <https://doi.org/10.1002/anie.200250648> ISSN 1433-7851. DOI <https://doi.org/10.1002/anie.200250648>.

74. KOECKELBERGHS, G., et al. Improved Synthesis of N-Alkyl Substituted Dithieno[3,2-B:2',3'-D]Pyrroles. *Tetrahedron*, 2005, vol. 61, no. 3. pp. 687-691. Available from: <http://www.sciencedirect.com/science/article/pii/S0040402004018447> ISSN 0040-4020. DOI <https://doi.org/10.1016/j.tet.2004.10.106>.

75. EVENSON, S.J. and RASMUSSEN, S.C. N-Acyldithieno[3,2-B:2',3'-D]Pyrroles: Second Generation Dithieno[3,2-B:2',3'-D]Pyrrole Building Blocks with Stabilized Energy Levels. *Organic Letters*, 2010, vol. 12, no. 18. pp. 4054-4057. Available from: <https://doi.org/10.1021/ol101647f> ISSN 1523-7060. DOI 10.1021/ol101647f.

76. GRONOWITZ, S. and HÖRNFELDT, A. *8 - Bi-, Ter- and Oligothiényls*. GRONOWITZ, Salo and HÖRNFELDT, Anna-Britta eds., Oxford: Academic Press, 2004 Available from: <http://www.sciencedirect.com/science/article/pii/B978012303953850014X> ISBN 1478-9914. DOI <https://doi.org/10.1016/B978-012303953-8/50014-X>.
77. KABIR, S.M.H., et al. New Syntheses of Tricyclic Thiophenes and Cyclic Tetrathiophenes using Transition-Metal-Catalyzed Cyclization. *Heterocycles*, 2000, vol. 52. pp. 761-774.
78. MARTÍN, R., LARSEN, C.H., CUENCA, A. and BUCHWALD, S.L. Cu-Catalyzed Tandem C–N Bond Formation for the Synthesis of Pyrroles and Heteroarylpyrroles. *Organic Letters*, 2007, vol. 9, no. 17. pp. 3379-3382. Available from: <https://doi.org/10.1021/ol7014225> ISSN 1523-7060. DOI 10.1021/ol7014225.
79. BARLOW, S., et al. Electronic and Optical Properties of 4H-Cyclopenta[2,1-B:3,4-B']Bithiophene Derivatives and their 4-Heteroatom-Substituted Analogues: A Joint Theoretical and Experimental Comparison. *The Journal of Physical Chemistry B*, 2010, vol. 114, no. 45. pp. 14397-14407. Available from: <https://doi.org/10.1021/jp100774r> ISSN 1520-6106. DOI 10.1021/jp100774r.
80. LEYSEN, P., QUATTROSOLDI, S., SALATELLI, E. and KOECKELBERGHS, G. Investigation of the Dithieno[3,2-B:2',3'-D]Pyrrole Polymerization using Cross-Coupling and Cationic Mechanisms. *Polymer Chemistry*, 2019, vol. 10, no. 8. pp. 1010-1017. Available from: <http://dx.doi.org/10.1039/C8PY01176A> ISSN 1759-9954. DOI 10.1039/C8PY01176A.
81. MABROUK, S., et al. Dithieno[3,2-B:2',3'-D]Pyrrole-Based Hole Transport Materials for Perovskite Solar Cells with Efficiencies Over 18%. *Journal of Materials Chemistry A*, 2018, vol. 6, no. 17. pp. 7950-7958. Available from: <http://dx.doi.org/10.1039/C8TA01773E> ISSN 2050-7488. DOI 10.1039/C8TA01773E.
82. YIN, X., et al. Dithieno[3,2-B:2',3'-D]Pyrrol-Cored Hole Transport Material Enabling Over 21% Efficiency Dopant-Free Perovskite Solar Cells. *Advanced Functional Materials*, 2019, vol. 29, no. 38. pp. 1904300. Available from: <https://doi.org/10.1002/adfm.201904300> ISSN 1616-301X. DOI <https://doi.org/10.1002/adfm.201904300>.
83. WONG, H., et al. Design and Synthesis of a New Class of Photochromic Diarylethene-Containing Dithieno[3,2-B:2',3'-D]Pyrroles and their Switchable Luminescence Properties. *Chemistry – A European Journal*, 2009, vol. 15, no. 39. pp. 10005-10009. Available from: <https://doi.org/10.1002/chem.200900581> ISSN 0947-6539. DOI <https://doi.org/10.1002/chem.200900581>.
84. MIYAURA, N. and SUZUKI, A. Palladium-Catalyzed Cross-Coupling Reactions of Organoboron Compounds. *Chemical Reviews*, 1995, vol. 95, no. 7. pp. 2457-2483. Available from: <https://doi.org/10.1021/cr00039a007> ISSN 0009-2665. DOI 10.1021/cr00039a007.

85. ODOM, S., et al. Bis[Bis-(4-Alkoxyphenyl)Amino] Derivatives of Dithienylethene, Bithiophene, Dithienothiophene and Dithienopyrrole: Palladium-Catalysed Synthesis and Highly Delocalised Radical Cations. *Chemistry – A European Journal*, 2007, vol. 13, no. 34. pp. 9637-9646. Available from: <https://doi.org/10.1002/chem.200700668> ISSN 0947-6539. DOI <https://doi.org/10.1002/chem.200700668>.
86. BALAJI, G., et al. Synthesis and Hole-Transporting Properties of Highly Fluorescent N-Aryl Dithieno[3,2-B:2',3'-D]Pyrrole-Based Oligomers. *The Journal of Physical Chemistry C*, 2010, vol. 114, no. 10. pp. 4628-4635. Available from: <https://doi.org/10.1021/jp909064n> ISSN 1932-7447. DOI 10.1021/jp909064n.
87. SANDOVAL-TORRIENTES, R., et al. Hole Transporting Materials Based on Benzodithiophene and Dithienopyrrole Cores for Efficient Perovskite Solar Cells. *Journal of Materials Chemistry A*, 2018, vol. 6, no. 14. pp. 5944-5951. Available from: <http://dx.doi.org/10.1039/C7TA11314E> ISSN 2050-7488. DOI 10.1039/C7TA11314E.
88. GRISORIO, R., et al. Monodispersed Vs. Polydispersed Systems for Bulk Heterojunction Solar Cells: The Case of Dithienopyrrole/Anthracene Based Materials. *Journal of Materials Chemistry*, 2012, vol. 22, no. 37. pp. 19752-19760. Available from: <http://dx.doi.org/10.1039/C2JM33795A> ISSN 0959-9428. DOI 10.1039/C2JM33795A.
89. YASSIN, A., et al. Evaluation of Bis-Dicyanovinyl Short-Chain Conjugated Systems as Donor Materials for Organic Solar Cells. *Solar Energy Materials and Solar Cells*, 2011, vol. 95, no. 2. pp. 462-468. Available from: <http://www.sciencedirect.com/science/article/pii/S0927024810005179> ISSN 0927-0248. DOI <https://doi.org/10.1016/j.solmat.2010.08.032>.
90. LIN, G., et al.  $\Pi$ -Conjugated Dithieno[3,2-B:2',3'-D]Pyrrole (DTP) Oligomers for Organic Thin-Film Transistors. *RSC Advances*, 2016, vol. 6, no. 6. pp. 4872-4876. Available from: <http://dx.doi.org/10.1039/C5RA24845K> DOI 10.1039/C5RA24845K.
91. YASSIN, A., LERICHE, P. and RONCALI, J. Synthesis and Chain-Length Dependence of the Electronic Properties of  $\Pi$ -Conjugated Dithieno[3,2-B:2',3'-D]Pyrrole (DTP) Oligomers. *Macromolecular Rapid Communications*, 2010, vol. 31, no. 16. pp. 1467-1472. Available from: <https://doi.org/10.1002/marc.201000174> ISSN 1022-1336. DOI <https://doi.org/10.1002/marc.201000174>.
92. KOECKELBERGHS, G., DE CREMER, L., PERSOONS, A. and VERBIEST, T. Influence of the Substituent and Polymerization Methodology on the Properties of Chiral Poly(Dithieno[3,2-B:2',3'-D]Pyrrole)S. *Macromolecules*, 2007, vol. 40, no. 12. pp. 4173-4181. Available from: <https://doi.org/10.1021/ma062808v> ISSN 0024-9297. DOI 10.1021/ma062808v.
93. ZHOU, E., et al. Synthesis and Photovoltaic Properties of a Novel Low Band Gap Polymer Based on N-Substituted Dithieno[3,2-B:2',3'-D]Pyrrole. *Macromolecules*, 2008, vol. 41, no. 22. pp. 8302-8305. Available from: <https://doi.org/10.1021/ma802052w> ISSN 0024-9297. DOI 10.1021/ma802052w.

94. TAMILAVAN, V., et al. Synthesis of N-[4-Octylphenyl]Dithieno[3,2-B:2',3'-D]Pyrrole-Based Broad Absorbing Polymers and their Photovoltaic Applications. *Polymer*, 2013, vol. 54, no. 13. pp. 3198-3205. Available from: <http://www.sciencedirect.com/science/article/pii/S0032386113003960> ISSN 0032-3861. DOI <https://doi.org/10.1016/j.polymer.2013.04.049>.
95. GENG, Y., et al. Synthesis and Properties of D–A Copolymers Based on Dithienopyrrole and Benzothiadiazole with various Numbers of Thienyl Units as Spacers. *Polymer Chemistry*, 2014, vol. 5, no. 23. pp. 6797-6803. Available from: <http://dx.doi.org/10.1039/C4PY00975D> ISSN 1759-9954. DOI 10.1039/C4PY00975D.
96. ZHOU, E., CONG, J., HASHIMOTO, K. and TAJIMA, K. Introduction of a Conjugated Side Chain as an Effective Approach to Improving Donor–acceptor Photovoltaic Polymers. *Energy & Environmental Science*, 2012, vol. 5, no. 12. pp. 9756-9759. Available from: <http://dx.doi.org/10.1039/C2EE23383E> ISSN 1754-5692. DOI 10.1039/C2EE23383E.
97. LI, W., et al. High Quantum Efficiencies in Polymer Solar Cells at Energy Losses Below 0.6 eV. *Journal of the American Chemical Society*, 2015, vol. 137, no. 6. pp. 2231-2234. Available from: <https://doi.org/10.1021/ja5131897> ISSN 0002-7863. DOI 10.1021/ja5131897.
98. POPOVIĆ, D., et al. Preparation of Efficient Oligomer-Based Bulk-Heterojunction Solar Cells from Eco-Friendly Solvents. *Journal of Materials Chemistry C*, 2017, vol. 5, no. 38. pp. 9920-9928. Available from: <http://dx.doi.org/10.1039/C7TC02131C> ISSN 2050-7526. DOI 10.1039/C7TC02131C.
99. WESSENDORF, C.D., et al. Understanding the Effect of Solvent Vapor Annealing on Solution-Processed A–D–A Oligothiophene Bulk-Heterojunction Solar Cells: The Role of Alkyl Side Chains. *Journal of Materials Chemistry A*, 2016, vol. 4, no. 7. pp. 2571-2580. Available from: <http://dx.doi.org/10.1039/C5TA07713C> ISSN 2050-7488. DOI 10.1039/C5TA07713C.
100. MISHRA, A., et al. High Performance A–D–A Oligothiophene-Based Organic Solar Cells Employing Two-Step Annealing and Solution-Processable Copper Thiocyanate (CuSCN) as an Interfacial Hole Transporting Layer. *Journal of Materials Chemistry A*, 2016, vol. 4, no. 44. pp. 17344-17353. Available from: <http://dx.doi.org/10.1039/C6TA07640H> ISSN 2050-7488. DOI 10.1039/C6TA07640H.
101. DONG, Z., et al. A Dithieno[3,2-B:2',3'-D]Pyrrole-Cored Four-Arm Hole Transporting Material for Over 19% Efficiency Dopant-Free Perovskite Solar Cells. *Journal of Materials Chemistry C*, 2019, vol. 7, no. 31. pp. 9455-9459. Available from: <http://dx.doi.org/10.1039/C9TC03111A> ISSN 2050-7526. DOI 10.1039/C9TC03111A.
102. ZHOU, J., et al. Dithieno[3,2-B:2',3'-D]Pyrrole Cored P-Type Semiconductors Enabling 20 % Efficiency Dopant-Free Perovskite Solar Cells. *Angewandte Chemie*

*International Edition*, 2019, vol. 58, no. 39. pp. 13717-13721. Available from: <https://doi.org/10.1002/anie.201905624> ISSN 1433-7851. DOI <https://doi.org/10.1002/anie.201905624>.

103. BHARATH, D., et al. Synthesis of New 2-((5-(4-Alkyl-4H-Dithieno[3,2-B:2',3'-D]Pyrrol-2-Yl)Thiophen-2-Yl)Methylene)Malononitrile: Dopant Free Hole Transporting Materials for Perovskite Solar Cells with High Power Conversion Efficiency. *Solar Energy*, 2018, vol. 174. pp. 130-138. Available from: <http://www.sciencedirect.com/science/article/pii/S0038092X1830865X> ISSN 0038-092X. DOI <https://doi.org/10.1016/j.solener.2018.09.002>.

104. WANG, J., et al. Indeno[1,2-B]Carbazole as Methoxy-Free Donor Group: Constructing Efficient and Stable Hole-Transporting Materials for Perovskite Solar Cells. *Angewandte Chemie International Edition*, 2019, vol. 58, no. 44. pp. 15721-15725. Available from: <https://doi.org/10.1002/anie.201909117> ISSN 1433-7851. DOI <https://doi.org/10.1002/anie.201909117>.

105. RASMUSSEN, S.C., EVENSON, S.J. and MCCAUSLAND, C.B. Fluorescent Thiophene-Based Materials and their Outlook for Emissive Applications. *Chemical Communications*, 2015, vol. 51, no. 22. pp. 4528-4543. Available from: <http://dx.doi.org/10.1039/C4CC09206F> ISSN 1359-7345. DOI 10.1039/C4CC09206F.

106. BURKHART, B., KHLIYABICH, P.P. and THOMPSON, B.C. Solar Cells Based on Semi-Random P3HT Analogues Containing Dithienopyrrole: Influence of Incorporating a Strong Donor. *Journal of Photonics for Energy*, 2012, vol. 2, no. 1. pp. 1-15. Available from: <https://doi.org/10.1117/1.JPE.2.021002> DOI 10.1117/1.JPE.2.021002.

107. VANORMELINGEN, W., et al. Enhanced Open-Circuit Voltage in Polymer Solar Cells by Dithieno[3,2-B:2',3'-D]Pyrrole N-Acylation. *Journal of Materials Chemistry A*, 2014, vol. 2, no. 20. pp. 7535-7545. Available from: <http://dx.doi.org/10.1039/C4TA00525B> ISSN 2050-7488. DOI 10.1039/C4TA00525B.

108. HENDRIKS, K.H., LI, W., WIENK, M.M. and JANSSEN, R.A.J. Small-Bandgap Semiconducting Polymers with High Near-Infrared Photoresponse. *Journal of the American Chemical Society*, 2014, vol. 136, no. 34. pp. 12130-12136. Available from: <https://doi.org/10.1021/ja506265h> ISSN 0002-7863. DOI 10.1021/ja506265h.

109. NELSON, T.L., et al. Transistor Paint: High Mobilities in Small Bandgap Polymer Semiconductor Based on the Strong Acceptor, Diketopyrrolopyrrole and Strong Donor, Dithienopyrrole. *Advanced Materials*, 2010, vol. 22, no. 41. pp. 4617-4621. Available from: <https://doi.org/10.1002/adma.201001599> ISSN 0935-9648. DOI <https://doi.org/10.1002/adma.201001599>.

110. HONSHO, Y., SAEKI, A. and SEKI, S. Effects of Molecular Structure on Intramolecular Charge Carrier Transport in Dithieno [3,2-B: 2 □ , 3 □ -D] Pyrrole-Based Conjugated Copolymers. *International Journal of Spectroscopy*, 2012, vol.



2012. pp. 983523. Available from: <https://doi.org/10.1155/2012/983523> ISSN 1687-9449. DOI 10.1155/2012/983523.

111. CONNELLY, N.G. and GEIGER, W.E. Chemical Redox Agents for Organometallic Chemistry. *Chemical Reviews*, 1996, vol. 96, no. 2. pp. 877-910. Available from: <https://doi.org/10.1021/cr940053x> ISSN 0009-2665. DOI 10.1021/cr940053x.

112. PAVLISHCHUK, V.V. and ADDISON, A.W. Conversion Constants for Redox Potentials Measured Versus Different Reference Electrodes in Acetonitrile Solutions at 25°C. *Inorganica Chimica Acta*, 2000, vol. 298, no. 1. pp. 97-102. Available from: <http://www.sciencedirect.com/science/article/pii/S0020169399004077> ISSN 0020-1693. DOI [https://doi.org/10.1016/S0020-1693\(99\)00407-7](https://doi.org/10.1016/S0020-1693(99)00407-7).

113. REISS, H. and HELLER, A. The Absolute Potential of the Standard Hydrogen Electrode: A New Estimate. *The Journal of Physical Chemistry*, 1985, vol. 89, no. 20. pp. 4207-4213. Available from: <https://doi.org/10.1021/j100266a013> ISSN 0022-3654. DOI 10.1021/j100266a013.

114. CORREA-BAENA, J., et al. The Rapid Evolution of Highly Efficient Perovskite Solar Cells. *Energy & Environmental Science*, 2017, vol. 10, no. 3. pp. 710-727. Available from: <http://dx.doi.org/10.1039/C6EE03397K> ISSN 1754-5692. DOI 10.1039/C6EE03397K.

115. DOMANSKI, K., et al. Not all that Glitters is Gold: Metal-Migration-Induced Degradation in Perovskite Solar Cells. *ACS Nano*, 2016, vol. 10, no. 6. pp. 6306-6314. Available from: <https://doi.org/10.1021/acsnano.6b02613> ISSN 1936-0851. DOI 10.1021/acsnano.6b02613.

116. MALINAUSKAS, T., et al. Enhancing Thermal Stability and Lifetime of Solid-State Dye-Sensitized Solar Cells Via Molecular Engineering of the Hole-Transporting Material Spiro-OMeTAD. *ACS Applied Materials & Interfaces*, 2015, vol. 7, no. 21. pp. 11107-11116. Available from: <https://doi.org/10.1021/am5090385> ISSN 1944-8244. DOI 10.1021/am5090385.

117. ABATE, A., et al. Silolothiophene-Linked Triphenylamines as Stable Hole Transporting Materials for High Efficiency Perovskite Solar Cells. *Energy & Environmental Science*, 2015, vol. 8, no. 10. pp. 2946-2953. Available from: <http://dx.doi.org/10.1039/C5EE02014J> ISSN 1754-5692. DOI 10.1039/C5EE02014J.

118. KIM, S., et al. Relationship between Ion Migration and Interfacial Degradation of CH<sub>3</sub>NH<sub>3</sub>PbI<sub>3</sub> Perovskite Solar Cells Under Thermal Conditions. *Scientific Reports*, 2017, vol. 7, no. 1. pp. 1200. Available from: <https://doi.org/10.1038/s41598-017-00866-6> ISSN 2045-2322. DOI 10.1038/s41598-017-00866-6.

119. KIM, H., LIM, K. and LEE, T. Planar Heterojunction Organometal Halide Perovskite Solar Cells: Roles of Interfacial Layers. *Energy & Environmental Science*, 2016, vol. 9, no. 1. pp. 12-30. Available from: <http://dx.doi.org/10.1039/C5EE02194D> ISSN 1754-5692. DOI 10.1039/C5EE02194D.

120. ABATE, A., et al. Lithium Salts as “redox Active” P-Type Dopants for Organic Semiconductors and their Impact in Solid-State Dye-Sensitized Solar Cells. *Physical Chemistry Chemical Physics*, 2013, vol. 15, no. 7. pp. 2572-2579. Available from: <http://dx.doi.org/10.1039/C2CP44397J> ISSN 1463-9076. DOI 10.1039/C2CP44397J.
121. ABATE, A., et al. Influence of Ionizing Dopants on Charge Transport in Organic Semiconductors. *Physical Chemistry Chemical Physics*, 2014, vol. 16, no. 3. pp. 1132-1138. Available from: <http://dx.doi.org/10.1039/C3CP53834F> ISSN 1463-9076. DOI 10.1039/C3CP53834F.
122. CORREA-BAENA, J., et al. Identifying and Suppressing Interfacial Recombination to Achieve High Open-Circuit Voltage in Perovskite Solar Cells. *Energy & Environmental Science*, 2017, vol. 10, no. 5. pp. 1207-1212. Available from: <http://dx.doi.org/10.1039/C7EE00421D> ISSN 1754-5692. DOI 10.1039/C7EE00421D.
123. HAWASH, Z., et al. Air-Exposure Induced Dopant Redistribution and Energy Level Shifts in Spin-Coated Spiro-MeOTAD Films. *Chemistry of Materials*, 2015, vol. 27, no. 2. pp. 562-569. Available from: <https://doi.org/10.1021/cm504022q> ISSN 0897-4756. DOI 10.1021/cm504022q.
124. CAPPEL, U.B., DAENEKE, T. and BACH, U. Oxygen-Induced Doping of Spiro-MeOTAD in Solid-State Dye-Sensitized Solar Cells and its Impact on Device Performance. *Nano Letters*, 2012, vol. 12, no. 9. pp. 4925-4931. Available from: <https://doi.org/10.1021/nl302509q> ISSN 1530-6984. DOI 10.1021/nl302509q.
125. WANG, S., et al. Role of 4-Tert-Butylpyridine as a Hole Transport Layer Morphological Controller in Perovskite Solar Cells. *Nano Letters*, 2016, vol. 16, no. 9. pp. 5594-5600. Available from: <https://doi.org/10.1021/acs.nanolett.6b02158> ISSN 1530-6984. DOI 10.1021/acs.nanolett.6b02158.
126. HABISREUTINGER, S.N., NOEL, N.K., SNAITH, H.J. and NICHOLAS, R.J. Investigating the Role of 4-Tert Butylpyridine in Perovskite Solar Cells. *Advanced Energy Materials*, 2017, vol. 7, no. 1. pp. 1601079. Available from: <https://doi.org/10.1002/aenm.201601079> ISSN 1614-6832. DOI <https://doi.org/10.1002/aenm.201601079>.
127. HAWASH, Z., ONO, L.K. and QI, Y. Moisture and Oxygen Enhance Conductivity of LiTFSI-Doped Spiro-MeOTAD Hole Transport Layer in Perovskite Solar Cells. *Advanced Materials Interfaces*, 2016, vol. 3, no. 13. pp. 1600117. Available from: <https://doi.org/10.1002/admi.201600117> ISSN 2196-7350. DOI <https://doi.org/10.1002/admi.201600117>.
128. NGUYEN, W.H., BAILIE, C.D., UNGER, E.L. and MCGEHEE, M.D. Enhancing the Hole-Conductivity of Spiro-OMeTAD without Oxygen Or Lithium Salts by using Spiro(TFSI)<sub>2</sub> in Perovskite and Dye-Sensitized Solar Cells. *Journal of the American Chemical Society*, 2014, vol. 136, no. 31. pp. 10996-11001. Available from: <https://doi.org/10.1021/ja504539w> ISSN 0002-7863. DOI 10.1021/ja504539w.

129. SANCHEZ, R.S. and MAS-MARZA, E. Light-Induced Effects on Spiro-OMeTAD Films and Hybrid Lead Halide Perovskite Solar Cells. *Solar Energy Materials and Solar Cells*, 2016, vol. 158. pp. 189-194. Available from: <http://www.sciencedirect.com/science/article/pii/S0927024816001264> ISSN 0927-0248. DOI <https://doi.org/10.1016/j.solmat.2016.03.024>.
130. BARANWAL, A.K., et al. 100 °C Thermal Stability of Printable Perovskite Solar Cells using Porous Carbon Counter Electrodes. *ChemSusChem*, 2016, vol. 9, no. 18. pp. 2604-2608. Available from: <https://doi.org/10.1002/cssc.201600933> ISSN 1864-5631. DOI <https://doi.org/10.1002/cssc.201600933>.
131. LEIJTENS, T., et al. Hydrophobic Organic Hole Transporters for Improved Moisture Resistance in Metal Halide Perovskite Solar Cells. *ACS Applied Materials & Interfaces*, 2016, vol. 8, no. 9. pp. 5981-5989. Available from: <https://doi.org/10.1021/acsami.5b10093> ISSN 1944-8244. DOI 10.1021/acsami.5b10093.
132. MALINAUSKAS, T., et al. Branched Methoxydiphenylamine-Substituted Fluorene Derivatives as Hole Transporting Materials for High-Performance Perovskite Solar Cells. *Energy & Environmental Science*, 2016, vol. 9, no. 5. pp. 1681-1686. Available from: <http://dx.doi.org/10.1039/C5EE03911H> ISSN 1754-5692. DOI 10.1039/C5EE03911H.
133. VÖLKER, S.F., COLLAVINI, S. and DELGADO, J.L. Organic Charge Carriers for Perovskite Solar Cells. *ChemSusChem*, 2015, vol. 8, no. 18. pp. 3012-3028. Available from: <https://doi.org/10.1002/cssc.201500742> ISSN 1864-5631. DOI <https://doi.org/10.1002/cssc.201500742>.
134. VÖLKER, S.F., et al. Fullerene-Based Materials as Hole-Transporting/Electron-Blocking Layers: Applications in Perovskite Solar Cells. *Chemistry – A European Journal*, 2018, vol. 24, no. 34. pp. 8524-8529. Available from: <https://doi.org/10.1002/chem.201801069> ISSN 0947-6539. DOI <https://doi.org/10.1002/chem.201801069>.
135. YUE, Y., et al. Enhanced Stability of Perovskite Solar Cells through Corrosion-Free Pyridine Derivatives in Hole-Transporting Materials. *Advanced Materials*, 2016, vol. 28, no. 48. pp. 10738-10743. Available from: <https://doi.org/10.1002/adma.201602822> ISSN 0935-9648. DOI <https://doi.org/10.1002/adma.201602822>.
136. DIVITINI, G., et al. In Situ Observation of Heat-Induced Degradation of Perovskite Solar Cells. *Nature Energy*, 2016, vol. 1, no. 2. pp. 15012. Available from: <https://doi.org/10.1038/nenergy.2015.12> ISSN 2058-7546. DOI 10.1038/nenergy.2015.12.
137. BAG, M., et al. Kinetics of Ion Transport in Perovskite Active Layers and its Implications for Active Layer Stability. *Journal of the American Chemical Society*, 2015, vol. 137, no. 40. pp. 13130-13137. Available from: <https://doi.org/10.1021/jacs.5b08535> ISSN 0002-7863. DOI 10.1021/jacs.5b08535.
138. CARRILLO, J., et al. Ionic Reactivity at Contacts and Aging of Methylammonium Lead Triiodide Perovskite Solar Cells. *Advanced Energy*

- Materials*, 2016, vol. 6, no. 9. pp. 1502246. Available from:  
<https://doi.org/10.1002/aenm.201502246> ISSN 1614-6832. DOI  
<https://doi.org/10.1002/aenm.201502246>.
139. LEE, J., et al. Verification and Mitigation of Ion Migration in Perovskite Solar Cells. *APL Materials*, 2019, vol. 7, no. 4. pp. 041111. Available from:  
<https://doi.org/10.1063/1.5085643> DOI 10.1063/1.5085643.
140. LI, J., DONG, Q., LI, N. and WANG, L. Direct Evidence of Ion Diffusion for the Silver-Electrode-Induced Thermal Degradation of Inverted Perovskite Solar Cells. *Advanced Energy Materials*, 2017, vol. 7, no. 14. pp. 1602922. Available from:  
<https://doi.org/10.1002/aenm.201602922> ISSN 1614-6832. DOI  
<https://doi.org/10.1002/aenm.201602922>.
141. DOMANSKI, K., et al. Migration of Cations Induces Reversible Performance Losses Over Day/Night Cycling in Perovskite Solar Cells. *Energy & Environmental Science*, 2017, vol. 10, no. 2. pp. 604-613. Available from:  
<http://dx.doi.org/10.1039/C6EE03352K> ISSN 1754-5692. DOI  
10.1039/C6EE03352K.
142. ZHANG, T., et al. Profiling the Organic Cation-Dependent Degradation of Organolead Halide Perovskite Solar Cells. *Journal of Materials Chemistry A*, 2017, vol. 5, no. 3. pp. 1103-1111. Available from:  
<http://dx.doi.org/10.1039/C6TA09687E> ISSN 2050-7488. DOI  
10.1039/C6TA09687E.
143. SHLENSKAYA, N.N., et al. Light-Induced Reactivity of Gold and Hybrid Perovskite as a New Possible Degradation Mechanism in Perovskite Solar Cells. *Journal of Materials Chemistry A*, 2018, vol. 6, no. 4. pp. 1780-1786. Available from:  
<http://dx.doi.org/10.1039/C7TA10217H> ISSN 2050-7488. DOI  
10.1039/C7TA10217H.
144. DUALEH, A., et al. Thermal Behavior of Methylammonium Lead-Trihalide Perovskite Photovoltaic Light Harvesters. *Chemistry of Materials*, 2014, vol. 26, no. 21. pp. 6160-6164. Available from:  
<https://doi.org/10.1021/cm502468k> ISSN 0897-4756. DOI 10.1021/cm502468k.
145. RAKSTYS, K., IGCI, C. and NAZEERUDDIN, M.K. Efficiency Vs. Stability: Dopant-Free Hole Transporting Materials Towards Stabilized Perovskite Solar Cells. *Chemical Science*, 2019, vol. 10, no. 28. pp. 6748-6769. Available from:  
<http://dx.doi.org/10.1039/C9SC01184F> ISSN 2041-6520. DOI  
10.1039/C9SC01184F.
146. ZHOU, Y., et al. Enhancing Chemical Stability and Suppressing Ion Migration in CH<sub>3</sub>NH<sub>3</sub>PbI<sub>3</sub> Perovskite Solar Cells Via Direct Backbone Attachment of Polyesters on Grain Boundaries. *Chemistry of Materials*, 2020, vol. 32, no. 12. pp. 5104-5117. Available from:  
<https://doi.org/10.1021/acs.chemmater.0c00995> ISSN  
0897-4756. DOI 10.1021/acs.chemmater.0c00995.
147. WANG, R., et al. A Review of Perovskites Solar Cell Stability. *Advanced Functional Materials*, 2019, vol. 29, no. 47. pp. 1808843. Available from:

<https://doi.org/10.1002/adfm.201808843> ISSN 1616-301X. DOI <https://doi.org/10.1002/adfm.201808843>.

148. MAGOMEDOV, A., et al. Self-Assembled Hole Transporting Monolayer for Highly Efficient Perovskite Solar Cells. *Advanced Energy Materials*, 2018, vol. 8, no. 32. pp. 1801892. Available from: <https://doi.org/10.1002/aenm.201801892> ISSN 1614-6832. DOI <https://doi.org/10.1002/aenm.201801892>.

149. AL-ASHOURI, A., et al. Conformal Monolayer Contacts with Lossless Interfaces for Perovskite Single Junction and Monolithic Tandem Solar Cells. *Energy & Environmental Science*, 2019, vol. 12, no. 11. pp. 3356-3369. Available from: <http://dx.doi.org/10.1039/C9EE02268F> ISSN 1754-5692. DOI 10.1039/C9EE02268F.

150. ZHAO, J., et al. Is Cu a Stable Electrode Material in Hybrid Perovskite Solar Cells for a 30-Year Lifetime?. *Energy & Environmental Science*, 2016, vol. 9, no. 12. pp. 3650-3656. Available from: <http://dx.doi.org/10.1039/C6EE02980A> ISSN 1754-5692. DOI 10.1039/C6EE02980A.

151. JÄGER, K., KORTE, L., RECH, B. and ALBRECHT, S. Numerical Optical Optimization of Monolithic Planar Perovskite-Silicon Tandem Solar Cells with Regular and Inverted Device Architectures. *Optics Express*, 2017, vol. 25, no. 12. pp. A473-A482. Available from: <http://www.opticsexpress.org/abstract.cfm?URI=oe-25-12-A473> DOI 10.1364/OE.25.00A473.

152. BUSH, K.A., et al. 23.6%-Efficient Monolithic Perovskite/Silicon Tandem Solar Cells with Improved Stability. *Nature Energy*, 2017, vol. 2, no. 4. pp. 17009. Available from: <https://doi.org/10.1038/nenergy.2017.9> ISSN 2058-7546. DOI 10.1038/nenergy.2017.9.

153. MALINKIEWICZ, O., et al. Perovskite Solar Cells Employing Organic Charge-Transport Layers. *Nature Photonics*, 2014, vol. 8, no. 2. pp. 128-132. Available from: <https://doi.org/10.1038/nphoton.2013.341> ISSN 1749-4893. DOI 10.1038/nphoton.2013.341.

154. DOCAMPO, P., et al. Efficient Organometal Trihalide Perovskite Planar-Heterojunction Solar Cells on Flexible Polymer Substrates. *Nature Communications*, 2013, vol. 4, no. 1. pp. 2761. Available from: <https://doi.org/10.1038/ncomms3761> ISSN 2041-1723. DOI 10.1038/ncomms3761.

155. CHEN, W., et al. Efficient and Stable Large-Area Perovskite Solar Cells with Inorganic Charge Extraction Layers. *Science*, 2015, vol. 350, no. 6263. pp. 944-948. Available from: <http://science.sciencemag.org/content/350/6263/944.abstract> DOI 10.1126/science.aad1015.

156. MOMBLONA, C., et al. Efficient Vacuum Deposited P-i-N and N-i-P Perovskite Solar Cells Employing Doped Charge Transport Layers. *Energy & Environmental Science*, 2016, vol. 9, no. 11. pp. 3456-3463. Available from: <http://dx.doi.org/10.1039/C6EE02100J> ISSN 1754-5692. DOI 10.1039/C6EE02100J.

157. HOTCHKISS, P.J., et al. The Modification of Indium Tin Oxide with Phosphonic Acids: Mechanism of Binding, Tuning of Surface Properties, and Potential for use in Organic Electronic Applications. *Accounts of Chemical Research*, 2012, vol. 45, no. 3. pp. 337-346. Available from: <https://doi.org/10.1021/ar200119g> ISSN 0001-4842. DOI 10.1021/ar200119g.
158. PANIAGUA, S.A., et al. Phosphonic Acids for Interfacial Engineering of Transparent Conductive Oxides. *Chemical Reviews*, 2016, vol. 116, no. 12. pp. 7117-7158. Available from: <https://doi.org/10.1021/acs.chemrev.6b00061> ISSN 0009-2665. DOI 10.1021/acs.chemrev.6b00061.
159. PARAMONOV, P.B., et al. Theoretical Characterization of the Indium Tin Oxide Surface and of its Binding Sites for Adsorption of Phosphonic Acid Monolayers. *Chemistry of Materials*, 2008, vol. 20, no. 16. pp. 5131-5133. Available from: <https://doi.org/10.1021/cm8014622> ISSN 0897-4756. DOI 10.1021/cm8014622.
160. PANIAGUA, S.A., et al. Phosphonic Acid Modification of Indium–Tin Oxide Electrodes: Combined XPS/UPS/Contact Angle Studies. *The Journal of Physical Chemistry C*, 2008, vol. 112, no. 21. pp. 7809-7817. Available from: <https://doi.org/10.1021/jp710893k> ISSN 1932-7447. DOI 10.1021/jp710893k.
161. PANIAGUA, S.A., LI, E.L. and MARDER, S.R. Adsorption Studies of a Phosphonic Acid on ITO: Film Coverage, Purity, and Induced Electronic Structure Changes. *Physical Chemistry Chemical Physics*, 2014, vol. 16, no. 7. pp. 2874-2881. Available from: <http://dx.doi.org/10.1039/C3CP54637C> ISSN 1463-9076. DOI 10.1039/C3CP54637C.
162. KEGELMANN, L., et al. It Takes Two to Tango—Double-Layer Selective Contacts in Perovskite Solar Cells for Improved Device Performance and Reduced Hysteresis. *ACS Applied Materials & Interfaces*, 2017, vol. 9, no. 20. pp. 17245-17255. Available from: <https://doi.org/10.1021/acsami.7b00900> ISSN 1944-8244. DOI 10.1021/acsami.7b00900.
163. TANG, Z., et al. Modulations of various Alkali Metal Cations on Organometal Halide Perovskites and their Influence on Photovoltaic Performance. *Nano Energy*, 2018, vol. 45. pp. 184-192. Available from: <http://www.sciencedirect.com/science/article/pii/S2211285517308236> ISSN 2211-2855. DOI <https://doi.org/10.1016/j.nanoen.2017.12.047>.
164. WANG, C., et al. Low-Temperature Processed, Efficient, and Highly Reproducible Cesium-Doped Triple Cation Perovskite Planar Heterojunction Solar Cells. *Solar RRL*, 2018, vol. 2, no. 2. pp. 1700209. Available from: <https://doi.org/10.1002/solr.201700209> ISSN 2367-198X. DOI <https://doi.org/10.1002/solr.201700209>.
165. DEEPA, M., et al. Cesium Power: Low Cs<sup>+</sup> Levels Impart Stability to Perovskite Solar Cells. *Physical Chemistry Chemical Physics*, 2017, vol. 19, no. 5. pp. 4069-4077. Available from: <http://dx.doi.org/10.1039/C6CP08022G> ISSN 1463-9076. DOI 10.1039/C6CP08022G.

166. ZHENG, X., et al. Defect Passivation in Hybrid Perovskite Solar Cells using Quaternary Ammonium Halide Anions and Cations. *Nature Energy*, 2017, vol. 2, no. 7. pp. 17102. Available from: <https://doi.org/10.1038/nenergy.2017.102> ISSN 2058-7546. DOI 10.1038/nenergy.2017.102.
167. LIN, Y., et al. Excess Charge-Carrier Induced Instability of Hybrid Perovskites. *Nature Communications*, 2018, vol. 9, no. 1. pp. 4981. Available from: <https://doi.org/10.1038/s41467-018-07438-w> ISSN 2041-1723. DOI 10.1038/s41467-018-07438-w.
168. CHEN, B., et al. Synergistic Effect of Elevated Device Temperature and Excess Charge Carriers on the Rapid Light-Induced Degradation of Perovskite Solar Cells. *Advanced Materials*, 2019, vol. 31, no. 35. pp. 1902413. Available from: <https://doi.org/10.1002/adma.201902413> ISSN 0935-9648. DOI <https://doi.org/10.1002/adma.201902413>.
169. BOCCARD, M. and BALLIF, C. Influence of the Subcell Properties on the Fill Factor of Two-Terminal Perovskite–Silicon Tandem Solar Cells. *ACS Energy Letters*, 2020, vol. 5, no. 4. pp. 1077-1082. Available from: <https://doi.org/10.1021/acsenergylett.0c00156> DOI 10.1021/acsenergylett.0c00156.
170. BUSH, K.A., et al. 23.6%-Efficient Monolithic Perovskite/Silicon Tandem Solar Cells with Improved Stability. *Nature Energy*, 2017, vol. 2, no. 4. pp. 17009. Available from: <https://doi.org/10.1038/nenergy.2017.9> ISSN 2058-7546. DOI 10.1038/nenergy.2017.9.
171. NAYAK, P.K., MAHESH, S., SNAITH, H.J. and CAHEN, D. Photovoltaic Solar Cell Technologies: Analysing the State of the Art. *Nature Reviews Materials*, 2019, vol. 4, no. 4. pp. 269-285. Available from: <https://doi.org/10.1038/s41578-019-0097-0> ISSN 2058-8437. DOI 10.1038/s41578-019-0097-0.
172. GUILLEMOLES, J., KIRCHARTZ, T., CAHEN, D. and RAU, U. Guide for the Perplexed to the Shockley–Queisser Model for Solar Cells. *Nature Photonics*, 2019, vol. 13, no. 8. pp. 501-505. Available from: <https://doi.org/10.1038/s41566-019-0479-2> ISSN 1749-4893. DOI 10.1038/s41566-019-0479-2.
173. GREEN, M.A. and HO-BAILLIE, A. Pushing to the Limit: Radiative Efficiencies of Recent Mainstream and Emerging Solar Cells. *ACS Energy Letters*, 2019, vol. 4, no. 7. pp. 1639-1644. Available from: <https://doi.org/10.1021/acsenergylett.9b01128> DOI 10.1021/acsenergylett.9b01128.
174. CAPRIOGLIO, P., et al. On the Origin of the Ideality Factor in Perovskite Solar Cells. *Advanced Energy Materials*, 2020, vol. 10, no. 27. pp. 2000502. Available from: <https://doi.org/10.1002/aenm.202000502> ISSN 1614-6832. DOI <https://doi.org/10.1002/aenm.202000502>.
175. AVILA, J., et al. Influence of Doped Charge Transport Layers on Efficient Perovskite Solar Cells. *Sustainable Energy Fuels*, 2018, vol. 2, no. 11. pp. 2429-2434. Available from: <http://dx.doi.org/10.1039/C8SE00218E> DOI 10.1039/C8SE00218E.
176. JEON, N.J., et al. A Fluorene-Terminated Hole-Transporting Material for Highly Efficient and Stable Perovskite Solar Cells. *Nature Energy*, 2018, vol. 3, no.

8. pp. 682-689. Available from: <https://doi.org/10.1038/s41560-018-0200-6> ISSN 2058-7546. DOI 10.1038/s41560-018-0200-6.
177. SEKIMOTO, T., et al. Influence of a Hole-Transport Layer on Light-Induced Degradation of Mixed Organic–Inorganic Halide Perovskite Solar Cells. *ACS Applied Energy Materials*, 2019, vol. 2, no. 7. pp. 5039-5049. Available from: <https://doi.org/10.1021/acsaem.9b00709> DOI 10.1021/acsaem.9b00709.
178. KÖHNEN, E., et al. Highly Efficient Monolithic Perovskite Silicon Tandem Solar Cells: Analyzing the Influence of Current Mismatch on Device Performance. *Sustainable Energy Fuels*, 2019, vol. 3, no. 8. pp. 1995-2005. Available from: <http://dx.doi.org/10.1039/C9SE00120D> DOI 10.1039/C9SE00120D.
179. GREEN, M.A., et al. Solar Cell Efficiency Tables (Version 55). *Progress in Photovoltaics: Research and Applications*, 2020, vol. 28, no. 1. pp. 3-15. Available from: <https://doi.org/10.1002/pip.3228> ISSN 1062-7995. DOI <https://doi.org/10.1002/pip.3228>.
180. CHEN, B., et al. Enhanced Optical Path and Electron Diffusion Length Enable High-Efficiency Perovskite Tandems. *Nature Communications*, 2020, vol. 11, no. 1. pp. 1257. Available from: <https://doi.org/10.1038/s41467-020-15077-3> ISSN 2041-1723. DOI 10.1038/s41467-020-15077-3.
181. A. Richter, M. Hermle and S. W. Glunz. *Reassessment of the Limiting Efficiency for Crystalline Silicon Solar Cells.* , 2013 ISBN 2156-3403. DOI 10.1109/JPHOTOV.2013.2270351.
182. SAHLI, F., et al. Fully Textured Monolithic Perovskite/Silicon Tandem Solar Cells with 25.2% Power Conversion Efficiency. *Nature Materials*, 2018, vol. 17, no. 9. pp. 820-826. Available from: <https://doi.org/10.1038/s41563-018-0115-4> ISSN 1476-4660. DOI 10.1038/s41563-018-0115-4.
183. CHEN, B., et al. Blade-Coated Perovskites on Textured Silicon for 26%-Efficient Monolithic Perovskite/Silicon Tandem Solar Cells. *Joule*, 2020, vol. 4, no. 4. pp. 850-864. Available from: <http://www.sciencedirect.com/science/article/pii/S2542435120300350> ISSN 2542-4351. DOI <https://doi.org/10.1016/j.joule.2020.01.008>.
184. JOŠT, M., et al. Perovskite Solar Cells Go Outdoors: Field Testing and Temperature Effects on Energy Yield. *Advanced Energy Materials*, 2020, vol. 10, no. 25. pp. 2000454. Available from: <https://doi.org/10.1002/aenm.202000454> ISSN 1614-6832. DOI <https://doi.org/10.1002/aenm.202000454>.
185. MIYAMOTO, E., YAMAGUCHI, Y. and YOKOYAMA, M. Ionization Potential of Organic Pigment Film by Atmospheric Photoelectron Emission Analysis. *DENSHI SHASHIN GAKKAISHI (Electrography)*, 1989, vol. 28, no. 4. pp. 364-370 DOI 10.11370/isjepj.28.364.
186. CARDONA, M. and LEY, L. *Photoemission in Solids I: General Principles*. M. CARDONA, and L. LEY eds., Berlin Heidelberg: Springer-Verlag, 1978 [viewed Nov 26, 2020]. Available from: <https://www.springer.com/gp/book/9783662309193> ISBN 9783662309193.



187. VAEZI-NEJAD, S. Xerographic Time of Flight Experiment for the Determination of Drift Mobility in High Resistivity Semiconductors. *Null*, 1987, vol. 62, no. 3. pp. 361-384. Available from: <https://doi.org/10.1080/00207218708920988> ISSN 0020-7217. DOI 10.1080/00207218708920988.
188. CHAN, A.Y.C. and JUHASZ, C. Xerographic-Mode Transient Charge Technique for Probing Drift Mobility in High-Resistivity Materials. *Null*, 1987, vol. 62, no. 4. pp. 625-632. Available from: <https://doi.org/10.1080/00207218708921013> ISSN 0020-7217. DOI 10.1080/00207218708921013.
189. GIORDANO, F., et al. Enhanced Electronic Properties in Mesoporous TiO<sub>2</sub> Via Lithium Doping for High-Efficiency Perovskite Solar Cells. *Nature Communications*, 2016, vol. 7, no. 1. pp. 10379. Available from: <https://doi.org/10.1038/ncomms10379> ISSN 2041-1723. DOI 10.1038/ncomms10379.
190. BI, D., et al. Efficient Luminescent Solar Cells Based on Tailored Mixed-Cation Perovskites. *Science Advances*, 2016, vol. 2, no. 1. pp. e1501170. Available from: <http://advances.sciencemag.org/content/2/1/e1501170.abstract> DOI 10.1126/sciadv.1501170.
191. ARANDA, C., GUERRERO, A. and BISQUERT, J. Ionic Effect Enhances Light Emission and the Photovoltage of Methylammonium Lead Bromide Perovskite Solar Cells by Reduced Surface Recombination. *ACS Energy Letters*, 2019, vol. 4, no. 3. pp. 741-746. Available from: <https://doi.org/10.1021/acsenergylett.9b00186> DOI 10.1021/acsenergylett.9b00186.
192. WAGHRAY, D., DE VET, C., KARYPIDOU, K. and DEHAEN, W. Oxidative Transformation to Naphthodithiophene and Thia[7]Helicenes by Intramolecular Scholl Reaction of Substituted 1,2-Bis(2-Thienyl)Benzene Precursors. *The Journal of Organic Chemistry*, 2013, vol. 78, no. 22. pp. 11147-11154. Available from: <https://doi.org/10.1021/jo401807x> ISSN 0022-3263. DOI 10.1021/jo401807x.
193. GALI, H., PRABHU, K.R., KARRA, S.R. and KATTI, K.V. Facile Ring-Opening Reactions of Phthalimides as a New Strategy to Synthesize Amide-Functionalized Phosphonates, Primary Phosphines, and Bisphosphines. *The Journal of Organic Chemistry*, 2000, vol. 65, no. 3. pp. 676-680. Available from: <https://doi.org/10.1021/jo991067b> ISSN 0022-3263. DOI 10.1021/jo991067b.

## 7. CURRICULUM VITAE

### Personal information

Name, Surname	Ernestas Kasparavičius
Date of birth	1990 09 21
Place of birth	Rokiškis, Lithuania
Nationality	Lithuanian
Email	ernestas.kasparavicius@ktu.lt

### Education

2016–2020	Kaunas University of Technology PhD studies, Chemistry
2014–2016	Kaunas University of Technology Master of chemistry
2010–2014	Kaunas University of Technology Bachelor of chemistry
2008–2010	Rokiškio r. Juodupės gymnasium
1998–2008	Rokiškio r. Lukštų Primary School

### Work experience

05.2019–present	Project junior researcher
04.2016–12.2018	Project engineer
01.2014–03.2016	Laboratory assistant

### Scientific work

<b>01.2014–present</b>	Research work in Prof. Dr. Vytautas Getautis scientific group. Synthesis and characterization of stable amorphous organic photoconductors for novel applications in electronics (PSC, OLED, DSSC etc.).
<b>2012–2013</b>	2 times participant of the Research Council of Lithuania projects “ <i>Students scientific practice</i> ”, “ <i>Students scientific researches</i> ” and “ <i>Students scientific work stimulation</i> ”.

### Languages

Lithuanian – mother tongue. English (C1), German (A2).

## **Awards**

- 17.04.2019 The Lithuanian Academy of Sciences (LMA) best young researcher and graduate student research work award.
- 21.03.2019 “Infobalt” 9th young researchers conference “Interdisciplinary Research in Physical and Technological Sciences” scholarship laureate.
- 14.02.2017 Lithuanian Academy of Sciences award for the best student research work in the field of physics, chemistry and mathematics

## 8. LIST OF PUBLICATIONS AND CONFERENCES

### Publications

1. Al-Ashouri, Amran; Köhnen, Eike; Li, Bor; Magomedov, Artiom; Hempel, Hannes; Caprioglio, Pietro; Márquez, José A.; Vilches, Anna Belen Morales; **Kasparavicius, Ernestas**; Smith, Joel A.; Phung, Nga; Menzel, Dorothee; Grischek, Max; Kegelmann, Lukas; Skroblin, Dieter; Gollwitzer, Christian; Malinauskas, Tadas; Jošt, Marko; Matič, Gašper; Rech, Bernd; Schlatmann, Rutger; Topič, Marko; Korte, Lars; Abate, Antonio; Stannowski, Bernd; Neher, Dieter; Stolterfoht, Martin; Unold, Thomas; Getautis, Vytautas; Albrecht, Steve. Monolithic perovskite/silicon tandem solar cell with >29 % efficiency by enhanced hole extraction // Science. Washington, DC : American Association for the Advancement of Science. ISSN 0036-8075. eISSN 1095-9203. 2020, vol. 370, iss. 6522, p. 1300-1309. DOI: [10.1126/science.abd4016](https://doi.org/10.1126/science.abd4016). [Science Citation Index Expanded (Web of Science); Scopus] [IF: 41,846; AIF: 5,327; IF/AIF: 7,855; Q1 (2019, InCites JCR SCIE)] [CiteScore: 45,30; SNIP: 7,521; SJR: 13,110; Q1 (2019, Scopus Sources)]
2. Al-Ashouri, Amran; Magomedov, Artiom; Roß, Marcel; Jošt, Marko; Talaikis, Martynas; Chistiakova, Ganna; Bertram, Tobias; Márquez, José A.; Köhnen, Eike; **Kasparavičius, Ernestas**; Levenco, Sergiu; Gil-Escrig, Lidón; Hages, Charles J.; Schlatmann, Rutger; Rech, Bernd; Malinauskas, Tadas; Unold, Thomas; Kaufmann, Christian A.; Korte, Lars; Niaura, Gediminas; Getautis, Vytautas; Albrecht, Steve. Conformal monolayer contacts with lossless interfaces for perovskite single junction and monolithic tandem solar cells // Energy & Environmental Science. Cambridge : Royal Society of Chemistry. ISSN 1754-5692. eISSN 1754-5706. 2019, Vol. 12, iss. 11, p. 3356-3369. DOI: 10.1039/c9ee02268f. [Science Citation Index Expanded (Web of Science); Scopus] [IF: 30,289; AIF: 5,393; IF/AIF: 5,616; Q1 (2019, InCites JCR SCIE)].
3. **Kasparavicius, Ernestas**; Magomedov, Artiom; Malinauskas, Tadas; Getautis, Vytautas. Long-term stability of the oxidized hole transporting materials used in perovskite solar cells // Chemistry - A European journal. Weinheim : Wiley-VCH. ISSN 0947-6539. 2018, vol. 24, iss. 39, p. 9910-9918. DOI: 10.1002/chem.201801441. [Science Citation Index Expanded (Web of Science); Scopus; PubMed] [IF: 5,160; AIF: 5,878; IF/AIF: 0,877; Q1 (2018, InCites JCR SCIE)].

### Patents

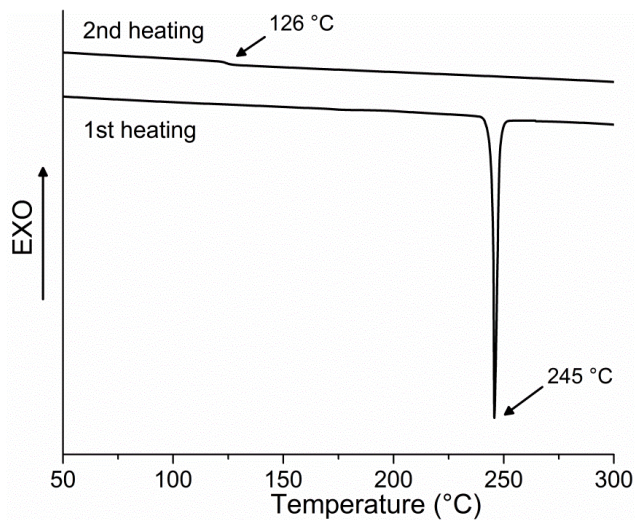
1. EP18000405.3; DE102018115379 (B3). Artiom Magomedov, Amran Al-Ashouri, Ernestas Kasparavicius, Steve Albrecht, Vytautas Getautis, Marko Jost, Tadas Malinauskas, Lukas Kegelmann, Eike Köhnen. Hole Transporting Self-Assembled Monolayer for Perovskite Solar Cells /

Applicants: Helmholtz-Berlin (HZB); Kaunas Univ of Tech (KTU). April 25, 2018.

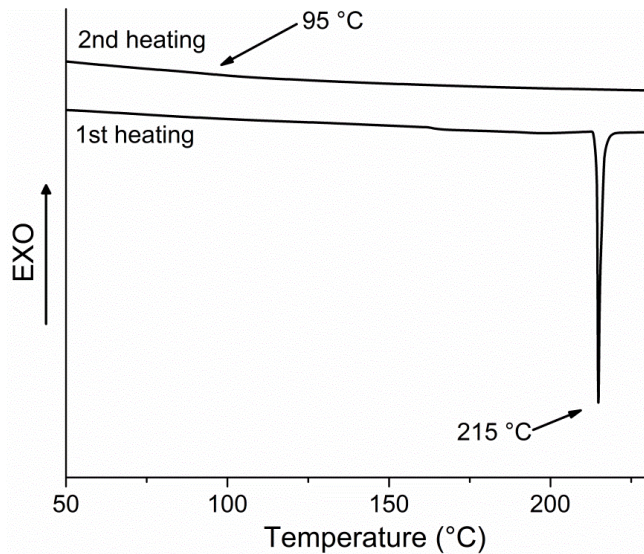
### **Presentation in conferences**

- 4–8.11.2019 “NanoGe Fall Meeting19” Berlin, Germany  
Poster presentation “*Stability of Oxidized Spiro-MeOTAD Under Influence of Perovskite and its Components*”
- 26–27.09.2019 “Lithuania-Poland Workshop on Physics and Technology”, Vilnius, Lithuania  
Oral presentation “*Oxidized SPIRO-MEOTAD Stability Investigation*”
- 7–17.07.2019 “13th International Conference on Optical Probes of Organic and Hybrid Optoelectronic Materials and Applications” Vilnius, Lithuania  
Poster presentation “*Stability Research of Oxidized Spiro-Meotad*”
- 19–22.03.2019 “Open Readings 2019: 62nd International Conference for Students of Physics and Natural Sciences” Vilnius, Lithuania  
Poster presentation “*Stability Investigation of Oxidized Spiro-MeOTAD*”
- 12.03.2019 “Interdisciplinary Research in Physical and Technological Sciences: 9th Conference of Young Scientists”, Vilnius, Lithuania  
Oral presentation “*Oksiduotų skylių transportuojančių medžiagų, naudojamų perovskitinėse saulės celėse, stabilumo tyrimas*”
- 27–30.08.2018 “Advanced Materials and Technologies: Book of Abstracts of 20th International Conference – School”, Palanga, Lithuania  
Poster presentation “*Stability Investigation of Oxidized Hole-Transporting Materials*”
- 10–14.06.2018 “XLIII ‘A. Corbella’ International Summer School on Organic Synthesis – ISOS 2018”, Gargnano, Italy  
Poster presentation “*Stability Investigation of Oxidized Charge-Transporting Materials*”
- 27.08.–02.09. 2017 “ECME 2017: 14th European Conference on Molecular Electronics”, Dresden, Germany  
Poster presentation “*Investigation of Stability of Hole-Transporting Materials Used in Perovskite Solar Cells*”

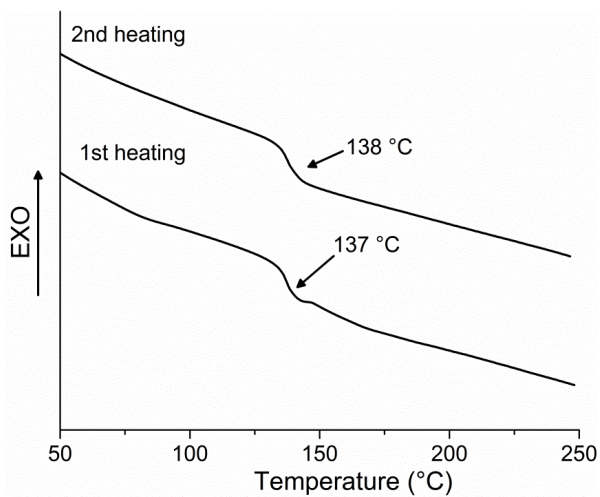
## 9. APPENDIX



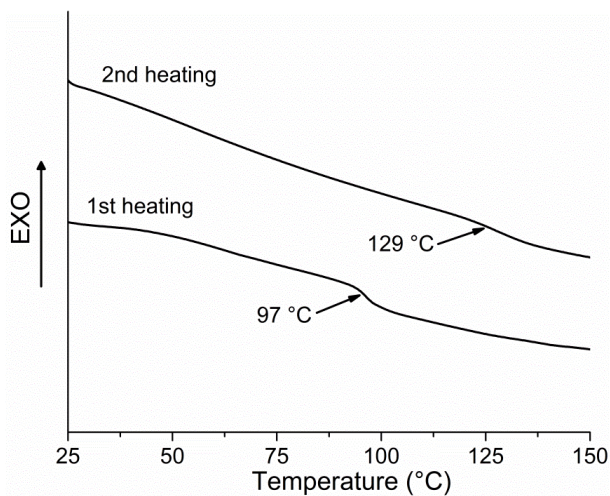
**Figure S1.** DSC first and second heating curves for spiro-OMeTAD (heating rate  $10\text{ }^{\circ}\text{C min}^{-1}$ )



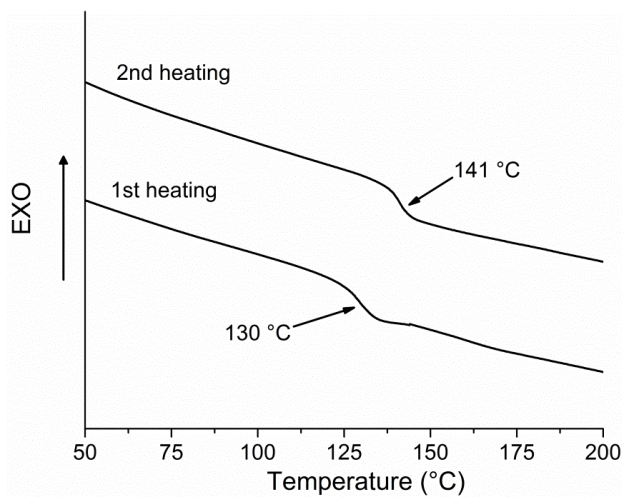
**Figure S2.** DSC first and second heating curves for spiro[TFPI]<sub>2</sub> (heating rate  $10\text{ }^{\circ}\text{C min}^{-1}$ )



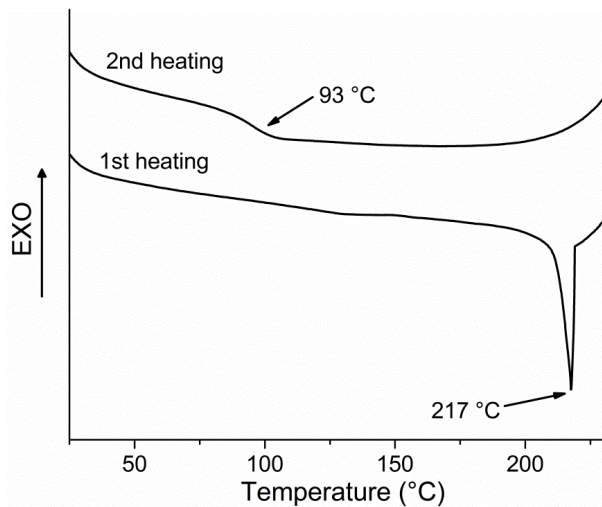
**Figure S3.** DSC first and second heating curves for V862 (heating rate 10 °C min<sup>-1</sup>)



**Figure S4.** DSC first and second heating curves for V862[TFPI] (heating rate 10 °C min<sup>-1</sup>)

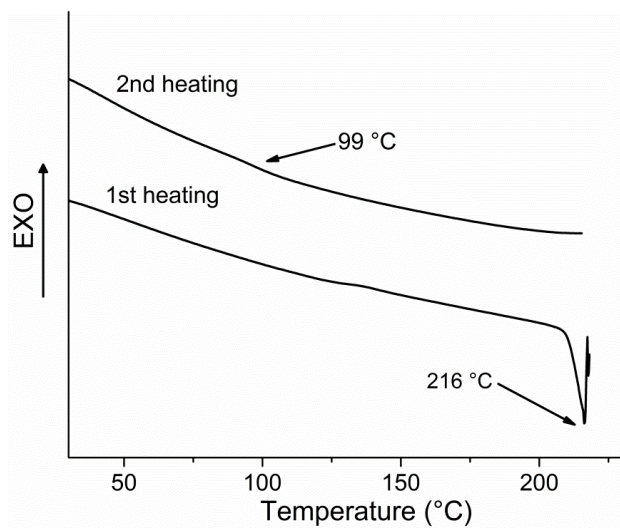


**Figure S5.** DSC first and second heating curves for V886 (heating rate  $10\text{ }^{\circ}\text{C min}^{-1}$ )

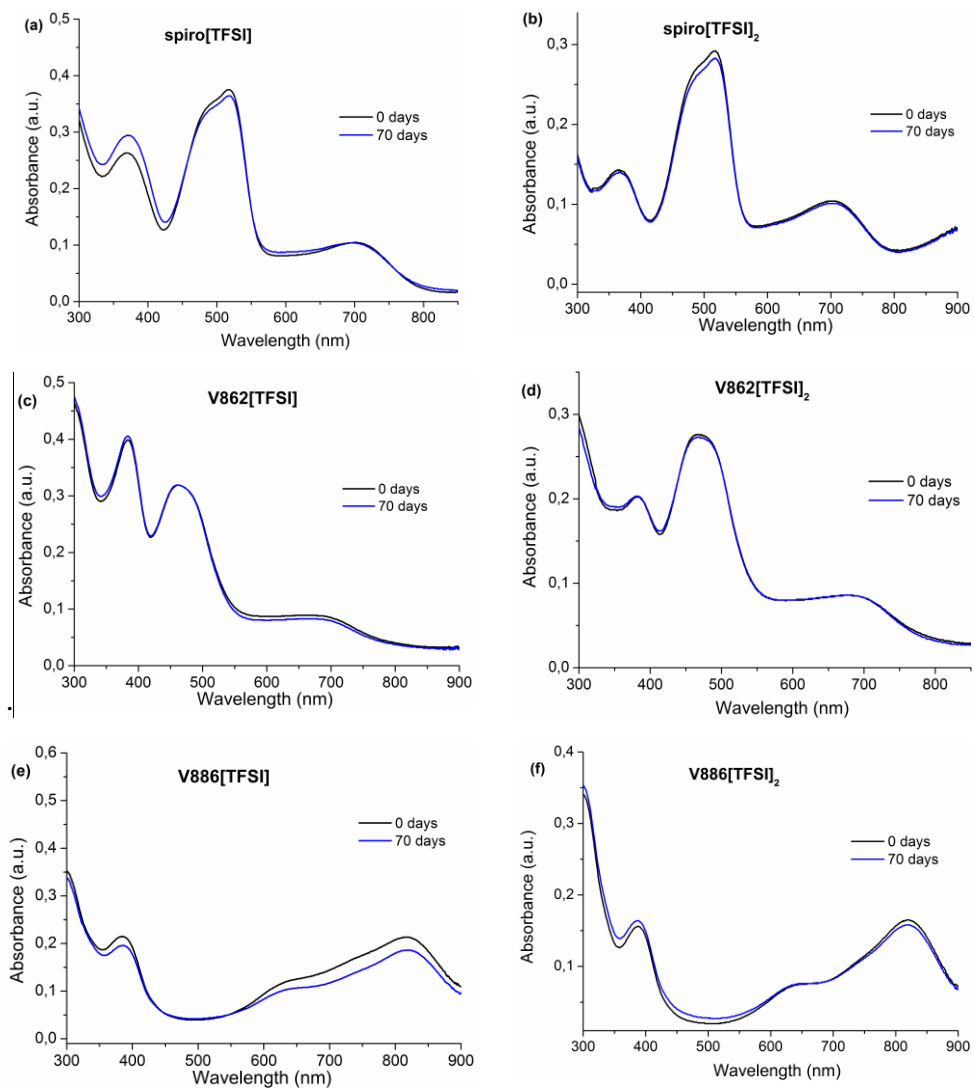


**Figure S6.** DSC first and second heating curves for V886[TFSI] (heating rate  $10^{\circ}\text{C min}^{-1}$ )

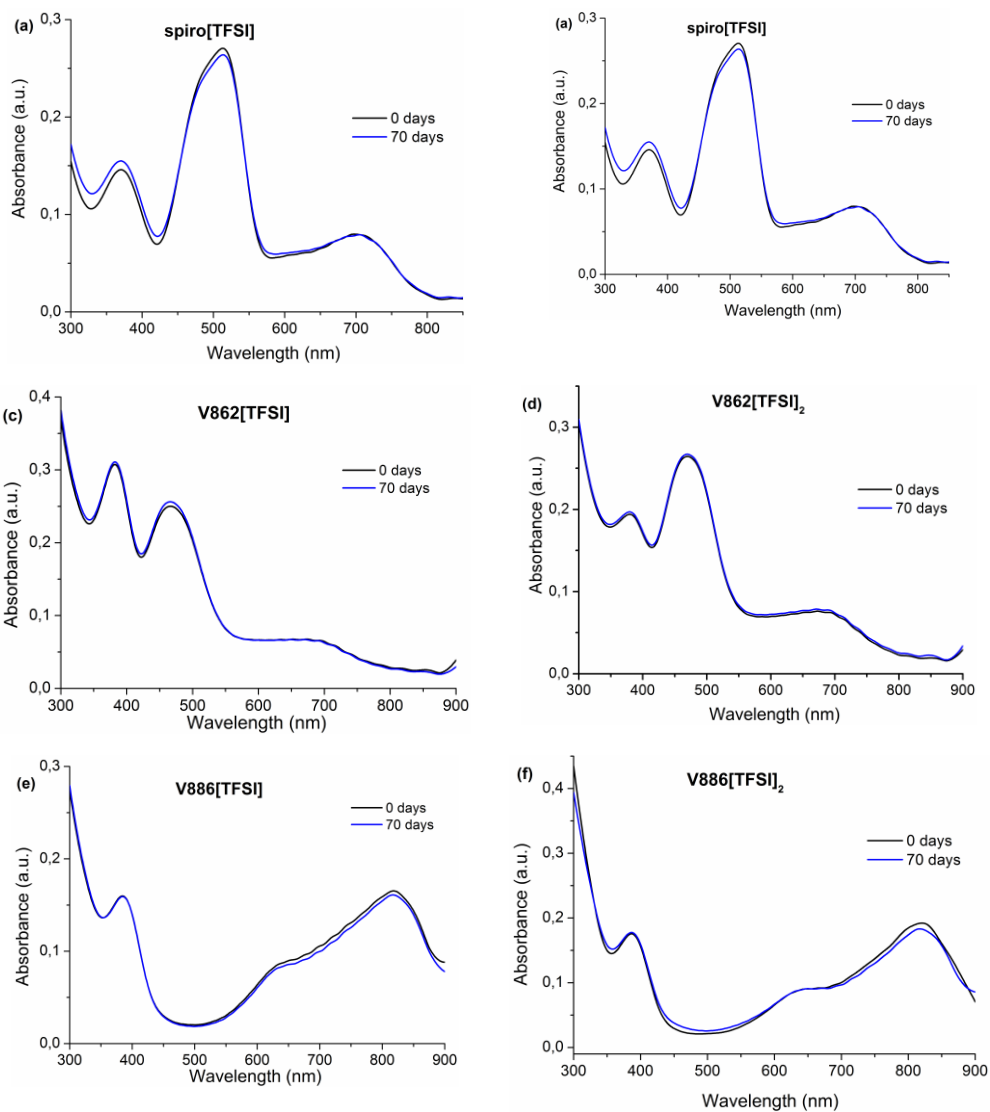




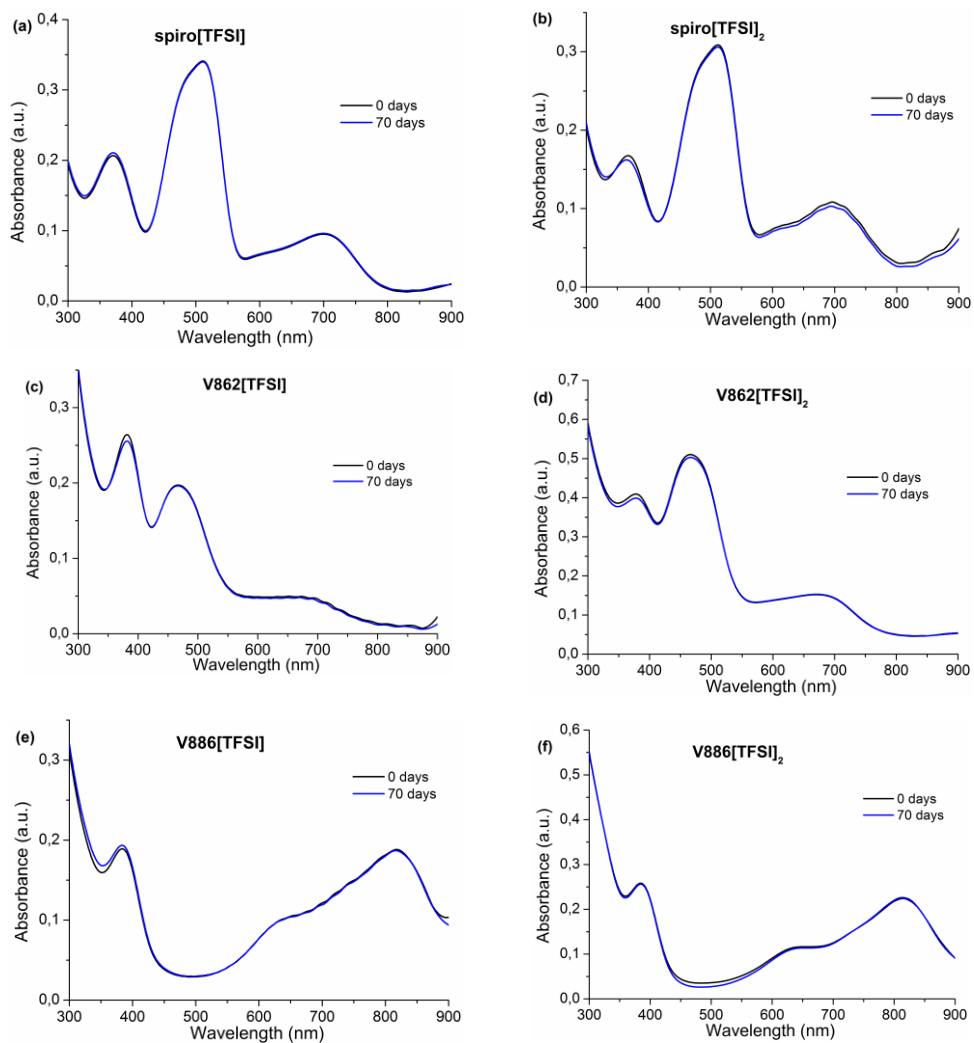
**Figure S7.** DSC first and second heating curves for V886[TFPI]<sub>2</sub> (heating rate 10 °C min<sup>-1</sup>)



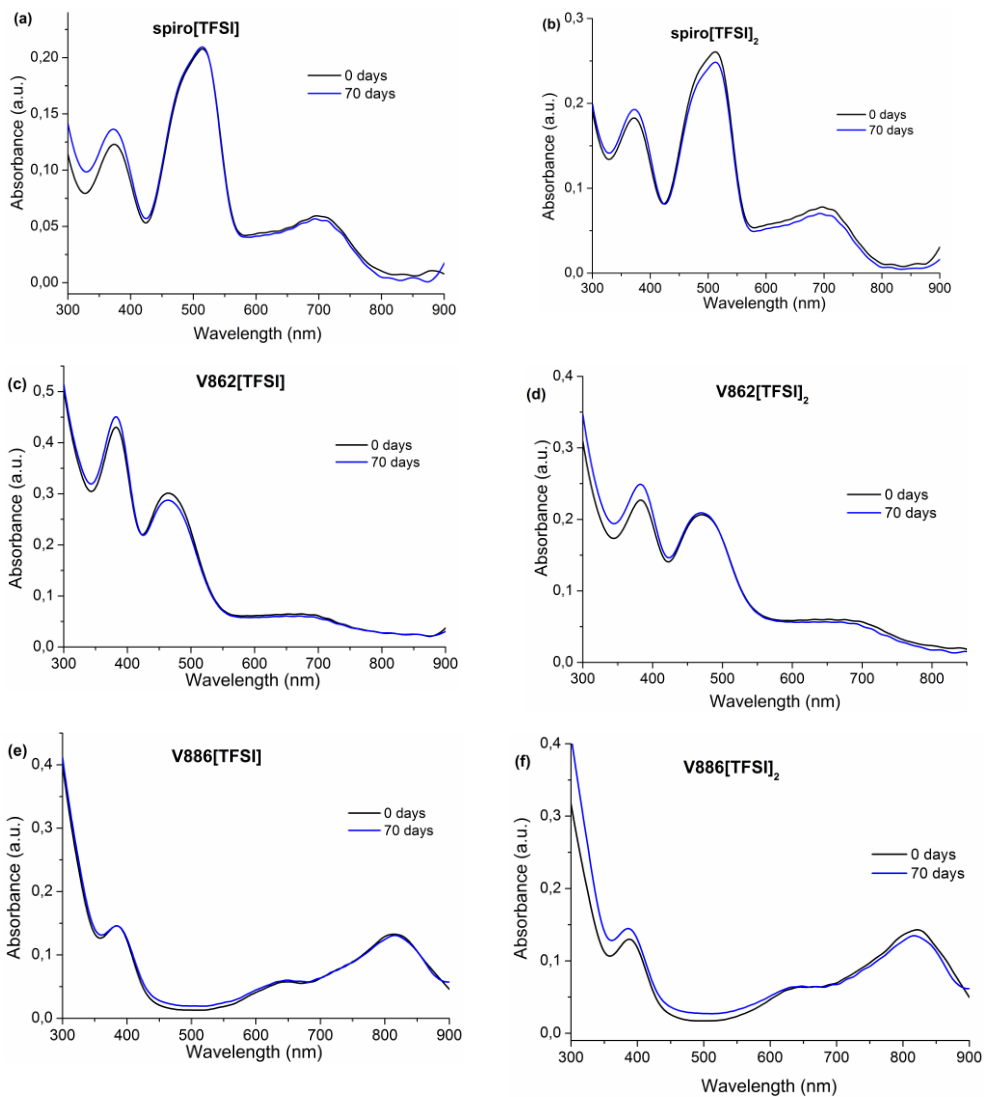
**Figure S8.** Stability of the nonencapsulated films containing spiro[TFSI] (a), spiro[TFSI]<sub>2</sub> (b), V862[TFSI] (c), V862[TFSI]<sub>2</sub> (d), V886[TFSI] (e), V886[TFSI]<sub>2</sub> (f) at RT



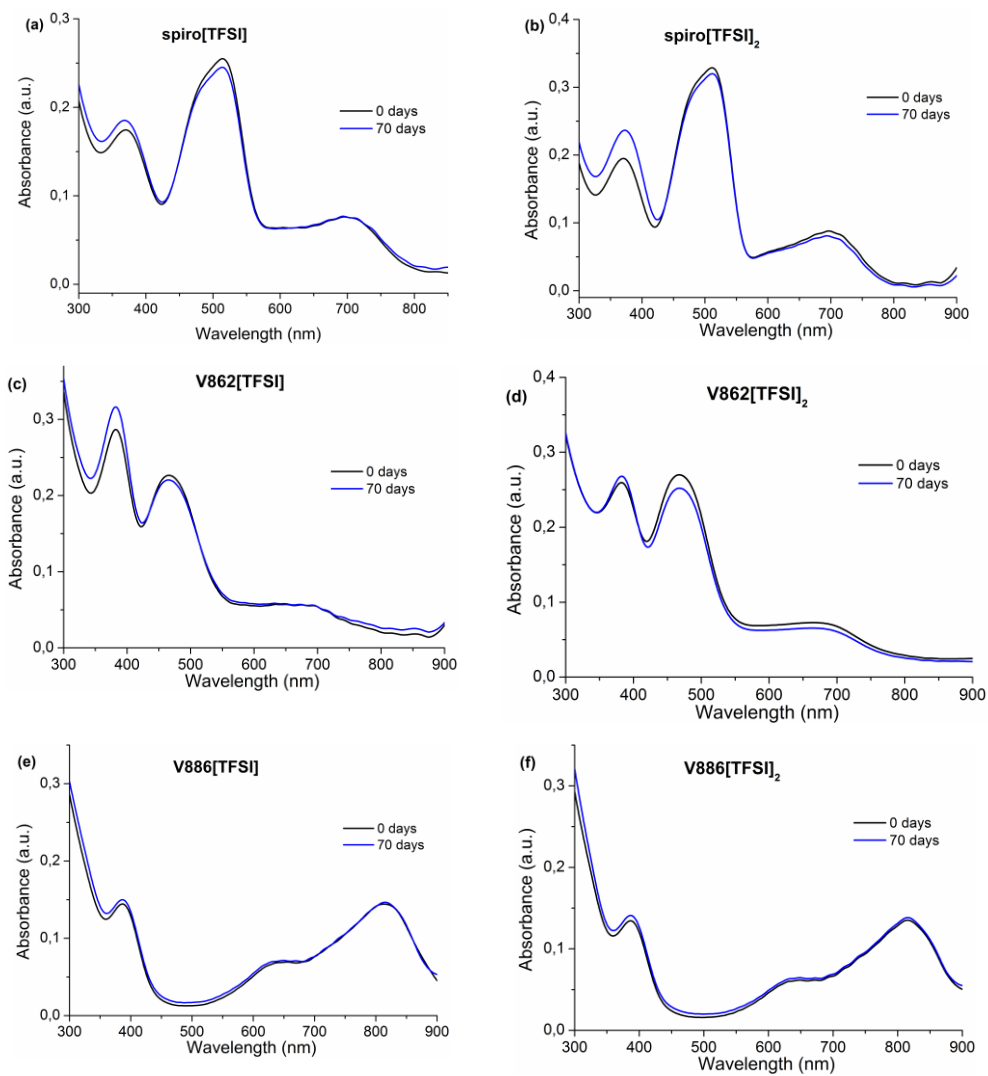
**Figure S9.** Stability of the encapsulated films containing spiro[TFSI] (a), spiro[TFSI]<sub>2</sub> (b), V862[TFSI] (c), V862[TFSI]<sub>2</sub> (d), V886[TFSI] (e), V886[TFSI]<sub>2</sub> (f) at RT



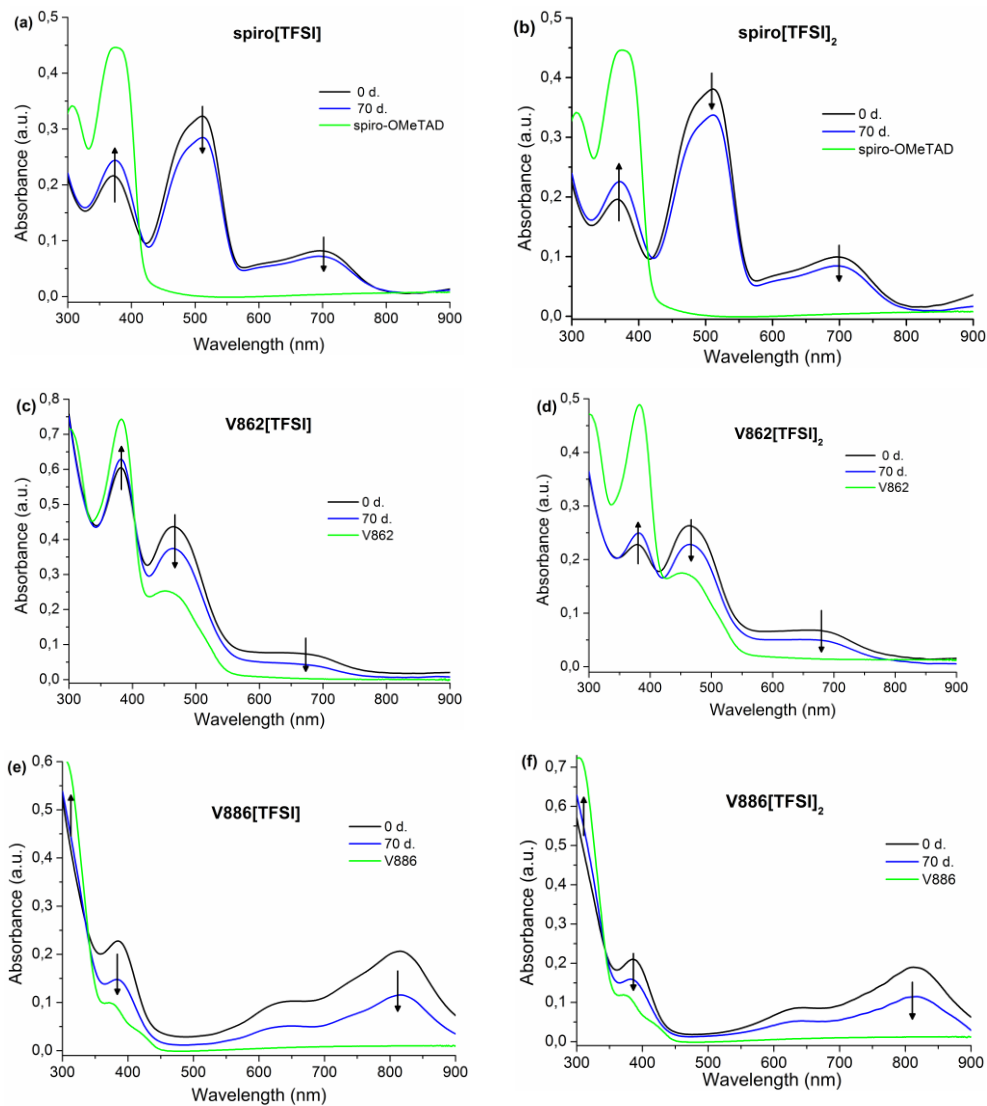
**Figure S10.** Stability of the encapsulated films containing LiTFSI and spiro[TFSI] (a), spiro[TFSI]<sub>2</sub> (b), V862[TFSI] (c), V862[TFSI]<sub>2</sub> (d), V886[TFSI] (e), V886[TFSI]<sub>2</sub> (f) at RT



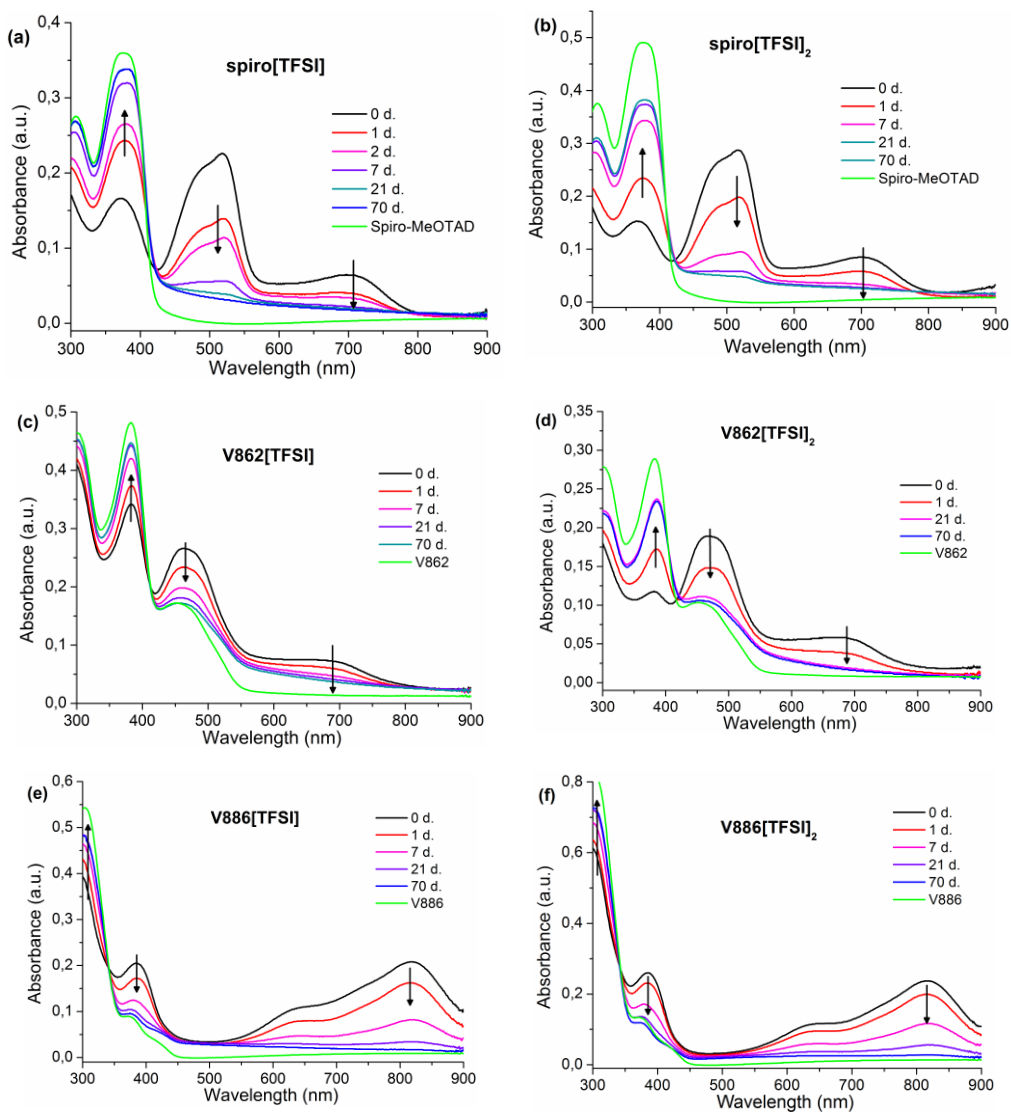
**Figure S11.** Stability of the encapsulated films containing tBP and spiros[TFSI] (a), spiros[TFSI]<sub>2</sub> (b), V862[TFSI] (c), V862[TFSI]<sub>2</sub> (d), V886[TFSI] (e), V886[TFSI]<sub>2</sub> (f) at RT



**Figure S12.** Stability of the encapsulated films containing LiTFSI, tBP and spiro[TFSI] (a), spiro[TFSI]<sub>2</sub> (b), V862[TFSI] (c), V862[TFSI]<sub>2</sub> (d), V886[TFSI] (e), V886[TFSI]<sub>2</sub> (f) at RT

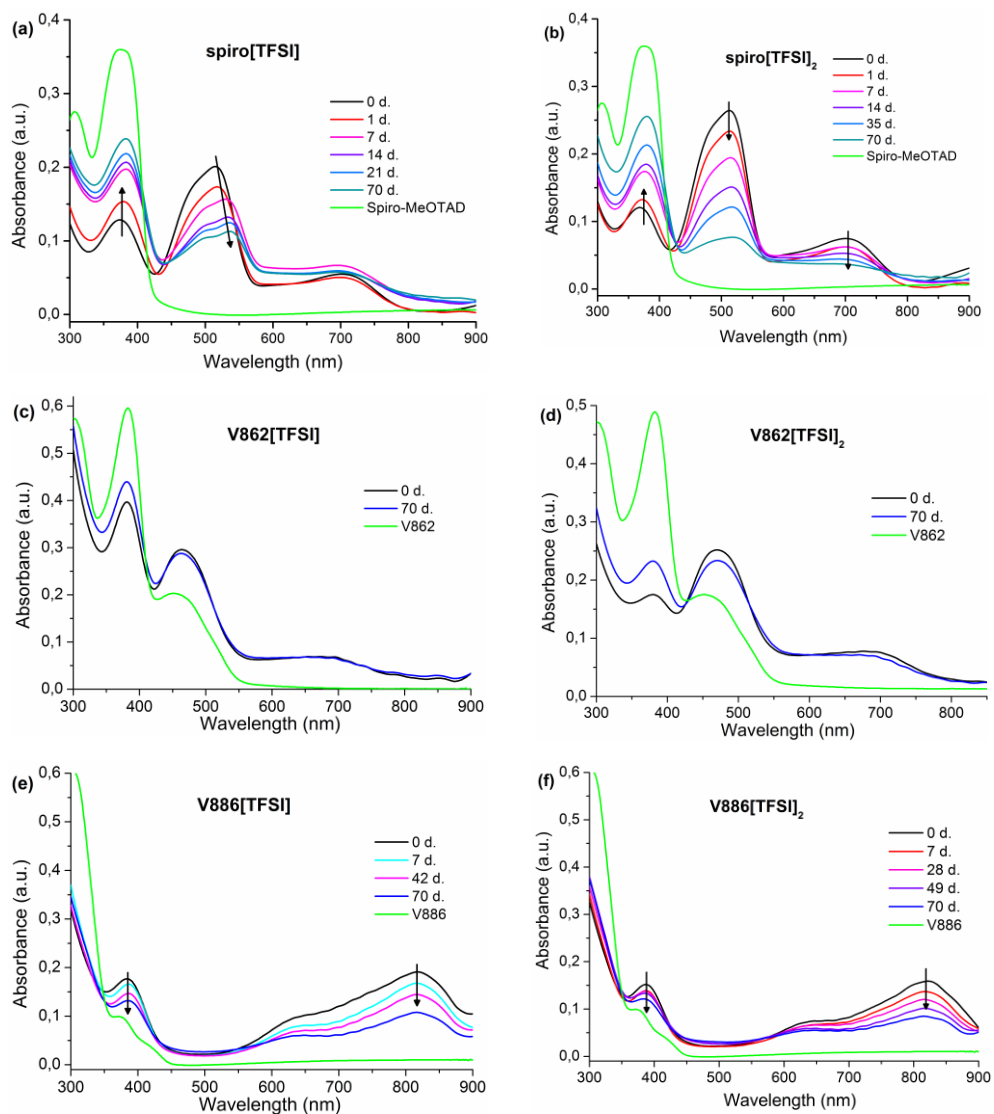


**Figure S13.** Stability of the encapsulated films containing LiTFSI, tBP, FK209 and spiro[TFSI] (a), spiro[TFSI]<sub>2</sub> (b), V862[TFSI] (c), V862[TFSI]<sub>2</sub> (d), V886[TFSI] (e), V886[TFSI]<sub>2</sub> (f) at RT

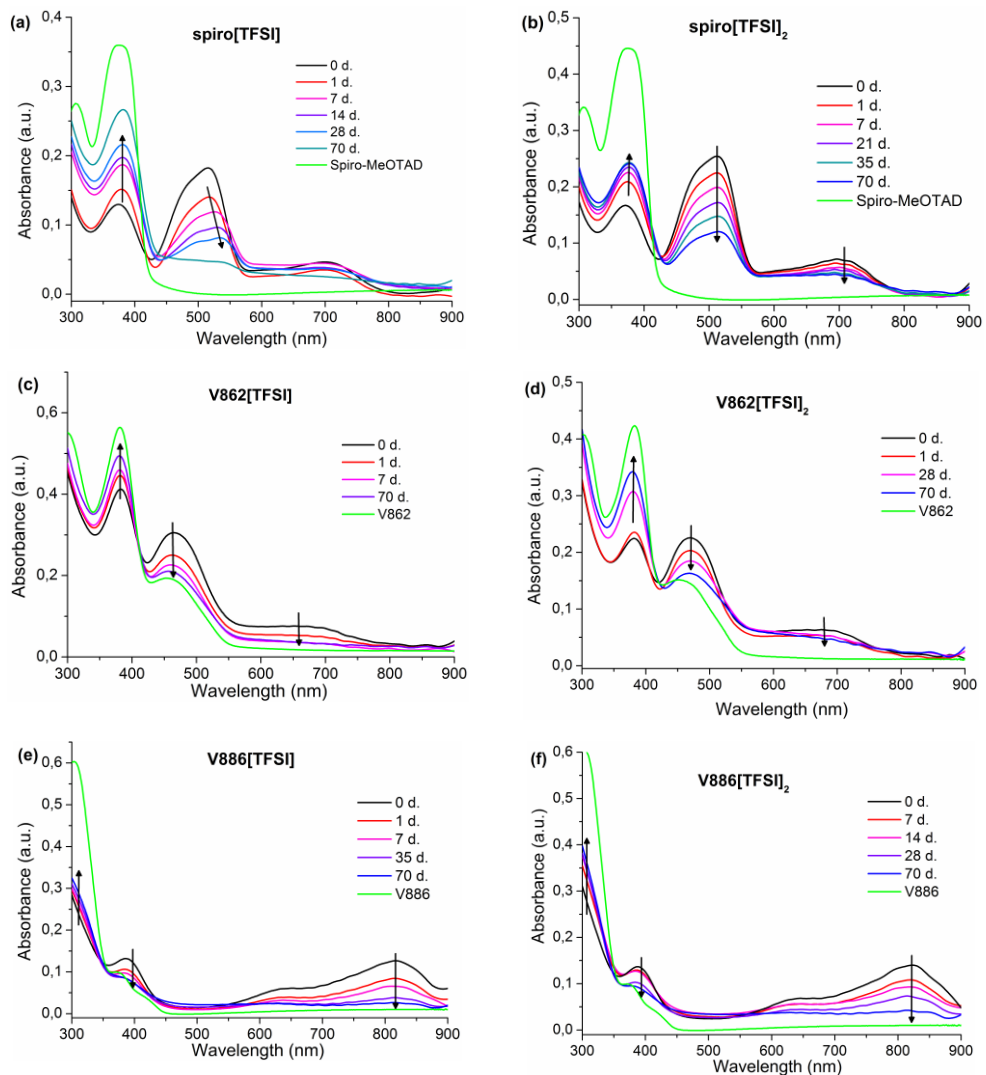


**Figure S14.** Stability of the nonencapsulated films containing spiro[TFSI] (a), spiro[TFSI]<sub>2</sub> (b), V862[TFSI] (c), V862[TFSI]<sub>2</sub> (d), V886[TFSI] (e), V886[TFSI]<sub>2</sub> (f) at 100 °C

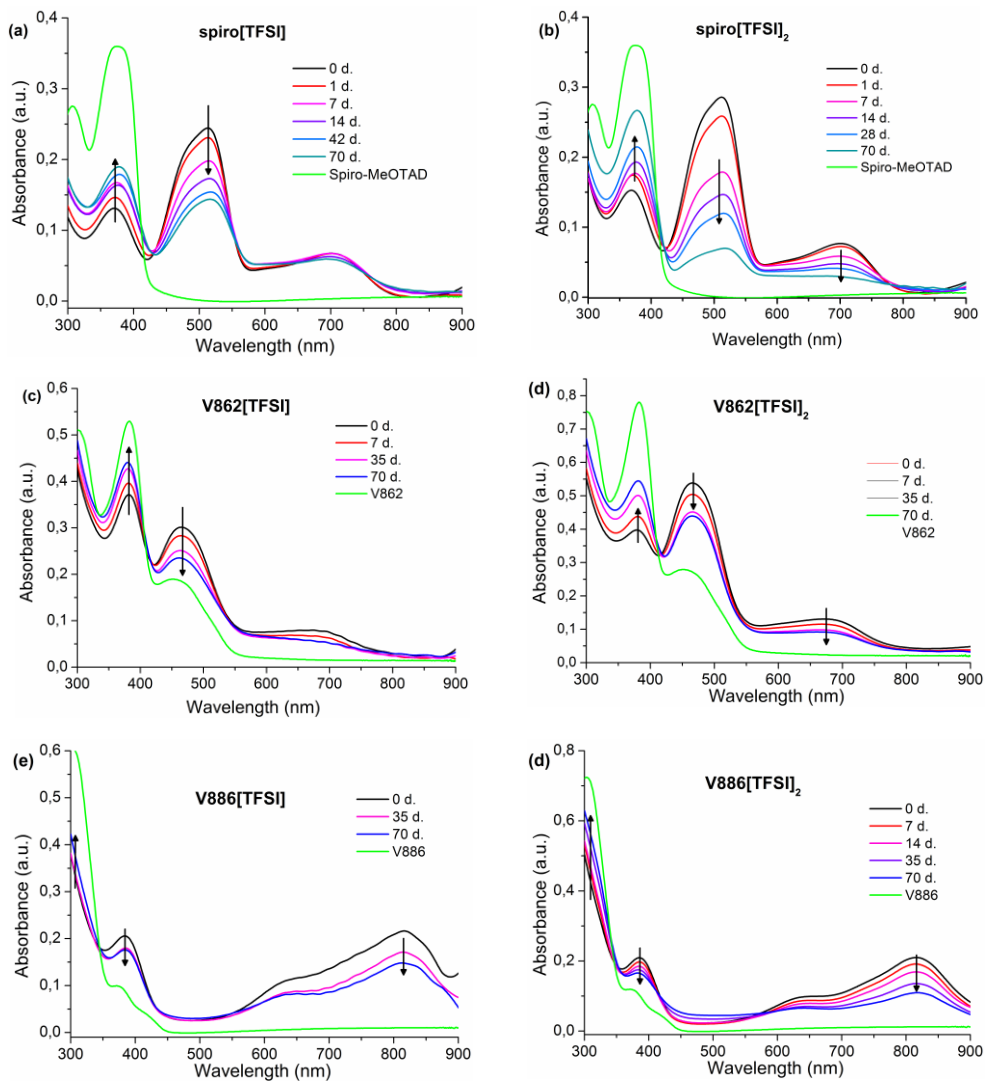




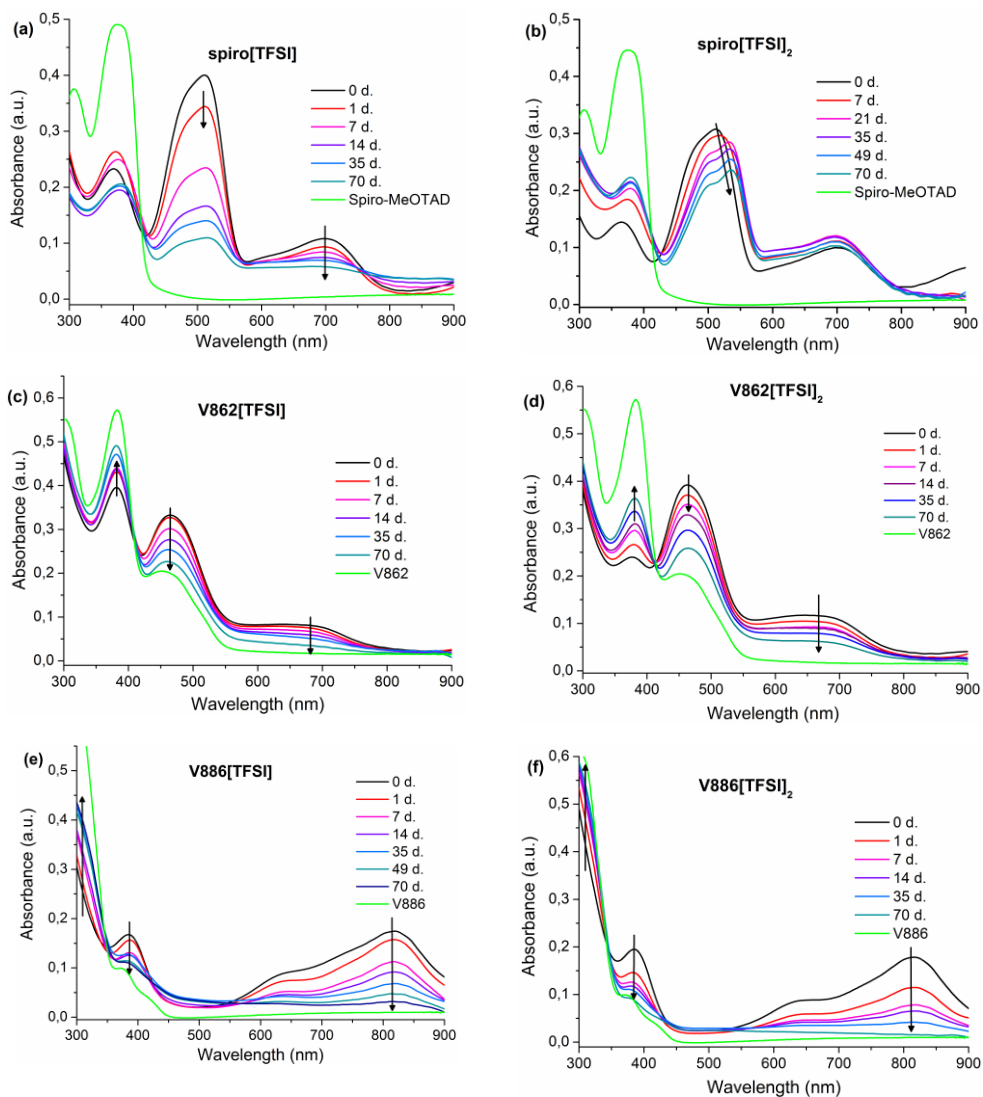
**Figure S15.** Stability of the encapsulated films containing spiro[TFSI] (a), spiro[TFSI]<sub>2</sub> (b), V862[TFSI] (c), V862[TFSI]<sub>2</sub> (d), V886[TFSI] (e), V886[TFSI]<sub>2</sub> (f) at 100 °C



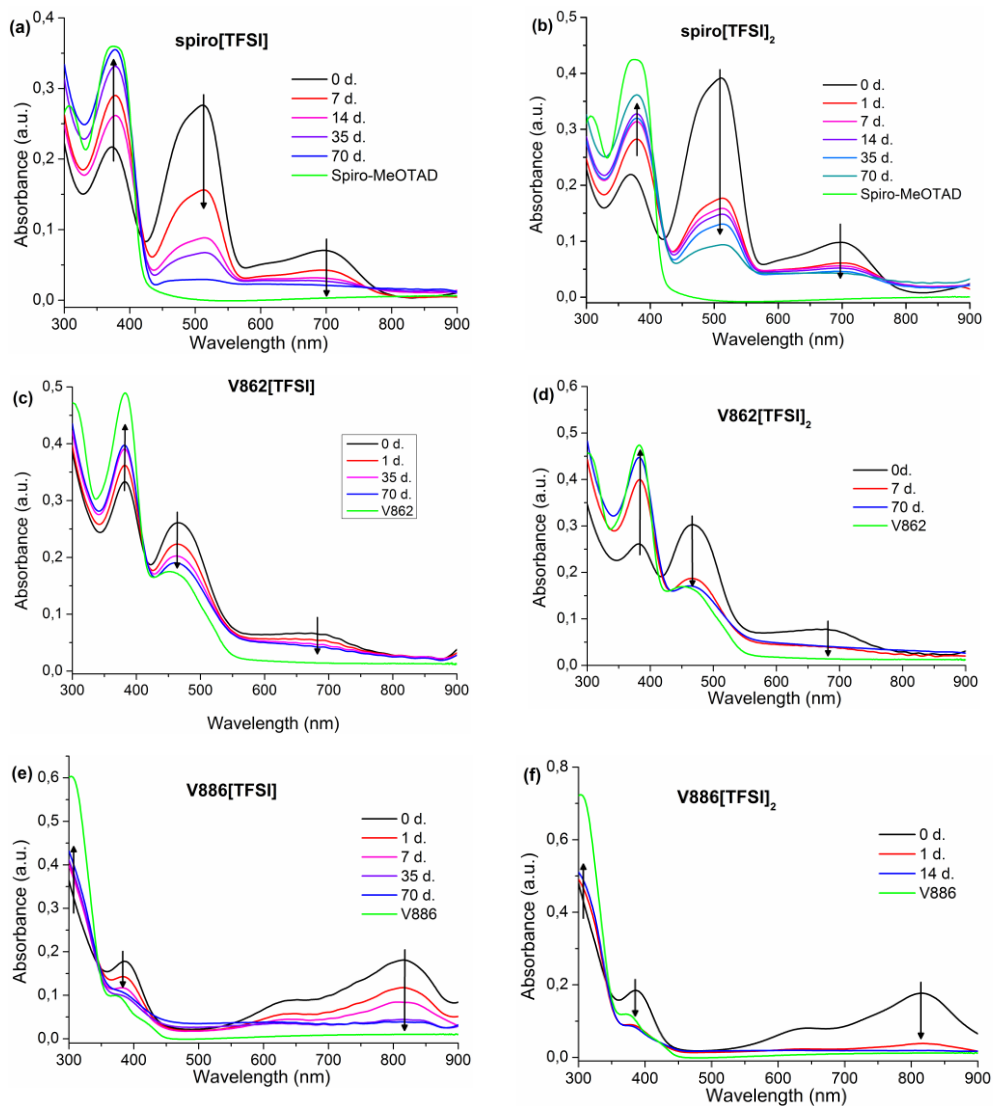
**Figure S16.** Stability of the encapsulated films containing tBP, spiro[TFSI] (a), spiro[TFSI]<sub>2</sub> (b), V862[TFSI] (c), V862[TFSI]<sub>2</sub> (d), V886[TFSI] (e), V886[TFSI]<sub>2</sub> (f) at 100 °C



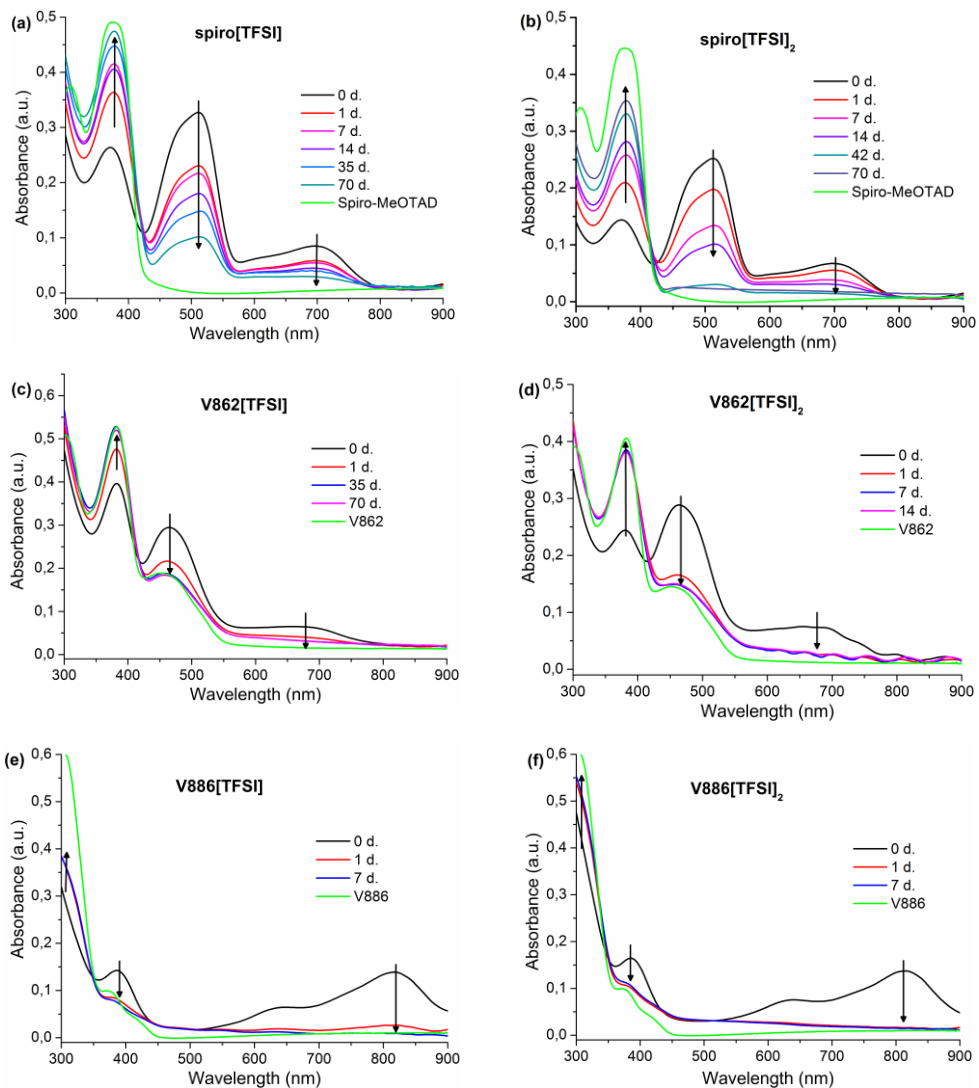
**Figure S17.** Stability of the encapsulated films containing LiTFSI, spiro[TFSI] (a), spiro[TFSI]<sub>2</sub> (b), V862[TFSI] (c), V862[TFSI]<sub>2</sub> (d), V886[TFSI] (e), V886[TFSI]<sub>2</sub> (f) at 100 °C



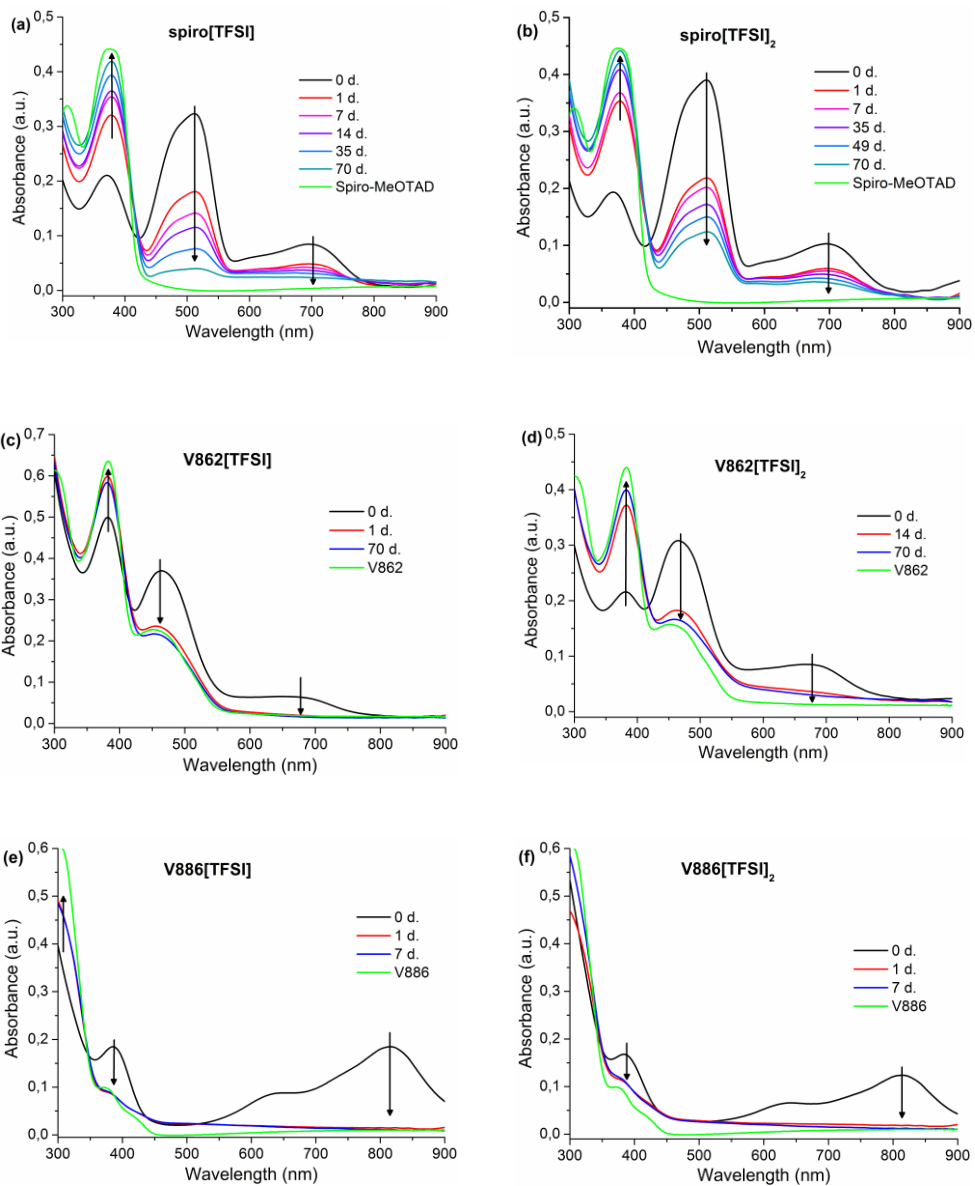
**Figure S18.** Stability of the encapsulated films containing FK209, spiro[TFSI] (a), spiro[TFSI]<sub>2</sub> (b), V862[TFSI] (c), V862[TFSI]<sub>2</sub> (d), V886[TFSI] (e), V886[TFSI]<sub>2</sub> (f) at 100 °C



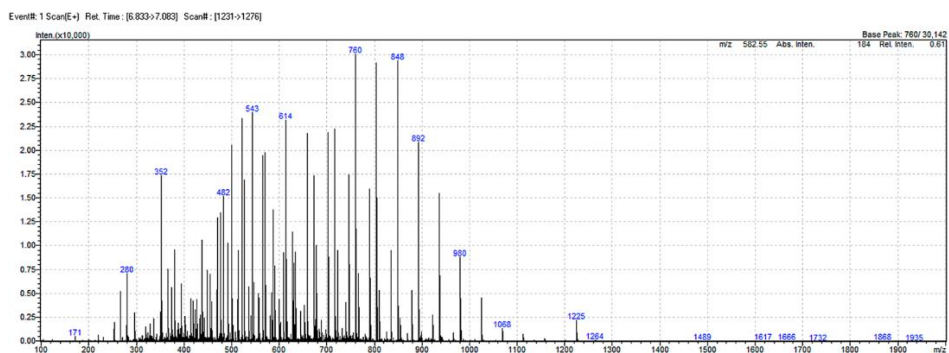
**Figure S19.** Stability of the encapsulated films containing LiTFSI, tBP, spiro[TFSI] (a), spiro[TFSI]<sub>2</sub> (b), V862[TFSI] (c), V862[TFSI]<sub>2</sub> (d), V886[TFSI] (e), V886[TFSI]<sub>2</sub> (f) at 100 °C



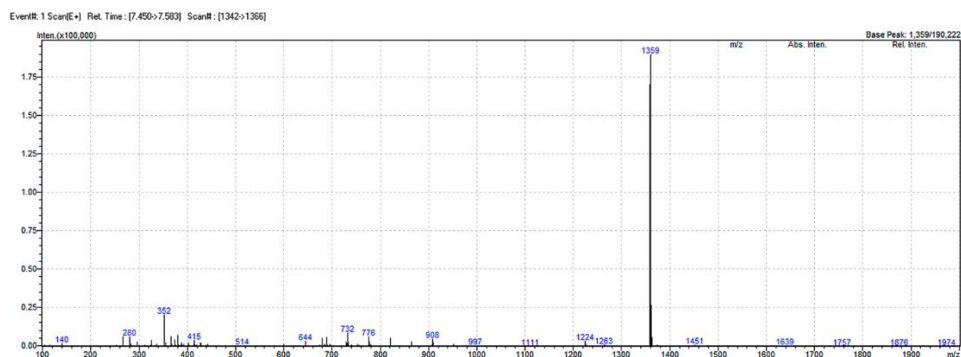
**Figure S20.** Stability of the encapsulated films containing tBP, FK209, spiro[TFSI] (a), spiro[TFSI]<sub>2</sub> (b), V862[TFSI] (c), V862[TFSI]<sub>2</sub> (d), V886[TFSI] (e), V886[TFSI]<sub>2</sub> (f) at 100 °C



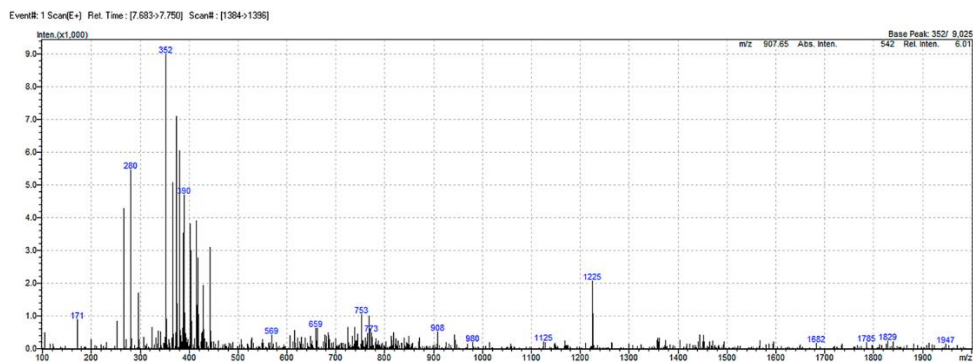
**Figure S21.** Stability of the encapsulated films containing LiTFSI, tBP, FK209, spiro[TFSI] (a), spiro[TFSI]<sub>2</sub> (b), V862[TFSI] (c), V862[TFSI]<sub>2</sub> (d), V886[TFSI] (e), V886[TFSI]<sub>2</sub> (f) at 100 °C



**Figure S22.** Mass spectra of the first fraction (retention time 6.9 min) detected in the sample prepared from encapsulated film containing LiTFSI, tBP, FK209 and spiro[TFSI]<sub>2</sub> kept at 100 °C for 70 days

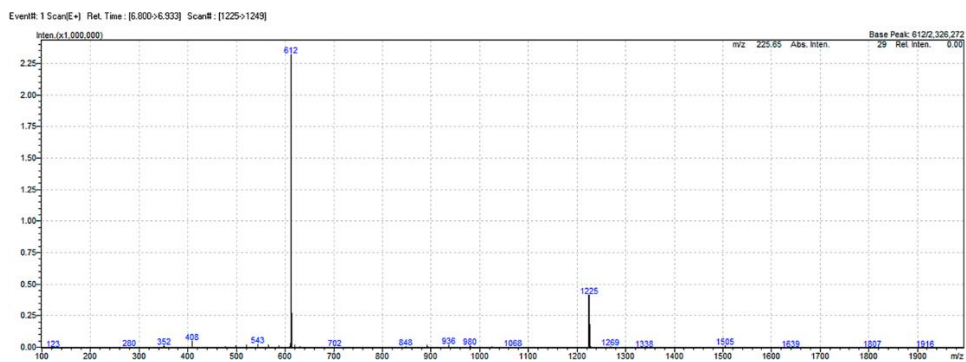


**Figure S23.** Mass spectra of the second fraction (retention time 7.5 min) detected in the sample prepared from encapsulated film containing LiTFSI, tBP, FK209 and spiro[TFSI]<sub>2</sub> kept at 100 °C for 70 days

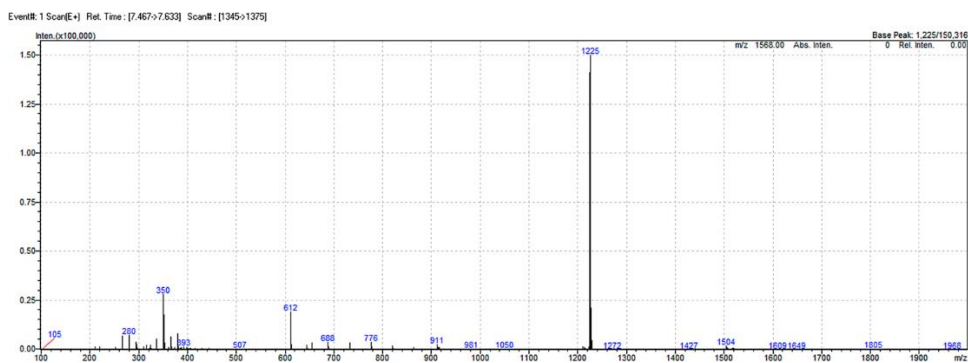


**Figure S24.** Mass spectra of the third fraction (retention time 7.6 min) detected in the sample prepared from encapsulated film containing LiTFSI, tBP, FK209 and spiro[TFSI]<sub>2</sub> kept at 100 °C for 70 days

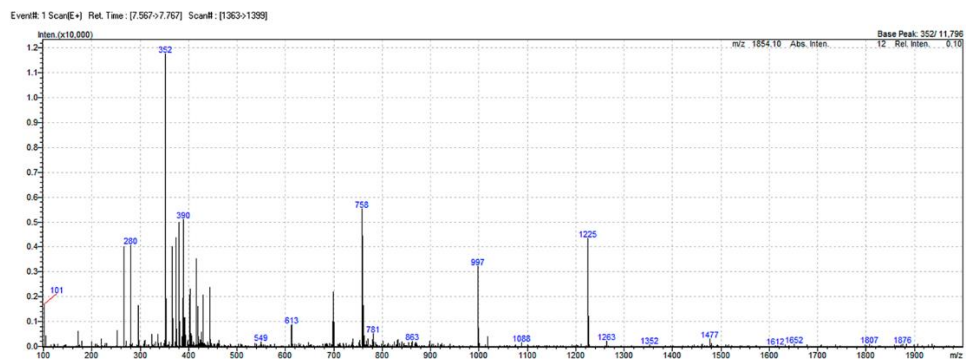




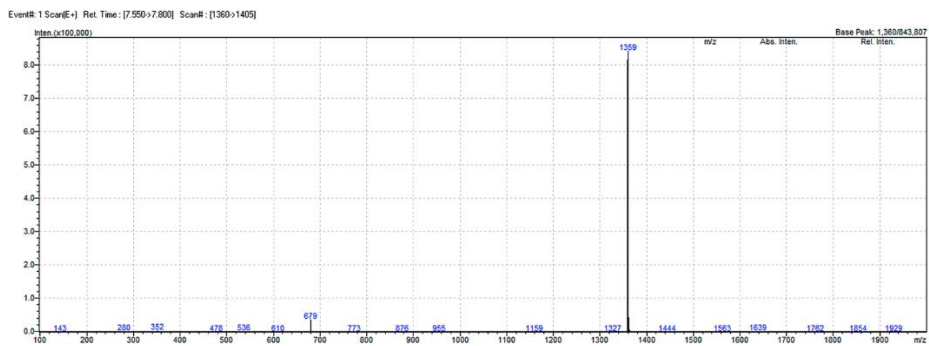
**Figure S25.** Mass spectra of the first fraction (retention time 6.9 min) detected in the sample prepared from the pure spiro[TFSI]<sub>2</sub>



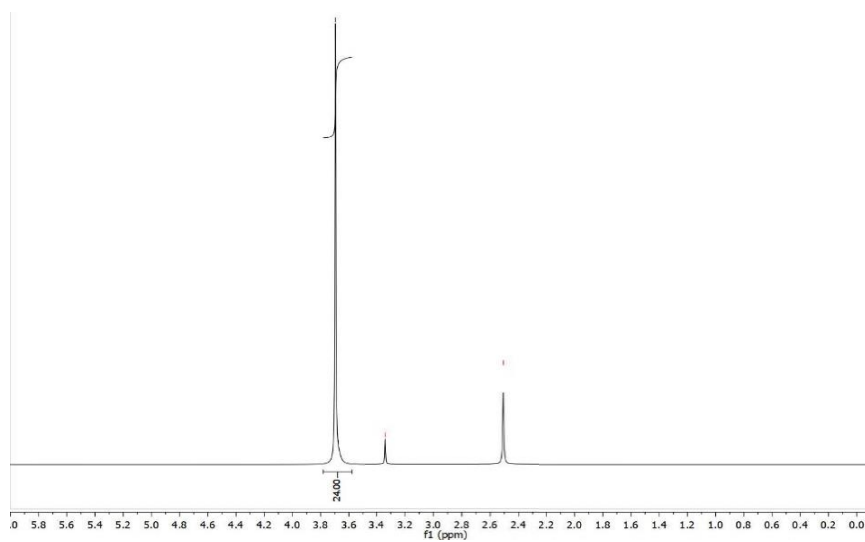
**Figure S26.** Mass spectra of the first fraction (retention time 7.6 min) detected in the sample prepared from the pure spiro[TFSI]<sub>2</sub>

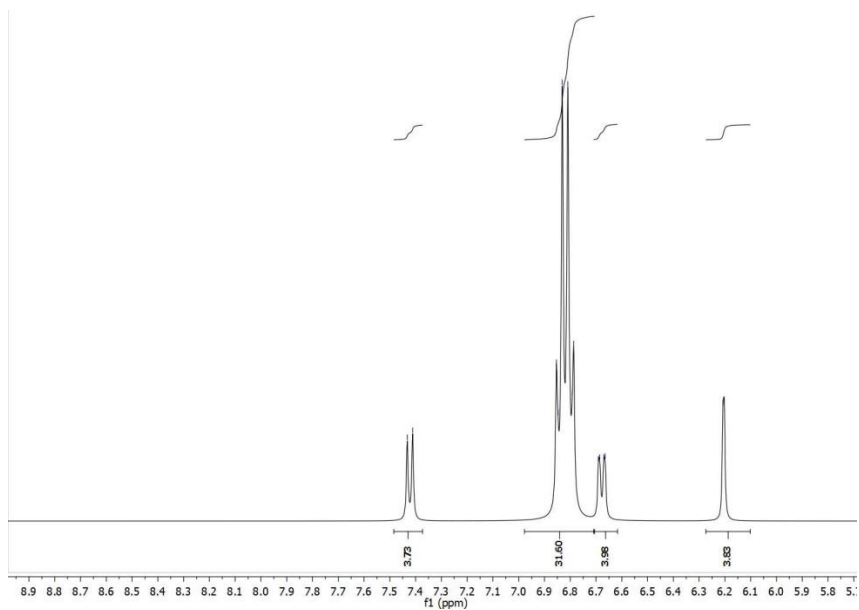


**Figure S27.** Mass spectra of the pure spiro-OMeTAD (retention time 7.6 min)

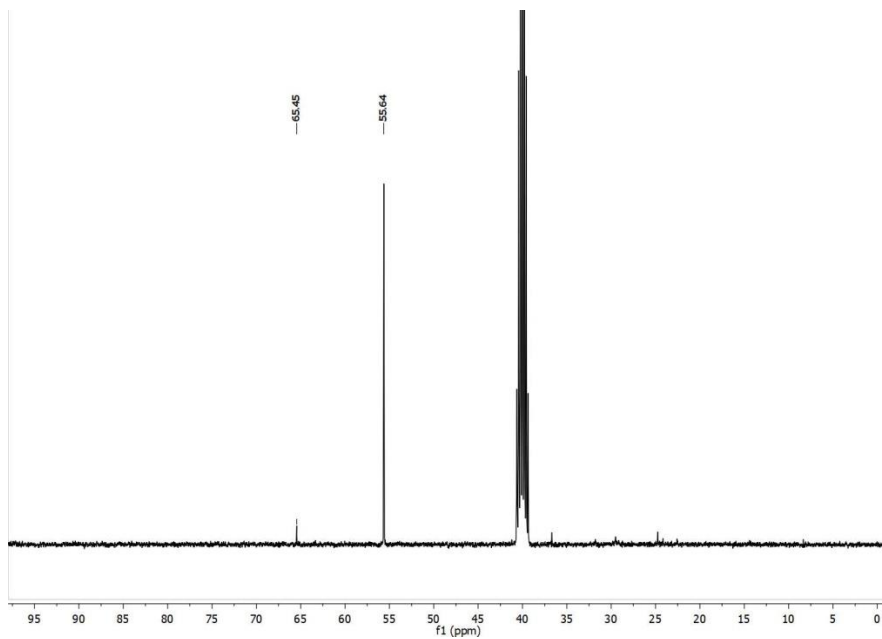


**Figure S28.** Mass spectra of the pure pyridinated spiro-OMeTAD (retention time 7.5 min)





**Figure S29.** <sup>1</sup>H NMR spectra of the obtained spiro-OMeTAD (400 MHz, DMSO-*d*<sub>6</sub>, δ, ppm)



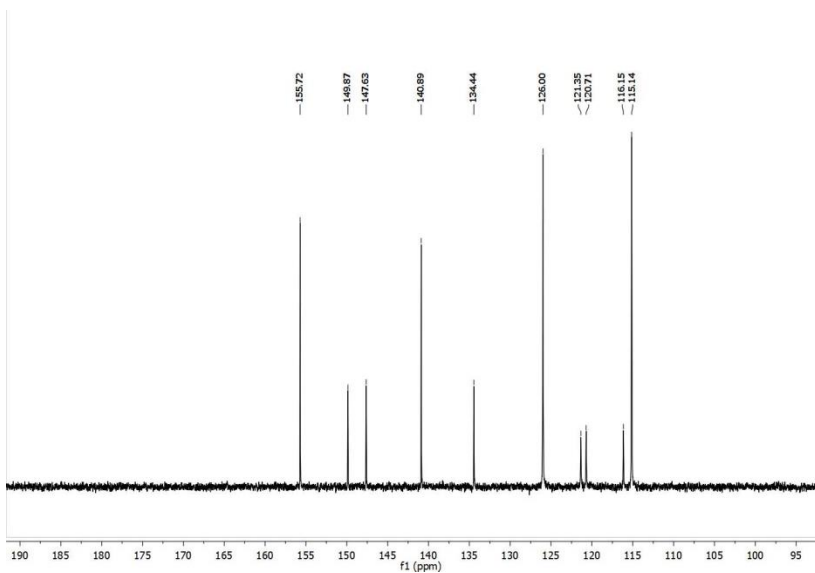


**Figure S30.**  $^{13}\text{C}$  NMR spectra of the obtained spiro-OMeTAD (100 MHz,  $\text{DMSO-}d_6$ ,  $\delta$ , ppm)

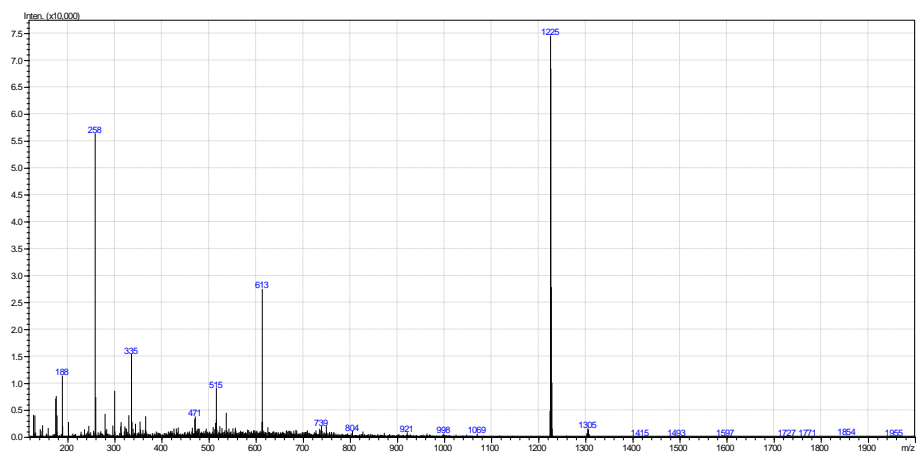


**Figure S31.** Mass spectra of the obtained spiro-OMeTAD after reaction (retention time 7.5 to 7.8 min)

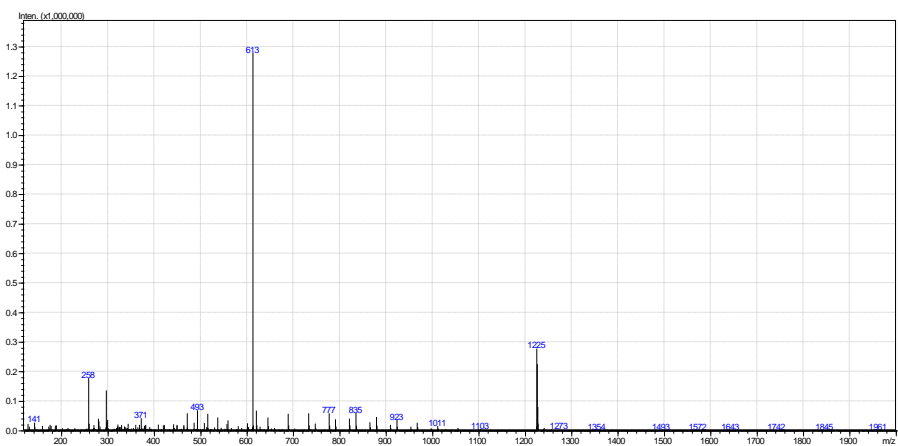


**Figure S32.** Mass spectra of the first fraction (retention time 6.6 to 6.95 min) detected in the sample prepared from mixture of MABr and spiro[TFSI]<sub>2</sub> in acetonitrile, kept at RT for 24 days in the dark

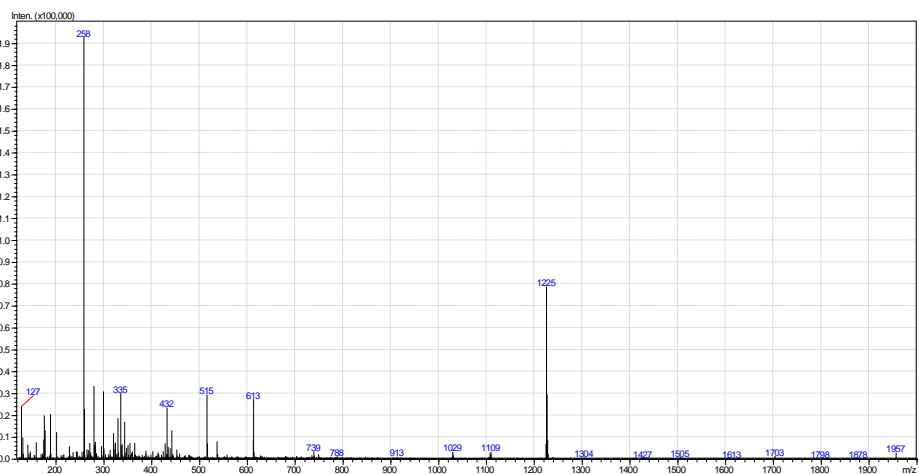


**Figure S33.** Mass spectra of the second fraction (retention time 7.5 to 7.8 min) detected in the sample prepared from mixture of MABr and spiro[TFSI]<sub>2</sub> in acetonitrile, kept at RT for 24 days in the dark

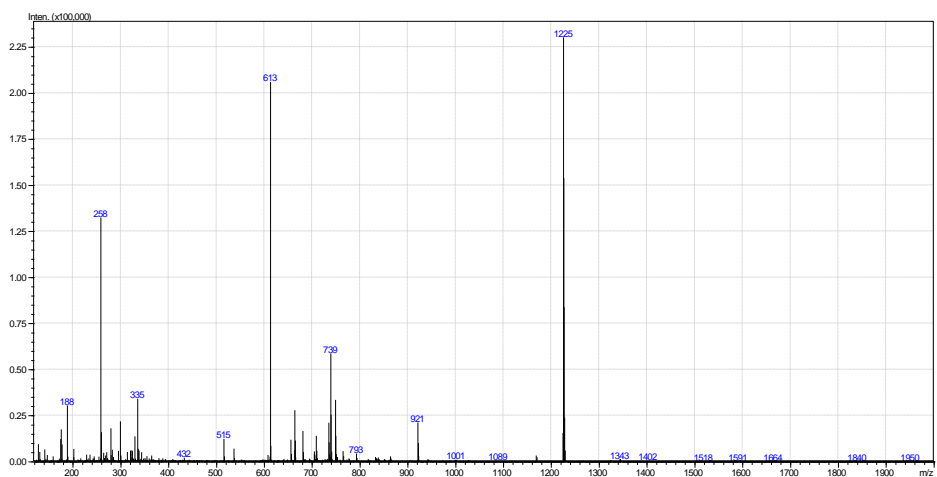


**Figure S34.** Mass spectra of the first fraction (retention time 7.5 to 7.8 min) detected in the sample prepared from mixture of FAI and spiro[TFSI]<sub>2</sub> in acetonitrile, kept at RT for 6 hours in the dark

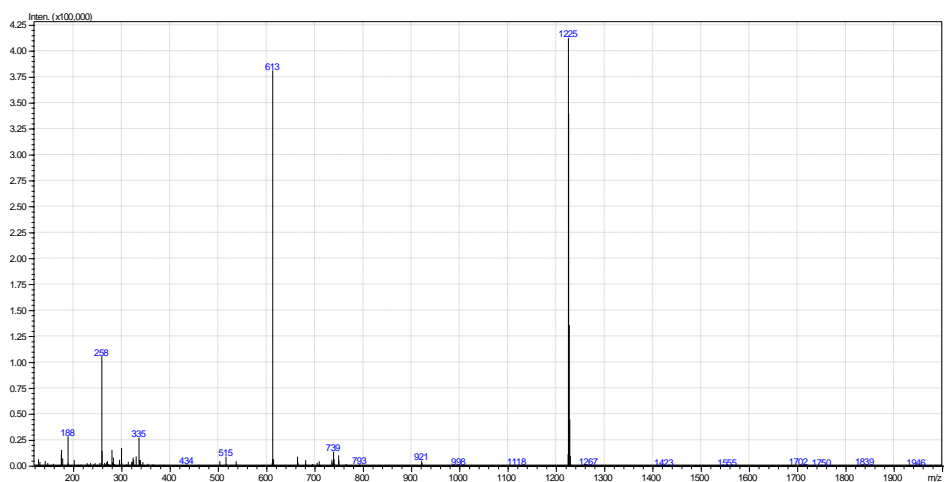


**Figure S35.** Mass spectra of the first fraction (retention time 7.5 to 7.8 min) detected in the sample prepared from mixture of MAI and spiro[TFSI]<sub>2</sub> in acetonitrile, kept at RT for 6 hours in the dark

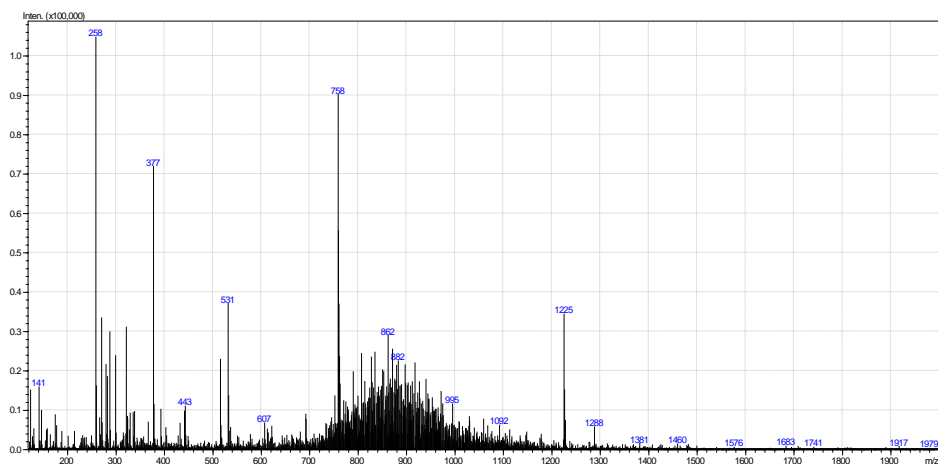


**Figure S36.** Mass spectra of the fraction (retention time 7.5 to 7.8 min) detected in the sample prepared from encapsulated film containing  $\text{Cs}_5(\text{MA}_{0.17}\text{FA}_{0.83})_{95}\text{Pb}(\text{I}_{0.83}\text{Br}_{0.17})_3$  and spiro[TFSI]<sub>2</sub> kept at 100 °C for 56 days

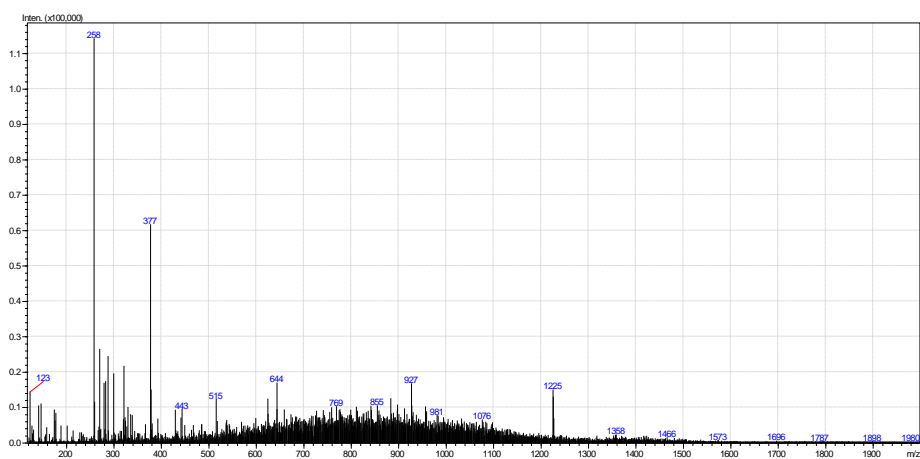


**Figure S37.** Mass spectra of the fraction (retention time 7.5 to 7.8 min) detected in the sample prepared from encapsulated film containing  $\text{MA}_{0.17}\text{FA}_{0.83}\text{Pb}(\text{I}_{0.83}\text{Br}_{0.17})_3$  and spiro[TFSI]<sub>2</sub> kept at 100 °C for 56 days

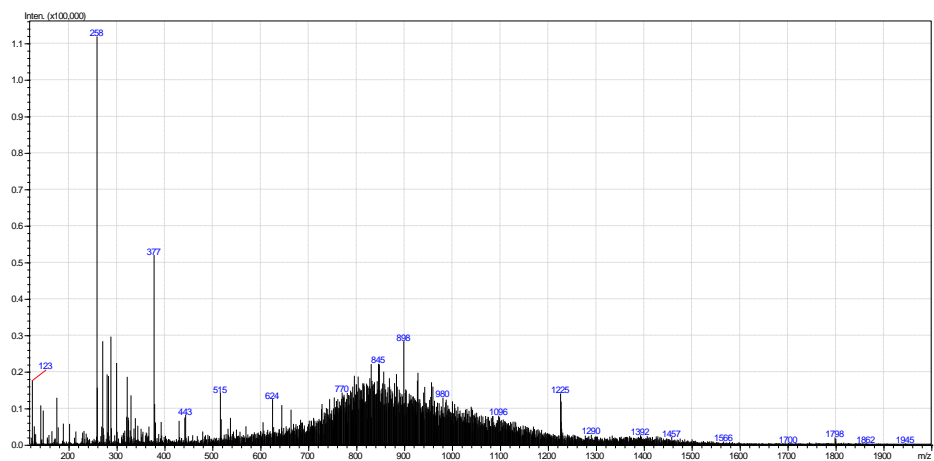


**Figure S38.** Mass spectra of the fraction (retention time 7.5 to 7.8 min) detected in the sample prepared from encapsulated film containing MAPbI<sub>3</sub> and spiro[TFSI]<sub>2</sub> kept at 100 °C for 56 days

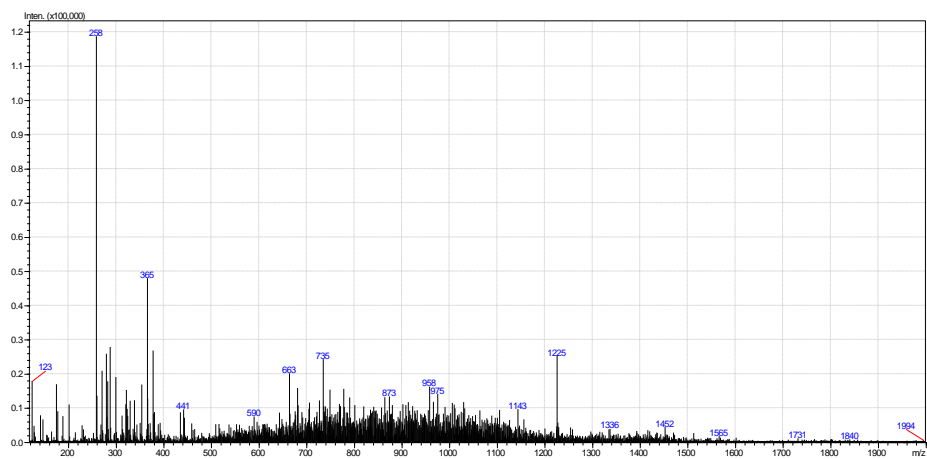


**Figure S39.** Mass spectra of the fraction (retention time 7.5 to 7.8 min) detected in the sample prepared from encapsulated film containing FA<sub>0.83</sub>Cs<sub>0.17</sub>Pb(I<sub>0.83</sub>Br<sub>0.17</sub>)<sub>3</sub> and spiro[TFSI]<sub>2</sub> kept at 100 °C for 56 days



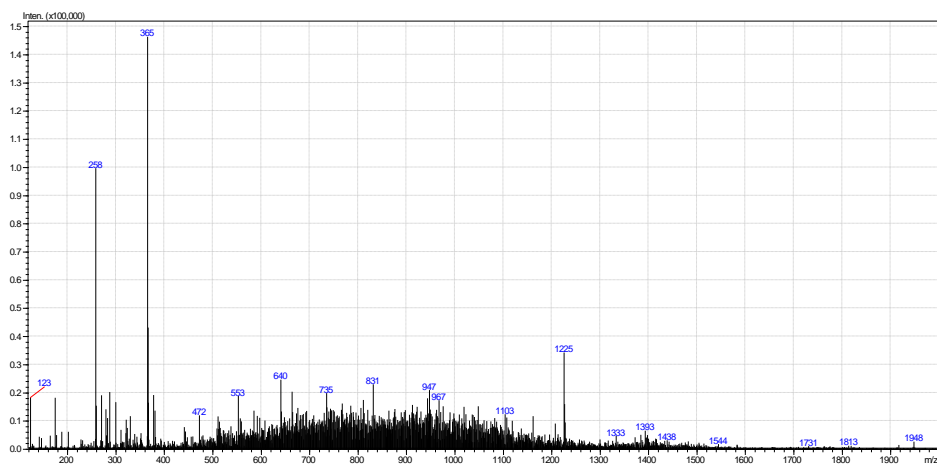


**Figure S40.** Mass spectra of the fraction (retention time 7.5 to 7.8 min) detected in the sample prepared from encapsulated film containing MAPbBr<sub>3</sub> and spiro[TFPI]<sub>2</sub> kept at 100 °C for 56 days

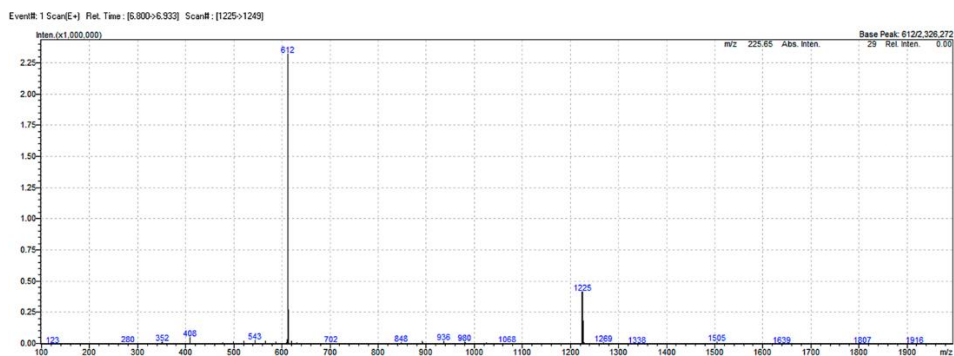


**Figure S41.** Mass spectra of the first fraction (retention time 6.9 min) detected in the sample prepared from the pure spiro[TFPI]<sub>2</sub>

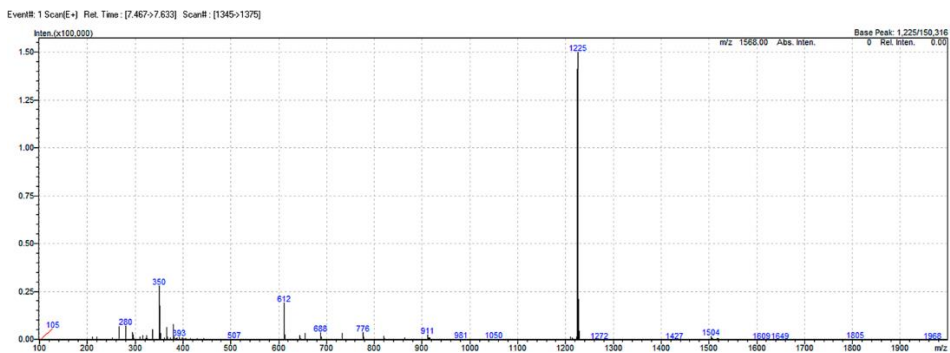


**Figure S42.** Mass spectra of the second fraction (retention time 7.6 min) detected in the sample prepared from the pure spiro[TFSI]<sub>2</sub>

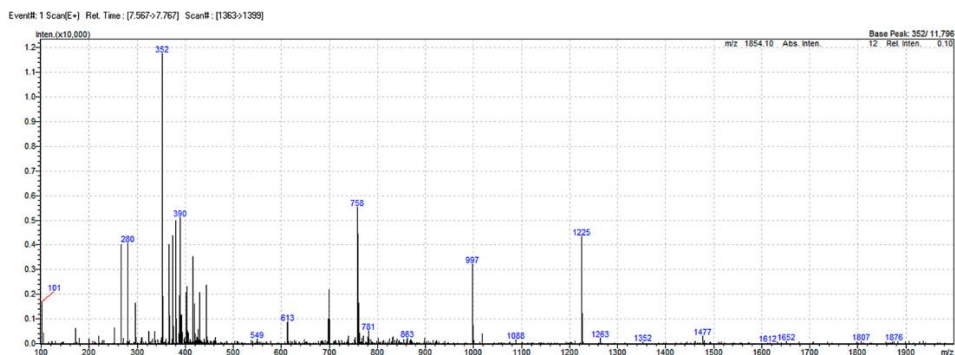


**Figure S43.** Mass spectra of the pure spiro-OMeTAD (retention time 7.6 min)

## Experiments with MAPbI<sub>3</sub> perovskite

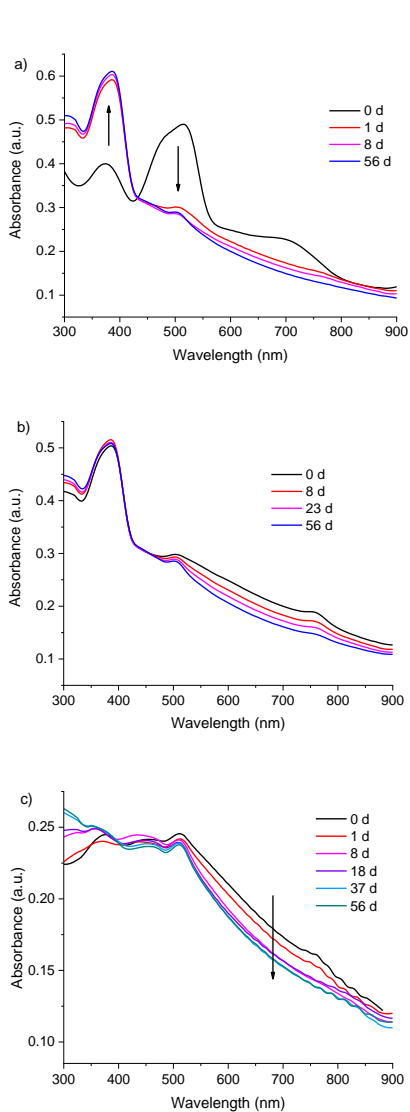


**Figure S44.** Stability of the encapsulated spiro[TFSI]<sub>2</sub> (a), spiro-OMeTAD (b) films on MAPbI<sub>3</sub> perovskite as well as pristine perovskite (c) at 100 °C in the dark

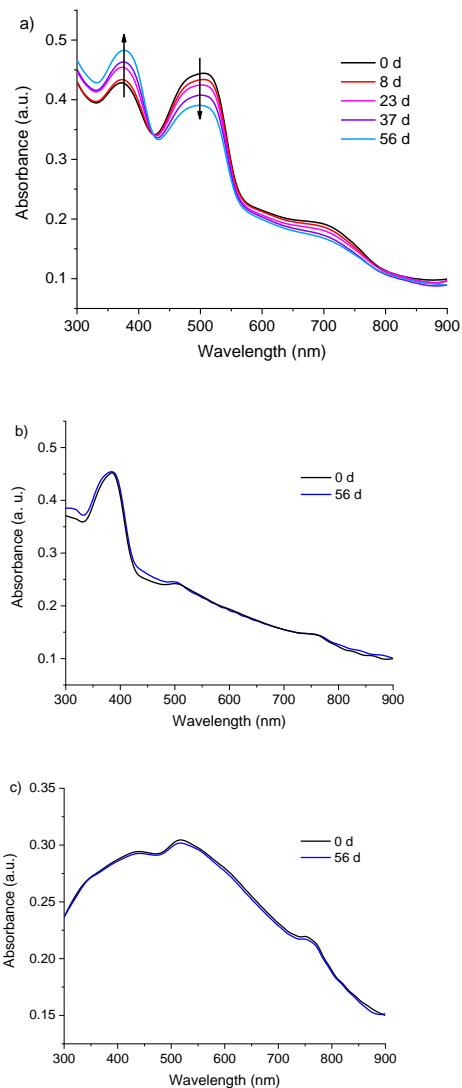


**Figure S45.** Stability of the encapsulated spiro[TFSI]<sub>2</sub> (a), spiro-OMeTAD (b) films on MAPbI<sub>3</sub> perovskite as well as pristine perovskite (c) at RT in the dark

Experiments with  
 $\text{MA}_{0.17}\text{FA}_{0.83}\text{Pb}(\text{I}_{0.83}\text{Br}_{0.17})_3$  perovskite

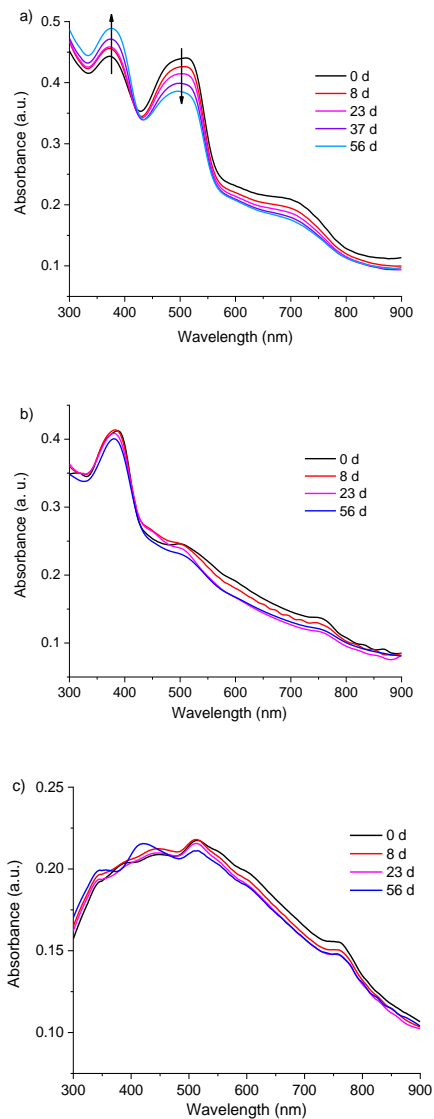


**Figure S46.** Stability of the encapsulated spiro[TFSI]<sub>2</sub> (a), spiro-OMeTAD (b) films on  $\text{MAPbI}_3$  perovskite as well as pristine perovskite (c) at RT under ambient light

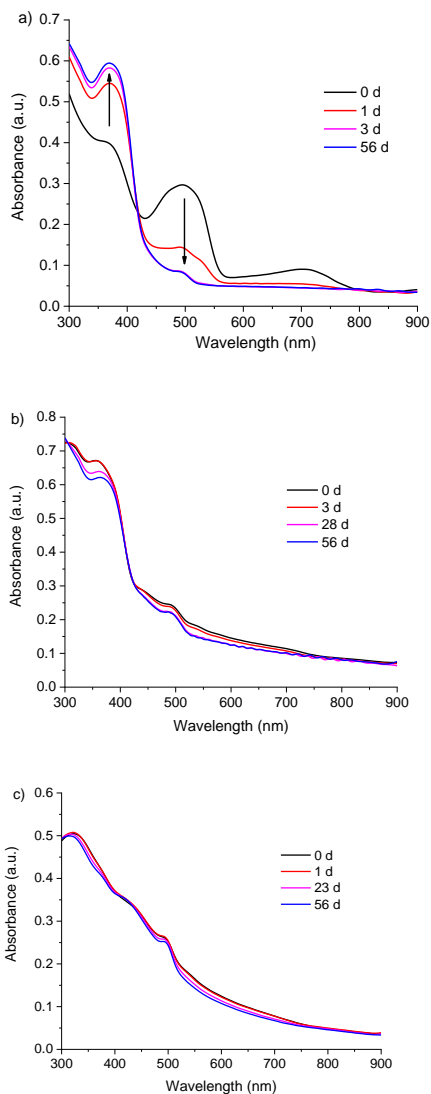


**Figure S47.** Stability of the encapsulated spiro[TFSI]<sub>2</sub> (a), spiro-OMeTAD (b) films on  $\text{MA}_{0.17}\text{FA}_{0.83}\text{Pb}(\text{I}_{0.83}\text{Br}_{0.17})_3$  perovskite as well as pristine perovskite (c) at 100 °C in the dark

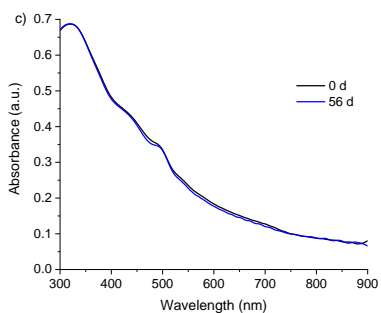
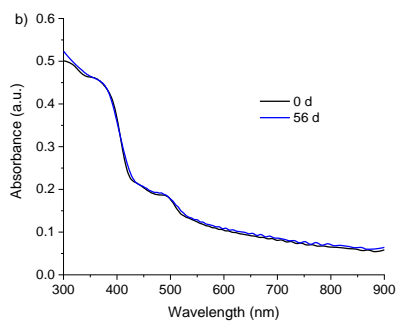
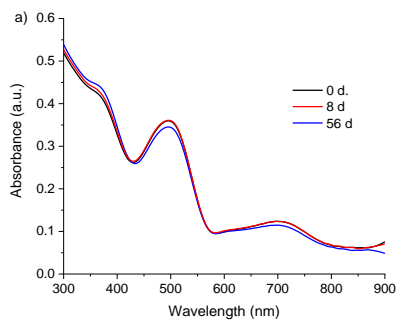


**Figure S48.** Stability of the encapsulated spiro[TFSI]<sub>2</sub> (a), spiro-OMeTAD (b) films on MA<sub>0.17</sub>FA<sub>0.83</sub>Pb(I<sub>0.83</sub>Br<sub>0.17</sub>)<sub>3</sub> perovskite as well as pristine perovskite (c) at RT in the dark

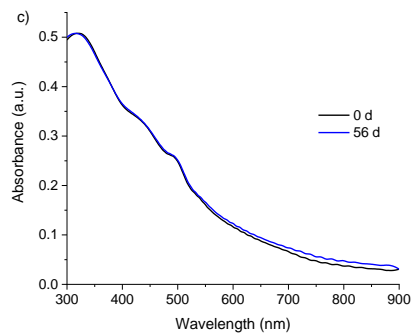
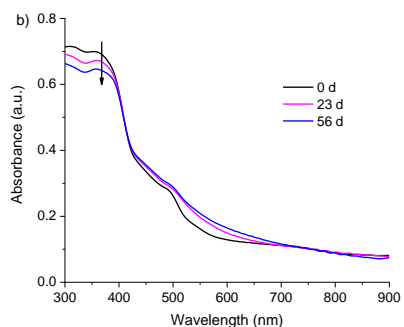
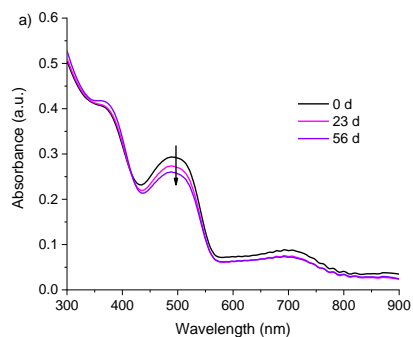


**Figure S49.** Stability of the encapsulated spiro[TFSI]<sub>2</sub> (a), spiro-OMeTAD (b) films on MA<sub>0.17</sub>FA<sub>0.83</sub>Pb(I<sub>0.83</sub>Br<sub>0.17</sub>)<sub>3</sub> perovskite as well as pristine perovskite (c) at RT under ambient light

Experiments with  
 $\text{Cs}_{0.05}(\text{MA}_{0.17}\text{FA}_{0.83})_{0.95}\text{Pb}(\text{I}_{0.83}\text{Br}_{0.17})_3$   
 perovskite

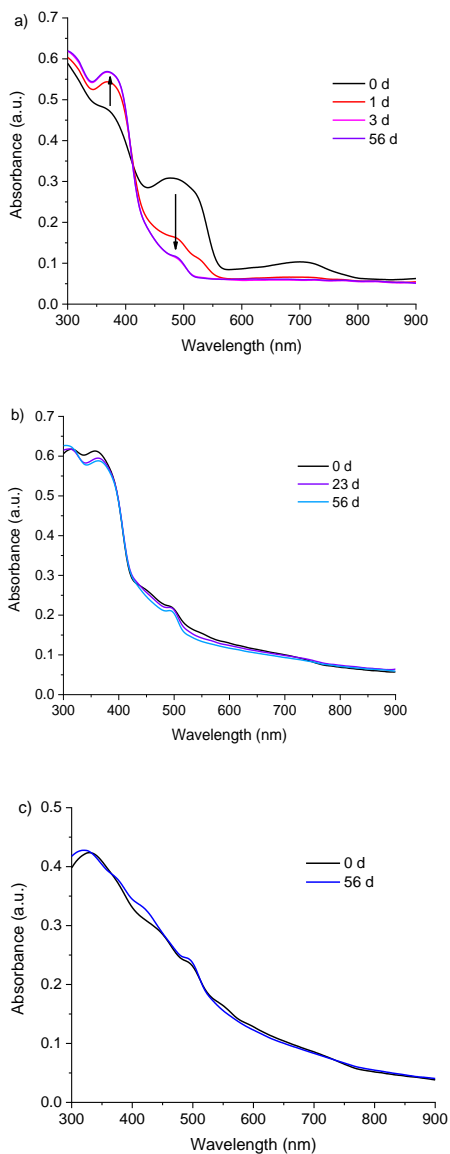


**Figure S50.** Stability of the encapsulated spiro[TFSI]<sub>2</sub> (a), spiro-OMeTAD (b) films on  $\text{Cs}_{0.05}(\text{MA}_{0.17}\text{FA}_{0.83})_{0.95}\text{Pb}(\text{I}_{0.83}\text{Br}_{0.17})_3$  perovskite as well as pristine perovskite (c) at 100 °C in the dark

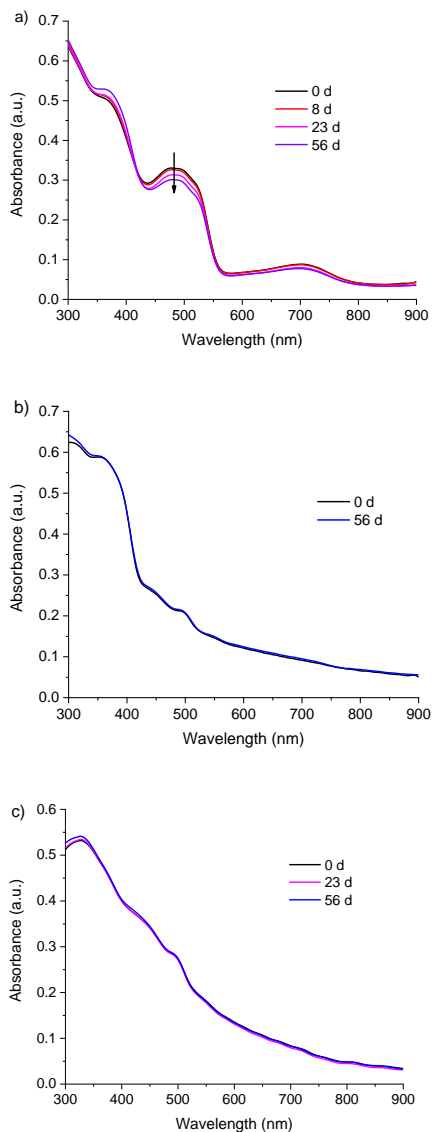


**Figure S51.** Stability of the encapsulated spiro[TFSI]<sub>2</sub> (a), spiro-OMeTAD (b) films on  $\text{Cs}_{0.05}(\text{MA}_{0.17}\text{FA}_{0.83})_{0.95}\text{Pb}(\text{I}_{0.83}\text{Br}_{0.17})_3$  perovskite as well as pristine perovskite (c) at RT in the dark

## Experiments

with

## FA<sub>0.83</sub>CS<sub>0.17</sub>Pb(I<sub>0.83</sub>Br<sub>0.17</sub>)<sub>3</sub> perovskite

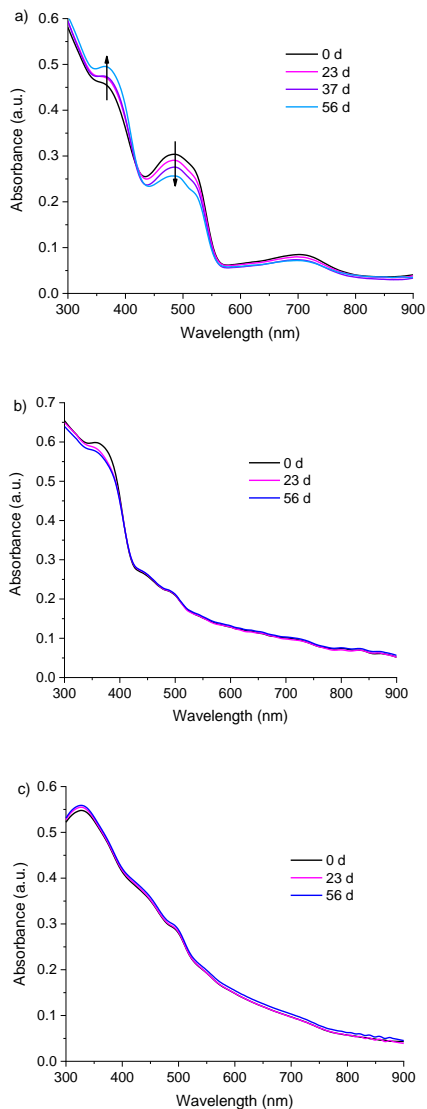


**Figure S52.** Stability of the encapsulated spiro[TFSI]<sub>2</sub> (a), spiro-OMeTAD (b) films on Cs<sub>0.05</sub>(MA<sub>0.17</sub>FA<sub>0.83</sub>)<sub>0.95</sub>Pb(I<sub>0.83</sub>Br<sub>0.17</sub>)<sub>3</sub> perovskite as well as pristine perovskite (c) at RT under ambient light

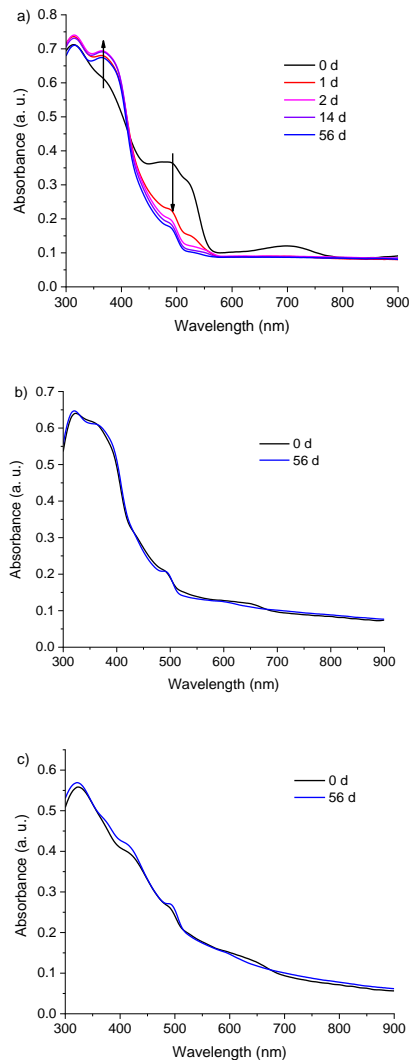


**Figure S53.** Stability of the encapsulated spiro[TFSI]<sub>2</sub> (a), spiro-OMeTAD (b) films on FA<sub>0.83</sub>CS<sub>0.17</sub>Pb(I<sub>0.83</sub>Br<sub>0.17</sub>)<sub>3</sub> perovskite as well as pristine perovskite (c) at 100 °C in the dark

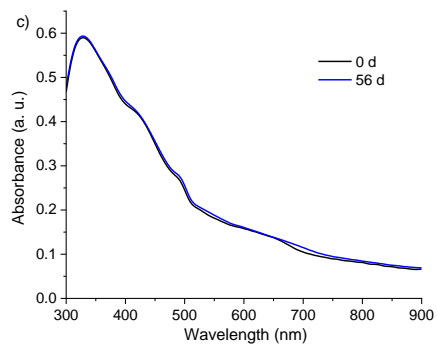
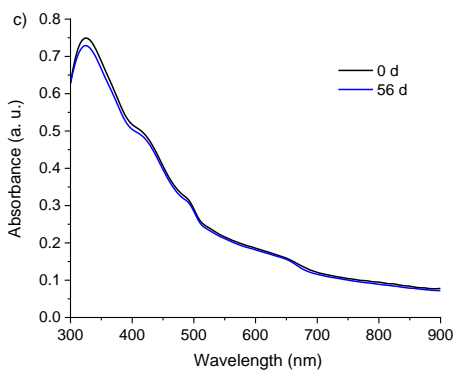
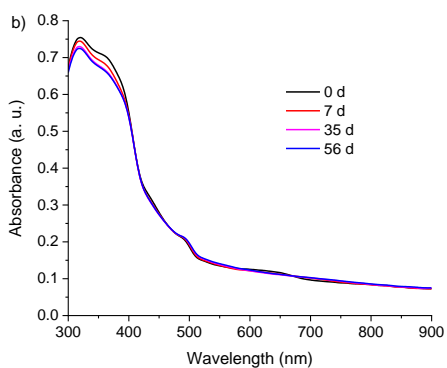
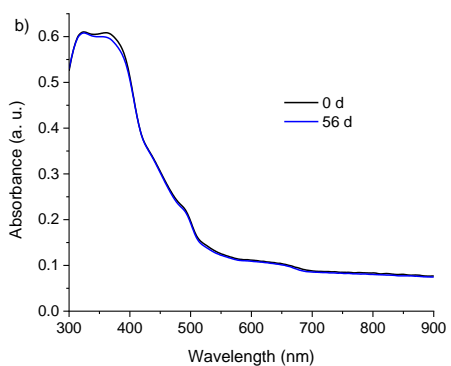
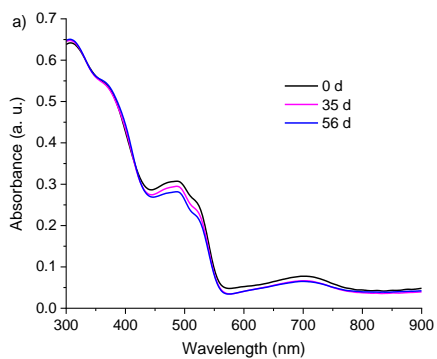
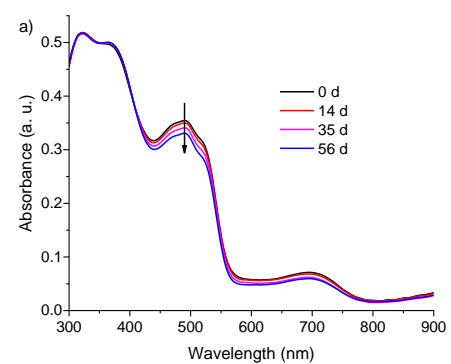


**Figure S54.** Stability of the encapsulated spiro[TFSI]<sub>2</sub> (a), spiro-OMeTAD (b) films on FA<sub>0.83</sub>CS<sub>0.17</sub>Pb(I<sub>0.83</sub>Br<sub>0.17</sub>)<sub>3</sub> perovskite as well as pristine perovskite (c) at RT in the dark

**Figure S55.** Stability of the encapsulated spiro[TFSI]<sub>2</sub> (a), spiro-OMeTAD (b) films on FA<sub>0.83</sub>CS<sub>0.17</sub>Pb(I<sub>0.83</sub>Br<sub>0.17</sub>)<sub>3</sub> perovskite as well as pristine perovskite (c) at RT under ambient light



## Experiments with MAPbBr<sub>3</sub>

perovskite

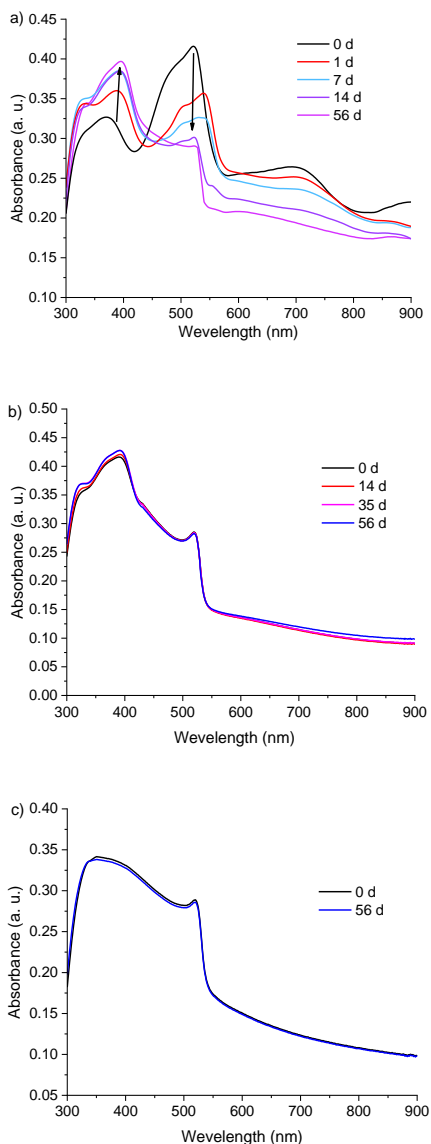


**Figure S56.** Stability of the encapsulated spiro[TFSI]<sub>2</sub> (a), spiro-OMeTAD (b) films on MAPbBr<sub>3</sub> perovskite as well as pristine perovskite (c) at 100 °C in the dark

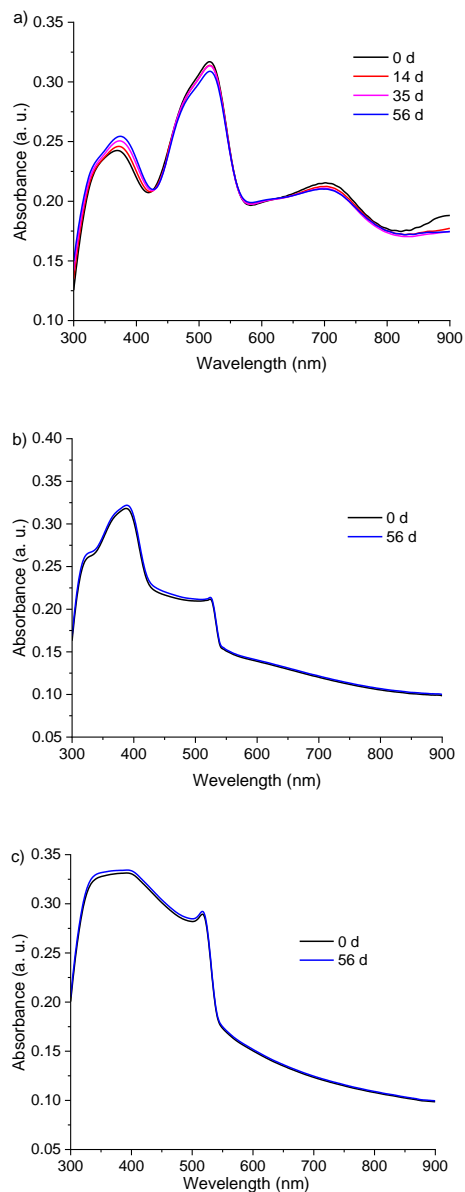


**Figure S57.** Stability of the encapsulated spiro[TFSI]<sub>2</sub> (a), spiro-OMeTAD (b) films on MAPbBr<sub>3</sub> perovskite as well as pristine perovskite (c) at RT in the dark

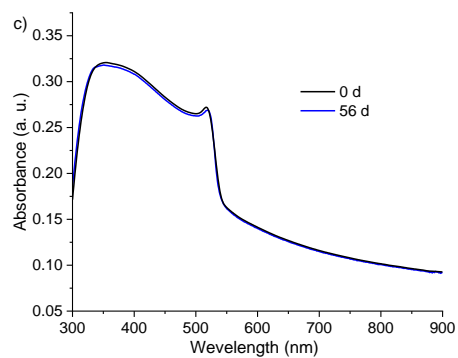
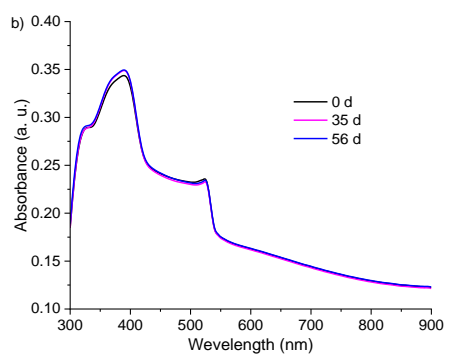
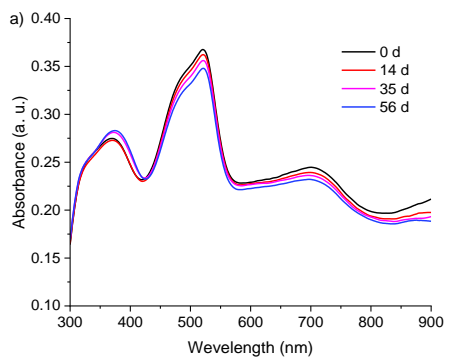


**Figure S58.** Stability of the encapsulated spiro[TFSI]<sub>2</sub> (a), spiro-OMeTAD (b) films on MAPbBr<sub>3</sub> perovskite as well as pristine perovskite (c) at RT under ambient light

## 10. ACKNOWLEDGEMENTS

The author of the dissertation is the most grateful to Assoc. Prof. Dr. T. Malinauskas for comprehensive assistance, useful advices in conducting research and studies as well as patience in editing this work.

Sincere appreciations are sent to Prof. Dr. V. Getautis (Department of Organic Chemistry, Kaunas University of Technology) for giving an opportunity to work in his research group and Dr. M. Daškevičienė (Department of Organic Chemistry, Kaunas University of Technology) for helpful advice.

Feeling especially thankful to Prof. Dr. Steve Albrecht, Amran Al-Ashouri, Eike Köhnen, Bor Li, Pietro Caprioglio, Dorothee Menzel, Max Grischek, Lukas Kegelmann, Marko Jošt (Young Investigator Group Perovskite Tandem Solar Cells, Helmholtz-Zentrum Berlin) for the fabrication and characterization of the PSCs.

The author of the dissertation would like to kindly thank Dr. B. Barvainienė, A. Urbonavičienė, Dr. L. Pečiulytė, Dr. P. P. Danilovas, Dr. J. Simokaitienė, Dr. G. Ragaitė and A. Bieliauskas (Faculty of Chemical Technology, Kaunas University of Technology) for their help with elemental analysis, MS, DSC, TGA, NMR measurements.

Special thanks go to Dr. V. Gaidelis, Assoc. Prof. Dr. V. Jankauskas (Institute of Chemical Physics, Vilnius University) for the measurements of ionization potentials, charge carrier mobilities.

Sincere thanks go to colleagues: Dr. A. Magomedov, Dr. S. Urnikaitė, M. Steponaitis, Dr. K. Rakštys, Dr. Titas Braukyla (Department of Organic Chemistry, KTU) and others for their help, advice, encouragement and for keeping the atmosphere warm.

Moreover, warm thanks go to the family and friends for their patience and support over the long years of studies.

SL344. 2021-xx-xx, 11,5 leidyb. apsk. l. Tiražas xx egz.  
Išleido Kauno technologijos universitetas, K. Donelaičio g. 73, 44249 Kaunas  
Spausdino leidyklos „Technologija“ spaustuvė, Studentų g. 54, 51424 Kaunas